NASA Reference Publication 1080

November 1981

ATS-6 Final Engineering Performance Report

Volume VI - Scientific Experiments

NASA

NASA Reference Publication 1080

1981

ATS-6 Final Engineering Performance Report

Volume VI - Scientific Experiments

Robert O. Wales, *Editor*
Goddard Space Flight Center
Greenbelt, Maryland

National Aeronautics and Space Administration

Scientific and Technical Information Branch

An Engineering Evaluation

in

Six Volumes

This document makes use of international metric units according to the Système International d'Unités (SI). In certain cases, utility requires the retention of other systems of units in addition to the SI units. The conventional units stated in parentheses following the computed SI equivalents are the basis of the measurements and calculations reported.

For sale by the National Technical Information Service
Springfield, Virginia 22161
Price

VOLUME VI
CONTENTS

VOLUME VI
CONTENTS (continued)

VOLUME VI
CONTENTS (continued)

VOLUME VI
CONTENTS (continued)

VOLUME VI
CONTENTS (continued)

VOLUME VI
CONTENTS (continued)

VOLUME VI
CONTENTS (continued)

LIST OF ILLUSTRATIONS

VOLUME VI
CONTENTS (continued)

VOLUME VI
CONTENTS (continued)

VOLUME VI
CONTENTS (continued)

LIST OF TABLES

VOLUME VI
CONTENTS (continued)

FOREWORD

ATS-6 has been referred to as Arthur C. Clarke's "Star," because Mr. Clarke originated the idea for synchronous communications satellites in an article that he wrote in 1945. In 1975, Mr. Clarke was actively engaged in monitoring the Indian Satellite Instructional Television Experiment on ATS-6 and giving feedback to the Indian Space Research Organization. We, therefore, felt that it would be appropriate for him to contribute the foreword for this report.

An excerpt from his response to our request and selected paragraphs from his contribution, "Schoolmaster Satellite," follow.

ශ්‍රී ලංකා මොරටුව විශ්වවිද්‍යාලයේ
කුලපති කාර්යාලයෙනි

FROM THE DESK OF THE CHANCELLOR
UNIVERSITY OF MORATUWA, SRI LANKA

ආතර් සී. ක්ලාර්ක්
බී.ඇස්.සී., එෆ්.ආර්.ඒ.ඇස්., ඇෆ්.බී.අයි ඇස්.
ලන්ඩනයේ කිංග්ස් විද්‍යාලයේ අයි සාමාජික
Arthur C. Clarke
B.Sc., F.R.A.S., F.B.I.S.
Fellow of King's College, London.

ටැලිපෝනය: 94255
කේබල්: අන්ඩර්සී
කොළඹ
Tel: 94255
Cable: Undersea
Colombo

"ලෙස්ලීගෙ නිවස"
25, බාන්ස් පෙදෙස,
කොළඹ 7.
"Leslie's House"
25, Barnes Place,
Colombo 7.

24th September 1980

The extracts that follow are from an essay that was written in 1971, almost five years before the SITE program became fully operational, and originally appeared in the *Daily Telegraph Colour Magazine* for 17 December 1971. It was later read into the *Congressional Record* (27 January 1972) by Representative William Anderson, first commander of the nuclear submarine *Nautilus*, and now forms Chapter 12 of *The View From Serendip* (Random House, 1977; Ballantine, 1978).

To me, it brings back vivid recollections of my meetings with Dr. Sarabhai, the chief instigator of the program. I would like to dedicate it to his memory – and to that of another good friend, also closely associated with the project – Dr. Wernher von Braun.

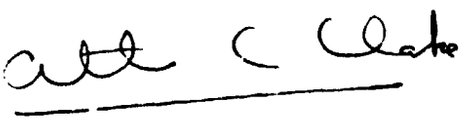

Arthur C. Clarke
Chancellor
University of Moratuwa
Sri Lanka

Arthur C. Clarke
Vikram Sarabhai Professor, Physical Research
Laboratory, Ahmedabad
India

SCHOOLMASTER SATELLITE

"For thousands of years, men have sought their future in the starry sky. Now this old superstition has at last come true, for our destinies do indeed depend upon celestial bodies—those that we have created ourselves . . .

"In 1974 there will be a new Star of India; though it will not be visible to the naked eye, its influence will be greater than that of any zodiacal signs. It will be the satellite ATS-F (Applications Technology Satellite F), the latest in a very successful series launched by America's National Aeronautics and Space Administration. For one year, under an agreement signed on September 18, 1969, ATS-F will be loaned to the Indian Government by the United States, and will be "parked" 22,000 miles above the Equator, immediately to the south of the sub-continent. At this altitude it will complete one orbit every 24 hours and will therefore remain poised over the same spot on the turning Earth; in effect, therefore, India will have a TV tower 22,000 miles high, from which programmes can be received with almost equal strength over the entire country . . .

"ATS-F, now being built by the Fairchild-Hiller Corporation, represents the next step in the evolution of communications satellites. Its signals will be powerful enough to be picked up, not merely by multi-million dollar Earth stations, but by simple receivers, costing two or three hundred dollars, which all but the poorest communities can afford. This level of cost would open up the entire developing world to every type of electronic communication—not only TV; the emerging societies of Africa, Asia and South America could thus by-pass much of today's ground-based technology, and leap straight in to the space age. Many of them have already done something similar in the field of transportation, going from ox-cart to aeroplane with only a passing nod to roads and railways.

"It can be difficult for those from nations which have taken a century and a half to slog from semaphore to satellite to appreciate that a few hundred pounds in orbit can now replace the continent-wide networks of microwave towers, coaxial cables and ground transmitters that have been constructed during the last generation. And it is perhaps even more difficult, to those who think of television exclusively in terms of old Hollywood movies, giveaway contests and soap commercials to see any sense in spreading these boons to places which do not yet enjoy them. Almost any other use of the money, it might be argued, would be more beneficial . . .

"Those who actually live in the East, and know its problems, are in the best position to appreciate what cheap and high-quality communications could do to improve standards of living and reduce social inequalities. Illiteracy, ignorance and superstitution are not merely the results of poverty—they are part of its cause, forming a self-perpetuating system which has lasted for centuries, and which cannot be changed without fundamental advances in education. India is now beginning a Satellite Instructional Television Experiment (SITE) as a bold attempt to harness the technology of space for this task; if it succeeds, the implications for all developing nations will be enormous.

"Near Ahmedabad is the big 50-foot diameter parabolic dish of the Experimental Satellite Communication Ground Station through which the programmes will be beamed up to the hovering satellite. Also in this area is AMUL, the largest dairy co-operative in the world, to which more than a quarter of a million farmers belong. After we had finished filming at the big dish, our camera team drove out to the AMUL headquarters, and we accompanied the Chief Veterinary Officer on his rounds.

SCHOOLMASTER SATELLITE

"At our first stop, we ran into a moving little drama that we could never have contrived deliberately, and which summed up half the problems of India in a single episode. A buffalo calf was dying, watched over by a tearful old lady who now saw most of her worldly wealth about to disappear. If she had called the vet a few days before–there was a telephone in the village for this very purpose–he could easily have saved the calf. But she had tried charms and magic first; they are not always ineffective, but antibiotics are rather more reliable . . .

"I will not quickly forget the haggard, tear-streaked face of that old lady in Gujerat; yet her example could be multiplied a million times. The loss of real wealth throughout India because of ignorance or superstition must be staggering. If it saved only a few calves per year, or increased productivity only a few per cent, the TV set in the village square would quickly pay for itself. The very capable men who run AMUL realise this; they are so impressed by the possibilities of TV education that they plan to build their own station to broadcast to their quarter of a million farmers. They have the money, and they cannot wait for the satellite–though it will reach an audience two thousand times larger, for over 500 million people will lie within range of ATS-F . . .

"And those who are unimpressed by mere dollars should also consider the human aspect as demonstrated by the great East Pakistan cyclone of 1971. That was tracked by the weather satellites–but the warning network that might have saved several hundred thousand lives did not exist. Such tragedies will be impossible in a world of efficient space communications.

"Yet it is the quality, not the quantity, of life that really matters. Men need information, news, mental stimulus, entertainment. For the first time in 5,000 years, a technology now exists which can halt and perhaps even reverse the flow from the country to the city. The social implications of this are profound; already, the Canadian Government has discovered that it has to launch a satellite so that it can develop the Arctic. Men accustomed to the amenities of civilisation simply will not live in places where they cannot phone their families, or watch their favourite TV show. The communications satellite can put an end to cultural deprivation caused by geography. It is strange to think that, in the long run, the cure for Calcutta (not to mention London, New York, Tokyo), may lie 22,000 miles out in space . . .

"The SITE project will run for 1 year, and will broadcast to about 5,000 TV sets in carefully selected areas. This figure may not seem impressive when one considers the size of India, but it requires only one receiver to a village to start a social, economic and educational revolution. If the experiment is as great a success as Dr. Sarabhai and his colleagues hope (and deserves), then the next step would be for India to have a full-time communications satellite of her own. This is, in any case, essential for the country's internal radio, telegraph, telephone and telex services . . .

"Kipling, who wrote a story about "wireless" and a poem to the deep-sea cables, would have been delighted by the electronic dawn that is about to break upon the sub-continent. Gandhi, on the other hand, would probably have been less enthusiastic; for much of the India that he knew will not survive the changes that are now coming.

SCHOOLMASTER SATELLITE

"One of the most magical moments of Satyajit Ray's exquisite Pather Panchali is when the little boy Apu hears for the first time the Aeolean music of the telegraph wires on the windy plain. Soon those singing wires will have gone forever; but a new generation of Apus will be watching, wide-eyed, when the science of a later age draws down pictures from the sky—and opens up for all the children of India a window on the world."

A. C. Clarke

ACKNOWLEDGMENTS

Many scientists, engineers, and technicians, too numerous to mention by name, have contributed to these volumes. Engineers at Fairchild Space and Electronics Company and Westinghouse Defense and Electronic Systems Center composed the chapters from material supplied by subsystems designers of the various systems and experiments, and have worked closely with the editors to complete this report. They have the editor's gratitude.

In particular, thanks go to Mr. Ralph Hall at Fairchild Space and Electronics Company and Mr. James Meenen of Westinghouse Defense and Electronic Systems Center for their patient cooperation, thorough review, and constructive comments and suggestions.

INTRODUCTION

ATS-6 was the final satellite in a series of six of the Applications Technology Satellite Program of the National Aeronautics and Space Administration. It was designed and built by Fairchild Space and Electronics Company, Germantown, Maryland, under NASA Contract NAS5-21100 from NASA Goddard Space Flight Center.

At the time of its launch, it was the largest and most powerful communications satellite to go into orbit.

The mission of ATS-6 was to demonstrate and evaluate the application of new technologies for future satellite systems. This it accomplished by demonstrating the first direct-broadcast television from geosynchronous orbit; by demonstrating many new communications technologies; by relaying data from, and tracking, low-orbiting satellites; by relaying communications and positions of ships and aircraft; and by supporting a variety of other experiments involving communications, meteorology, particle and radiation measurements, and spacecraft technology.

The purpose of this report is to document the lessons learned from the 5-year ATS-6 mission that might be applicable to spacecraft programs of the future. To satisfy this purpose, the six volumes of this report provide an engineering evaluation of the design, operation, and performance of the system and subsystems of ATS-6 and the effect of their design parameters on the various scientific and technological experiments conducted.

The overall evaluation covers the following:

- A summary of the ATS-6 mission objectives, operations, and results
- A summary description of the spacecraft system and subsystem requirements, the designs evolved to meet these requirements, and special analyses and ground testing performed to validate these designs and to confirm the flight integrity of the spacecraft
- A comparative evaluation of the 5-year performance and operations in orbit relative to those specified and demonstrated during ground tests prior to launch
- A summary of anomalies that occurred in the hardware, probable causes, and recommendations for future spacecraft systems
- A summary evaluation of the various technological and scientific experiments conducted
- A summary of conclusions and recommendations at the spacecraft system and subsystems levels that address considerations that might be relevant to future spacecraft programs or similar experiments.

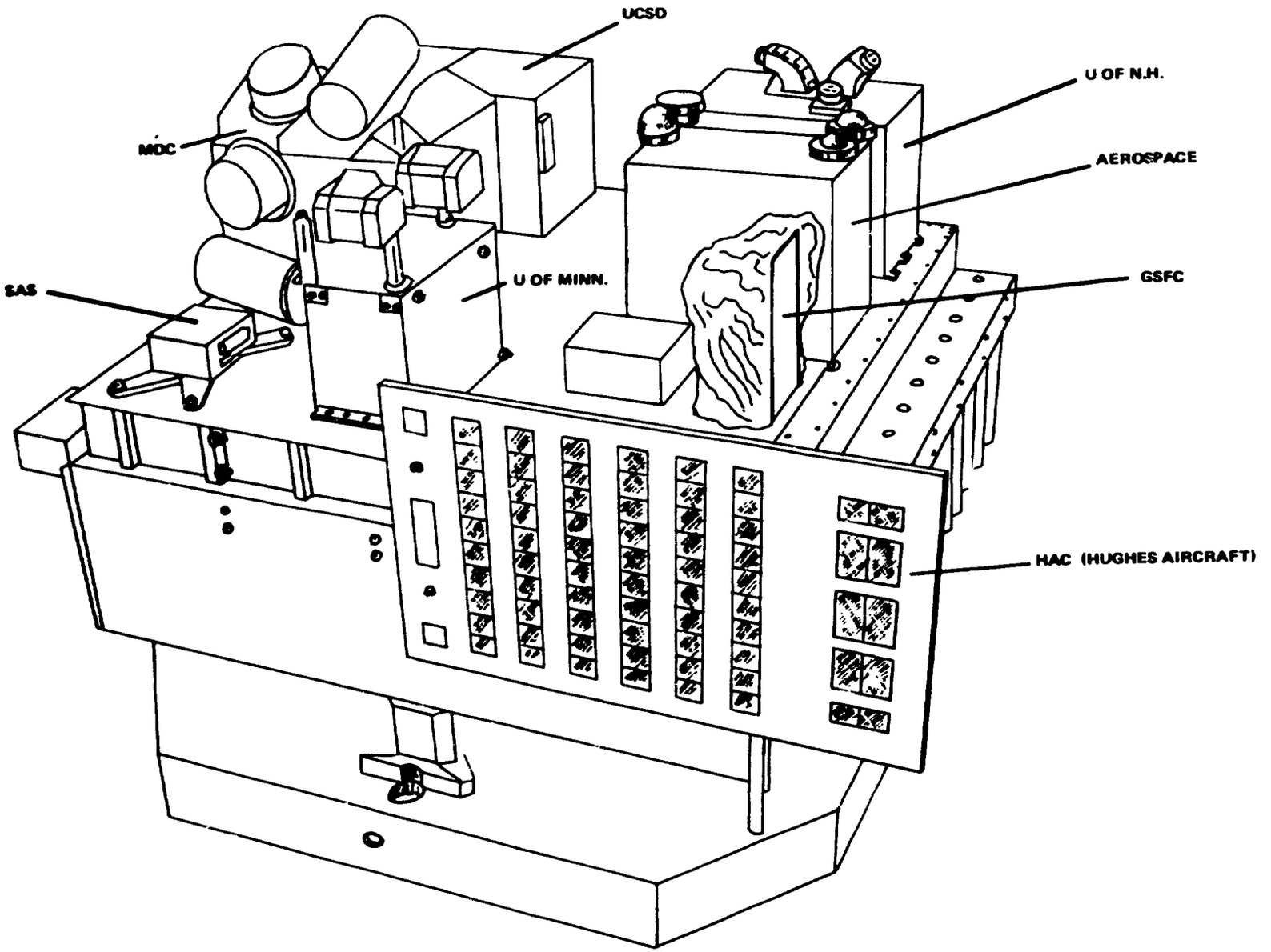

Environmental Measurements Experiment

ATS-6

Final Engineering Performance Report

Volume VI

CHAPTER 1

VERY HIGH RESOLUTION RADIOMETER

INTRODUCTION

The ATS-6 Very High Resolution Radiometer (VHRR) was the first such instrument to be installed on a three-axis stabilized geosynchronous satellite for meteorological purposes. The stable platform provided by ATS-6 made it possible to take many sequential pictures of the same meteorological event with much better resolution than was provided by previous radiometers. The forerunners of the VHRR were mounted on spin-stabilized satellites and looked at the Earth once every spin or 20 degrees out of 360 degrees. ATS-6 could be pointed so that the radiometer could view the Earth continuously.

The primary objectives of this experiment were to determine wind velocities from the motion of cloud formations, to study the life cycles of severe local storms, tropical and extratropical cyclones, and to investigate improved methods of determining the temperatures of the land and sea surfaces and of cloud tops.

DESIGN DESCRIPTION

The VHRR instrument consisted of two separate packages. The optical package contained the sensors and their associated lenses, filters, mirrors, calibration sources, and temperature control devices. The electronics package contained the circuitry for supplying power, processing the data stream, and controlling and monitoring the functions of the optical package.

The optical package, which was thermally isolated from the spacecraft structure, was approximately 64 X 38 X 31 centimeters (cm) and weighed 43.5 kilograms (kg). It was installed in the northwest corner of the spacecraft Earth-viewing module with the optical port on the Earth-viewing face and the radiant cooler on the north face. The electronics package was mounted on the spacecraft structure and used the structure as a heat sink.

Figure 1-1 is a sketch of the VHRR instrument showing the optical arrangement.

The telescope and sensors were stationary with respect to the spacecraft, and scanning of the 20-degree by 20-degree field-of-view was accomplished by tilting the scan mirror in two axes. The fast-scan axis scanned alternately east and west and the slow-scan axis scanned from south to north. The instantaneous field-of-view of each of the two visible sensors was 0.15 milliradians that covered approximately a 5.5-kilometer (km) square on the Earth. The infrared (IR) sensor had an instantaneous field-of-view of 0.30 milliradians or an 11-km square on the Earth.

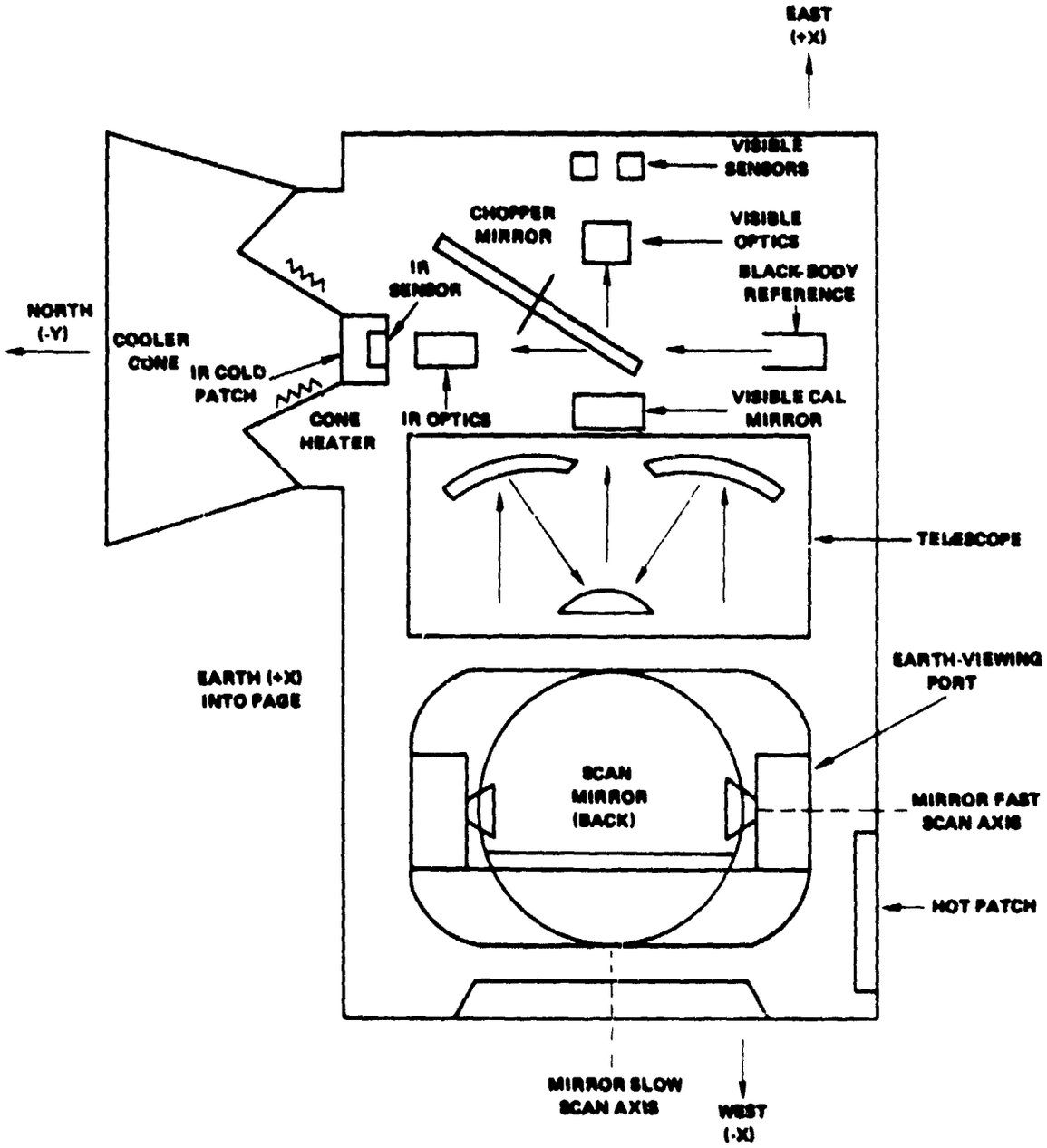

Figure 1-1. VHRR Instrument Showing Optical Arrangement (Sheet 1)

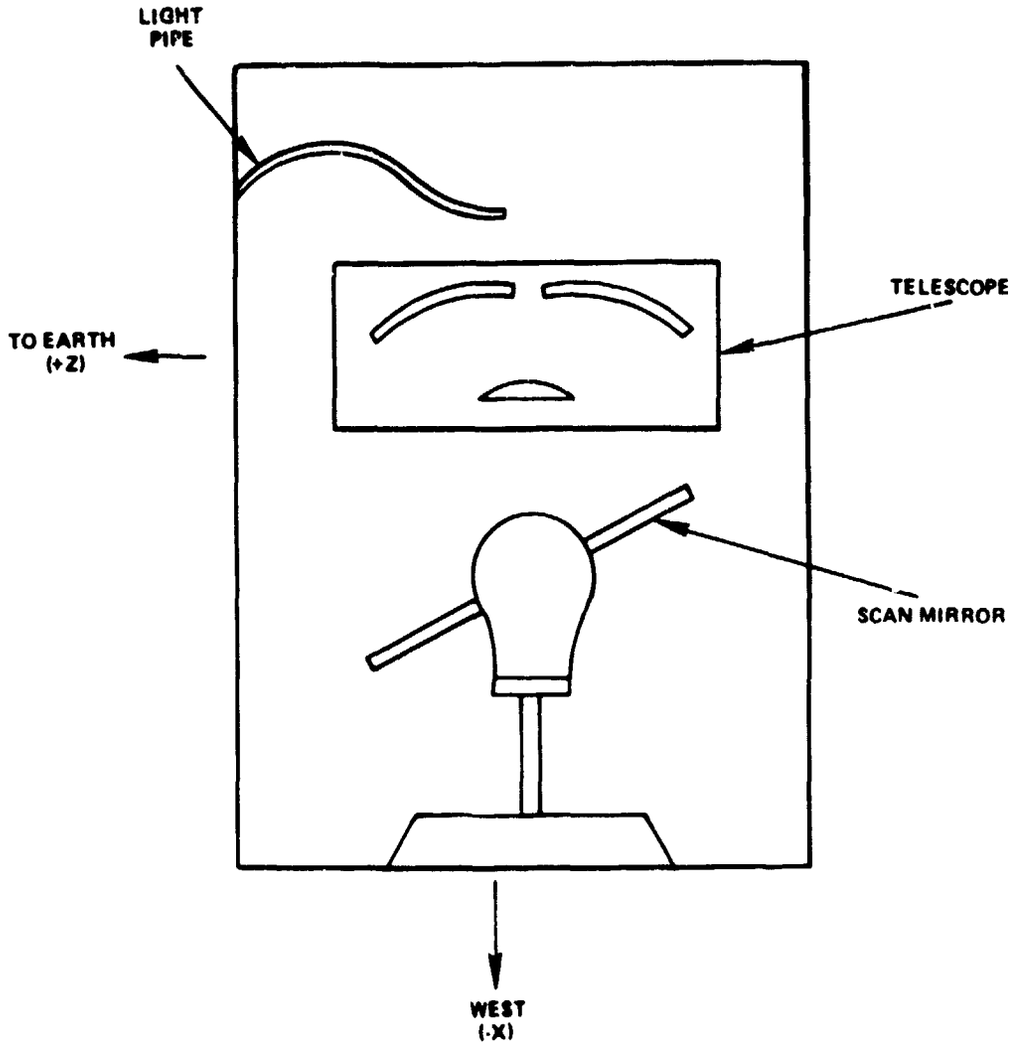

Figure 1 1. VHRR Instrument Showing Optical Arrangement (Sheet 2)

A reflective chopper wheel, which rotated at 3000 revolutions per minute (rpm) was located in the light path between the telescope and the visible sensors so that when a tooth of the wheel was in the path, the image would be reflected 90 degrees to the IR sensor, and when a tooth was not in the path, the image would pass between the teeth to the two identical visible sensors.

Calibration of the optical package was accomplished using a reference black body, a hot patch, deep space, and sunlight.

The reference black body was positioned so that when the image of the Earth was reflected off the front of a chopper wheel tooth to the IR sensor, the visible sensors saw the reference black body

by reflection off the back of the tooth. When the visible sensors saw the image between two teeth, the IR sensors saw the reference black body between the same teeth.

The hot patch was used for calibration of the IR sensor by slewing the scan mirror to look at the hot patch at the end of each complete picture sequence.

Deep space was viewed at the start and end of each scan off the edge of the Earth. This was used for the cold calibration point for both the visible and IR sensors.

A fiber-optics light pipe and mirror were incorporated in the instrument to view the Sun through a filter and the visible calibration port on the Earth-viewing side of the instrument at an appropriate time of the day. The mirror could be commanded to a position between the telescope and the chopper wheel so that the Sun would be reflected into the sensors instead of the normal Earth image. The instrument failed prior to performing the visible calibration in orbit.

A radiant cooler passively maintained the IR detector at 115 K. Automatic protection was provided against inadvertent overheating from the Sun by a shutter that would close over the inner portion of the cooler if the temperature of the IR detector reached 210 K. Decontamination of the cooler was provided by closing the Sun shutter and turning on two heaters in the cooler cone.

The electronics package contained amplifiers for each of the three sensors, analog-to-digital converters, a line-sync generator, analog and digital multiplexers, and a calibration-voltage generator to check linearity and calibration accuracy of the three amplifiers. Figure 1-2 is a block diagram of the electronics package.

The VHRR system was designed with a primary (digital) mode and a backup (analog) mode to provide redundancy in the electronics.

In the primary mode, the VHRR housekeeping telemetry was merged with the image data and relayed to the ground station via the communications subsystem C-band transmitter. In the backup mode, telemetry was available only by the normal very high frequency (vhf) telemetry from the telemetry and command subsystem.

The linearity and gain of the electronics was checked by insertion of a precise six-step calibration voltage waveform into the amplifiers at the end of each line of data.

ORBIT OPERATIONS AND PERFORMANCE

ATS-6 was launched with the VHRR chopper motor running and the radiant cooler-cone door closed. After achieving synchronous orbit, the cooler-cone heaters were commanded on for two weeks to outgas any contaminants that might have gotten into the radiant cooler.

When the heaters were turned off and the cone door opened, the patch temperature dropped to 115 K and maintained the IR detector at that temperature as long as the Sun elevation angle to the cooler remained below the design specification of 23.5 degrees.

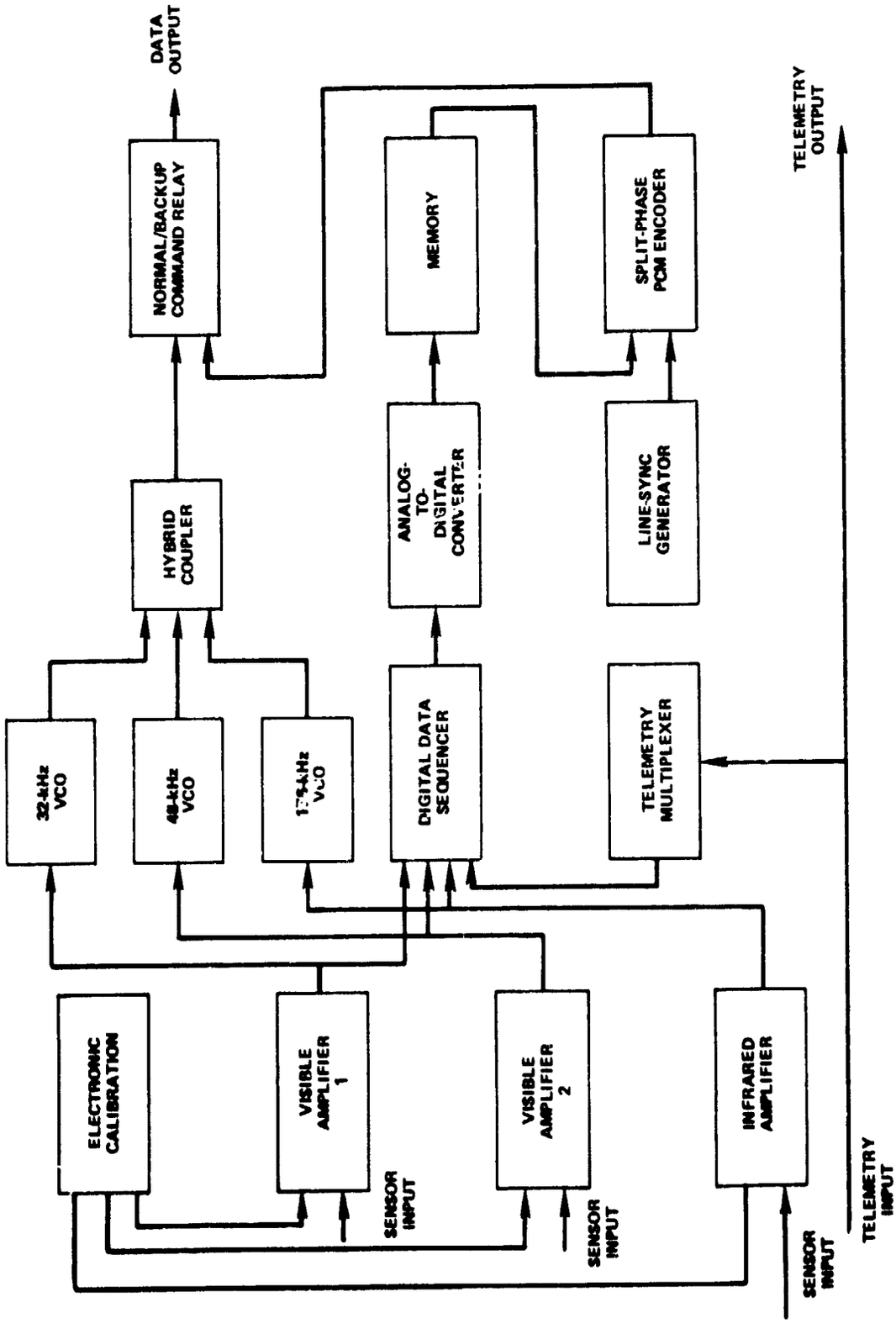

Figure 1-2. VHRR Electronics Block Diagram

During the end-of-life tests, the IR patch temperature was checked; however, the cooler-cone door was closed and, therefore, not operating. The patch temperature was 174 K.

The boresight alignment of the instrument was 1.5 degrees to the northeast of the design goal. This misalignment was easily corrected by changing the pointing of ATS-6 during VHRR operations.

Figure 1-3 is an example of a visible frame and Figure 1-4 shows an IR frame obtained in orbit.

Figure 1-3. Example of a Visible Frame

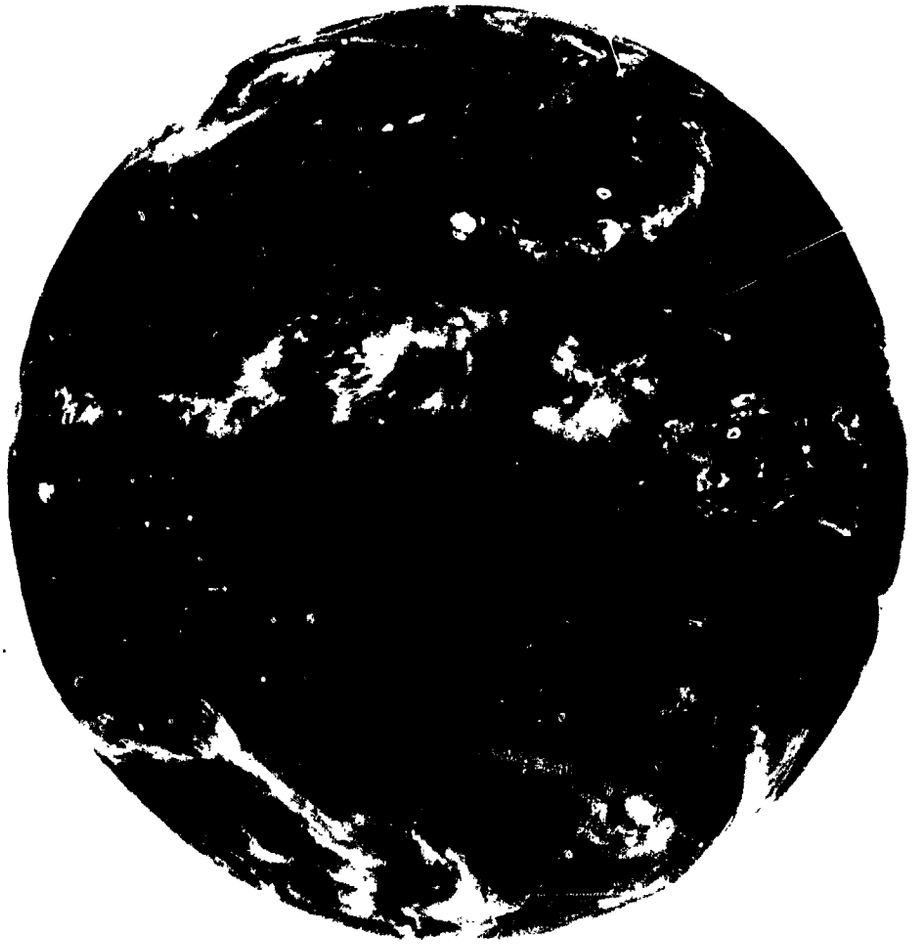

Figure 1-4. Example of an IR Frame

IN-ORBIT ANOMALIES

Shortly after launch, the spacecraft telemetry showed a slight unexplained increase in VHRR total current drain. There did not appear to be any associated degradation in performance.

The chopper motor ran continuously from before launch until its failure 2½ months after launch except for a few brief periods when it was turned off. After the instrument failed, the telemetry showed that the current drawn by the VHRR was within ten percent of the known stall current of the chopper motor. Tests of similar units on the ground did not produce any conclusive results as to why or how the failure occurred.

Unreliable scan starts and scan servo ringing were observed throughout the life of the instrument. These occurrences complicated the data reduction process, but were satisfactorily overcome.

CONCLUSIONS AND RECOMMENDATIONS

Analysis of the VHRR data showed that estimating wind velocities from the movement of clouds is feasible.

The VHRR instrument failed in mid-August, prior to the 1974 hurricane season, resulting in a complete lack of severe storm data.

Analysis of cloud and Earth surface temperature was not performed.

The multimission ATS-6 was not an ideal vehicle for a meteorological instrument like the VHRR. Many of the experiments on ATS-6 required the spacecraft to be aimed at points on the Earth that were incompatible with the VHRR, and many used so much power that they could not be performed simultaneously with the VHRR. These incompatibilities required advanced scheduling of ATS-6 usage, whereas, the VHRR experimenter would have preferred to have priority during significant meteorological events.

CHAPTER 2

RADIO BEACON EXPERIMENT

INTRODUCTION

Experiment Objectives

The Radio Beacon Experiment (RBE) provided a multifrequency spacecraft-to-ground link for investigating the mechanisms of radio propagation through the Earth's plasmasphere and ionosphere. Three coherently related modulated carriers were used simultaneously operating near the frequencies of 40 megahertz (MHz), 140 MHz, and 360 MHz. This technique enabled unambiguous measurement of phase and Faraday rotation of polarization of the received signals for the determination of the columnar electron content, its density distribution along the propagation path, and its geographic and temporal variations. The geosynchronous orbit of the beacon, for the first time, permitted measurements with high-time resolution for fixed geographic-geomagnetic propagation path configuration.

The specific areas of investigation included the behavior of the plasmasphere during and following plasmaspheric storms, solar flare effects, large and small scale structures, including traveling disturbances, micropulsations, diffraction effects of small intense ionospheric lenses, and further study of radio scintillation.

Participants

In 1970, K. Davies of the Space Environment Laboratory (SEL) of the National Oceanic and Atmospheric Administration's Environmental Research Laboratory, Boulder, Colorado, was appointed Principal Investigator with the responsibility for coordination between experimenters and the National Aeronautics and Space Administration. R. N. Grubb of SEL, who wrote the specification for the beacon; A. deRosa of Stanford University, United States; G. H. Hartmann of the Max-Planck Institute fuer Aeronomie, Lindau/Harz, West Germany; and R. G. Rastogi of the Physical Research Laboratory, Ahmedabad, India, were later appointed coinvestigators.

The extent of the international cooperation among the radio-beacon community is demonstrated by the number of cooperative ventures during the life of ATS-6. Table 2-1 presents some examples of these ventures.

Long before the launch of ATS-6, a forum was provided by the Cospar Satellite Beacon Group (under Panel 1 B) chaired by R. Leitinger of the Universitaet Graz, Graz, Austria. A series of symposia were held: Lindau, W. Germany, 1970; Graz, Austria, 1972; Moscow, U.S.S.R., 1974; Boston,

Table 2-1
Examples of ATS-6 Cooperation Between Organizations
on an International Basis

Organizations	Stations	Investigators
Phase 1 – 94°W Longitude		
NOAA + MPIA + Graz	Boulder (F, G, A)*, Fort Morgan (F), Elbert (F) Bozeman (F, G, A), Dallas (F, G, A)	Davies, Hartmann Leitinger
GDR Acad. Sci. + Cuba Acad. Sci.	Havana (F)	Felske Luzo
IZMIRAN Cuba Acad. Sci.	Havana (F)	Sinel'nikov Jiminez
Phase 2 – 35°E Longitude		
NOAA + PRL	Ootacamund (F, G, A)	Davies, Rastogi
Univ. Ill. + Polish Acad. Sci.	Warsaw (F, G, A)	Yeh, Wernik
Wales + AFGL	Aberystwyth (F, G), Boston (F, G)	Kersley, Klobuchar
PRL + AFGL	Ahmedabad (F, G, A)	Rostogi, Klobuchar
MPAE + Graz	Lindau (F, G, A), Graz (F, G, A)	Hartmann. Leitinger
Israel + Ft. Monmouth	Haifa (F)	Soicher, Keroub
Phase 3 – 140°W Longitude		
Alcorn St. Univ. + Graz	Lorman, Miss. (F, G)	Paul, Leitinger
Lancaster + Geophys. Inst.	Fairbanks, Aka. (F, G)	Hargreaves, Hunsucker

*G = group delay, F = Faraday rotation, A = amplitude

Massachusetts, United States, 1976; and Florence, Italy, 1978. A great deal of information on the ATS-6 Radio Beacon Experiment and other beacons is available from the proceedings of these symposia.

This report relies heavily on the information contained in technical papers provided by K. Davies, the Principal Investigator, concerning the various investigations made with the beacon.

Experiment Scheduling

The Radio Beacon Experiment was designed to operate continuously throughout the life of ATS-6. Prime power limitations during the equinox periods and beacon interference to other experiments prevented meeting this goal. In this regard, operation of the radio beacon was relegated to a low order of priority with relation to the other onboard experiments.

SYSTEM DESCRIPTION

General Description

The radio beacon package consisted of a low-power, three-frequency transmitter, and an array of half V-beam antennas. The transmitter was mounted in the communications module of the Earth-viewing module (EVM) and the antennas were mounted on the east and west face as shown in Figure 2-1.

A block diagram of the transmitter is shown in Figure 2-2. The three carriers near 40, 140, and 360 MHz and the modulation frequencies were derived from a pair of redundant 20-MHz oscillators and synthesizers. After multiplication and filtering to generate the common frequencies, the carriers were double-sidebanded, partially suppressed, carrier-modulated and then amplified to the required power level by wideband power amplifiers.

The requirement to maintain the 40-MHz carrier output power constant at 0.1 decibel (dB) necessitated a feedback loop for level control. Because of the presence of the amplitude envelope on the carrier, a synchronous detector with a zero-order, phase-controlled loop was used to sample the output carrier power independently of the sidebands.

The antenna design was constrained between the two XY faces of the EVM (prime-focus feed and Earth-viewing face) and the fields-of-view of the Sun sensors. A summary of the performance is presented in Table 2-2.

Physical Description

The RBE electronics packages were mounted within the communications module. Their relatively low power dissipation (23 watts) enabled them to be mounted on the east side of the transverse beam (Figure 2-3).

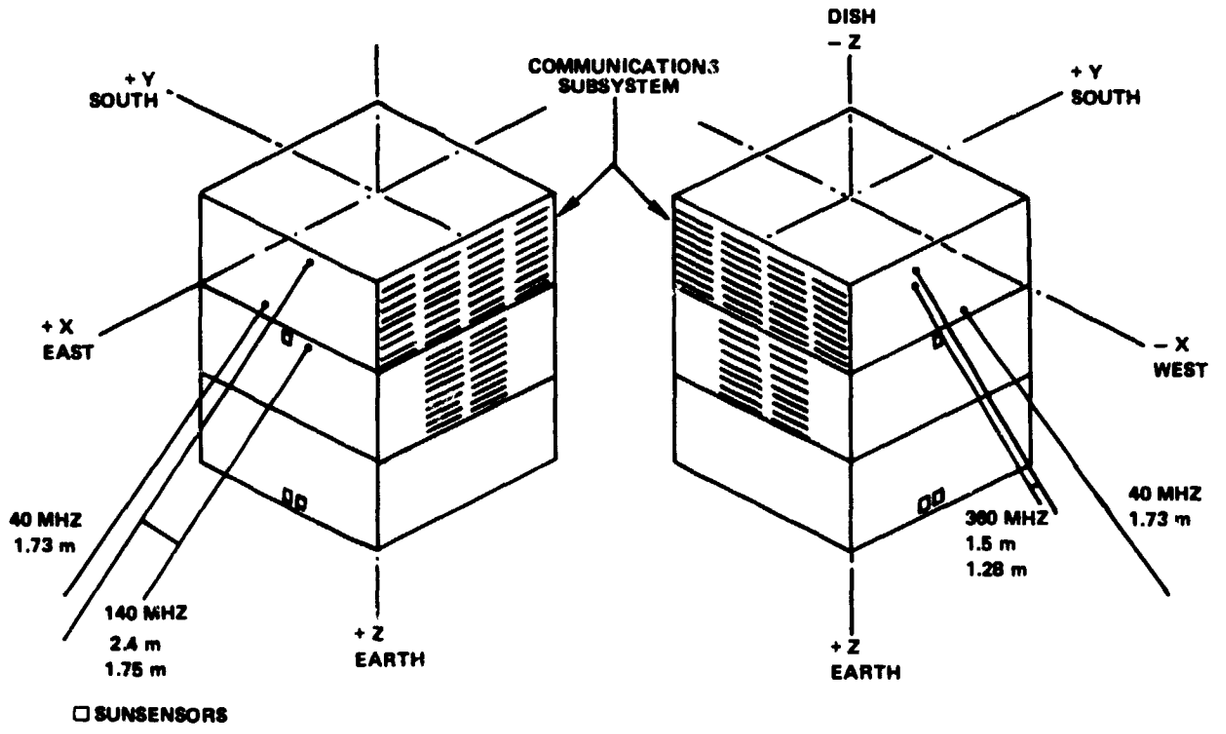

Figure 2-1. Layout Showing Location of Radio Beacon Antennas

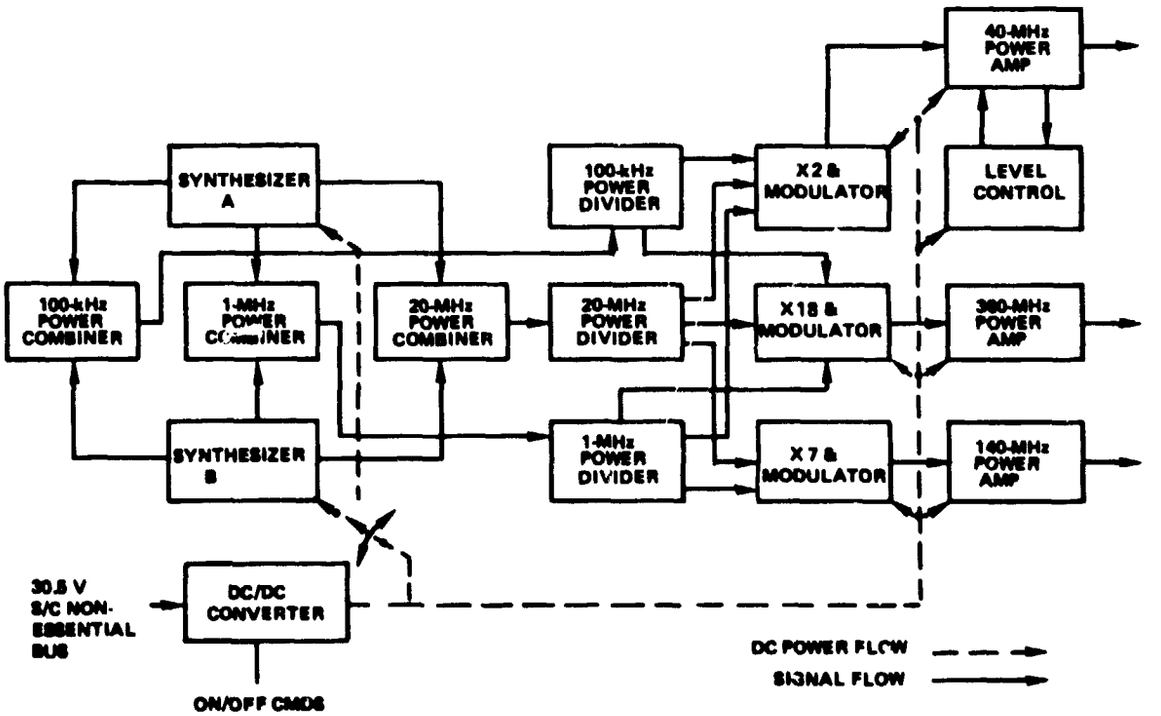

Figure 2-2. Radio Beacon Experiment Functional Block Diagram

Table 2-2
Summary of Electrical Characteristics, Prelaunch

Parameter	Value	
	Target	Actual (25°)
Effective Isotropic Radiated Power:		
40-MHz Carrier	500 mW	758 mW
100-kHz sidebands (on 40 MHz)	250 mW	239 mW
1-MHz sidebands (on 40 MHz)	250 mW	478 mW
140-MHz Carrier	1600 mW	1698 mW
1-MHz sidebands (on 40 MHz)	400 mW	426 mW
360-MHz Carrier	2000 mW	3090 mW
1-MHz sidebands (on 360 MHz)	250 mW	360 mW
100-kHz sidebands (on 360 MHz)	250 mW	295 mW
Measured Antenna Gains:		
At 40 MHz and sideband		3.2 dB
At 140 MHz and sideband		3.7 dB
At 360 MHz and sideband		4.1 dB
Transmitter Carrier Outputs at Antenna Input:		
40 MHz		363 mW
140 MHz		724 mW
360 MHz		1202 mW
1 MHz Modulation (on 40- and 140-MHz Carriers) Phase Stability	±21°	
100 kHz Modulation (on 40- and 360-MHz Carriers) Phase Stability	±2°	
100 kHz Modulation Relative to 1 MHz ÷ 10 (on 40-MHz Carrier) Phase Stability	±2°	
Frequency Stability vs. Temperature	±2 parts in 10^7	
Oscillator Aging (Preaged)/2 Year Mission	±2 parts in 10^7	
Prime Power Requirements	23 watts max.	
Qualification Temperature Range	-11°C to +53°C	
Package Size (Excluding Antenna)		3458 cu cm (35.6 cm X 13 cm X 9.4 cm)

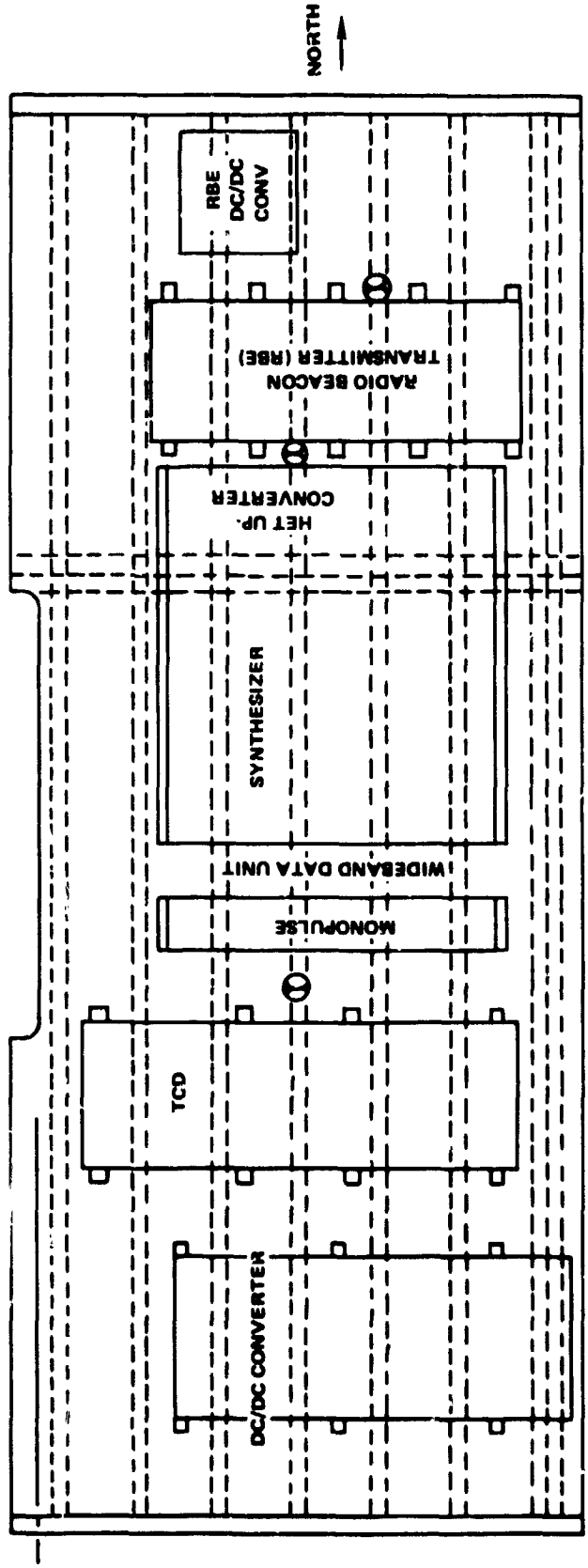

Figure 2-3. Communications Module—Transverse Beam (East Face)

The RBE antenna system consisted of three separate antennas for the three basic frequencies. These were mounted on the -X (west) side and the +X (east) side of the EVM (Figure 2-1). During launch, the antenna elements were retained within the fairing dynamic envelope by loosely-fitting, teflon-lined sheaths, as shown in Figure 2-4. The elements slid out of these during separation from the Titan III transtage and sprang into their in-orbit configuration.

Electrical Description

The major transmitter design goal was that of obtaining a high order of phase stability to enable measurement of group delay to the required precision. No means of verifying the in-orbit performance was provided; hence, great care was taken to ensure long term stability and to minimize short term environmental effects. The performance of the 20-MHz oscillator and synthesizer assemblies was crucial in obtaining the desired overall electrical performance of the beacon.

The master oscillator employed was a highly-stable, temperature compensated crystal oscillator followed by a buffer amplifier to reduce the effects of load variations on the oscillator. By employing a large capacitance-to-inductance ratio and closely controlling the mechanical layout, the effect of stray capacitance variations on frequency was minimized. A series operated third-overtone crystal, preaged for stability, was used to enable widerange temperature compensation. Compensation was

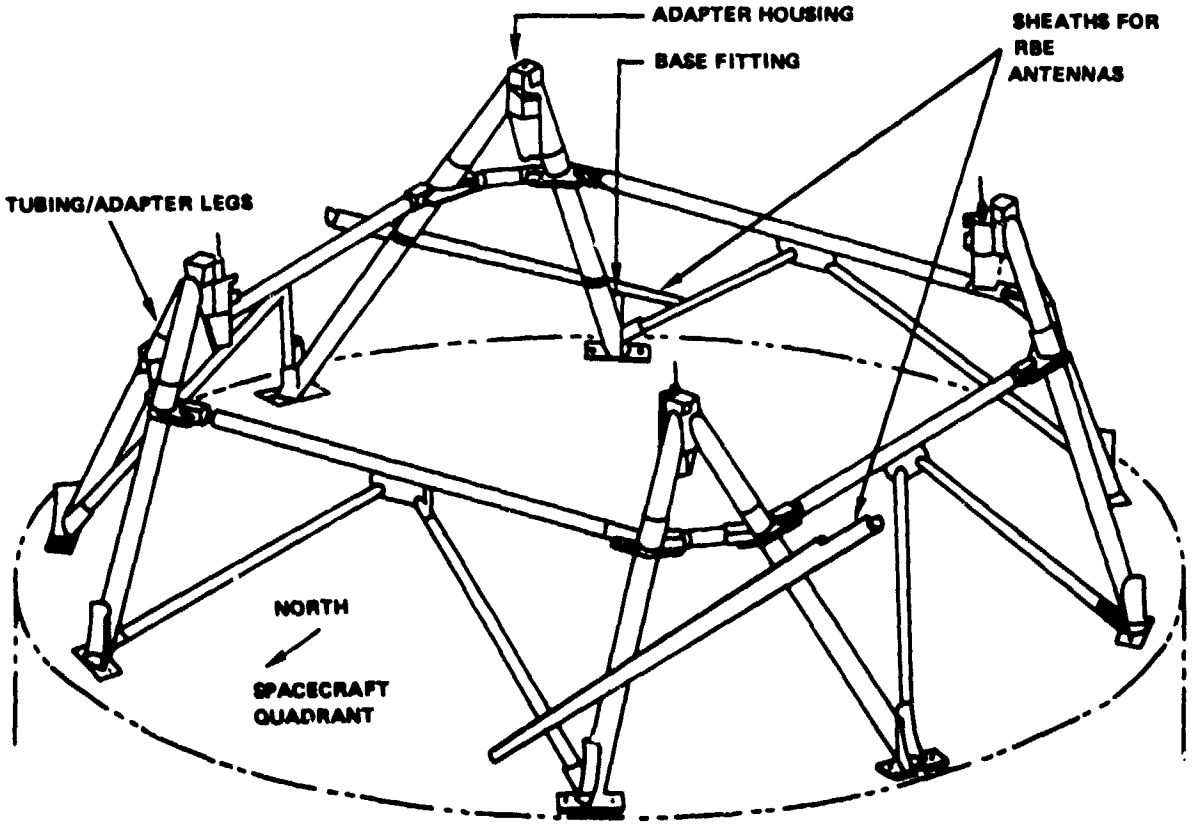

Figure 2-4. Separation Adapter Assembly Showing RBE Sheaths

achieved by a thermistor-diode-capacitor network that sensed the temperature and retuned the oscillator circuit to offset the frequency shift. The short term frequency stability was obtained by using a 2N918 transistor biased for minimum noise.

The buffer amplifier used a 2N2369 transistor in a common base configuration operating at a point for minimum noise figure and maximum power gain. The output power was 0.2 milliwatt (mW) delivered to a 50-ohm load. The performance specifications of the oscillator are summarized in Table 2-3. Typical frequency stability with temperature for the flight unit is shown in Figure 2-5.

A detailed block diagram of the radio beacon transmitter is shown in Figure 2-6. Synthesis of the various frequencies began with the 20-MHz signal from each of the redundant master oscillators, after buffer-amplification, by means of a hybrid divider. One portion of the divider output was used to drive the multiplication stages and amplifiers that generated the three radio frequency carriers. The other portion was fed to dividers and filters that generated the 1-MHz and 100-kilohertz (kHz) modulation signals. The duplicated outputs of the redundant chains were respectively fed to hybrid power combiners. This arrangement enabled a changeover between the two synthesizers to be performed by simply switching the direct current (d.c.) power from one to the other.

The 20-MHz signal from the power combiner was fed to a hybrid that split the signal into two paths. One path was applied to an X7 multiplier and amplifier to drive the 140-MHz modulator and power amplifier. The other path fed another hybrid divider that again divided the 20-MHz signal

Table 2-3
Master Oscillator Performance Characteristics

Parameter	Specifications
Frequency vs. temperature (qualification test)	Freq = ±1 part in 10^6 for a temperature range of -11°C to 53°C.
Frequency vs. temperature (acceptance test)	Freq = ±2 parts in 10^7 for a temperature range of 5°C to 38°C.
Frequency accuracy at 19°C	±1 part in 10^7
Power output	0.2 mW delivered to a 50-Ω load.
Short term stability measured at 20 MHz	1 part in 10^{-10} for 0.25-sec average time.
Power consumption at 25°C	200 mW, maximum
Supply voltage variation effect on frequency at 25°C (v_s ±10 percent)	Less than 3 parts in 10^7 measured at 25°C.
Size	6.17 X 4.14 X 2.03 or 51.9 cu cm
Weight	71 grams

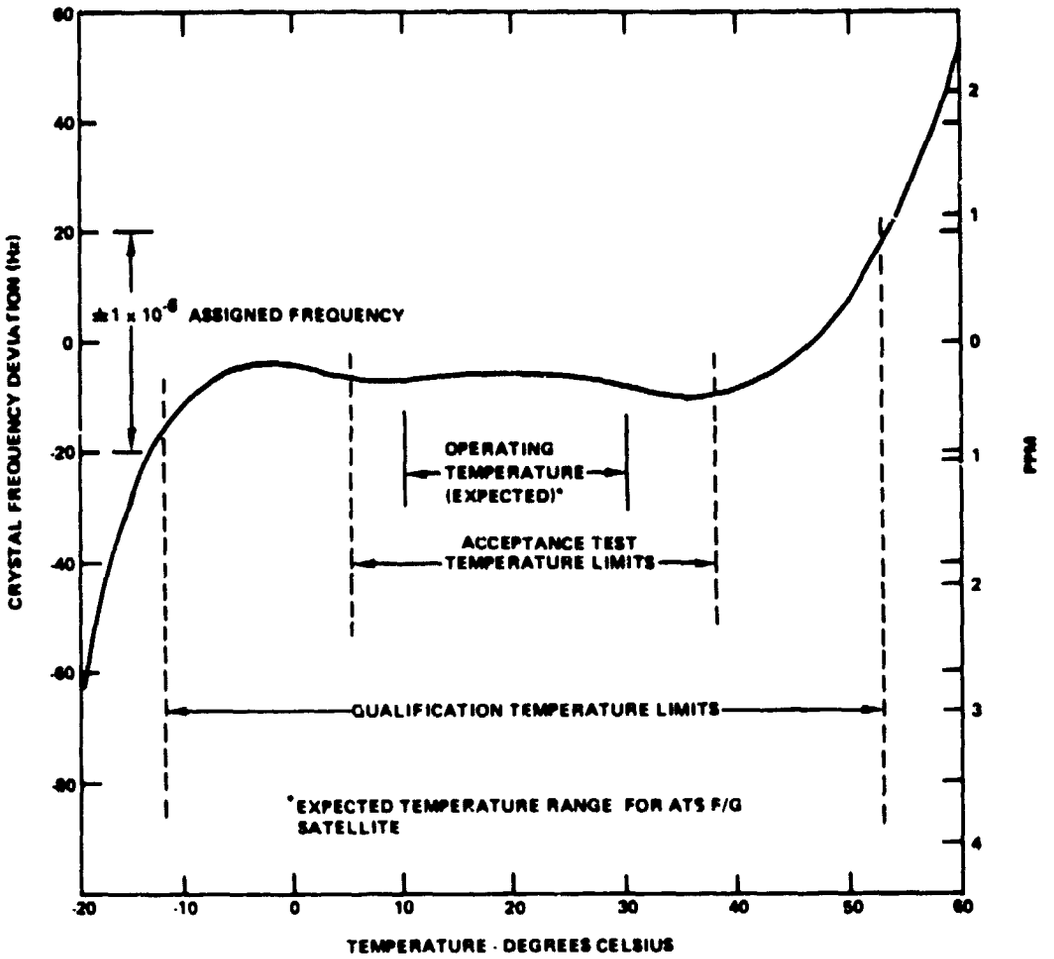

Figure 2-5. Frequency Deviation vs. Temperature Curve

into two paths. One path drove an X2 multiplier, bandpass filter, and amplifier for deriving the 40-MHz signal; the other path fed cascaded X6 and X2 multiplier stages and an amplifier that drove the modulator and power amplifier for the 360-MHz carrier. A diode-ring double balanced modulator with appropriate bias to control the partially suppressed carrier was used in each chain.

Each of the three power amplifiers consisted of two stages. The first stage was a common-emitter driver operating in a Class A mode. The second stage employed a push-pull Class B configuration. This approach was used to minimize amplitude modulation distortion while conserving supply power.

To maintain the 40-MHz carrier output power level constant to within ±0.1 dB, it was necessary to use a high-gain, automatic-level control loop. This loop operated in the following manner: A 15-dB miniature directional coupler was used to provide a sample signal. This signal drove two double-balanced mixers used as phase detectors. A sample of the unmodulated carrier was used as a reference to provide a dc output from one detector proportional to the carrier amplitude. To ensure that

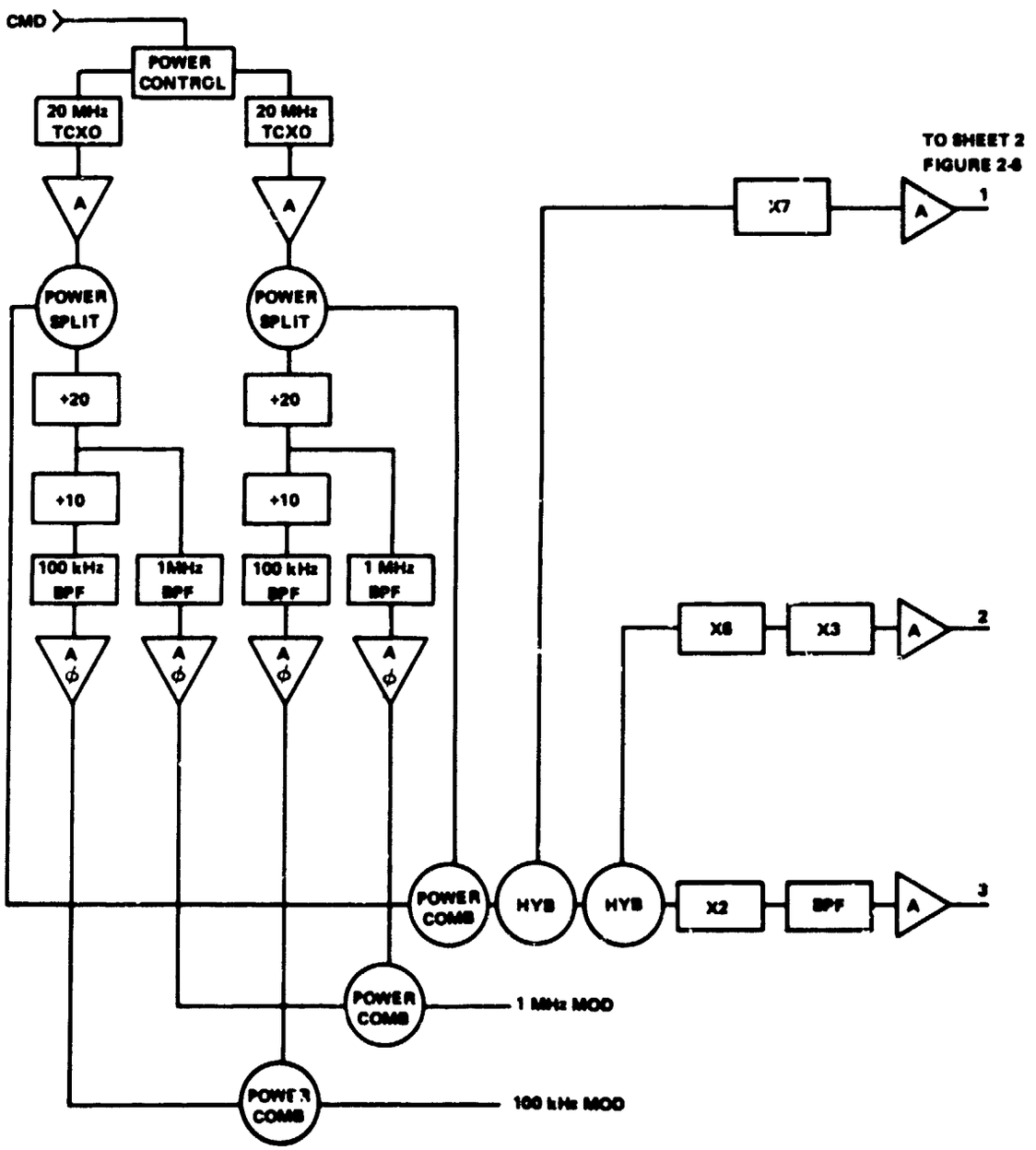

Figure 2-6. Radio Beacon Detailed Block Diagram (Sheet 1)

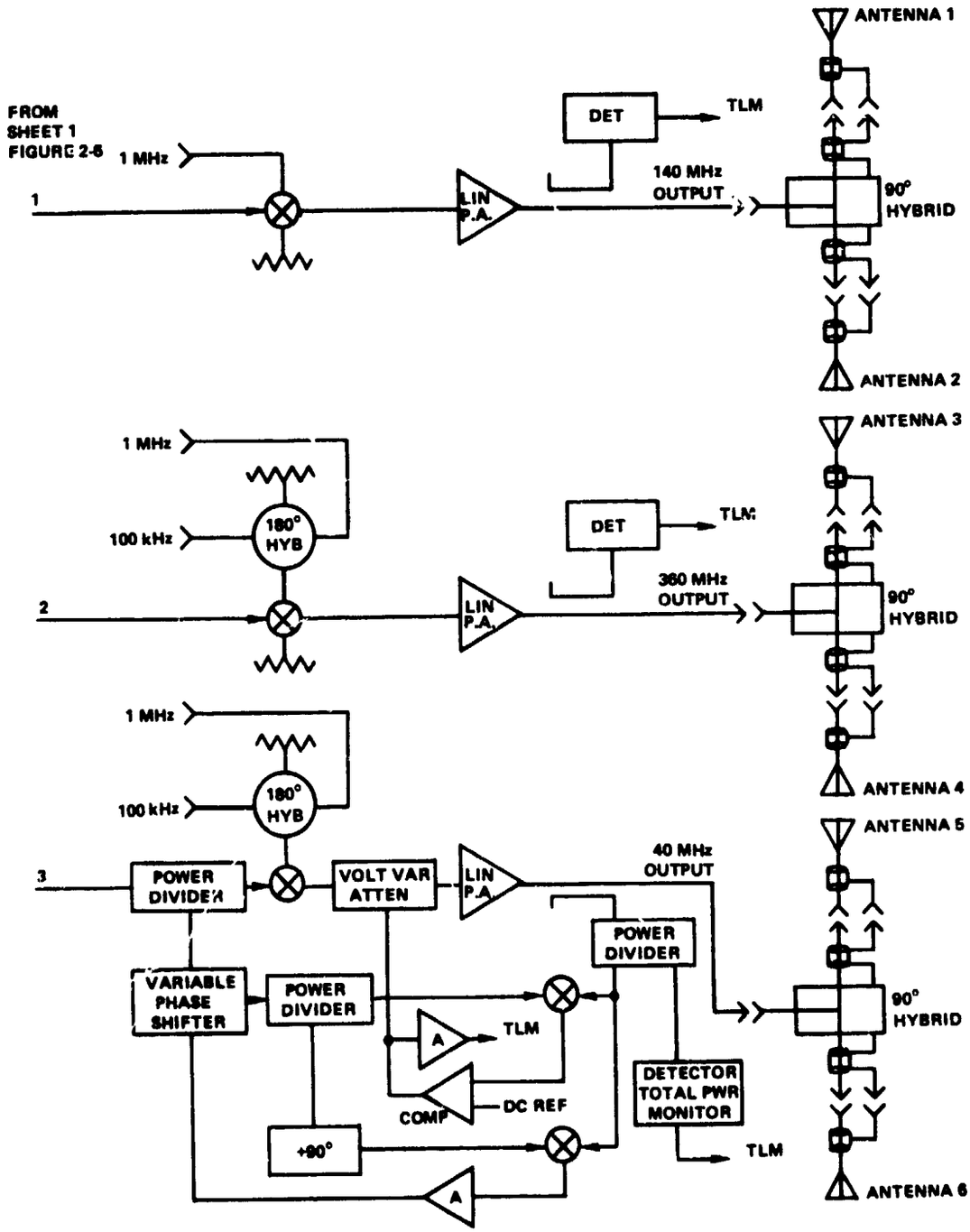

Figure 2-6. Radio Beacon Detailed Block Diagram
(Sheet 2)

this reference signal was in phase with the output carrier sample, a second detector, driven in quadrature, was used in a zero-order, phase-correction loop. The dc output of the carrier detector was compared with a dc reference and the amplified difference was applied to a voltage-controlled amplifier in the transmitter chain.

The radio beacon was provided with its own dc/dc converter that was intended to permit its operation during eclipse periods that severely restricted spacecraft power consumption. The separate converter was also intended to minimize potentially adverse interaction with other communications equipment aboard.

Antenna Description

The design and location of the radio beacon antennas was constrained by the physical restrictions imposed by the other experiments. Protrusions into the bottom plane of the Earth-viewing module (EVM) would degrade the interferometer performance. Protrusions into the top plane of the EVM would cause interaction with the prime-focus feed. Thus, the only locations left were the sides of the EVM that were covered with sensors and thermal louvers.

Various types of antennas were investigated. Included were a variety of V-beam antennas, yagis, simple dipoles, and rhombic antennas. After the investigation, it became obvious that the V-beam antenna had distinct advantages because of its simplicity and its broadband characteristics.

The biggest difficulty, at the two higher frequencies, was avoiding significant illumination of the parabolic reflector. The reflections caused cancellations or enhancement to appear in the resulting pattern making it difficult to obtain the desired uniform coverage of the Earth. The antenna configurations finally selected are those shown in Figure 2-1 and detailed in Figure 2-7.

The antenna selected for 40 MHz consisted of two $\lambda/4$ elements located on the east and west faces of the EVM. These were fed in phase by a 180-degree hybrid transformer. The result was a broadside array pattern with four lobes, one of which was directed toward the Earth. The pattern, obtained by range tests on a one-tenth scale model (Figure 2-8), showed nearly uniform Earth illumination (less than 1 dB variation) with an average gain of 3.2 dBi (gain, relative to an isotropic antenna). The model was considered more reliable than full scale range tests that were plagued by the presence of ground reflections and the resulting disturbances to the pattern and gain measurements.

The antenna designs selected for 140 and 360 MHz were basically similar to each other. The 140-MHz array was located on the east side of the EVM and the 360-MHz array on the west face. These consisted of two terminated V beams placed as an end-fire array. The gains obtained were 3.7 and 4.1 dBi respectively. The polar diagrams obtained in tests of these antennas are shown in Figures 2-9 through 2-12.

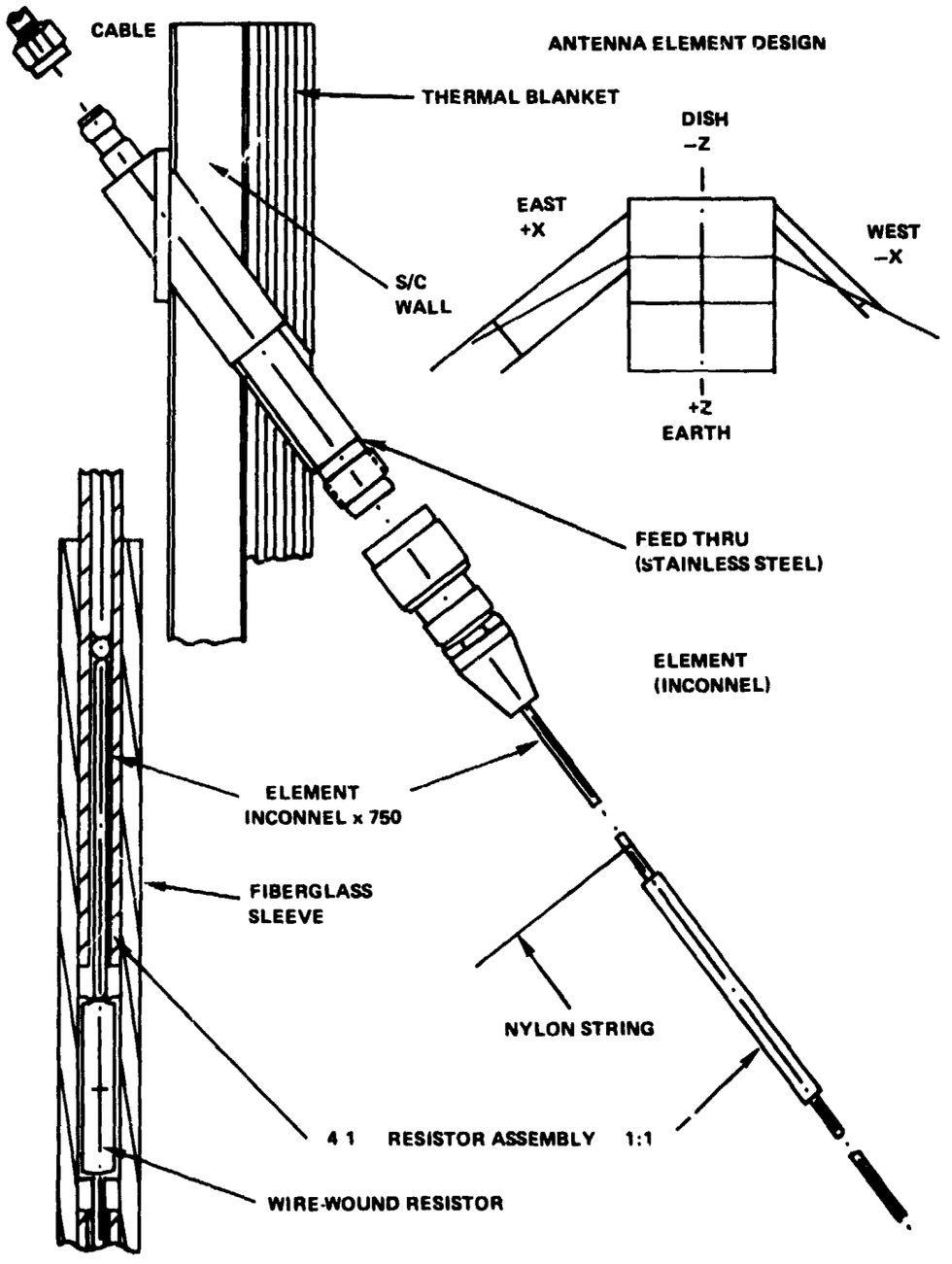

Figure 2-7. Antenna Arrangement

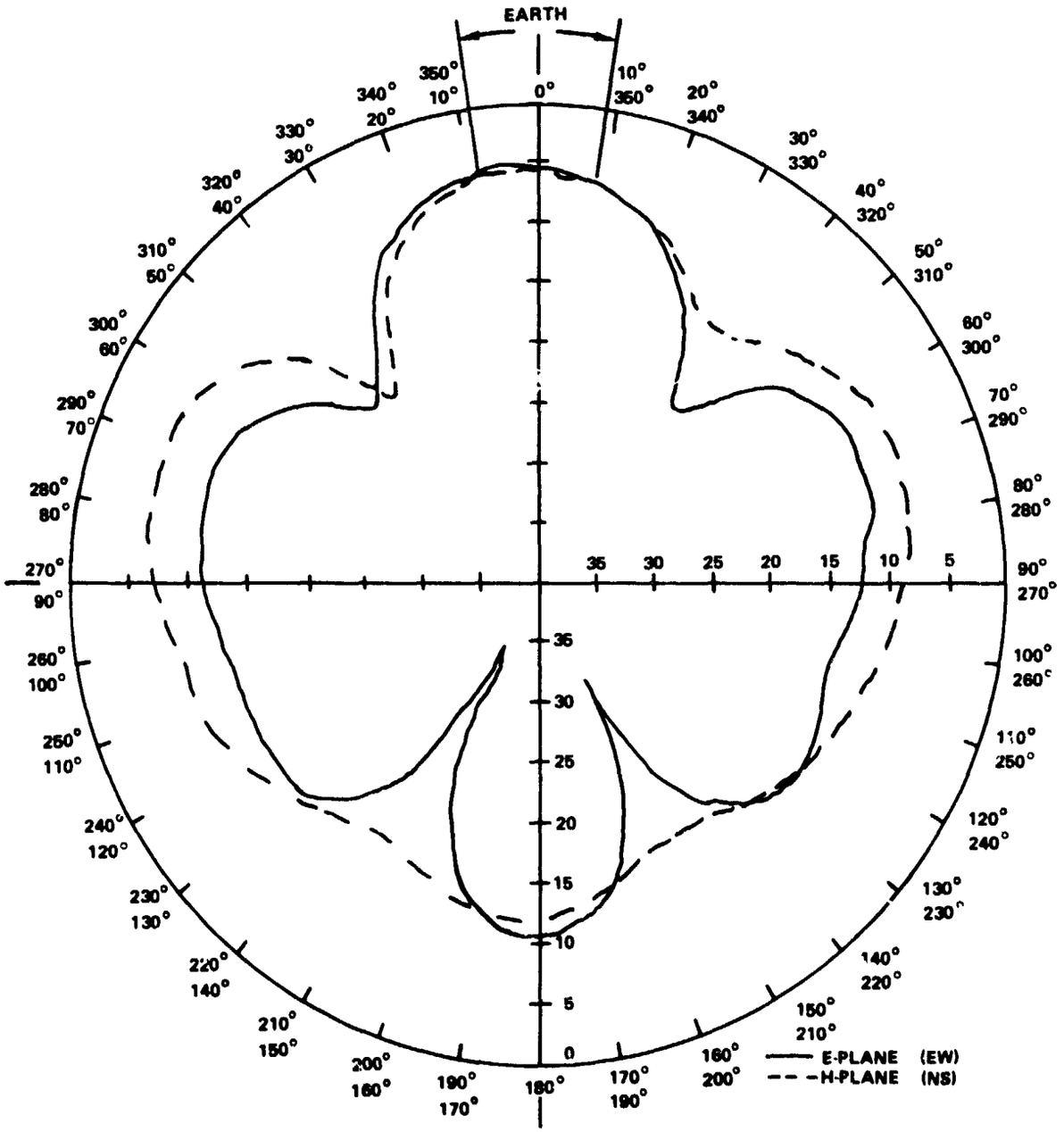

Figure 2-8. Radiation Patterns of 40-MHz Antenna on One-Tenth Scale Spacecraft

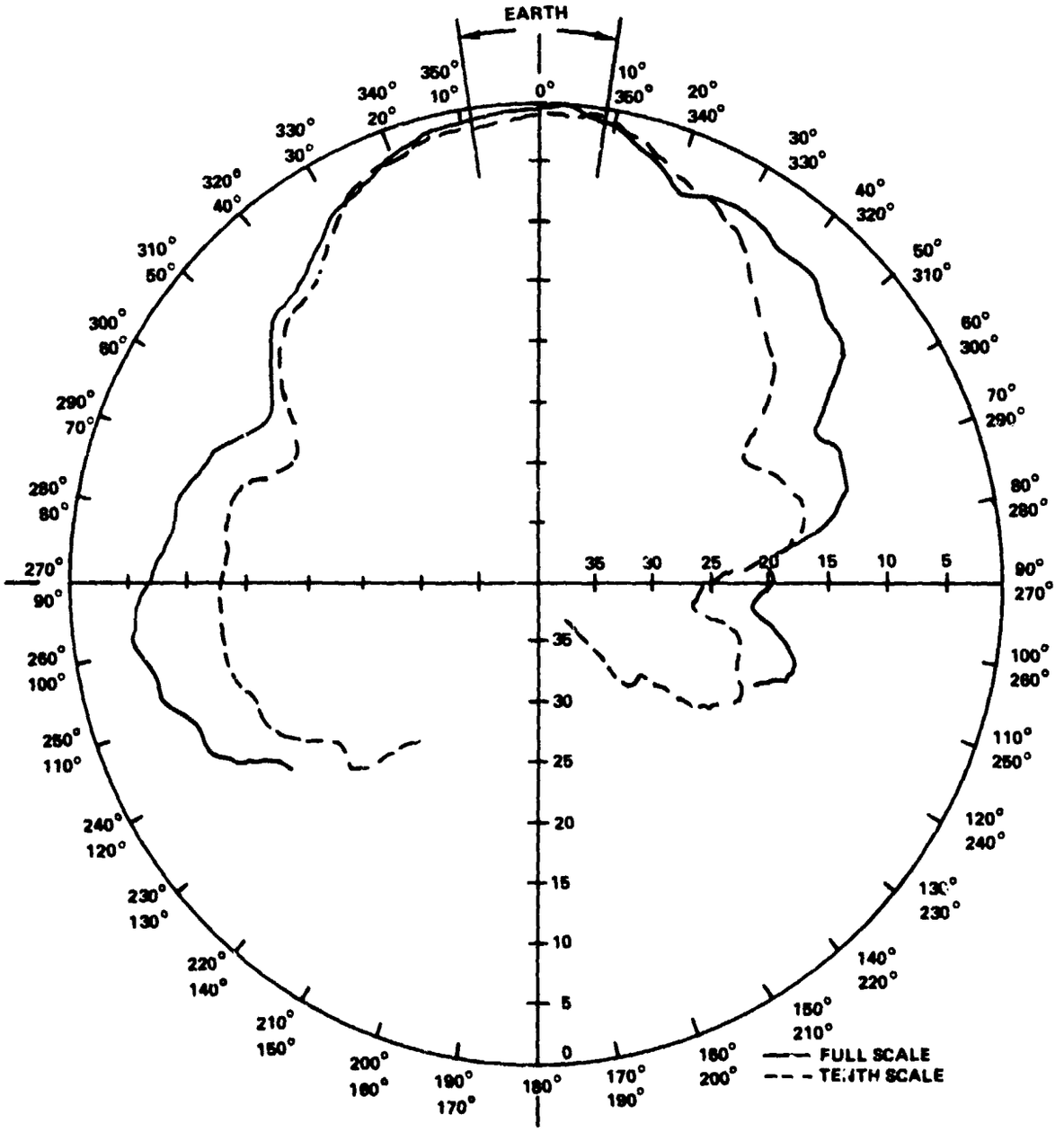

Figure 2-9. E-Plane (E-W) Patterns of 140-MHz Antenna

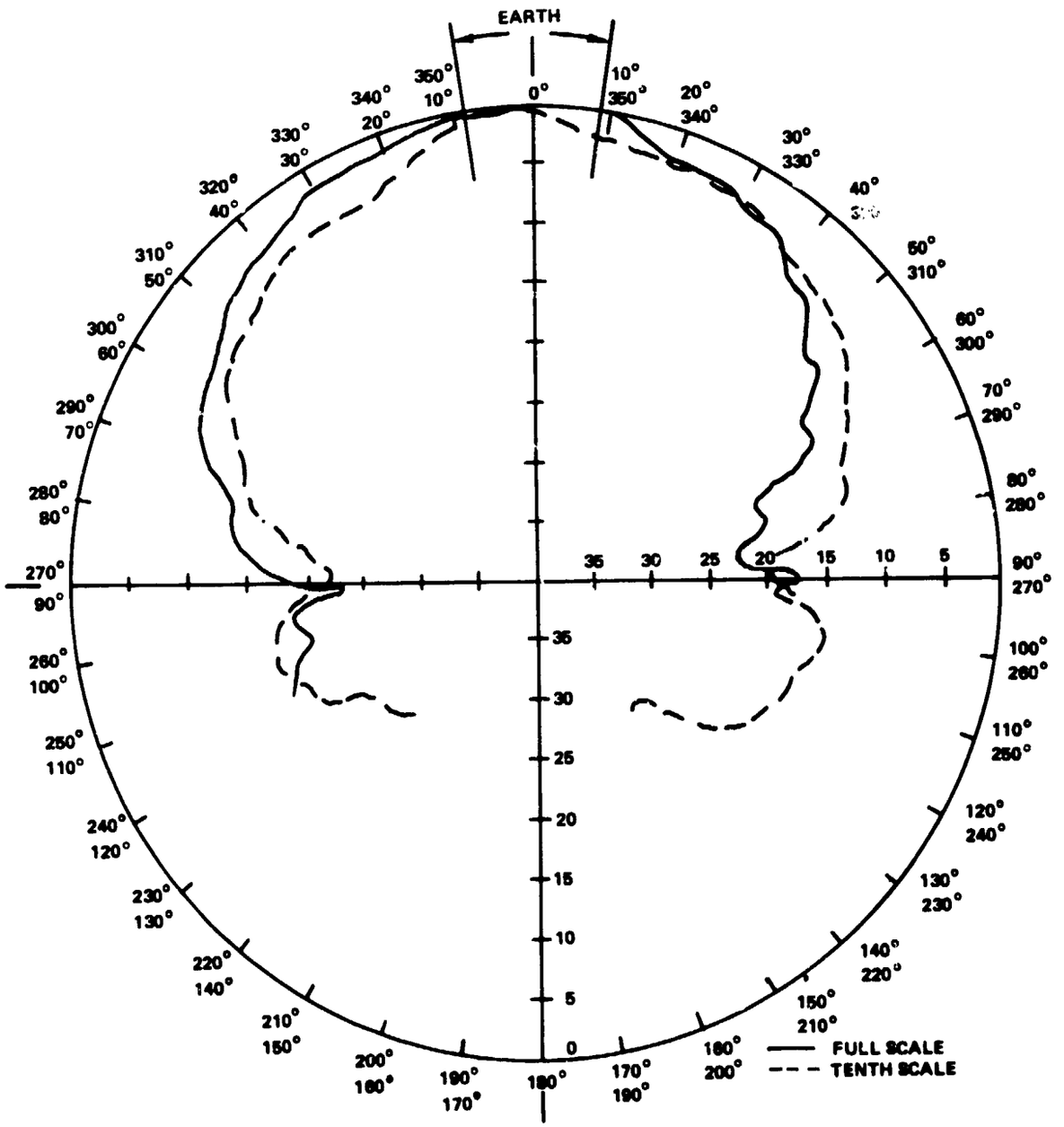

Figure 2-10. H-Plane (N-S) Patterns of 140-MHz Antenna

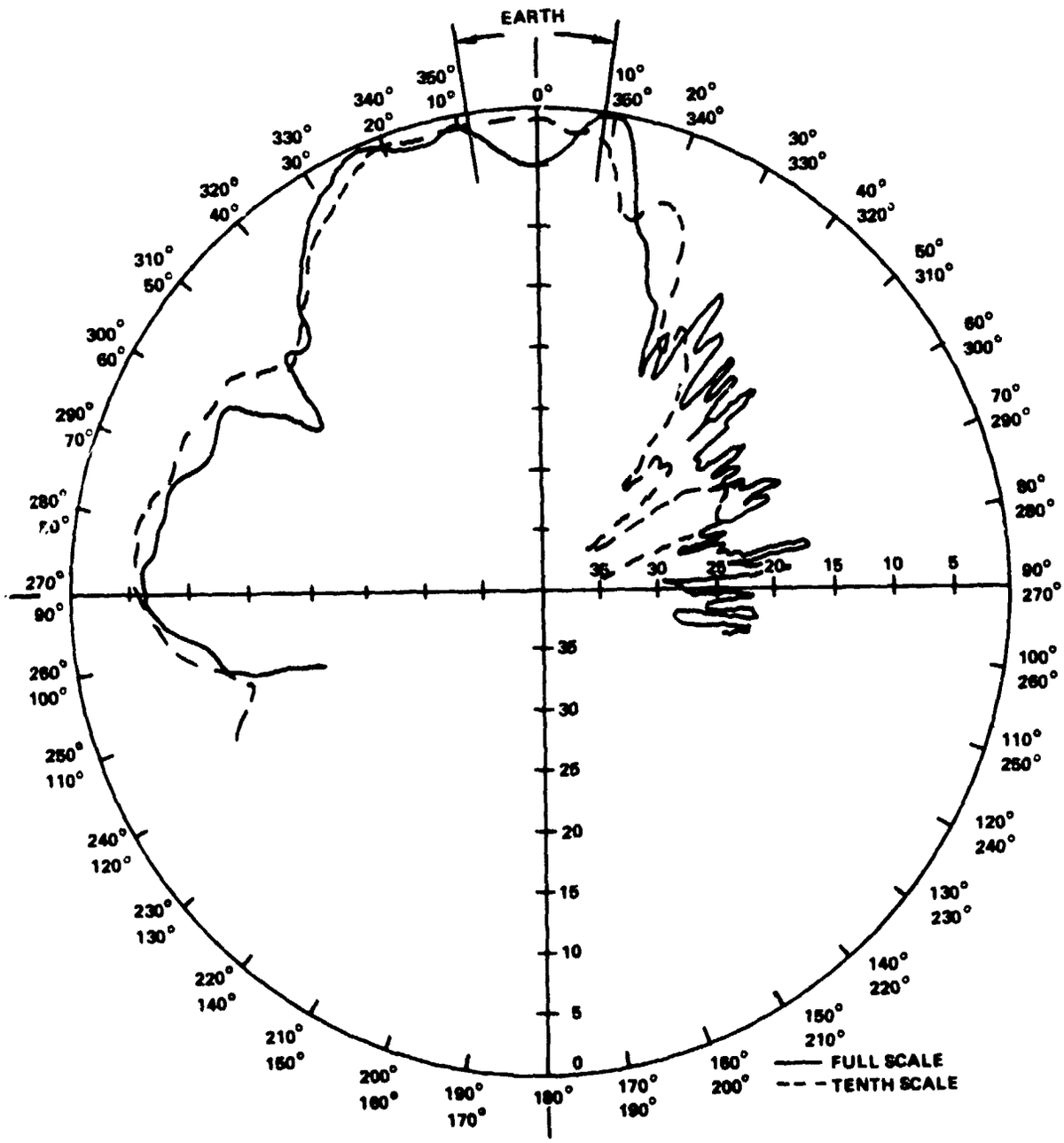

Figure 2-11. E-Plane (E-W) Pattern of 360-MHz Antenna

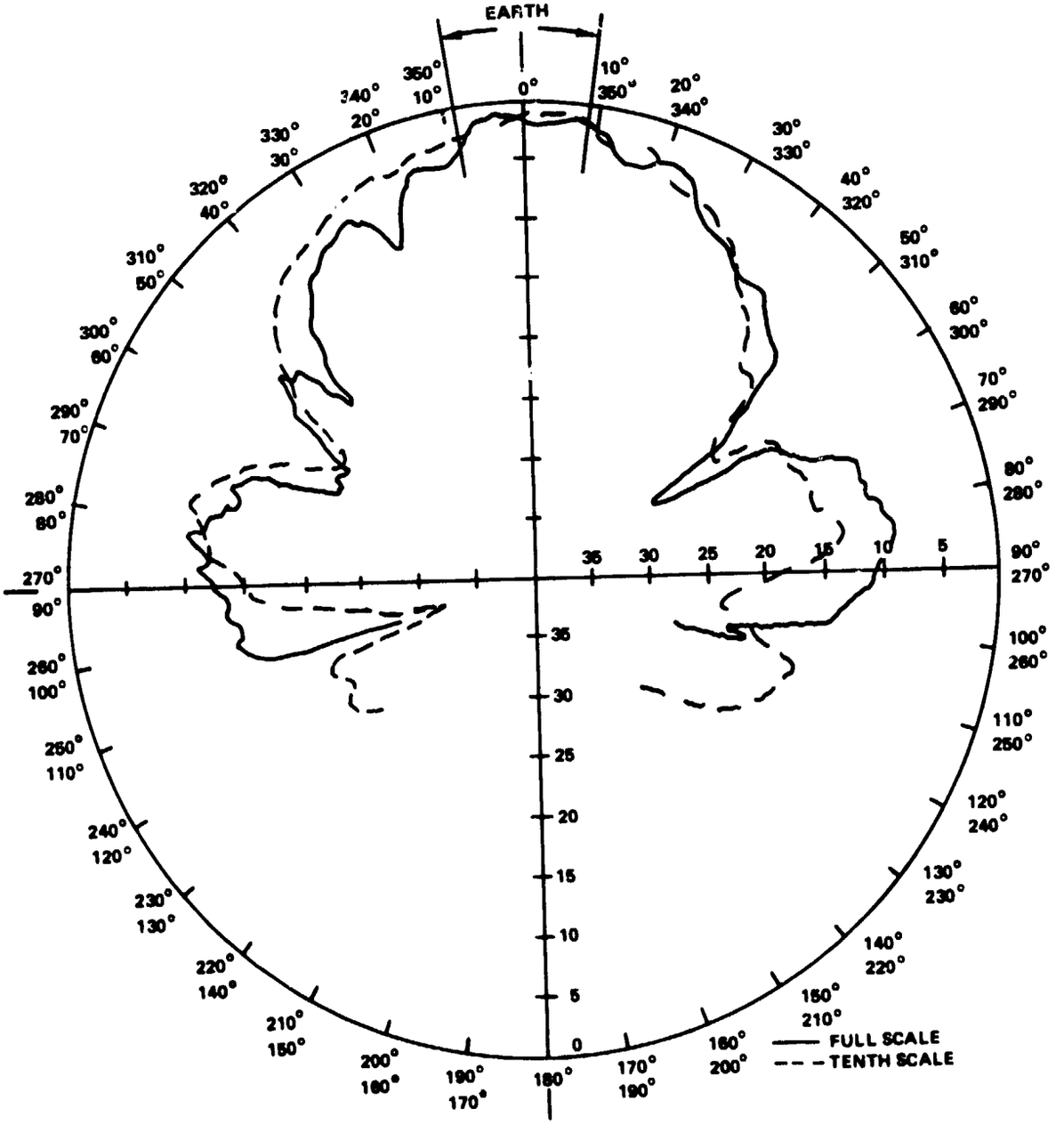

Figure 2-12. H-Plane (N-S) Patterns of 360-MHz Antenna

MEASUREMENT CONSIDERATIONS

Historical Background

In the design of the Radio Beacon Experiment is found a logical extension of measurement techniques that were developed during the evolution of knowledge of the upper atmosphere. The historical account of this development is a fascinating example of the way in which the efforts of many individuals in diverse fields coalesced to form the present body of knowledge that even today is by no means complete.

Balfour Stewart (Reference 1) in 1882, in connection with the dynamic theory of the variation of the Earth's magnetic field, postulated the existence of an "electrified" layer in the upper atmosphere as being the seat of electric currents causing magnetic compass variations. Kennelly (Reference 2) and Heaviside (Reference 3) in 1902 independently suggested that the strength of Marconi's December 1901, transatlantic signals indicated that these must have been reflected from such a region above the Earth because their amplitude was far greater than could be explained on a diffraction basis. During the period 1912 to 1914, DeForest (Reference 4) and Fuller (Reference 5) of the Federal Telegraph Co. made the first rough height estimates on the 3900-kilometer (km) San Francisco, California–Honolulu, Hawaii, path in the 3,000 to 12,000 meter wavelength range. The technique used by them depended upon wave interference of the received ground and postulated reflected waves. The height of the reflecting layer was deduced by varying the transmitted frequency and noting the variation in the received signal strength.

During the period 1920 to 1923, the amateur radio fraternity discovered the skip phenomenon. A spate of intense interest and activity arose and many of the more serious amateurs kept records that proved to be invaluable to the scientific community. Notably, Hulbert and Taylor (Reference 6) undertook the task of delineating the worldwide properties of the reflecting layer in the 16 to 40 meter range, its diurnal and seasonal changes, and its latitude dependencies. They included estimates of electronic density versus height based upon wavelength and transmission distances achieved. But up to the early 1920's, no way of experimentally verifying the existence of an ionized upper atmosphere had been conceived. Breit and Tuve (Reference 7) of the Carnegie Institute changed all that when in December 1924, they first demonstrated vertical incident reflections at a 70-meter wavelength using pulse techniques.

Meanwhile, Appleton and Barnett (Reference 8) of the United Kingdom seemed to have reinvented DeForest's method of frequency change and conducted experiments at a 400-meter wavelength that also included measurements of the angle of arrival. So, by 1925, three measurement procedures had been independently developed–skip-distance, frequency-variation, and pulse-sounding. The work in the United Kingdom at 400 meters indicated a reflecting height of 90 to 120 km while that at Carnegie at 70 meters indicated a height of 200 to 240 km. This seeming conflict led to the notion proposed by Appleton in 1926 that these were two distinct layers which he suggested be called the E-layer and F-layer, respectively. Later, the term "ionosphere" was first employed by Watson-Watt (Reference 9) in 1929 and, perhaps, independently by Plendle (Reference 9) of Germany in 1931. These embryonic beginnings in understanding the nature of the ionosphere were aided immensely by laboratory research on the electrical properties of ionized gases at subatmospheric pressures and work done on the role of the physics of neutral gases in the upper atmosphere.

Chapman (Reference 10) in 1931 presented a mathematical formulation of the layer structure in which he included the effect of the Earth's magnetic field. Lassen (Reference 11) in Germany also undertook similar work and, although he did not take into account the magnetic field effects, the formulation developed by him was identical to Chapman's at vertical incidence.

Following the pioneering work of Breit and Tuve (loc. cit.), swept-frequency pulse sounders were developed. The measurements performed by these not only led to a better understanding of the physics of the ionosphere, but also provided a firm basis for high-frequency communications circuit design and worldwide forecasting services.

Prior to 1935, significant ionization above the 400-km height was not even suspect. Eckersley's work (Reference 12) on whistlers in the 1-kHz to 10-kHz frequency range, first reported out in 1925, under the pun-like title "A Note on Musical Atmospheric Disturbances," led to his important paper (Reference 13) in 1935 on the mechanism of whistler production. In it he advanced the theory that whistlers resulted from radiation from lightning discharges in the atmosphere traveling long distances (a few Earth radii) along the lines of flux of the Earth's magnetic field. It was very much later that Smith et al. (Reference 14) in 1960 showed that whistler propagation is only possible guided by tubes of magnetic flux that included enhanced ionization. Experiments by Storey (Reference 15) in 1953 essentially resulted in the discovery of the plasmasphere.

The existence of a magnetosphere was unsuspected prior to 1960. Up to that time, the region surrounding the Earth had been considered to be a static region occasionally disturbed by corpuscular matter ejected from the Sun. The Smith et. al. (loc. cit.) 1960 study of whistlers made a major contribution to the understanding of the magnetosphere and led to the "knee whistler" discovery of the plasmapause by Carpenter (Reference 16) in 1963. The Lunik II 1960, Mariner II 1962, and Explorer XII 1963 observations of the plasma in this region resulted in discarding the static concept entirely as it became evident that the region was bathed in the solar corona in continuous expansion.

Before space vehicles became available, the three regions of major uncertainty that existed in the knowledge of electronic concentrations deduced from ground-based ionospheric sounders were:

- The topside of the F-layer.
- In the 110- to 200-km region, between the upper E- and lower F-layer, it was unknown whether a substantial valley existed in the ionization profile, particularly at night.
- The D-region below 90 km.

After 1950, four new techniques evolved that circumvented some of these limitations of the sounders. They were:

- Wave-interaction (cross-modulation) experiments
- Partial-reflection sounding

- Incoherent scatter techniques
- Moon-reflection experiments.

The wave-interaction experiments and partial-reflection sounding probed the region between the 60-km upper limit capability of meteorological sounding rockets and 90 km. The wave-interaction technique was born of the accidental discovery of the "Luxemburg Effect" in 1933. Partial-reflection sounding uses frequencies near the electron gyrofrequency and either measures the differential absorption of the ordinary and extraordinary wave components or the phase difference between these reflected signals arising from the differing group velocity of the two propagation modes.

The incoherent scatter techniques, still very much in use today, stemmed from the discovery of ionospheric turbulence in the early 1950's. The method employed provides data on electron densities and electron and ion temperatures throughout the E- and F-layers and into the magnetosphere. It is also possible thereby to obtain information on ion composition, neutral temperature, neutral abundances, neutral winds and waves, and electric fields. The discovery of ionospheric turbulence also was the basis for a whole new breed of communication systems.

Moon-reflection experiments above 100 MHz commenced in 1946 and Murray and Hargreaves (Reference 17) in 1954 at Jodrell Bank, England, discovered a slow fading component produced by the rotation of the plane of polarization in the ionosphere. Means were developed later of resolving the ambiguity in the total number of rotations by observing the difference in rotation on a pair of closely spaced frequencies. Other methods available included the simultaneous measurements at a frequency sufficiently high for the rotation to be less than $\pi/2$ and measurement of the peak electron density of the F-layer with an ionosonde. The Moon-reflection experiments provided the earliest reliable information on the upper portion of the F-layer prior to the advent of satellites. The measurements for the first time showed that the F-layer electron density profile differed from that of an isothermal Chapman layer. Later on, F_2 layer topside ionograms were obtained by the Alouette and ISIS satellites using pulse techniques.

The Moon-echo method of studying the ionosphere has been largely supplanted by the use of orbiting satellite beacons usually employing a telemetry transmitter. Up until the launch of ATS-6, the effort had been concentrated mainly on studying the total electron content and small scale irregularities since these properties have an important practical impact on the propagation time and amplitude/phase scintillation characteristics of satellite radio signals traversing the ionosphere. These low-orbiting beacons, using linearly polarized antennas, provided information on the horizontal ionospheric electron distribution derived from Faraday rotation measurements. The resulting data was not altogether satisfactory because of the rapidly changing ray path/geomagnetic field geometry, horizontal density gradients, the ground-based tracking requirement, and the difficulty in resolving ambiguities in the number of rotations.

The advantage of a synchronous satellite beacon, such as on ATS-6, was that the relatively fixed ray path/geomagnetic field geometry enabled measurements to be performed with fine-time resolutions at fixed geographical and geomagnetic configurations. The early, single-frequency beacons suffered the usual difficulty in determining the number of rotations and the rotation in the absence of an

ionosphere. The ATS-6 radio beacon was specifically designed to resolve this problem and, furthermore, to enable measurement of the plasmaspheric content and its spacial and temporal structure, particularly under disturbed conditions.

Overall Considerations

The Radio Beacon Experiment was designed to enable measurement of the total, N_T, and the Faraday (ionospheric), N_F, columnar electron contents along the ray path between the satellite and ground, and their temporal variations and spacial distribution. Special measurement techniques were employed to mitigate the historical problem of resolving cycle ambiguities in measured Faraday rotation and modulation/carrier phase. Estimation of plasmaspheric content, N_p, which is the difference between the total and Faraday contents, posed special problems under certain circumstances and required access to other auxiliary interpretive information that included data from polar orbiting navigation satellites and F2 layer topside and bottomside ionograms and geometric field modeling. The experiment was also designed to enable measurement of ground-received carrier amplitude variations, particularly at 40 MHz.

It will be shown in the following paragraphs that measurement of the Faraday rotation of polarization of the down-coming wave provided an estimate of the electron content of the ionosphere out to a height to which the influence of the Earth's magnetic field became negligible. Similarly, measurement of the received modulation phase and carrier phase determined the total columnar content to a high order of accuracy.

Faraday Rotation

The Faraday rotation, Ω_f, of the plane of polarization of the down-coming wave is given by the expression:

$$\Omega_f = \frac{4.84 \times 10^{-5}}{f^2} \cdot \int_0^S f_L N \, ds, \text{ in half revolutions} \qquad (2\text{-}1)$$

where,

- f is the beacon frequency in Hz.
- f_L is the electron gyrofrequency corresponding to the component B_L of the geomagnetic field in teslas along the ray path and is equal to $2.80 \times 10^{10} B_L$ Hz.
- N is the electron content contained in a square meter cross section along the ray path.
- S is the spacecraft-to-ground path.

The integration is taken over the path between the ground and the satellite. Equation 2-1 is valid for the very high frequencies employed by the beacon but ignores refraction. Refraction causes the actual path length to be 1.7 percent longer at 40 MHz than that at 360 MHz.

B_L, and hence f_L, is height dependent, so in practice f_L is replaced by an average value that is taken outside the integral and N is thus determined from measuring Ω_f. This approach is possible because f_L becomes nearly zero at very high altitudes. N is then a measure of N_F, the Faraday content, out to a slant range, S_f, which at midlatitudes corresponds to a height, h_f, of about 2000 km.

Measurement of Ω_f at 140 MHz yields the estimated content with modest accuracy; cycle ambiguity can be resolved by keeping track of the number of half revolutions. Keeping track becomes impossible, though, if the beacon is shut down for any appreciable time. Much greater accuracy can be obtained by measuring Ω_f at 40 MHz, but the resolution of cycle ambiguity using the above method is usually impractical because of the large number of half rotations. Resolution can be achieved in this instance by measuring the differential Faraday rotation, $\Delta\Omega$, between closely spaced frequencies f and $f + \Delta f$ and unambiguously determine the rotation from

$$\Omega_f = \Delta\Omega \frac{f}{2\Delta f} \tag{2-2}$$

ATS-6 used the 40-MHz carrier and the 1-MHz upper sideband at 41 MHz for this purpose.

Measurements at 140 MHz are useful at midlatitudes but can lead to large measurement errors at low latitudes where the ray path becomes nearly perpendicular to the geomagnetic field. In this situation the resulting Faraday rotation lowers to a few tens of degrees at 140 MHz and better accuracy can be obtained by direct measurement of the rotation at 40 MHz.

Other problems can arise that reduce the accuracy of measurements at low latitudes. The diurnal excursion in latitude of the satellite due to its orbital inclination has an important effect both on orientation of the electric field as a function of the satellite aspect angle, and on the orientation of the electric field with respect to the geomagnetic field. Furthermore, quite apart from measurement accuracy considerations, the measured electron content tends to be lower than the actual content owing to the tight coupling between the ordinary and extraordinary waves. This is important because it leads to a gross overestimate (as much as 50 percent) of the plasmaspheric content as calculated from the expression $N_p = N_T - N_F$ where N_T is known accurately from phase measurements.

Accurate calibration is important, both of the beacon and the ground-based equipment. The initial orientation of the plane of polarization is not necessarily determined by the physical orientation of the linear transmitting antenna elements because of possible radiation from the antenna feed lines and reradiation from other satellite structures. With ATS-6, polarization measurements were conducted on the ground prior to launch and the orientation was expected to remain stable. In one instance, the polarization orientation at 140 MHz was confirmed by making lunar radar measurements when ATS-6 and the Moon were nearly aligned.

Accuracy of the ground-based polarimeters was the onus of the various experimenters. Since Faraday rotation is the consequence of the phase difference of the left-hand circularly polarized ordinary wave and the right-hand circularly polarized extraordinary wave, the usual technique is to employ cross dipoles to separate the two components by introducing a 90-degree phase advance or

90-degree retardation. Measurement errors arise from incomplete separation of the two components due to imbalances in the antenna elements and their feed system, and due to ground reflections, especially at low satellite elevations.

Group Delay and Carrier Phase

One way of determining the total electron content, N_T, is by measuring the differential group delay (modulation or phase dispersion) of two closely-spaced frequencies separated by a frequency difference Δf. By taking the measurements at two sets of frequencies spaced by the same difference Δf hertz (Hz), the effect of Doppler shift due to the line-of-sight motion of the satellite is removed. If f_1 and f_2 are the arithmetic averages in Hz of the two frequency sets, the phase difference, $\Delta\phi^R$, between the two ordinary waves can be shown to be

$$\Delta\phi^R = \frac{-k\Delta f}{2c}\left[\frac{1}{(f_2 + \bar{f}_L)} - \frac{1}{(f_1 + \bar{f}_L)^2}\right]\cdot\int_0^S N_T\,ds, \text{ in cycles} \qquad (2\text{-}3)$$

where $k = 80.61$, a constant

$c = 2.998 \times 10^8$ meters per second (m/s), the propagation velocity in vacuum

$\bar{f}_L$ = an average value of the longitudinal electron gyro frequency in Hz

from which the total electron content $N_T = \int_0^S N\,ds\ m^{-2}$ can be determined.

The appearance of f_L in the equation is a consequence of the phase refractive index of the ionosphere and is on the order of 1 MHz. The minimum frequency f_1 employed by the beacon was 40 MHz, so the error introduced by this term is small. Ionospheric refraction increases the actual path length at 40 MHz, necessitating a correction factor of 3.4 percent.

Modulation frequencies Δf of 1 MHz at 140 MHz and 360 MHz, and 100 kHz at 40 MHz are sufficiently low to resolve cycle ambiguity whereas a 1-MHz modulation frequency at 40 MHz can provide high sensitivity useful for determining the magnitude of small changes.

An alternate scheme that provides a higher order sensitivity is to reduce two widely spaced carrier frequencies to a reference frequency, f_R, and compare the phase difference. Letting $\Delta\phi^c$ be the phase difference at f_R, then

$$\Delta\phi^c = f_R\left[\frac{\phi_2}{f_2} - \frac{\phi_2}{f_1}\right] = \frac{kf_R}{2c}\left[\frac{1}{f_2(f_2 + \bar{f}_L)} - \frac{1}{f_1(f_1 + \bar{f}_L)}\right]N_T, \text{ in cycles} \qquad (2\text{-}4)$$

In comparing equations (2-3) and (2-4), an approximate expression for $\Delta\phi^c$ is obtained

$$\Delta\phi^c = \frac{f_R}{\Delta f} \tag{2-5}$$

thus, it can be seen that relatively large f_R permits a larger sensitivity than the modulation phase method. The cycle ambiguity resolution problem, however, increases with increasing f_R. ATS-6 used an f_R of 10 MHz, so that the sensitivity was increased tenfold in this instance.

One goal of the experiment was the measurement of the difference of the total and Faraday contents. The latter, during daylight hours, accounted for around 90 percent of the total. Hence, if a 10 percent accuracy in the difference is desired, the absolute measurements should be to the order of one percent accuracy. This imposes a minimum overall measurement accuracy in group delay of ±50 nanoseconds (ns), which is ±0.5 cycle or ±18 degrees at 1 MHz, and a similar requirement on the relative phase stability of the two modulating frequencies at 40 MHz to resolve cycle identification. The beacon transmitter performance met these goals (Table 2-2).

The modulation phase delays of the beacon were carefully measured prior to launch and were verified in flight from time to time by comparing the total content data from the different channels. A generator was constructed and used to provide a standard modulation phase for use in standardizing the beacon transmitter test equipment and in calibrating the ground equipment of the various experimenters.

EXPERIMENT SUMMARIES

In the following paragraphs, several of the many experiments conducted by numerous investigators have been summarized to illustrate the utility of the ATS-6 Radio Beacon. The particular experiments selected cover studies of electron content, the effects of storms, large and small irregularities, and scintillation. In many instances, auxiliary data have been introduced to enable interpretation of results. These auxiliary data were derived from ground-based ionograms, top-side sounding by medium-altitude orbiting satellites, incoherent scatter techniques, horizontal content from polar orbiting satellites, geomagnetic indices, and geomagnetic field modeling.

Maps showing the location of the beacon receiving sites in the United States and worldwide for ATS-6 related observations are shown in Figure 2-13 and Figure 2-14.

Electron Content Studies

The National Oceanic and Atmospheric Administration Environmental Research Laboratories, Max-Planck Institute, and Universitaet Graz conducted beacon measurements from a station near

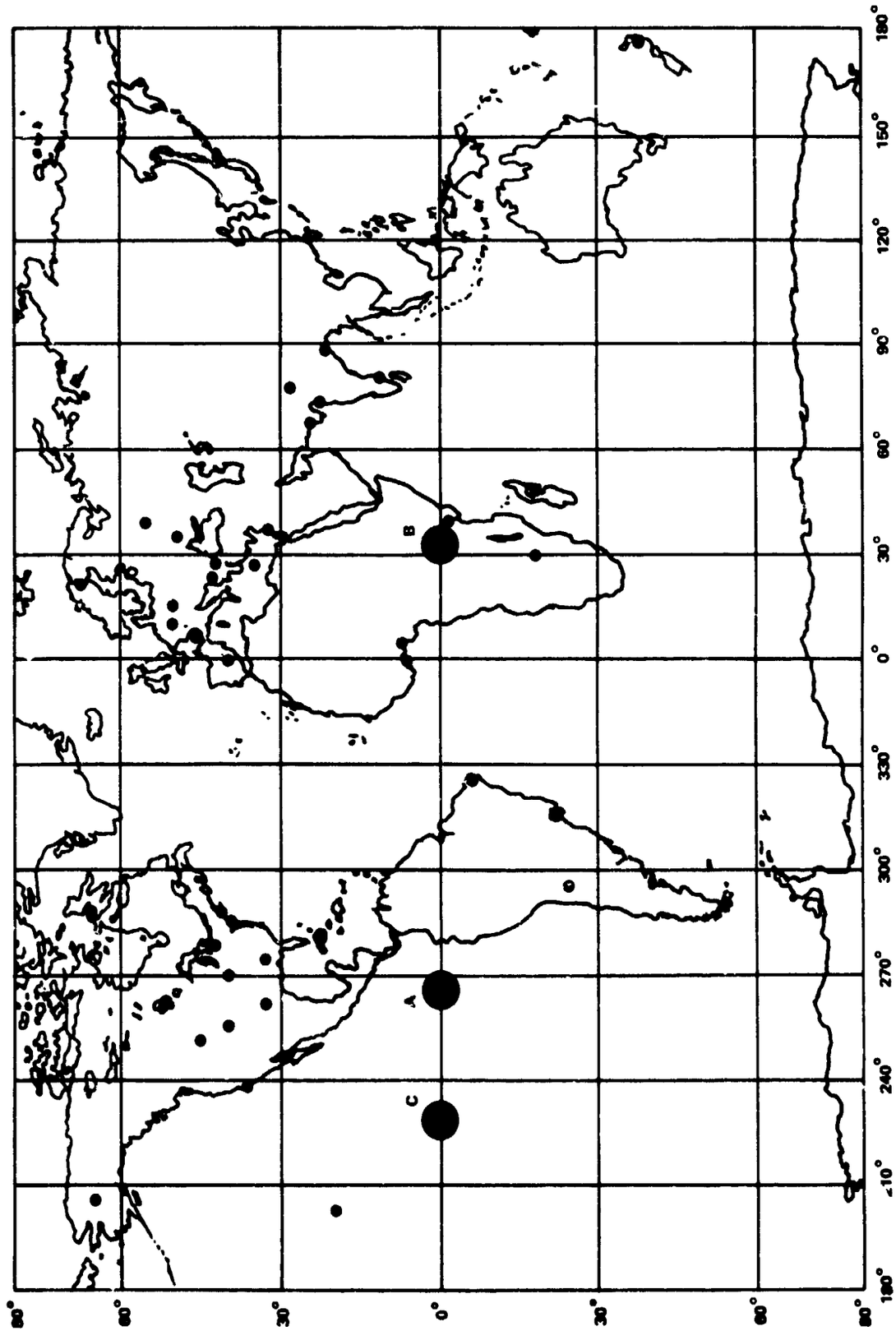

Figure 2-13. ATS-6 Radio Beacon Receiver Locations

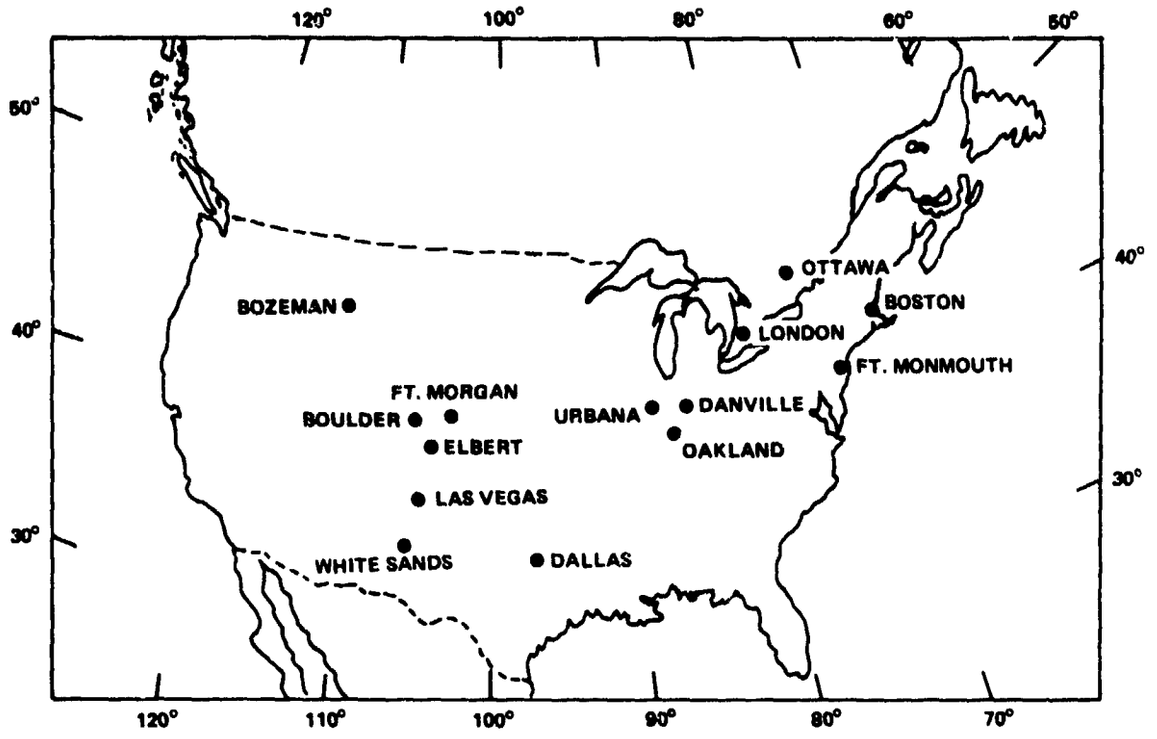

Figure 2-14. Location of Receiving Equipment for the ATS-6 Related Observations

Boulder, Colorado (40.13°N latitude, 105.24°W longitude) during the period July 1974 to May 20, 1975, when ATS-6 was positioned above 94°W longitude. Similar measurements were made later after ATS-6 was moved to 35°E longitude from Aberystwyth, Wales; from the European continent; from India; and from a few other locations throughout the world. At Boulder, auxiliary interpretive data were obtained from ionograms taken at White Sands, New Mexico; from Alouette satellite topside soundings; from horizontal content measurements from the Navy's polar orbiting satellite NNSS; and from geomagnetic field models. Measurements of total content, N_T, were derived from measurements of group delay (modulation phase), $\Delta\phi^R_{140}$, of the ordinary wave of the 1-MHz modulation on the 140-MHz carrier relative to that on the 360-MHz carrier, and from carrier phase measurements at 360 MHz and 40 MHz reduced to a 10-MHz reference, $\Delta\phi^C_{40}$. Estimates of Faraday content, N_F, were derived from the measurement of Faraday rotation at 140 MHz, Ω_{140}. Various methods previously described were used to resolve ambiguity in modulation phase and Faraday rotation. It was shown that the combination of group delay and Faraday measurements of the ATS-6 Radio Beacon provided the most reliable estimate of the columnar content of the plasmasphere. The data obtained enabled establishing models of the electron density–height profile, which although not perfect, were used by several other investigators in later work.

Before going into some of the results of the study, several parameters, in addition to those already described, require definition. Recall that the plasmaspheric content, N_p, can be estimated from the difference between the accurately determined total content, N_T, from modulation phase measurements and the estimated Faraday content, N_F, derived from Faraday rotation measurements. Equation (2-1) for Ω_f is repeated:

$$\Omega_f = \frac{4.84 \times 10^{-5}}{f^2} \int_0^s f_L \, N ds, \text{ in half revolutions}$$

where f_L varies with the distance along the ray path due to the increasing angle, θ, between the ray path and the geomagnetic field direction and the inverse cube variation of the value, B_o, of that field with height. To deduce the Faraday content,

$$N_F = \int_0^s f_L \, N ds,$$

from a measurement of Ω_f, a value, $\bar{F}$, must be assumed that represents the average f_L over the slant range, S_F, from the receiver to some profile height, h_f, generally assumed to be 2000 km, beyond which the contribution of f_L becomes negligible. The term f_L is brought outside the integral of equation (2-1) and so $\bar{F}$ is defined by the expression

$$\bar{F} \cdot N_F = \int_0^{S_F} f_L \, N ds \tag{2-6}$$

The term $\bar{F}$ is on the order of 1 MHz for ground stations at midlatitude viewing an equatorial beacon at geosynchronous altitude. It is useful to speak in terms of the height, h_{eff}, at which $f_L = \bar{F}$. This height is somewhat greater than the height h_m F2 at which the profile density peak N_m occurs. Although h_{eff} on the Boulder to ATS-6 (94°W longitude) path exhibits a diurnal variation between 300 km and 400 km, an average value of 380 km was adopted for these studies. This value lies between the value of 420 km recommended earlier by Titheridge (Reference 18) derived from a generalized worldwide model based upon a wide variety of theoretical density profiles and ray geometries, and 350 km used by Poletti-Liuzzi et al. (Reference 19) for the specific Danville, Illinois-to-ATS-6 (94°W longitude) path.

The error is reasonably small in the estimate of N_T from the measurement of Ω_f assuming a fixed value of $\bar{F}$. A change of 100 km in h_{eff} produces a variation in $\bar{F}$ of about 3.5 percent for the Boulder-to-ATS-6 (94°W longitude) path. (Note, however, by contrast, that there is little variation in $\bar{F}$ at ionospheric heights over the Aberystwyth-to-ATS-6 [35°] path.)

A value of $\bar{F}$ = 1.15 MHz was used at Boulder corresponding to h_{eff} = 380 km to determine the ionospheric content, N_F, out to a height h_f = 2000 km from measurements of Ω_f. This combination of the values of $\bar{F}$ and h_f was adopted from the minimum dispersion point of the crossovers of

the plots shown in Figure 2-15 for Boulder. These are plots of the ratio:

$$f_L \, Nds \Big/ \int_0^{S(h)} Nsecidh \tag{2-7}$$

where i is the angle between the ray path and zenith direction, and are representative of the low sunspot numbers typical of the measurement period and reflect the diurnal and seasonal variations in the density profile.

A similar factor, F, is defined over the entire path from the receiver to the satellite, thusly:

$$F = \frac{\int_0^S f_L \, Nds}{N_T} \tag{2-8}$$

Since f_L becomes negligible at very high altitudes, mainly because of its dependence on B_o whose value varies as the inverse cube of height, then for all practical purposes

$$\int_0^S f_L \, Nds \simeq \int_0^{S_F} f_L \, Nds = \bar{F} N_F.$$

So from equations (2-6) and (2-8) the relationship

$$F N_T = \bar{F} N_F \tag{2-9}$$

is established. Thus, the slant plasmaspheric content, N_p, between the satellite beacon and the intersection of the ray path with the profile at 2000-km height, can be determined from

$$N_P = N_T \left(1 - \frac{F}{\bar{F}} \right) \tag{2-10}$$

From equation (2-9), $F = \bar{F} \, (N_F/N_T)$. The ratio, (N_F/N_T), can be obtained by simultaneous measurement at the ground-based beacon receiver of phase and Faraday rotation. The modulation phase gives an accurate measurement of N_T, so using some assumed value of $\bar{F}$, the plasmaspheric content, N_p, is calculated from equation (2-10).

Other shape factors useful in modeling are the slant total slab thickness, τ_{TS}, and the slant Faraday slab thickness, τ_{FS}, given respectively by

$$\tau_{TS} = N_T/N_m \text{ and} \tag{2-11}$$

$$\tau_{FS} = N_F/N_m \tag{2-12}$$

N_m is the F2 layer peak electron density determined from ground-based ionosound measurements.

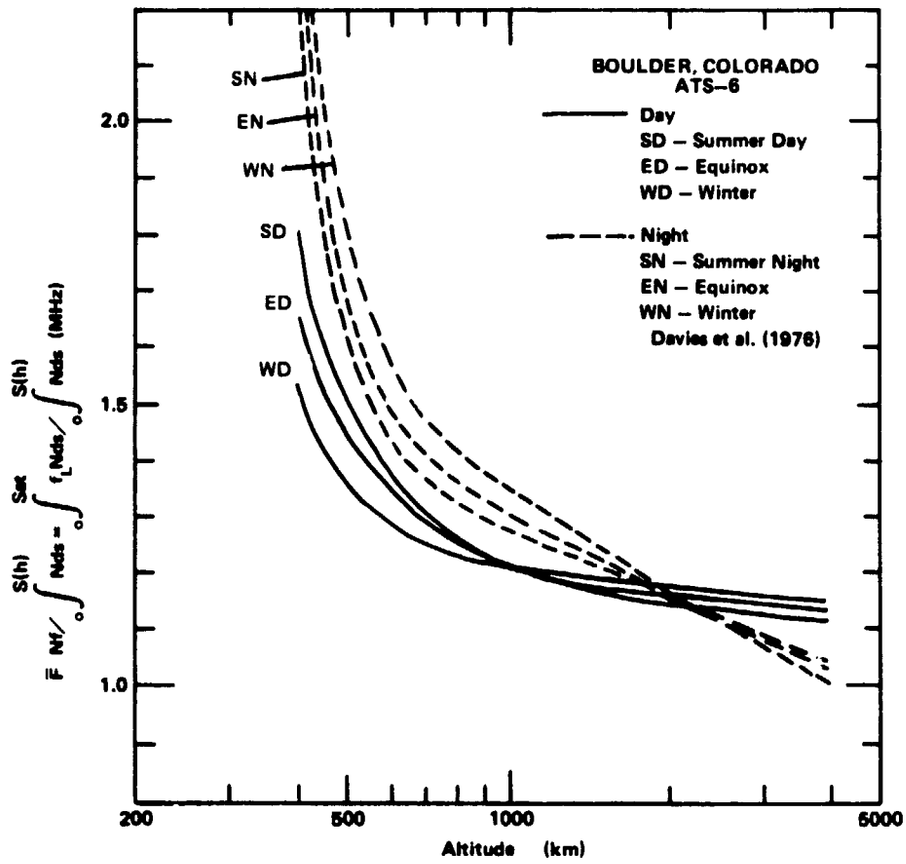

Figure 2-15. Determination of $\bar{F}$ from Plots of Reference 20; Boulder

Turning now to the experiments at Boulder, the radio beacon receiver was set up for measuring the modulation phase, $\Delta\phi^R_{141}$, at 140 MHz and 360 MHz using the carriers and 1-MHz modulation upper sidebands, and the Faraday rotation, Ω_{140}, at 140 MHz. The 140-MHz frequency was used rather than the 40-MHz to eliminate the need for refraction correction, to more easily keep track of total number cycles, and because there is less signal strength variation due to ionospheric absorption and scintillation. Using the expression for Ω_f from equation (2-1) and the expression for $\Delta\phi^R$ from equation (2-3) and inserting them into equation (2-8), the factor F in terms of measured Ω_{140} and $\Delta\phi^R_{141}$ turns out to be

$$F = \bar{F}(N_F/N_T) = R_f\ (\Omega_{140}/\Delta\phi^R_{141}) \qquad (2\text{-}13)$$

The constant R_f has a value that is frequency dependent as the subscript implies, but is relatively insensitive to $\bar{F}$. This is because R_f varies directly as $\bar{F}$, and Ω_f inversely as $\bar{F}$. Examination of equation (2-3) shows that as the frequency of observation increases, the effect of $\bar{F} = \bar{f}_L$ becomes progressively less important to $\Delta\phi^R$. At 140 MHz and midlatitudes, where $\bar{F} \simeq 1$ MHz, $R_{140} = 0.83$. Even at equatorial latitudes, where $\bar{F} \simeq 0.1$ MHz, R_{140} does not change much, being equal to 0.84.

The slab thickness data depended upon the determination of N_m, the peak electron density of the F2 layer, based on ground-based ionosonde data. The ionospheric heights of interest intersected by

the ray path lay neither directly over either the Boulder or the White Sands ionosonde stations. Hourly N_m data from these latter stations indicated frequent horizontal gradients of such magnitude as to inaccurately infer what the values might be along the ray path. Rather, monthly mean values of N_m were calculated for both Boulder and the geographical location of the subionospheric point of intersection of the ray path with the 450-km height and the ratios were applied to the smoothed Boulder ionosonde data (Reference 20).

The Radio Beacon Experiment data obtained at Boulder and at other locations in the United States, the United Kingdom, continental Europe, and India showed a number of diurnal and seasonal features in the variation of the electron content. Among these were the steady small decline of N_p and N_F during the summer from a midafternoon peak to a predawn minimum as contrasted to the winter behavior in which the decline occurred until shortly after sunset and thereafter remained quite constant. The winter daytime/nighttime ratio was greater in Europe and even more pronounced at low latitudes (Indian measurements) until dawn.

N_p was seen to maximize at night during the winter through the vernal equinox in the United States. This contrasted to European measurements conducted after ATS-6 had been drifted to 35°E which showed N_p maximizing during the day. N_p was also higher in Europe than in the United States with a marked winter to summer change. These features have been confirmed by several other workers in both Europe and the United States. Some of these behavioral details had been heretofore unknown and these, together with observations conducted at a number of diverse geographic locations, led to new theories concerning the interchange of plasma between the local ionosphere and plasmasphere, and the interchange between magnetically conjugate regions.

The secondary maximum in N_F, occurring during the latter part of the night, had been previously known to exist during the winter months. RBE data for Boulder, Bozeman, Montana, and Dallas, Texas showed the predawn maximum to occur year round. This phenomenon was confirmed by observations at Lindau, Germany (Reference 21). Prior to the ATS-6 RBE studies, the night maxima in N_F was thought to be brought about by a depletion of the N_p content. This hypothesis was subsequently disproved with the advent of the RBE observations. For example, at Boulder, Bozeman, and Dallas, a particularly large enhancement of 30 percent in N_F occurred during the early hours of December 2, 1974, following an isolated magnetic substorm, but little change was observed in N_p which at the time was 40 percent to 50 percent of the total content. These nighttime maxima are spacially confined as shown in the contour maps of vertical content constructed from the Radio Beacon Experiment (RBE) and the polar orbiting NNSS satellite observations at Lindau, Germany and Graz, Austria, that are separated by an ionospheric distance of 542 km. With receivers set up at Table Mountain, Fort Morgan, and Elbert, Colorado, it was also discovered that there is a general east-west movement of the nighttime maximum at a speed of about 70 meters per second (m/s). This and other wavelike phenomena called traveling ionospheric disturbances are discussed later under a heading entitled "Large and Medium Scale Irregularities."

Studies were conducted in India at low magnetic latitudes using the RBE when ATS-6 was positioned above 35°E longitude that showed the influence of the equational electrojet on the Appleton anomaly. This anomaly is characterized by a pronounced latitudinal dependence of the F2 layer

penetration frequency at hF that maximizes at ±15 degrees magnetic latitudes. During the afternoon on a normal electrojet day, the τ_s and F-factor measurements showed a pronounced electron density peak in the F2 layer profile during the afternoon at the latitude of the anomaly maximum, whereas near the magnetic equator just before dawn, a thick F-layer existed with a very little peak in evidence.

Storm Effects

One big advantage of satellite radio beacons is that they can be used to measure N_T and N_F continuously even during storm induced conditions. Abnormal distortion of the ionosphere profile, enhanced D-region absorption, and moderate amplitude and phase scintillations did not affect the RBE measurement of N_T. These phenomena are often met under disturbed conditions and limit the utility of conventional ionosonde measurements.

Ionospheric Storms

The temporal response of the ionosphere to geomagnetic storms has been known for some time. While storms behave in a highly individualistic manner, they do follow a general pattern at midlatitudes. This general pattern shows that following a sudden storm commencement (SSC), there is a fairly uniform distribution of an enhanced value of N_F over the day sector that persists past sunset. The onset of the enhancement rotates with the Earth and cuts off between 21 to 24 hours local time to a depressed value of N_F that persists for the next few days. Generally, only enhancement in N_F is observed near the equator. The enhancements appear to originate in the polar or auroral regions and propagate toward the equator as turbulence-convective cells giving rise to large latitudinal gradients in N_F. Steep longitudinal gradients exist at midlatitudes at a median value $(D_{st} + 2.5)$ hours local time where D_{st} is the storm time since SSC (Reference 22).

The temporal variation in N_F content was verified with RBE measurements made during periods of storm activity, July 3 to 6, September 14 to 19, and October 10 and 20, 1974. A marked increase in slab thickness was seen immediately following SSC. Analysis of Boulder RBE N_T data, August 15 to November 30, 1974, showed a 27-day solar rotational repetition wherein the nighttime N_T value varied over a range about 2 to 1. The corresponding variation was found to be less pronounced in N_F owing to the fact that trends in N_T and the F-factor tended to cancel. Correlation relationships were shown to exist between the midnight value of N_T and the values of the magnetic index K_p occurring a day or two earlier.

Plasmaspheric Storms

The advent of the ATS-6 Radio Beacon Experiment (and the beacon on the Japanese geosynchronous satellite ETS-II) for the first time enabled measurement of N_p and an opportunity to observe its storm related behavior.

Observations at several locations showed a marked depletion of N_p following enhancements of the geomagnetic indices K_p, A_p, and D_{st}. The July through November period revealed a 27-day periodic component in which a small increase in the daily average A_p accompanied a depletion in the daily

average of N_p followed by many days of recovery. N_p sometimes decreased before A_p increased. Over the July 1974 to February 1975 period, there was a gradual long term increase in the value of N_p as storms decreased in severity.

Reports by several workers of sudden enhancements in N_p occurring at storm onset, were ultimately interpreted as being upper F-region enhancements (in the h_m to 3000-km region) rather than significant increases in N_p. The initial conclusions regarding N_p enhancements came about because the derived values of N_F, and hence N_p, from the measured total content were based on an assumed constant ionospheric shape factor. This assumption proved to be invalid because it did not take into account the rapid distortions occurring in the ionospheric profile during storm onset.

During the N_p recovery phase following a storm, the maximum depression usually occurred on the third day following onset. During the following days, the content was seen to increase with superimposed diurnal filling and emptying; the daytime filling exceeding the nighttime emptying until after about a week, the N_p magnitudes and their diurnal variations become comparable with the monthly average values. These latter observations were based on RBE data at Aberystwyth.

Large and Medium Scale Irregularities

Contour maps of equivalent vertical ionospheric (Faraday) content were constructed from simultaneous RBE observations at Boulder, Bozeman, and Dallas aided by latitudinal gradient data derived from polar orbiting NNSS satellite observations at Boulder and Las Vegas, New Mexico. Similar maps were also constructed in India from multistation ATS-6/RBE observations (Reference 23).

Various features such as troughs, ridges, peaks, holes, etc., were evident in these maps. The advantage of such a map was that the day-to-day changes more truly reflected changes in solar-terrestrial conditions than content data from a single receiving station that were heavily weighted toward isolated local conditions. The accuracy of these contour maps was the greatest near the ATS-6/RBE receiver ray paths and the overall accuracy was considered to be about ±10 percent.

Traveling Ionospheric Disturbances

The use of geographically dispersed ground receivers for the simultaneous observation of Faraday rotation of geostationary beacon signals was a highly effective technique for studying traveling ionospheric disturbances. A number of workers used the ATS-6 Radio Beacon Experiment for this purpose. Both nonperiodic (isolated) and periodic disturbances were observed. The more common of these were wavelike disturbances resulting from the passage of atmospheric gravity waves.

In one experiment, three radio beacon receivers were set up at the apices of an equilateral triangle, approximately 125 km on a side, located at Table Mountain, Fort Morgan, and Elbert, Colorado. Two moving nighttime maxima, which were observed during the later part of 1974, showed speeds in the order of 70 meters per second (m/s) traveling in a southwesterly or westerly direction (References 24, 25).

Reference 25 discusses velocity distribution plots of 25 isolated irregularities based on data from a similar triad of ground receivers located in India at Delhi, Kurukshetra, and Pilani. These medium-scale disturbances occurred as often at night as during the day. The speeds ranged over 30 to 500 m/s with the most frequently observed values being 140 m/s during the day (compared to the U.S. value of 160 m/s) and 110 m/s during the night. The directions of travel, however, were quite different.

The observations in India also produced data on the size and horizontal shape of the irregularities, irregularity content, and the speed, direction and periodicity of periodic disturbances. Gravity-wave fluctuations in Faraday content were observed with periods ranging from 10 minutes to 200 minutes with only rare occurrences with periods of near 15 minutes in agreement with theory.

Sudden Increases in Total Content

Sudden increases in total electron and/or Faraday content (SITEC) are caused by extreme ultraviolet radiation from solar flares. Only the larger events are detected by the radio beacon technique since the ionization enhancements are relatively small and are superimposed on the diurnal variation. Observations at high frequency are subject to excessive absorption that limit the utility of such measurements. The SITEC's, which have been reported using the RBE, have averaged around 5 percent of the background content.

SITEC's are highly individualistic. Theories have been advanced that relate the enhancement mechanisms and sequence of events to the categories of solar flare ionizing radiations, and an altitude-time-enhancement model, for example, was constructed for the sustained type of SITEC (Reference 26).

Some work was done using the Radio Beacon Experiment to estimate the height at which the SITEC ionization occurs. The method depended upon calculating an average $\bar{I}_L$ from measured fractional changes in $\Delta\phi$ and Ω_f. Then, the height was determined from f_L (h) curves to estimate the height at which the additional ionization occurred. The most sensitive parameters needed to be used such as Ω_{40}, $\varphi^{\wedge}_{41}$ or ϕ^{C}_{40}. Careful regression analysis was required because of measurement nonlinearities. The results, however, agreed with those obtained through more conventional techniques.

Small Scale Irregularities

Micropulsations

A long train of small amplitude quasi-sinusoidal oscillations in total content were first noticed at the Bozeman receiver. They reflected Pc4 type geomagnetic pulsations having a period of 30 seconds to 50 seconds and occurred for several hours at midday on geomagnetically quiet days. These micropulsations in N_T were on the order of 0.01 percent to 0.1 percent of the background and could only be detected using the most sensitive carrier phase measurements (ϕ^{C}_{40}).

Quasi-periodic fluctuations were reported from Lindau during times of scintillation. These fluctuations had periods ranging from 1 to 60 seconds and the maximum occurrence took place in December 1975.

Fresnel Focusing by Small Intense Irregularities

Small intense irregularities in electron content occur in the ionosphere and produce a beacon-signal fading pattern characterized by a central minimum flanked on one or both sides by modulated-amplitude fluctuations that increase in frequency away from the minimum. A usually large event of this sort, recorded at Boulder on 40 MHz, 140 MHz and 360 MHz, was studied in detail (Reference 27).

In this study, it was postulated that the irregularity was due to a cylindrical lens of circular cross section with a Gaussian electron density distribution. The geometry is pictured in Reference 27 and it can be seen that there is overlapping of the interference between rays from various parts of such an irregularity. There is a critical phase shift, as observed on the ground, above which interference takes place. This phase shift is proportional to the wave frequency and the square of the cylinder diameter, and inversely proportional to the distance to the irregularity. In calculating the fading pattern, the usual precautions must be taken with respect to ray treatment versus diffraction theory.

Parameters for the lens model were found that closely produced the observed fading pattern. The approximation was excellent at 360 MHz, fair at 140 MHz, and poor at 40 MHz. The latter was explained as a failure of the transparent phase screen model assumed due to the central core of the lens being overdense (plasma frequency calculated to be 43 MHz and therefore opaque [reflecting]). (See Reference 27.)

The modeling indicated that the ionospheric lens was certainly of high intensity and elongated (spherical lens models failed). The actual cross-section could have been in the form of a sheet rather than circular. The diameter was on the order of 100 meters (m) and the velocity was about 50 m/s based on the assumption of a 100-km height rather than an F-layer height, as determined with excellent agreement at 140 MHz and 360 MHz from the amplitude peak separation in the fading patterns. The enhancement in the 40-MHz signal near 0015 universal time (UT) suggested focusing by a marked depression in the electronic content. Such a depression can be modeled by changing the sign of the phase function in the modeling equation.

Ionospheric irregularities frequently occur in closely spaced trains and the resulting defraction patterns have been calculated for a few cases. This work stresses the importance of conducting multi-frequency measurements to avoid erroneous conclusions based on single frequency observations as to the nature of the irregularities.

Faraday rotation and modulation phase measurements do not reflect the electron contents for waves passing through irregularities producing prominent diffraction patterns because of wave interference between the diffracted components.

Scintillation

Random irregularities in the relative dielectric permittivity in the ionosphere cause fluctuations of signal amplitude, phase, rotation of polarization, and angle of arrival of a radio wave propagating

through it. These fluctuations are known as scintillations. Historically, scintillation theories have been based on various approximations using mainly weak scintillation theory to interpret scintillation data. It is a physical fact that the random variation in the relative dielectric permittivity is inversely proportional to the frequency. So, when observations are made with a multifrequency beacon, such as the RBE, during periods in which weak signal fluctuations are seen at the highest frequencies, the lower frequencies will suffer much greater scintillation which may be so severe that weak scintillation theory does not apply.

Efforts to develop a unified scintillation theory had begun just before the time of ATS-6 launch and the RBE multifrequency data was valuable in the further development of that theory.

In the way of background, consider an elongated ellipsoid bounding the first Fresnel zone with the major axis coincident with the ray path, and with the foci situated at the beacon transmitter and the ground receiver. The size of the first Fresnel zone at the height of the irregularity can be shown to be $(\lambda s)^{1/2} = (cs/f)^{1/2}$ where s is the slant range of the irregularity from the receiver.

Irregularities drifting across the ray path produce temporal fluctuations in the parameters of the received signal under most conditions. Fluctuations are observed to be the greatest for drifting irregularities approximately the size of the first Fresnel zone.

One measure of the severity of scintillation is the S4 scintillation index defined as the ratio of the square root of the variance of the received power to the mean power. Multifrequency observations enable the determination of how S4 varies with carrier frequency in the form of f^n where n is defined for two carrier frequencies by

$$n = \frac{\log (S4_a/S4_b)}{\log (f_b/f_a)}$$

Analysis of the frequency spectrum of the scintillations yields a power law irregularity spectrum of the form κ-p where κ is the spacial frequency and p is the power index. The terms n and p are related by the expression $n = (p + 2)/4$. A value of p lying between 3.5 and 5 is typical of ionospheric scintillations and predicts an n of 1.4 to 1.7. For the weak scintillation case, both p and n are independent of the carrier frequency.

Other authors had shown the way in which the scintillation amplitude and phase spectra should be dependent upon a parameter, C_m^2, related to the variance of the refractive index of the medium; to the power index, p; to f_c, the "corner frequency" defined later; and to the irregularity mean drift velocity ν. These relationships had been formulated as follows:

$$\text{Amplitude spectra} \begin{cases} C_m^2 & \text{for } f_{\kappa c} < f_c \\ C_m^2 \left(\frac{f_{\kappa c}}{\nu}\right)^{1-p}, & \text{for } f_{\kappa c} > f_c \end{cases}$$

Phase spectra C_m^2 (f_{sc}/ν) 1-p for all f_{sc} where f_{sc} is the scintillation frequency, and $f_c \simeq \nu/2R$ Hz in which R is the first Fresnel zone radius at the mean height, h, of the irregularities.

The corner frequency, f_c, is the point of inflection seen in scintillation spectra. The time that irregularities fill the first Fresnel zone is R/ν, so that $f_{sc} > \nu R$ are due to irregularities moving through the zone and $f_{sc} < \nu R$ are due to those completely contained within the zone. The term f_c separates the two types. Scintillation frequencies less than f_c are due to propagation through a homogeneous medium of a refractive index other than unity. Those greater than f_c represent scattering. The ratio of mean velocity to height is inferred. The scintillation spectra of the three RBE carriers normalized to scintillation frequency (Reference 28) clearly indicated the f_c inflection.

Nine records at Boulder were analyzed in which the scintillation was weak; i.e., S4 (360) = 0.064 and yielded an n (140/40) of 1.5 to 1.7. Data on all three RBE frequencies showed an $n \simeq 1.6$, and hence inferred a $p \simeq 4.4$ suggesting that weak scintillation theory is valid for a low S4 index. On the other hand, data for high scintillation indices showed a marked decrease in n and p, and an n and p dependence upon carrier frequency indicating multiple scattering.

Scintillation studies on the RBE signals were conducted at many locations. In India, daytime scintillations appeared to be correlated with the occurrence of sporadic E, and nighttime with spread F. At Delhi, nighttime scintillations were greatest during the summer months and minimum at the equinoxes. These peaked at midnight at Delhi and at 2200 at Ootacamund further to the south. The onset of strong scintillations was associated with enhanced polarization rotation indicating large-scale F-region irregularities. Low values of n (0.5 to 0.8), were seen regularly at Delhi, Thumba (equatorial), and Ootacamund. At the later station, scintillation amplitude at 360 MHz sometimes exceeded that at 140 MHz and 40 MHz. Also, in India, nighttime scintillations were seen to commence earlier at the low frequencies but last longer at the high frequencies. At Trivandrum, the scintillations at the higher beacon frequencies always occurred more often than spread F (Reference 29).

The RBE and other satellite beacons were used to observe the effect of storms on scintillations. During the storm that occurred January 10 to 11, 1976, severe scintillations were observed on the RBE signals in India at all but the most northerly stations. Workers at Keflavik, Iceland, established a relationship between scintillation index and magnetic and sunspot indices, but no such definite correlation could be established at Lannion, France.

BEACON IN-ORBIT PERFORMANCE

The fact that the radio beacon transmitter performed well and maintained its calibration throughout the 5-year life of ATS-6 is much to the credit of those involved in putting it together. Continuous beacon operation was planned, but it turned out that this was not always possible because of beacon transmitter interference with other spacecraft experiments and because of prime-power budget limitations during the equinox periods. The monthly percentage on-time ranged from 63 percent to 99 percent for the first year in orbit. The impact on data gathering significantly exceeded actual beacon downtime because data was lost in reestablishing ground receiver lock, and often it was impossible to maintain the cycle count records that were necessary for resolution of measurement ambiguities.

Output Power

Table 2-4 compares the preflight measured effective isotropic radiated power and the in-orbit values measured by several investigators. The agreement with the preflight values was good except for 40 MHz which showed a higher than preflight effective isotropic radiated power and unequal modulation sidebands thought to be associated with the higher than expected antenna voltage standing-wave ratio. Measurements conducted, using the engineering model on a full scale mockup, confirmed the high voltage standing-wave ratio which also upset the output level control loop. This data, therefore, was not sufficient to indicate the exact power output and gave no information as to the power distribution amongst the carrier and sidebands. As a consequence, precise measurements of propagation path loss at 40 MHz, which was one of the experiment goals, were not possible.

Modulation Phase

The overall measurement accuracy of total content, N_T, depended upon how accurately the group delays, contributed by each element of the total system, were known. Furthermore, any in-orbit instabilities in radiated phase would reduce the precision of measurement. The sensitivity to these parameter uncertainties was particularly important in estimating the plasmaspheric electron content, N_p, which is on the order of 10 percent of N_T.

Table 2-4
Comparison of Preflight and In-Orbit Ground-Measured Radiated Power (dB)

Signal Component	Preflight		Ground Measurements		
	Nominal	Predicted	AFCRL*	U. of Ill.**	SEL Boulder***
40 MHz	+27	+28.8	+26.9		+27
40 MHz 100 kHz USB	+24	+23.8	+23.9		+24.7
40 MHz 100 kHz LSB	+24		+24.9		+24.1
40 MHz 1 MHz USB	+27	+26.8	+29.6		+31.2
40 MHz 1 MHz LSB	+27		+23.7		+26.5
140 MHz	+32	+32.3	+35.6	+32	+32
140 MHz 1 MHz USB	+26	+26.3	+26.6		+25.9
140 MHz 1 MHz LSB	+26				+26
360 MHz	+33	+34.9	+34.7	+32	+33
360 MHz 100 kHz USB	+24	+25.6	+24.4	+24	+24.1
360 MHz 100 kHz LSB	+24		+23.6	+25	+22.3
360 MHz 1 MHz USB	+24	+24.7	+21.9	+22	+22.6
360 MHz 1 MHz LSB	+24		+21.5	+22	+22.0

*Based on a radiometric measurement calibrated against CASS A source.
**Based on nominal illumination efficiency for a parabolic antenna.
***Based on nominal AFCRL pattern integration gains for SBF array antennas. Absolute values are ±2 dB. Relative sideband amplitudes are ±0.5 dB.

Table 2-5 presents the group delay contributions at 40.1 MHz, 41 MHz, and 141 MHz of the various elements of the system including the Boulder receiver antennas, and compares these contributions to the group delay expected for typical electron contents. The table shows that the ratio of the system group delay contribution to the overall delay encountered at 141 MHz was nearly ten times that at 41 MHz.

In-orbit simultaneous measurements of $\Delta\phi^R_{40.1}$, $\Delta\phi^R_{41}$, and $\Delta\phi^R_{141}$ were made from which values of N_T were computed. Assuming that equipment channel group delay perturbations were of an equally probable magnitude, a value ϕ_T of 141 MHz transmitted phase was calculated that would bring the 141-MHz N_T computation into agreement with that at 41 MHz. The prelaunch value of ϕ_T was -63 degrees.

After launch, the calibration was checked by comparing N_T calculated from 40.1-MHz and 41-MHz data to that from 141 MHz. During the period October 1974 to May 1975, 13 of 16 data points showed ϕ_T to lie between -65 degrees and -69 degrees. The remaining 3 data points unexplainably lay well out of this range at about -74 degrees. One degree in $\Delta\phi^R_{141}$ or $\Delta\phi^R_{40.1}$ corresponded to about 4×10^{14} e/m^2 and in $\Delta\phi^R_{41}$, one tenth that amount. One goal of the experiment was to measure $\Delta\phi^R_{41}$ to within ±0.05 cycle of ±18 which translated to an uncertainty of about 4 percent in the measurement of plasmaspheric content (average 2×10^{16} e/m^2). The phase stability of the beacon transmitters, as reflected in the first-year in-orbit value of ϕ_T, exceeded this goal by a large margin.

Antenna Performance

Gain changes as a function of satellite attitude were reasonably small at 40 MHz and 140 MHz and reflected the preflight antenna pattern shapes. At 360 MHz, rather large variations in received signal strength of the carrier and sidebands were observed with small pointing angle changes due to the presence of unwanted reflections from the 10-meter satellite reflector. The in-orbit performance reflected the fact that the preflight effort to reduce the 360-MHz beacon antenna backlobe illumination of the reflector was not altogether successful.

Table 2-5
Differential Group Delay Magnitudes

		Typical Minimum Total Content 2×10^{17} e/m^2 (ns)	Typical Plasmaspheric Content (10% Total) (ns)	Transmitter Group Delay (Inc. Ant.) (ns)	Receiving Antennas (ns)
140	1 MHz	1350	135	175	9
40	100 kHz	1650	165	222	46
40	1 MHz	16000	160	203	46

Variations also occurred in 361-MHz group delay with pointing angle and thus caused a variation of $\Delta\phi^{R}_{141}$ modulation phase. Figure 2-16 shows the change in $\Delta\phi^{R}_{141}$ during satellite maneuvers of August 20, 1975. One possible cause for this behavior was inadequate antenna bandwidth. The satellite was frequently maneuvered while it was stationed at 35°E; as a consequence, it was necessary to correct the modulation phase for satellite attitudes from calibrations, obtained during quiet ionospheric conditions, in reducing the Ootacamund data.

The polarization of the transmitted signals was measured prior to launch and it would have taken rather large mechanical distortions of the antenna system to alter their polarization characteristics. Consequently, a great deal of confidence existed that the in-orbit polarization characteristics were unchanged from those during preflight. The polarization rotation at 140 MHz was compared to that obtained using a lunar radar when the satellite and the Moon were nearly aligned and the radiated polarization was found to closely agree with the prelaunch calibration. The values of Faraday content, N_F, determined from 40-MHz and 140-MHz measurements were in good agreement. Cycle ambiguity in this case was resolved by measurement of the differential rotation at 40 MHz and 41 MHz.

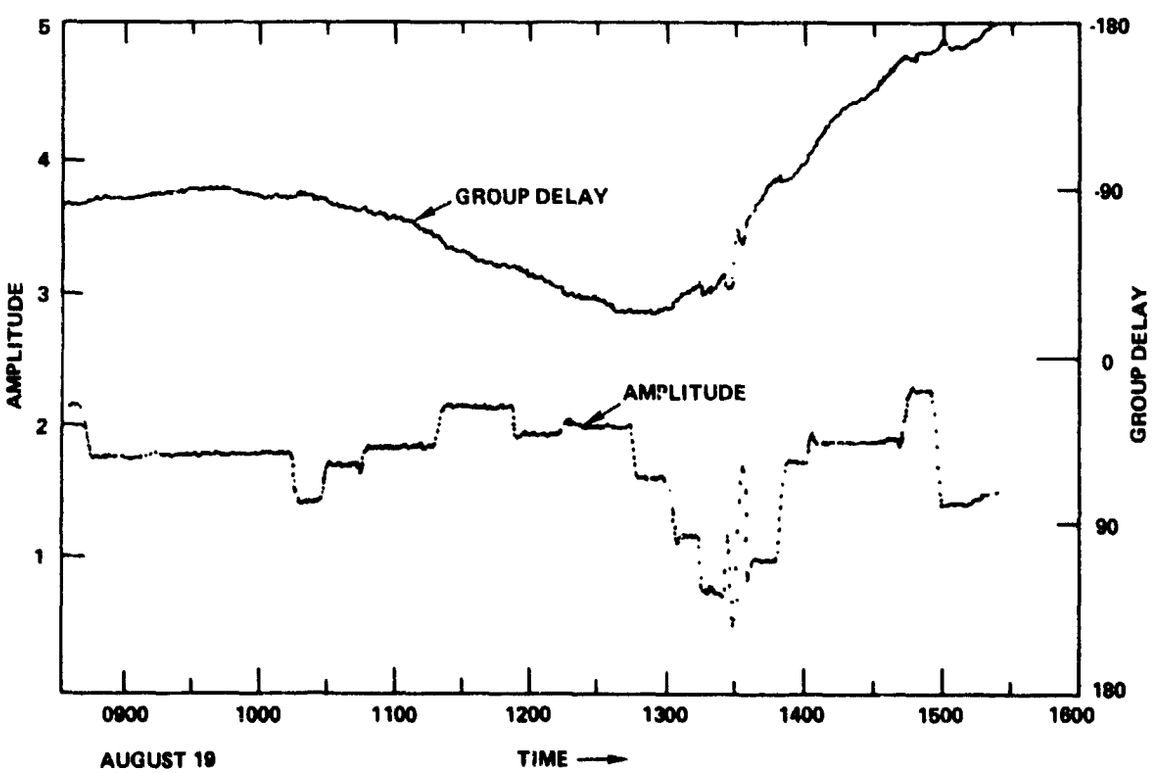

Figure 2-16. Variation in $\Delta\phi^{R}_{141}$ with Antenna Pointing (ATS-6 at 35 Degrees)

Interference to Other Experiments

Interference during beacon operation was evident in the ATS-6 transponder downlinks for all FT modes. The interference spurs appeared to be fifth order products resulting from intermodulation of either the 40-MHz or 140-MHz beacon carriers and the 136.23-MHz telemetry channel that entered the transponder amplifiers intermediate frequency (i.f.) in some undiscovered manner. The 1-MHz and 100-kHz beacon modulations appeared on the spurs. Products with the 137.11-MHz telemetry channel were occasionally evident and occurred at a much lower level than the products with the 136.23-MHz channel.

Based on the nominal frequency assignments, spurs under the condition of no beacon modulation would have appeared if they existed at (3 X 140.056) - (2 X 136.33) = 147.71 MHz and at (2 X 136.23) - (3 X 40.016) = 152.41 MHz (the corresponding products with the 137.11-MHz channel would have appeared at 145.95 MHz and 154.17 MHz, respectively). The actual frequencies observed were closer to 148.0 MHz and 152.1 MHz, suggesting that the 136.23-MHz telemetry carrier may have been low by about 160 kHz. For the ensuing discussion they will be referred to as the 148.0-MHz and 152.1-MHz spurs and all other observed frequencies at the Rosman receiver i.f. output will be referenced to the 150-MHz spacecraft intermediate frequency.

On July 16, 1974, spectrum analyzer photos were taken at the Rosman receiver i.f. output for various spacecraft transponder configurations. Most of the data dealt with the C-band downlink. The spacecraft configurations included the CxC and CxS-SxC FT modes with and without the beacon operating, and with beacon operating with and without applied modulation.

Figure 2-17 (A) shows the C-band downlink with the spacecraft in the CxC mode (with unknown uplink transmit power). The beacon is operating on 40 MHz and 360 MHz without modulation. In the center is the 3950-MHz downlink signal translated to 150 MHz. To the right is the 152.1-MHz spur. Figure 2-17 (B) shows the situation with the beacon operating on all three frequencies and with the 1-MHz modulation turned on. The 148.0-MHz spur appears at a low level and 1-MHz upper and lower sidebands can be seen associated with each. Figure 2-17 (D) shows the same spectrum with reduced uplink power. Figure 2-17 (C) shows the results of applying the 1-MHz and 100-kHz beacon modulations. The display has been moved to the left, expanded, and the resolution increased to show the 100-kHz and 1-MHz sidebands on the 152.1-MHz spur.

Figure 2-18 shows a series of photos of the downlink C-band spectrum with the transponder in the SxC FT mode and with the ground station at various S-band uplink powers. The tranponder was also configured in the CxS mode, but it is not clear whether a C-band uplink signal was applied. The first photo, Figure 2-18 (A), with the S-band uplink power at 50 watts and the beacon operating with 1-MHz modulation, shows the spectrum to be closely identical to that for the CxC configuration, Figures 2-17 (B) and 2-17 (D). There is also a suggestion of the 154.2-MHz spur associated with the 137.11-MHz telemetry channel.

For 50 watts of uplink power, the effective isotropic radiated power (e.i.r.p.) was about 64 dBW. Tracking and Data Relay Experiment tests used the Nimbus satellite with an e.i.r.p. of 20 dBW so that the impact on the tests of RBE operation was very real.

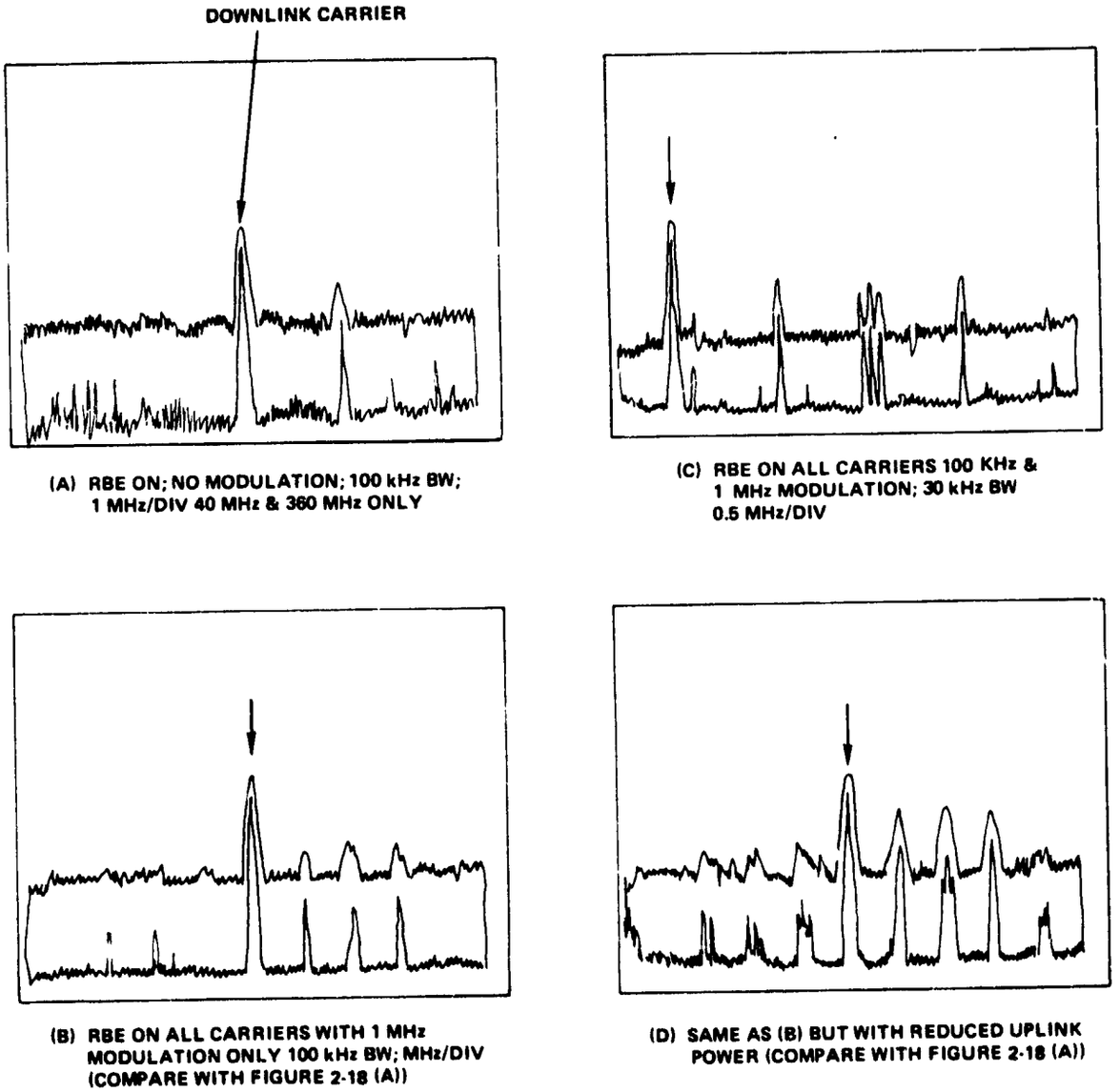

Figure 2-17. CxC Downlink Mode Spectra Near 3590 MHz with 6150-MHz Uplink Carrier—Rosman, July 16, 1974

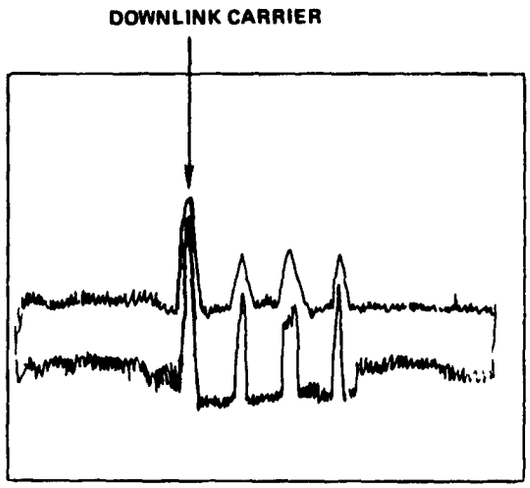

(A) 50W 2050MHz UPLINK. RBE WITH 1 MHz MODULATION; 100 kHz BW: 1 MHz/DIV

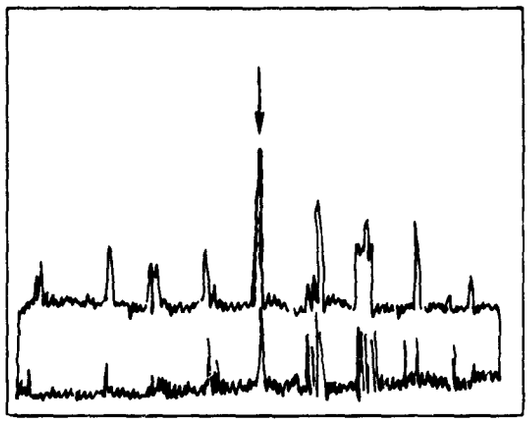

(C) 100W 2250 MHz UPLINK; RBE WITH 1 MHz & 100 kHz MODULATION; 10 kHz BW; 1 MHz/DIV

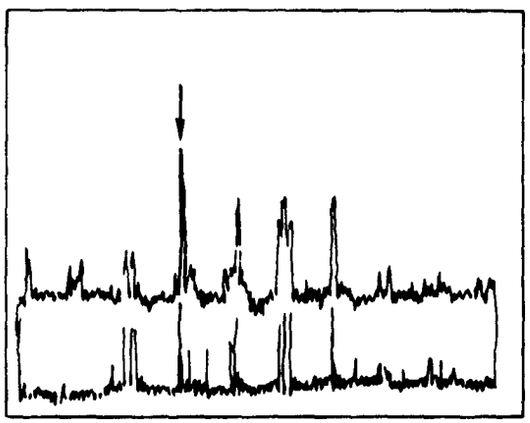

(B) 50W 2250 MHz UPLINK; RBE WITH 1 MHz & 100 kHz MODULATION; 10 kHz BW; 1 MHz/DIV

(D) 500W 2250 MHz UPLINK; RBE WITH 1 MHz & 100 kHz MODULATION 10 kHz BW; 1 MHz/DIV

Figure 2-18. SxC Downlink Mode Spectra Near 3950 kHz—
Rosman, July 16, 1974

Figure 2-19 presents a series of spectrum analyzer displays of the Rosman receiver i.f. output during tests conducted on December 27, 1974, with the transponder configured in the very high frequency (vhf) monopulse X C-band mode. Figure 2-19 (A) shows the spectrum with the command transmitter operating at 2.2 kilowatt (kW) at 153 MHz and the RBE shutdown. The next photo is of the spectrum with the RBE operating and with no uplink carrier. The vhf monopulse X C-band mode appeared to favor the 148.1-MHz, rather than the 152.1-MHz spurs that predominated in the FT modes. Sidebands in multiples of the 1-MHz beacon modulation frequency are very much in evidence. Figure 2-19 (C) shows the spectrum with the 154.2-MHz command carrier up at full power and with the RBE operating. Finally, Figure 2-19 (D) shows the condition for a 153-MHz uplink carrier at a much reduced power of 130 watts with the RBE on.

The desired carrier was only about 3 dB above the maximum spur levels in this case. Fortunately, tests showed that the operation of the RBE did not significantly affect the ability to command the spacecraft using an uplink power of 2.2 kW reflecting the fact the carrier-to-spur-level ratio was on the order of 13 dB.

One of the experiments conducted, during the period when ATS-6 was stationed at 35°E, was the U.S./U.S.S.R. Magnetometer Experiment (Mage). In this experiment, data collection platforms located in the U.S.S.R. transmitted data to the spacecraft in the 150-MHz range. The transponder was configured in the vhf monopulse C-band remodulation (Position Location and Aircraft Communication Experiment) mode. Several tests that were run indicated that the operation of the RBE reduced the already marginal signal-to-noise ratio by about 6 dB. As a consequence, the RBE was shut down during most of the Mage tests.

APPLICATION OF RESULTS

The Radio Beacon Experiment proved to be of great value to both the scientific and engineering communities. The measurement results made a direct contribution to the further understanding of the behavior of the ionosphere and the physical processes that take place within it. The new data obtained enabled refinement of transionospheric radio link refraction and time-of-flight correction, and provided an insight into the high-data rate bandwidth limitations and radio-link fade margins imposed by scintillations. The beacon provided integrated data as opposed to earlier in-situ techniques. This fact made possible a perspective of ionospheric behavior that previously had been difficult to achieve. The value of coincident data from polar orbiting satellites, radar, and incoherent scatter measurements cannot be overly stressed. Some of the specific outgrowths of the radio beacon work follows.

Earlier satellite beacons had measured only N_F, but it is N_T, the total content, that determines the propagation time and group delay of signals traveling through the ionosphere. From the RBE experiments, it was determined, for example at Boulder, that near midday, when N_F is the highest, the monthly mean of N_p is about 10 percent of N_F (15 percent of N_F in Europe), and at night is about 50 percent of N_p. There is not much diurnal variation of N_p during the summer. Thus, a rule of thumb was established to estimate N_T as a function of local time (LT) entirely from measurements of N_p by use of the equation

$$N_T\ (LT) = (0.1 \text{ or } 0.15)\, N_p\ (\max) + N_F\ (LT)$$

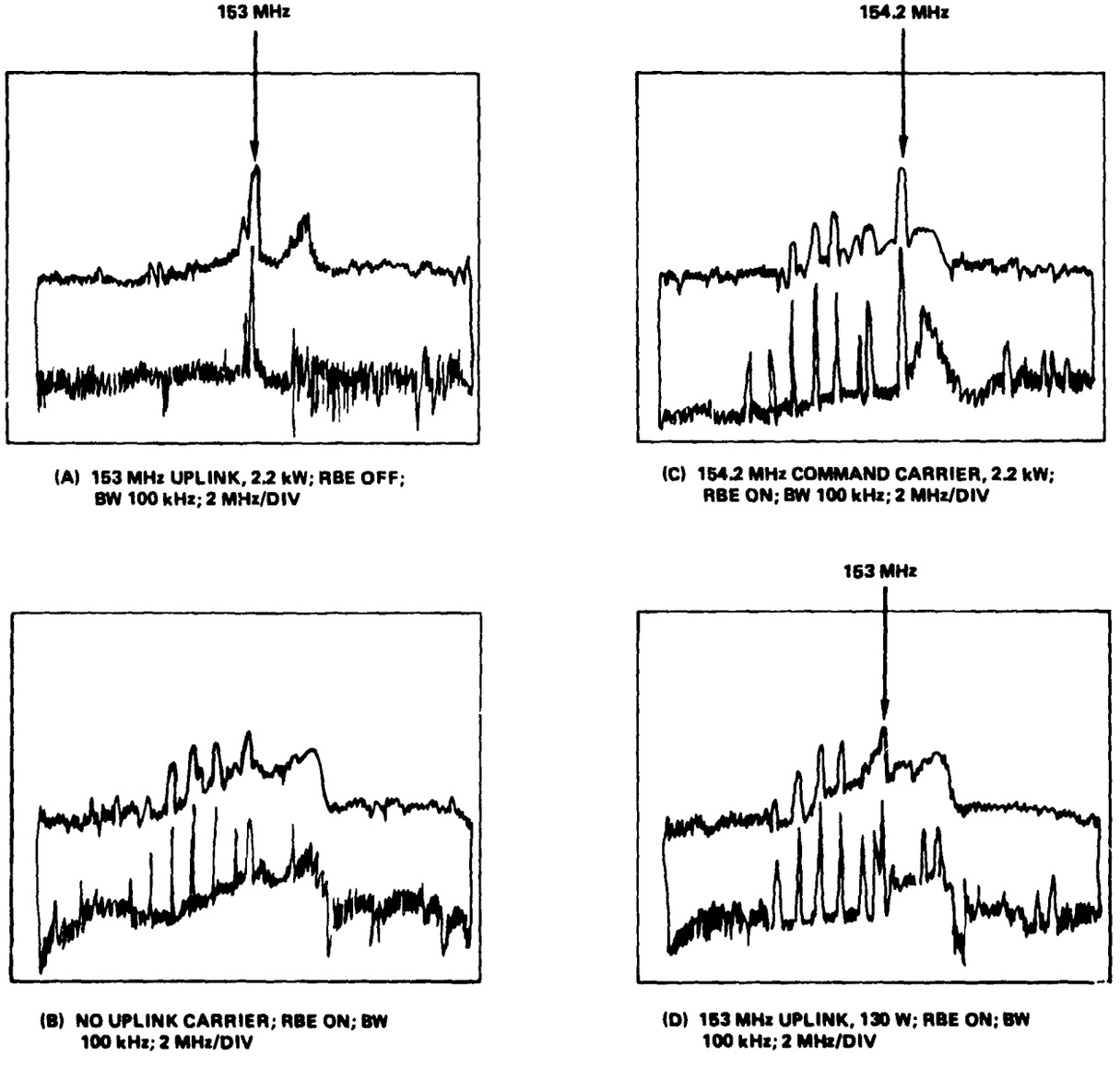

(A) 153 MHz UPLINK, 2.2 kW; RBE OFF; BW 100 kHz; 2 MHz/DIV

(C) 154.2 MHz COMMAND CARRIER, 2.2 kW; RBE ON; BW 100 kHz; 2 MHz/DIV

(B) NO UPLINK CARRIER; RBE ON; BW 100 kHz; 2 MHz/DIV

(D) 153 MHz UPLINK, 130 W; RBE ON; BW 100 kHz; 2 MHz/DIV

Figure 2-19. VHF Monopulse x C-Band Mode Spectra, Rosman, December 17, 1974

Correlation of the diurnal variations of N_F at Fort Monmouth, New Jersey, and Richmond, Florida, was found to be reasonably high, so it appears, at least at midlatitudes, that N_F observations at one location can be extrapolated to another.

Based on the fact that at midlatitudes, the monthly root mean square (rms) variation of total content was measured to be about 20 percent, error corrections were estimated for precise ranging systems using monthly averages. A numerical model of N_T at low magnetic latitude was developed for refraction corrections in satellite tracking and navigation at the low latitudes.

A number of workers have attempted to use scintillation data to predict radio link performance. Data was presented in the form of Nakagami distributions spectral indices, etc. Fade margin recommendations were made by one group in India for radio links subject to strong scintillation. They suggested that the margin ought to be 12 dB at 40 MHz and 140 MHz, and 7 dB at 360 MHz for signals to be received 100 percent of the time.

CONCLUSIONS AND RECOMMENDATIONS

In summarizing, the major accomplishments of the Radio Beacon Program were:

1. The beacon provided the first extensive measurements of electron content above 2000 km.

2. It enabled continuous measurements of the total electron content near the geomagnetic equator where the older Faraday technique had failed.

3. International cooperative programs in North America, Europe, and India provided concurrent electron content measurements as functions of geographical location and time.

4. High-time resolution (e.g., 1 second at Boulder and 0.1 second at Ootacamund) enabled detailed quantitative studies of transient phenomena such as sudden increases in total content caused by solar flares, effects of geomagnetic sudden commencements, micropulsations in total content, and Fresnel diffraction by small intense plasma lenses.

5. It discovered that, in winter, the plasmaspheric content maximizes at night in the United States, but maximizes near noon in Europe.

6. It discovered that the plasmaspheric content is highly sensitive to geomagnetic disturbances. Following the onset of a storm the plasmaspheric content decreases, reaches a minimum on the third day and may take 2 to 3 weeks to recover to the quiescent level.

Technically, the overall performance of the radio beacon was mainly excellent and it maintained its calibration very well. The notable exceptions were the failure of the 40-MHz automatic level control loop due to a high antenna voltage standing wave ratio (VSWR), beacon interference to other experiments, and the 360-MHz antenna bandwidth and pattern ripples causing variation of the 360-MHz modulation phase with the satellite pointing angle. The interference factor and the

satellite prime power limitations during the equinoxes were a serious detriment to the continuous taking of data; much data was lost, particularly equinocial data. In the future, the performance in these areas should be stressed.

Future beacon programs should adopt a multisatellite approach so that simultaneous data over wide geographical areas are available. In this regard, the decision not to launch ATS-G had a serious impact on the Radio Beacon Experiment. The 20-MHz channel, as originally planned, was sorely missed by the scientific community and should be incorporated in future radio beacon experiments.

REFERENCES

1. Stewart, Balfour, *Encyclopedia Britannica*, 9th Ed., Vol. 16, p. 181.

2. Kennelley, A. E., *Electrical World Engineering*, Vol. 39, p. 473.

3. Heaviside, O., *Encyclopedia Britannica*, 10th Ed., p. 215.

4. DeForest, Lee, *Proc IRE*, Vol. 1 (1913).

5. Fuller, L. F., *Trans AIEE*, Vol. 34, p. 567 (1915).

6. Hulbert, E. O. and A. H. Taylor, *Physical Review*, Vol. 27, p. 189 (1926).

7. Breit, G. and M. A. Tuve, *Physical Review*, Vol. 28, p. 554 (1926) and M. A. Tuve and G. Breit; *J Geophysical Res.*, Vol. 30, p. 15 (1925).

8. Appleton, E. V. and M. A. F. Barnet, *Nature*, London Vol. 115, p. 333 (1925). Proc. Royal Soc., Vol. A109, p. 621 (1925).

9. Dieminger, W., *J. Atmos. Terr. Physics*, Vol. 36, p. 2085 (1974).

10. Chapman, S., *Proc. Phys. Soc.*, Vol. 43, p. 26 (1931).

11. Lassen, H., *Ann. Phys.*, Vol. 6, p. 415.

12. Eckersley, T. L., *Philosophical Magazine*, Vol. 40, p. 1250 (1925).

13. Eckersley, T. L., *Nature*, London, Vol. 135, p. 104 (1935).

14. Smith, R. L., R. A. Helliruelle, and U. W. Yabroff, *J. Geophys. Res.*, Vol. 65, p. 815 (1960).

15. Storey, L. R. O., *Phil. Trans. Royal Society*, Vol. A246, p. 113 (1953).

16. Carpenter, D. C., *J. Geophys. Res.*, Vol. 68, p. 1675, March 1963.

17. Murray, W. A. S. and J. K. Hargreaves, *Nature*, London, Vol. 173, p. 44 (1954).

18. Titheridge, J. E., *Planetary Space Science*, Vol. 20, p. 353 (1972).

19. Poletti-Liuzzi, D. D., K. C. Yeh, and C. H. Liu, *J. Geophys. Res.*, Vol. 82, p. 1106 (1977).

20. Davies, K., R. B. Fritz, and T. B. Gray, *J. Geophys. Res.*, Vol. 81.

21. Davies, K., D. N. Anderson, et al., *J. Geophys. Res.*, Vol. 83 (In Press) (1979).

22. Hargreaves, J. K., and F. Bagenal, *J. Geophys. Res.*, Vol. 82, p. 731 (1977).

23. Davies, K., G. K. Hartmann, and R. Leitinger, *J. Atmos. Terr. Phys.*, Vol. 39, p. 571 (1977).

24. Davies, K., et al., *Joint Radio Beacon Program NOAA/MPAE/Graz.*, Max Planck Institute for Aeronomy, Lindau, West Germany.

25. Sigh, L., et al., *Indian J. Radio Space Physics*, Vol. 6, p. 245 (1977).

26. Donnelly, R. F., et al., *The Geophysical Use of Satellite Beacon Observations*, Ed. M. Mendillo, Boston University, p. 345 (1976).

27. Davies, K., and J. D. Whitehead, *J. Atmos. Terr. Phys.*, Vol. 39, p. 383 (1977). Davies, K. and J. D. Whitehead, *Propagation Limitations of Navigation and Repositioning Systems*, AGARD Conf. Proceedings No. 209, pp. 7-1 to 7-5 (1977).

28. Umeki, R., C. H. Kiu, and K. C. Yeh, *J. Geophys. Res.*, Vol. 82, p. 2752 (1977).

29. Rastogi, R. G., et al., *Pramana*, Vol. 8, p. 1 (1977).

CHAPTER 3

INTRODUCTION TO ENVIRONMENTAL MEASUREMENTS EXPERIMENTS

INTRODUCTION

The Environmental Measurements Experiments (EME) package was a comprehensive group of eight scientific experiments on ATS-6 that was designed to increase scientific and engineering knowledge of the spacecraft environment at synchronous altitude. The primary objective was to study the geosynchronous environment to gain information on electromagnetic-ionospheric interactions.

The EME included six particle instruments that were able to determine the nature of particle distribution for electrons and ions over a range in energy from less than 1 electron volt (eV) to greater than 1000 million eV, a range of over eight orders of magnitude in energy.

A seventh experiment, which was used in conjunction with the charged particle measurements, provided a sensitive, low noise, triaxial fluxgate magnetometer capable of providing measurements of the local magnetic field and its variation.

The eighth experiment was a continuation of previous Application Technology Satellite engineering studies, and provided measurements of the overall life characteristics and performance degradation of solar cells in space.

The EME package was located on ATS-6 on a structure at the base of the 9.14-meter parabolic reflector on the outboard side of the reflector hub. The EME package was rotated 13 degrees about the spacecraft Z-axis to align the package with the normal direction of the lines of the magnetic field at 35° East longitude. (See Figure 3-1.)

The EME structure provided a platform upon which the associated electronic packages were mounted. To satisfy the different view angle requirements of the experiments and the rigidity needed to keep the amplification of vibration to a minimum, a "honeycomb sandwich" shelf design was used. A substructure was designed to interface complimentary symmetry metal oxide semiconductor (COSMOS) devices used in the command interface control (CIC) and encoder units. The honeycomb shelf was enclosed around the edges by four magnesium hardbacks. These pieces served as a mounting surface for the louvers, thermal covers, and solar brackets.

The EME outer surface was covered with lightweight multilayer insulation. Openings were provided in the multilayer blanket to enable viewing by the experiments. Thermal insulation between the EME and the spacecraft was accomplished by the use of nine thermal isolators of known heat transfer characteristics. Electrically grounding the EME to the spacecraft was accomplished by a low "heat loss" ground strap.

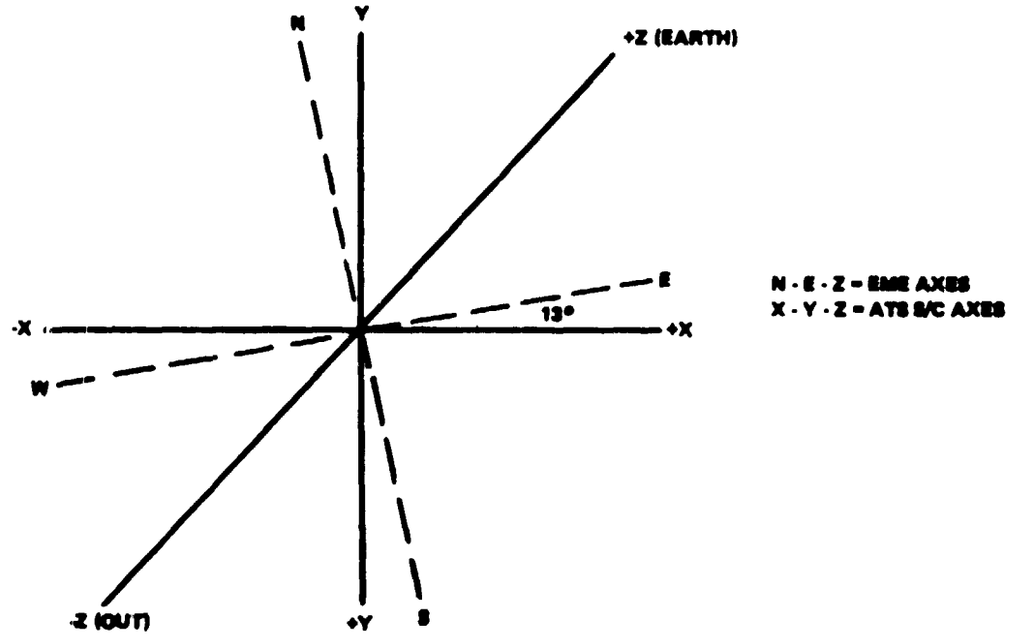

Figure 3-1. ATS-6/EME Coordinate System

A complete list of individual units, their purpose, and source is given in Table 3-1.

Figure 3-2 presents the EME package/spacecraft interface requirements. A block diagram of the EME system interconnections and data flow is given in Figure 3-3. Tables 3-2 and 3-3 itemize the data, programming, ground commands, power, and weight of the components in the EME.

A summary of these tables is as follows:

- Weight 73.5 kilograms (162 pounds)
- Power (average) 46 watts
- Data lines 188
- Programming 51
- Ground Commands 128

Table 3-1
EME Flight Equipment

Experiment	Experiment Characterization	Purpose	Experimenter
McDonnell Douglas Corp.	Solar Cosmic Ray	Study solar cosmic rays, entry and propagation within magnetosphere, make detailed measurements of trapped electrons.	A. J. Masley McDonnell Douglas Corp. Huntington Beach, Calif.
Univ. of New Hampshire	Low Energy Proton-Electron	Make swept and pitched angle measurements of low energy electrons and protons in the magnetosphere.	Dr. R. L. Arnoldy
NASA/GSFC/ NOAA	Low Energy Proton	Study low energy protons.	Dr. T. Fritz/Dr. A. Konradi
Univ. of Minnesota	Electron-Proton Spectrometer	Investigate the origin of the Van Allen trapped radiation.	Dr. J. R. Winckler
Univ. of Calif. at San Diego	Auroral Particles	Study the distribution of low energy electrons and protons.	Dr. C. McIlwain
Univ. of Calif. at Los Angeles	Magnetometer	Study the magnetic field at synchronous distances.	Dr. P. J. Coleman
Hughes Aircraft Co.	Solar Cell Radiation Damage	Measure life characteristics and performance degradation of solar cells in space.	W. C. Dunkerly Hughes Aircraft Co. Los Angeles, Calif.
Aerospace Corp.	Omnidirectional Spectrometer	Measure omnidirectional fluxes and spectra of electrons and protons.	Dr. G. A. Paulikas Aerospace Corp. Los Angeles, Calif.

Support Equipment	Purpose	Source
Telemetry Encoder	Convert analog and digital experiment output to a pulse code modulation format. Provide experiment programming signals and real-time clock information. Provide modulator buffer outputs for telemetry.	Westinghouse Electric Corp.
Power Supply	Supply regulated and/or unregulated voltages to the encoder, command interface control, thermistors, and solar aspect sensor. Monitor total EME power.	Westinghouse Electric Corp.
Command Interface Control	Convert spacecraft commands to control experiment power and modes. Provide verification of ground commands and mode status ID's.	Westinghouse Electric Corp.
Solar Aspect Sensor	Two-axis solar angle identification and turn-on control of Hughes Aircraft Co. experiment.	Westinghouse Electric Corp.
Structure and Substructure	Provide cable interconnections, radiation shielding, spacecraft interface, and suitable dynamic and thermal environments for all EME components.	Westinghouse Electric Corp.

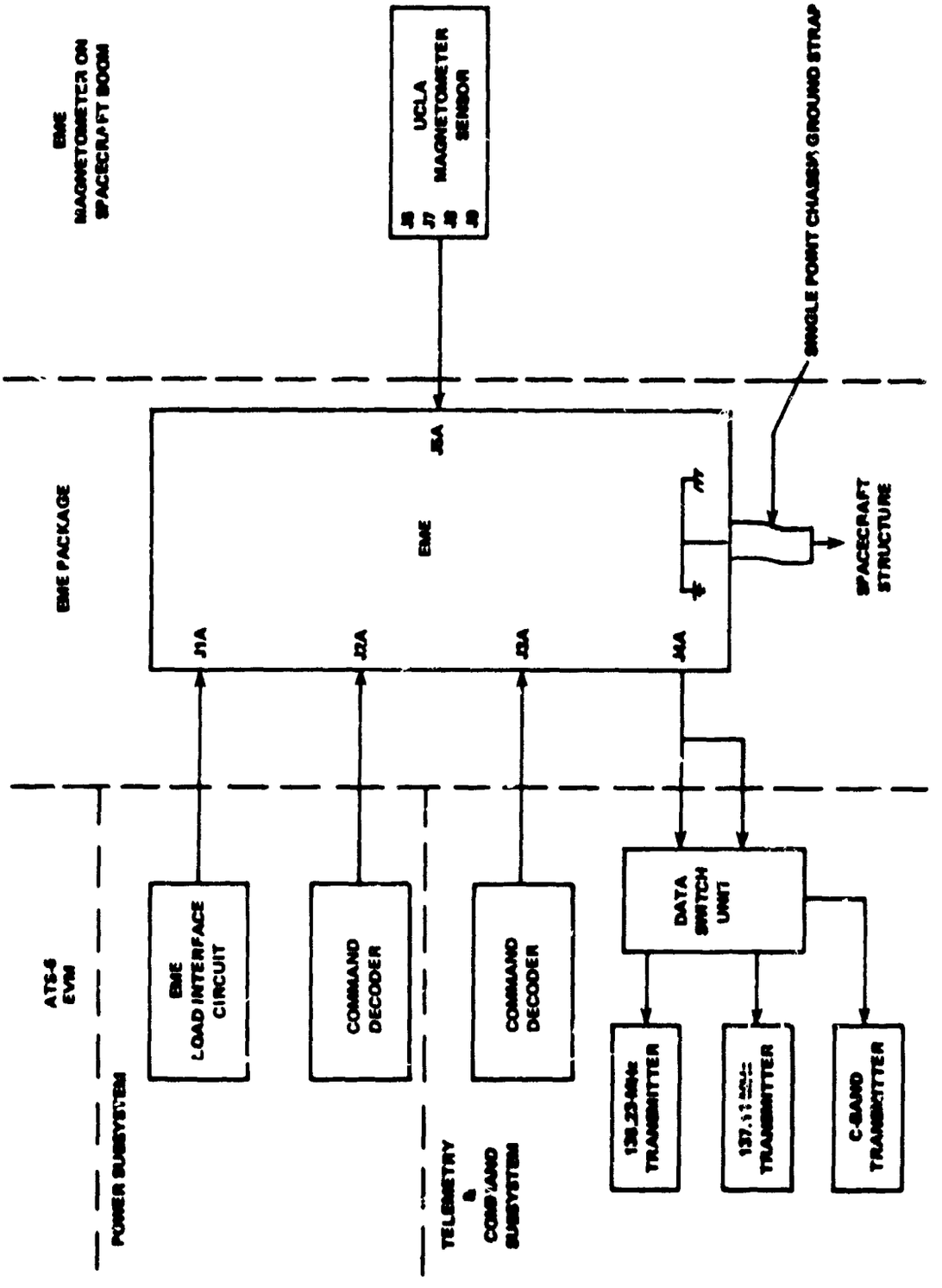

Figure 3-2. ATS-6/EME Interface Block Diagram

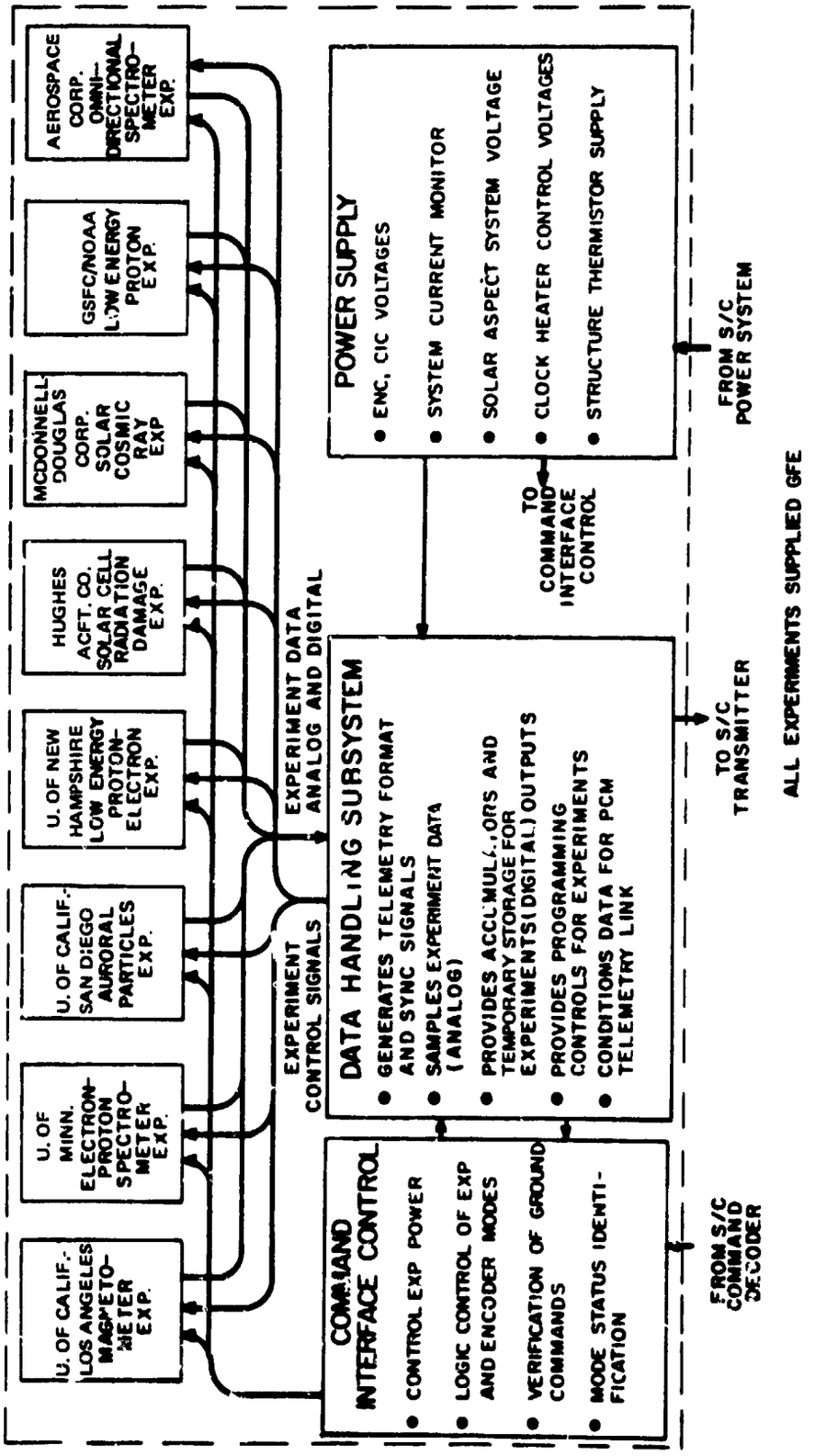

Figure 3-3. EME Data Flow Interconnections

Table 3-2
Experiment System Description

Experiment	Data				Program. Sig.	Mode Cmd.	Wgt.		Avg. Power (watts)
	Digital	Bilevel	Analog	P.P.			(kg)	(lb)	
McDonnell Douglas	10	0	0	14	11	1	6.83	15.07	2.27
U. of New Hampshire	8	0	0	4	5	9	2.98	6.58	5.12
NASA/GSFC/NOAA	3	0	2	7	9	9	2.46	5.43	1.0
U. of Minnesota	12	4	0	3	1	0	2.92	6.44	3.83
U of Calif. at San Diego	5	14	0	15	8	28	4.92	10.85	7.0
U. of Calif. at Los Angeles Electronics	0	1	6	3	2	0	3.26	7.18	3.83
U. of Calif. at Los Angeles Sensor	0	0	0	0	0	0	0.44	0.97	0
Hughes Sig. Proc. Units	0	0	6	0	2	0	2.60	5.73	7.80
Hughes Solar Panel	0	0	0	0	0	0	1.04	2.3	0
Aerospace	12	0	0	4	0	0	1.15	2.53	0.41
Totals	50	19	14	50	38	47	28.60	63.08	31.26

Table 3-3
Support Equipment System Description

Component	Data				Program. Sig.	Mode Cmd.	Wgt.		Avg. Power (watts)
	Digital	Bilevel	Analog	P.P.			(kg)	(lb)	
Encoder	–	–	2	7	–	12	3.56	7.85	1.2
Clocks and Controls									1.0
Power Supply	–	–	–	11	–	–	1.79	3.95	3.0
Command Interface Control	–	9*	–	1	13	–	3.83	8.44	2.5
Solar Aspect Sensor (2)	–	14	–	–	–	–	0.45	1.00	0.2
Structure and Harness				11			29.54	65.12 (a)	
Totals		23	2	30	13	12	39.17	86.36	7.9

*90 binary digits multiplexed into ten groups (words) of nine bits.

EME TELEMETRY

The following paragraphs give a brief description of the pulse code modulation (PCM) telemetry format and the methods employed by the encoder-programmer to encode experiment and housekeeping data. Details of the telemetry format and commands for each experiment are further described in the paragraphs dealing with the final results of each experiment. A comprehensive understanding of the overall EME telemetry system can help to better analyze the data and final results of each experiment.

The eight scientific experiments delivered both analog and digital outputs to the encoder, and required digital control signals from the encoder-programmer to initiate mode changes in the experiments. The commutation of experimental data that generated the required PCM format was performed in the encoder. Little or no subcommutation was required by the individual experiments.

Telemetry Format

The PCM telemetry main and Hughes format frames consisted of 200 words per second, each word consisting of nine bits. The resultant bit rate was 1,800 bits per second and each word time was 5 milliseconds. The first three words (27 bits) of each frame were used for frame synchronization and employed the following code:

Word 1			Word 2			Word 3		
111	110	101	101	001	011	110	000	000
MSB		LSB	MSB		LSB	MSB		LSB

In the telemetry bit stream, the most significant bit (MSB) of a word appeared first in time.

The encoder switched between the main and Hughes format. The Hughes format consisted primarily of data from the Hughes Aircraft Corporation (HAC) solar cell experiment, while the main format contained data for the other seven experiments. Switching to the Hughes format was accomplished through the command interface control unit in conjunction with a solar aspect sensor that detected Sun incidence to within ±2 degrees of normal to the Hughes solar panel. The command interface control turned on the solar cell experiment and sent a signal to the encoder which then switched formats to read out primarily solar cell experiment data for a period of 2 to 3 minutes. At the end of this period, the encoder reverted to the normal format mode and sent a signal to the command interface control that, in turn, removed power from the solar cell experiment and locked out the automatic feature for a period of 2 to 3 hours. The solar cell experiment and format was also obtained by ground command with lockout and lockon times being the same as for the automatic mode. The formats are shown in Figures 3-4 and 3-5.

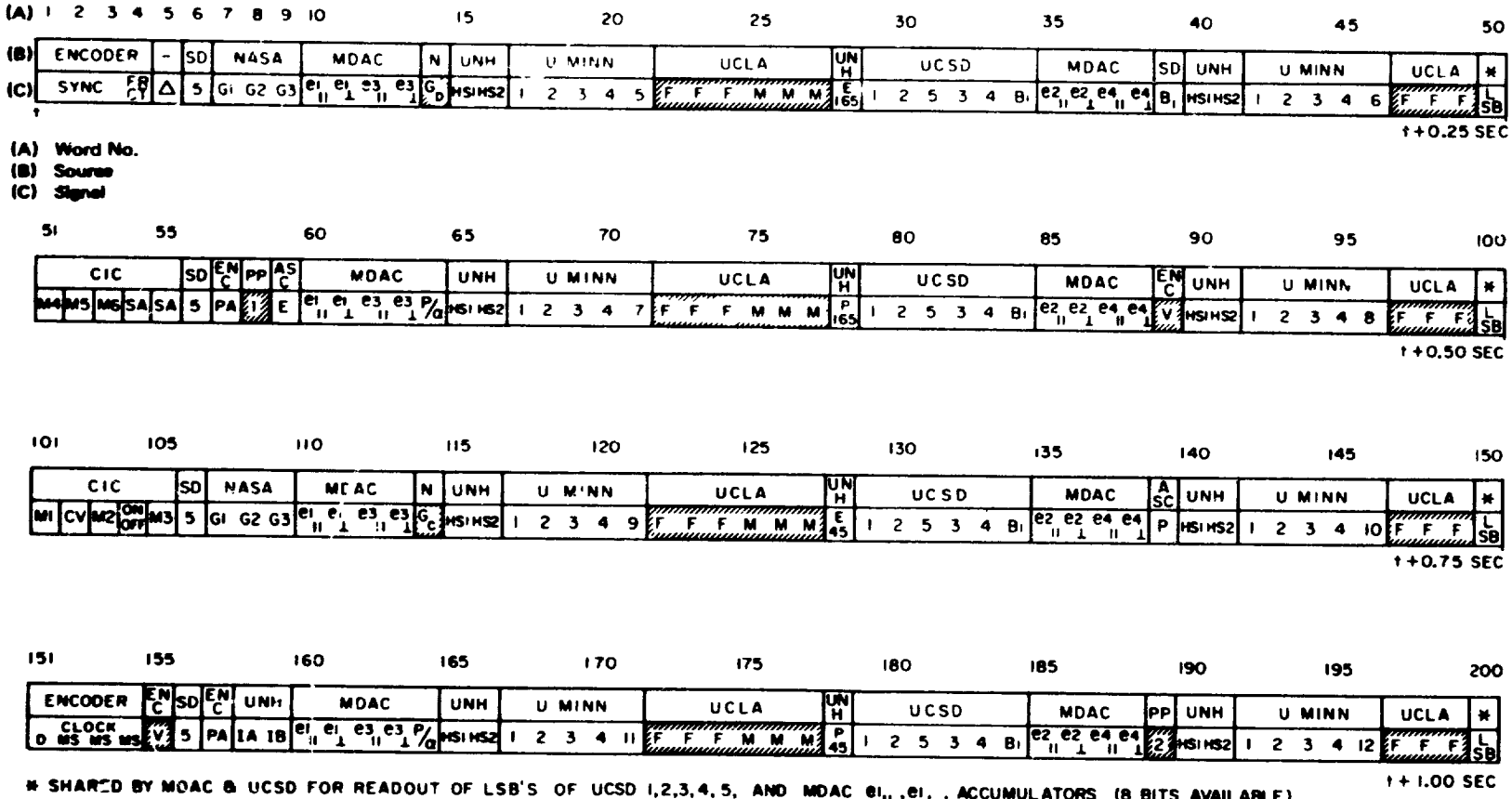

Figure 3-4. EME Telemetry Format–EME Main Frame

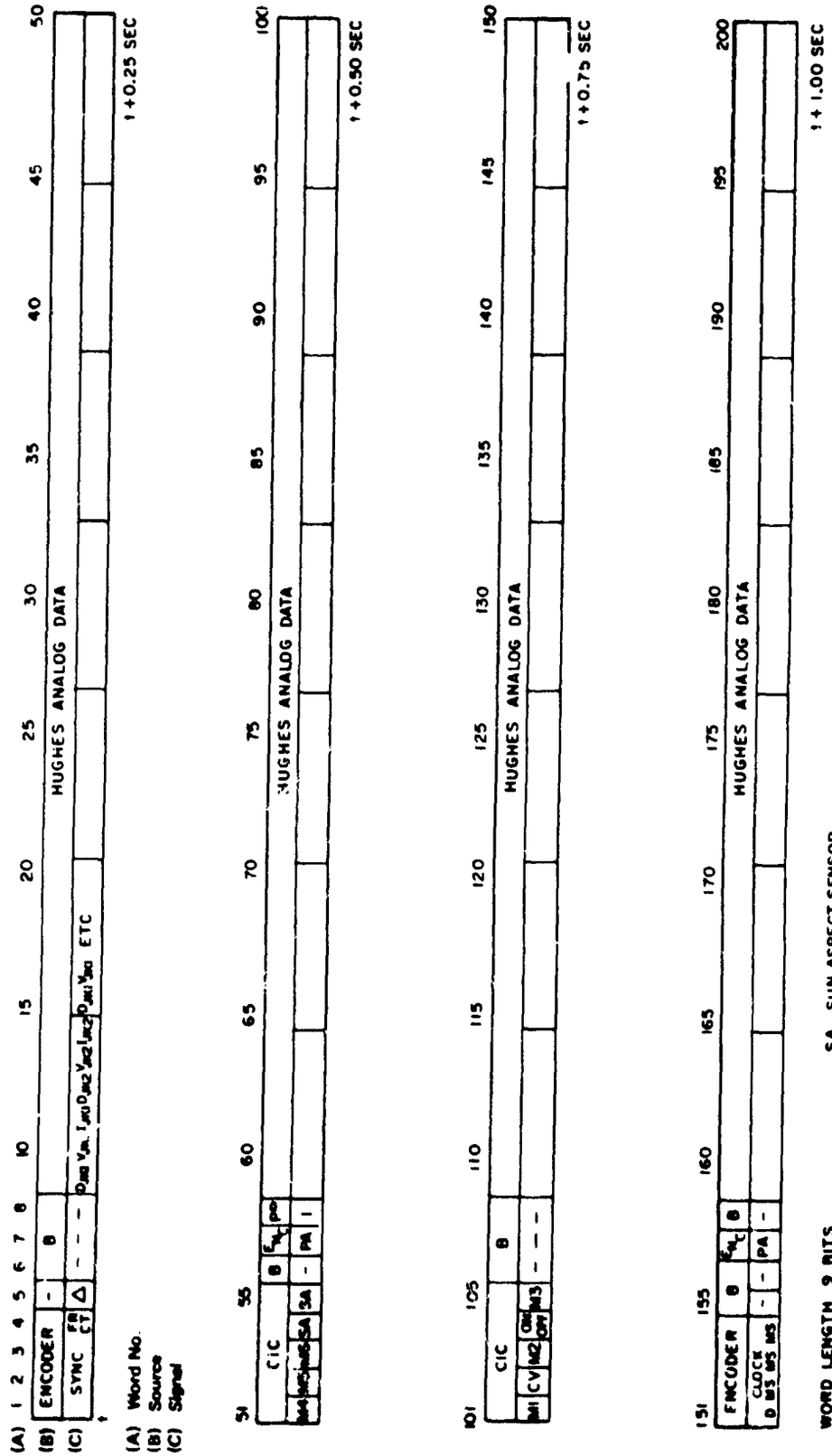

Figure 3-5. ATS-6 EME Telemetry Format—Hughes Solar Cell Experiment

More than 90 percent of each format was devoted to experiment data and housekeeping parameters. The remaining information was composed of synchronization, mode, parity, and real-time clock data that for ease of ground handling were placed in the first eight words of each quarter frame.

Handling of Digital Data

Digital data were buffered into the encoder through accumulators. Experiments with digital-data interfaces had one or more of their own accumulators. The encoder employed 16-bit accumulators that, in all cases except one, were log compressed to either 10 bits or 9 bits. For the lone exception, no compression took place. For purposes of illustration, the log-compression system (for 16B/9B) operates as follows:

For the 16 bits, the compressor accumulated the number of shifts required to reach, but not include, the first "1." The number of shifts required was then represented, in the 9-bit readout word, by the four MSB's of the nine (2^8 - 2^5). This was called the "exponent." The compressor then loaded the next five bits following, but not including the first "1," into the five least significant bits (LSB) (2^4 - 2^0) of the 9-bit word. For 10-bit compression, six bits were taken and the last, or LSB, was loaded into another word for readout.

Example

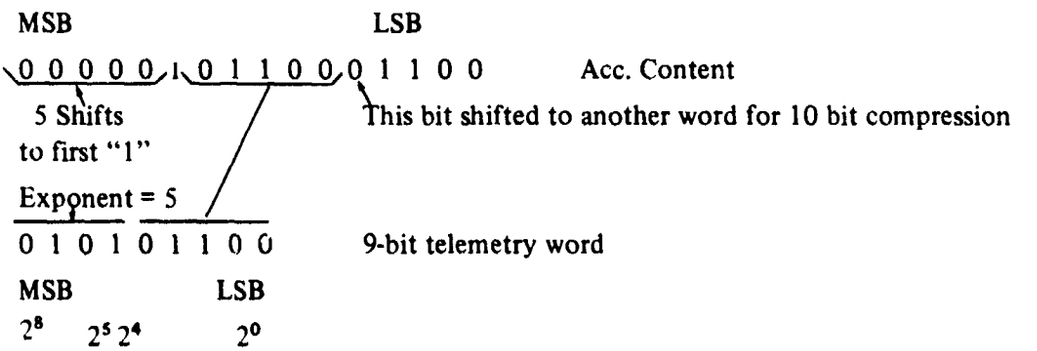

Following compression, data were shifted serially through a master gate into the split-phase output circuitry. All digital-data signals to the encoder were positive with a maximum-pulse pair occurrence of 1 megahertz (MHz). These signals were a nominal 0 volt in the quiescent state and a nominal +10 volts when a signal was present.

Handling of Bilevel (Discrete Digital Data)

The bilevel data were handled in a similar manner as the digital data, except the accumulators or log compressors were not required. Experiment data were presented to nine bit registers in the encoder from which they were shifted serially through the master gate into the split-phase output circuitry. Voltage levels remained the same for digital data.

Handling of Analog Data

The analog data received by the encoder varied between a level of 0 volt and +5.12 volts. These analog data were processed through one or two levels of multiplexing. One level of multiplexing was used where the accuracy of a data line was to be 9 bits ±1 bit. After multiplexing, the data were inserted into the binary-digital format by either of two double-ramp integrator analog-to-digital converters. The converter output was parallel loaded into a 9-bit shift register from which it was gated serially to the split-phase output circuitry.

Analog-data signals were clamped to prevent damage to the encoder multiplexers and, as designed, could not become more negative than -0.7 volt or more positive than +7.5 volts.

Performance Parameters

Performance parameters were treated as analog signals (0 to 5.12 volts). Two performance parameters were sampled per frame and a complete peak-to-peak cycle took 64 frames and was repetitive.

The encoder sampled 80 different performance parameters. Of these, 50 interface lines were used for experiments and 25 for EME package housekeeping. Three temperature monitors and the digital/analog (D/A) drift control monitor for each clock were internal to the encoder.

Performance parameter distribution was as follows:

Experiments		EME Package	
Univ. of Calif. at Los Angeles	3	Structure temperature	11
Goddard Space Flight Center	7	Encoder temperature	3
Univ. of Minnesota	3	Power supply temperature	2
Univ. of Calif. at San Diego	15	Clock ATC	2
McDonnell-Douglas Corporation	14	Command interface control temperature	1
Univ. of New Hampshire	4	Voltages	8
Aerospace Corporation	4	Current	1
		Digital/analog drift control (clocks)	2

CHAPTER 4

EME EXPERIMENTS

INTRODUCTION

A detailed description of the EME experiments is covered in the following paragraphs.

Abbreviations as they apply to the experiments are given below:

UCSD, SD	University of California, San Diego Auroral Particles Experiment
NASA	NASA/GSFC/NOAA Low Energy Proton Experiment
MDAC	McDonnell Douglas Solar Cosmic Ray Experiment
UNH	University of New Hampshire Low Energy Proton-Electron Experiment
U. Minn.	University of Minnesota Electron-Proton Spectrometer Experiment
UCLA	University of California at Los Angeles Magnetometer Experiment
ASC	Aerospace Corporation Omnidirectional Spectrometer Experiment
Hughes, HAC, Solar Cell	Hughes Aircraft Company Solar Cell Radiation Damage Experiment

UCLA MAGNETOMETER EXPERIMENT, UNIVERSITY OF CALIFORNIA, LOS ANGELES, DR. P. J. COLEMAN

Purpose

The purpose of the UCLA experiment was to study the properties and dynamics of the magnetosphere, magnetospheric tail, magnetopause, and magnetosheath of the Earth at synchronous altitudes. A secondary objective was to continuously monitor the strength of the Earth's magnetic field at synchronous altitudes. The dynamic range of the instrument was ±512 gamma (γ), with a resolution of $1/16\gamma$.

Physical Description

The system was physically divided into two parts, an electronics package and a sensor package. The electronics package was mounted in the EME structure, while the sensor was mounted on a spacecraft boom. The sensor and electronics were connected by a cable.

Description of Operation

Figure 4-1 is the block diagram of the ATS-6 UCLA experiment. The magnetometer consisted of four subsystems: the basic magnetometer, digital offset field generators, in-flight calibration, and the power supply.

Basic Magnetometer

Figure 4-2 is a block diagram of a basic-nulling type monoaxial second harmonic fluxgate magnetometer. Three such subsystems were combined to form the triaxial experiment for ATS-6. The sensor consisted of two cores of magnetically permeable material, with primary windings connected series opposing and secondary windings connected series aiding. In the absence of an external field, the cores were driven symmetrically into saturation in alternate directions by a current in the primary windings. An ambient field along the cores caused the cores to remain in saturation longer in one direction than in the other. A second-harmonic voltage, which was proportional to the impressed field along the core, was induced in the secondary windings.

This second-harmonic voltage was amplified and then rectified to obtain a d.c. voltage. A part of the demodulated output was applied back to the probe through the feedback winding in such a way as to oppose the field to be measured. A low-pass filter function was inherent in the demodulator mechanization, and it reduced the loop gain to less than one at the frequency where the phase shift was 180 degrees.

The amount of feedback necessary to null the field to be measured gave an indication of the field's strength. By changing resistors in the feedback circuit, the sensitivity of the probe could be altered. By using a high-loop gain, very stable operation and excellent linear sensitivity were obtained.

A synchronous demodulator was used to detect the direction of the field. The second-harmonic output of the sensor changed by 180 degrees when the field was reversed. The synchronous detector was sensitive to this change of phase. This detector had the further advantage of being insensitive to fundamental and odd harmonic components in the signal which had not been completely eliminated by the band-pass filters in the second harmonic amplifiers.

The basic magnetometer had a bandwidth that was much wider than could be handled by the ATS-6 telemetry; therefore, a four-pole, low-pass filter was inserted between the basic magnetometer output and the telemetry input.

The range of the basic magnetometer was $\pm 16\ \gamma$.

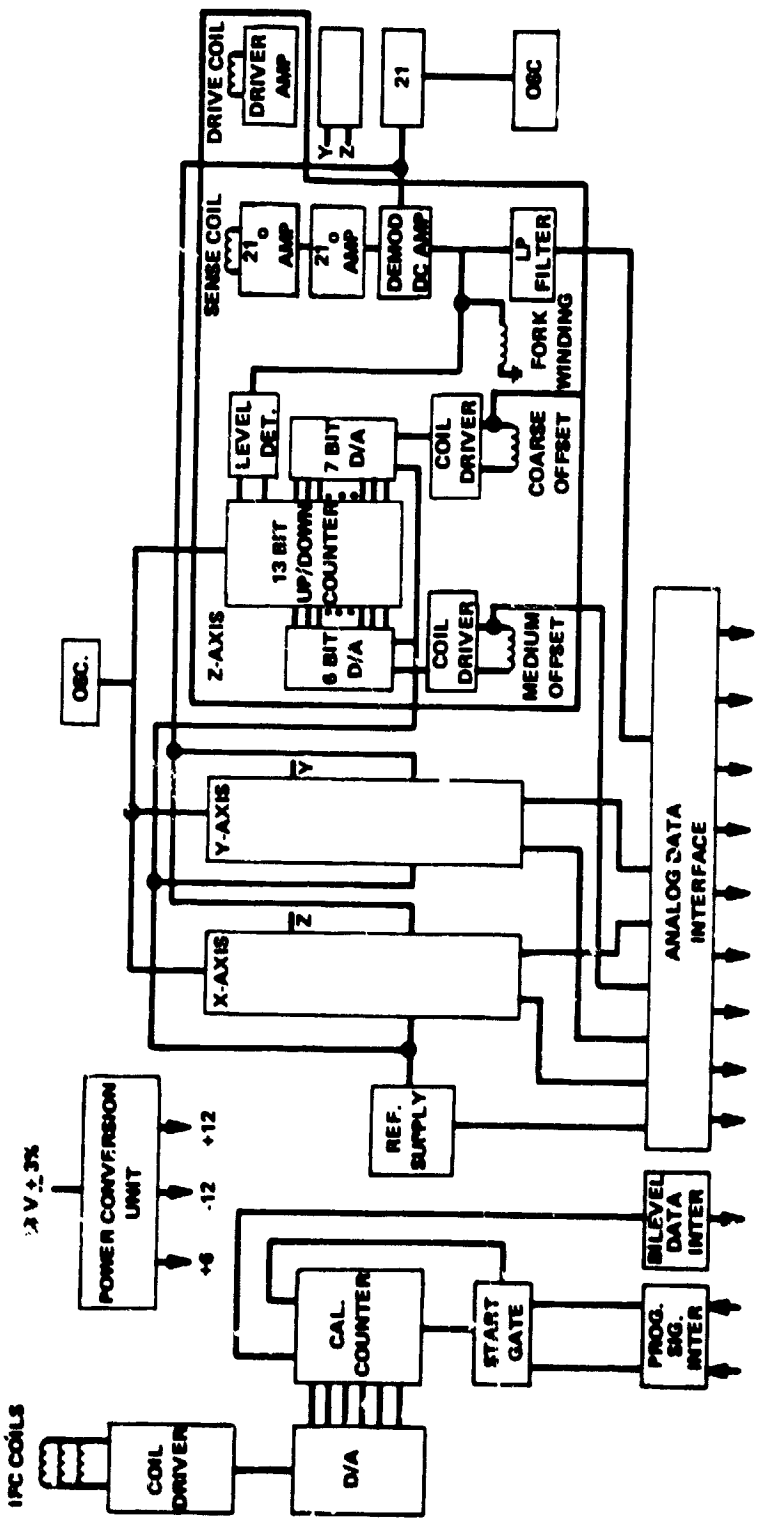

Figure 4 1. UCLA Block Diagram

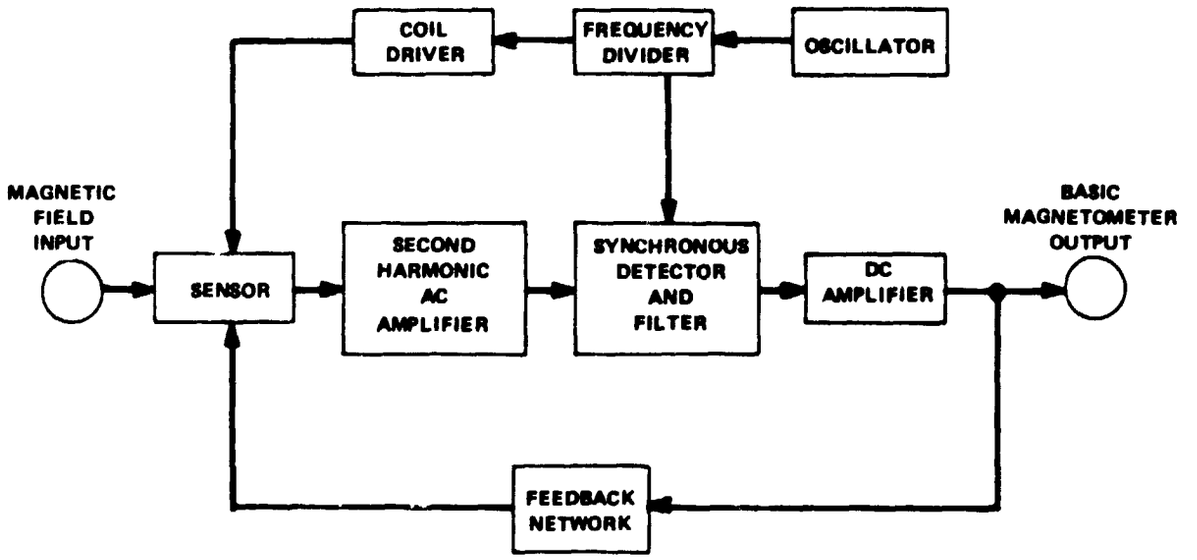

Figure 4-2. Basic Magnetometer Block Diagram

Digital Offset Field Generators

The purpose of the offset field generators was to extend the dynamic range of the experiment without sacrificing the resolving capability of the basic magnetometer. This was accomplished by applying localized offset fields, thus placing the basic magnetometer within its linear dynamic range. The localized fields were generated by supplying stable currents in discrete steps to an auxiliary coil wound around the magnetometer sensor.

The block diagram shown in Figure 4-3 is a basic magnetometer with offset field generator. The level detector indicated an off-scale condition of the basic magnetometer. When this occurs, counts were either added to or subtracted from the up-down counter. Each binary in the up-down counter drove a switch of a ladder-adder type digital-to-analog converter (R/2 resistor network). The output of the ladder-adder was a linear function of the state of the up-down counter. This output was applied to the coil driver circuit through a trimming (selectable) resistor R_t. The amplifier was biased at $1/2\ V_r$, the reference voltage, by the resistor divider network connected to the noninverting input. With the offset winding connected in the feedback of the operational amplifier, the current, I, through the winding was equal to $V/(R + R_T)$, no matter how the coil resistance might change. V was the output voltage of the ladder-adder, R was the characteristic resistance of the ladder, and R_T was the trimming resistor. Since the operational amplifier was biased at midscale, the current reversed direction as V passed through $1/2\ V_R$. When the output of the basic magnetometer activated either level detector, the offset field generator applied an incremental offset field to the sensor so that the basic magnetometer output was returned to center scale.

In the magnetometer design, the digital offset generator was divided into two sections, medium offset and coarse offset; however, only the medium offset was required for ATS-6. Each had a separate

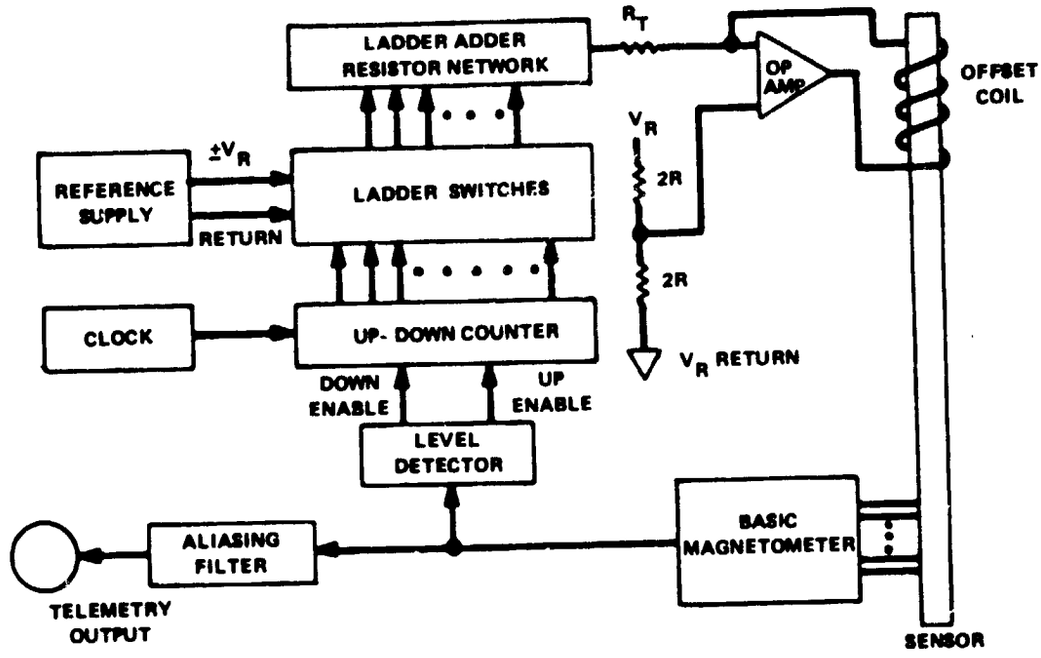

Figure 4-3. Offset Field Generator Block Diagram

coil on the sensor and separate D/A converter and coil driver. The up-down counter was a continuous 13-bit counter. The medium offset range was +496 to -512 γ in 16 γ steps.

Power Supply

The input LC line filter's purpose was to condition the +28 V input power for use by the inverter, limit inductive spiking on the input power lines, and limit noise reflected back on the input lines by the power supply. The +28 V input inverter produced two sets of square wave outputs. One set produced a 32-V peak-to-peak square wave with a center tap and the other set produced an 18-V peak-to-peak square wave with a center tap. The ac-to-dc full wave rectifier produced unregulated +15 V, -15 V, and +8 Vdc. Three voltage regulators operated from these voltages and produced regulated +12 V, -12 V, and +5 Vdc. The output of these regulators powered the experiment. All modules were internally protected against overvoltage, undervoltage, and reversed polarity.

The +28 Vdc input power return lines were isolated from signal and chassis.

In-Flight Calibrate

This subsystem produced four calibrate fields to the three axes simultaneously. It consisted of a voltage source, analog switches, a driver, and a digital counter.

The calibrate clock signal was a continuous 2-second square wave from the EME encoder. A gate blocked the clock signal from reaching the binary counter until a calibrate initiate signal set the control flip-flop. When the counter was not counting, it sat in the 111 state. After a calibrate initiate pulse, the next clock pulse caused the counter to switch to the 000 state, thus beginning the calibrate

sequence. The counter counted through an 011 state, the last step in the calibrate sequence. When it switched to 100, the calibrate sequence v s completed. The counter continued counting until it reached 111. The counter stayed in the 111 state until the next calibrate initiate pulse.

UNH EXPERIMENT, UNIVERSITY OF NEW HAMPSHIRE, DR. R. ARNOLDY

Purpose

The objective of the UNH experiment was the detection and measurement of low energy electrons and protons in the 0 to 22-keV range.

Physical Description

The experiment electronics and sensors were completely contained in one unit. The package was subdivided into three compartments, each with a separate cover. The compartments were the pitch angle, sweep, and logic sections. The pitch angle section contained two detector assemblies; one looking at 45 degrees between south and radially outward, and the other at 15 degrees radially outward from north (165 degrees from south).

The sweep section also contained two detector assemblies; one looking radially outward (90 degrees) and the other looking south (0 degree). The viewing half angles for all detectors was a maximum of 8 degrees.

Each of the four detector assemblies consisted of two Bendix Channeltron electron multipliers (CEM) located behind a set of curved (90-degree) electrostatic deflection electrodes. This configuration, termed double electrostatic analyzer (DESA), is shown schematically in Figure 4-4. By controlling the voltage across the electrodes of the DESA and the CEM, it was possible to select the charge and energy of the particles to be detected. The inner channel was biased for protons and the outer channel for electrons. Monitoring the count from the CEM gave the relative concentration of particles with a particular energy in the field of view of the DESA.

Description of Operation

A block diagram of the experiment is shown in Figure 4-5. Electrically, the pitch angle and sweep section were somewhat identical and each could be operated independently of the other, since separate on/off power commands were provided for each section. In normal operation, the current consumed by the sweep section averaged 93 mA and 90 mA for the pitch unit. This gave an average power for both units operating in the normal mode of approximately 5.12 watts.

Sweep Section

In normal operation, the voltage across the electrodes of the 0- and 90-degree DESA's was cycled from +2400 volts to 0 volt in a decreasing parabolic sweep once per second. All experiment data, except performance parameters, were digital and were handled by eight different accumulators. These were designated as "fast" accumulators and were read out eight times per telemetry frame,

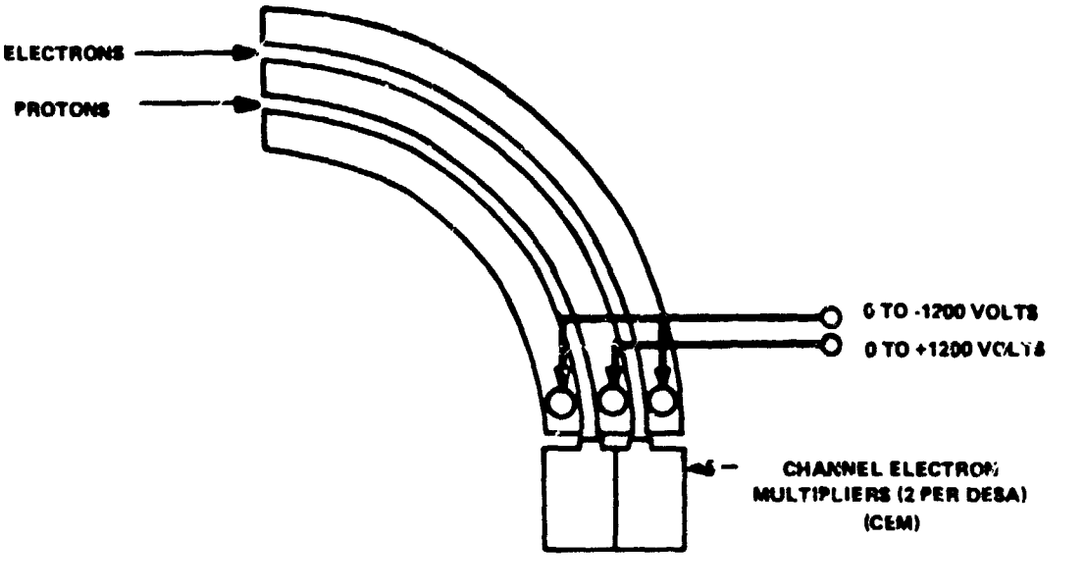

Figure 4-4. Double Electrostatic Analyzer

thus providing high resolution spectral data. The other two accumulators, INT A and INT B associated with the sweep section, were designated as "slow" accumulators and were read out once per telemetry frame, thus providing an integrated type of data.

Through ground command, it was possible to connect each of the CEM outputs to any of the four accumulators.

As the total number of particles detected by the CEM's increased, the output pulse amplitude tended to decrease. To offset these decreases an additional ground command, termed threshold level 1, was available and, in the "1" state, caused the sensitivity of all the sweep section CEM preamplifiers to increase. In the normal operating mode, this command was in the low or "0" state.

Pitch Angle Section

The DESA's in this section of the experiment were oriented at 45 and 165 degrees to determine the pitch angle distribution of the particles. The potentials across these DESA electrodes were stepped through eight decreasing voltage levels, each occurring one per second. The output of the pitch angle CEM preamplifiers were routed to the four encoder accumulators. Each of these accumulators were read out once per second.

The pitch angle CEM's operated in the same manner as the sweep units, therefore, one additional command, termed threshold level 2, was assigned to this section. It operated in the same manner as TL-1 to increase the sensitivity of the preamplifiers when necessary due to a high counting rate by the detectors.

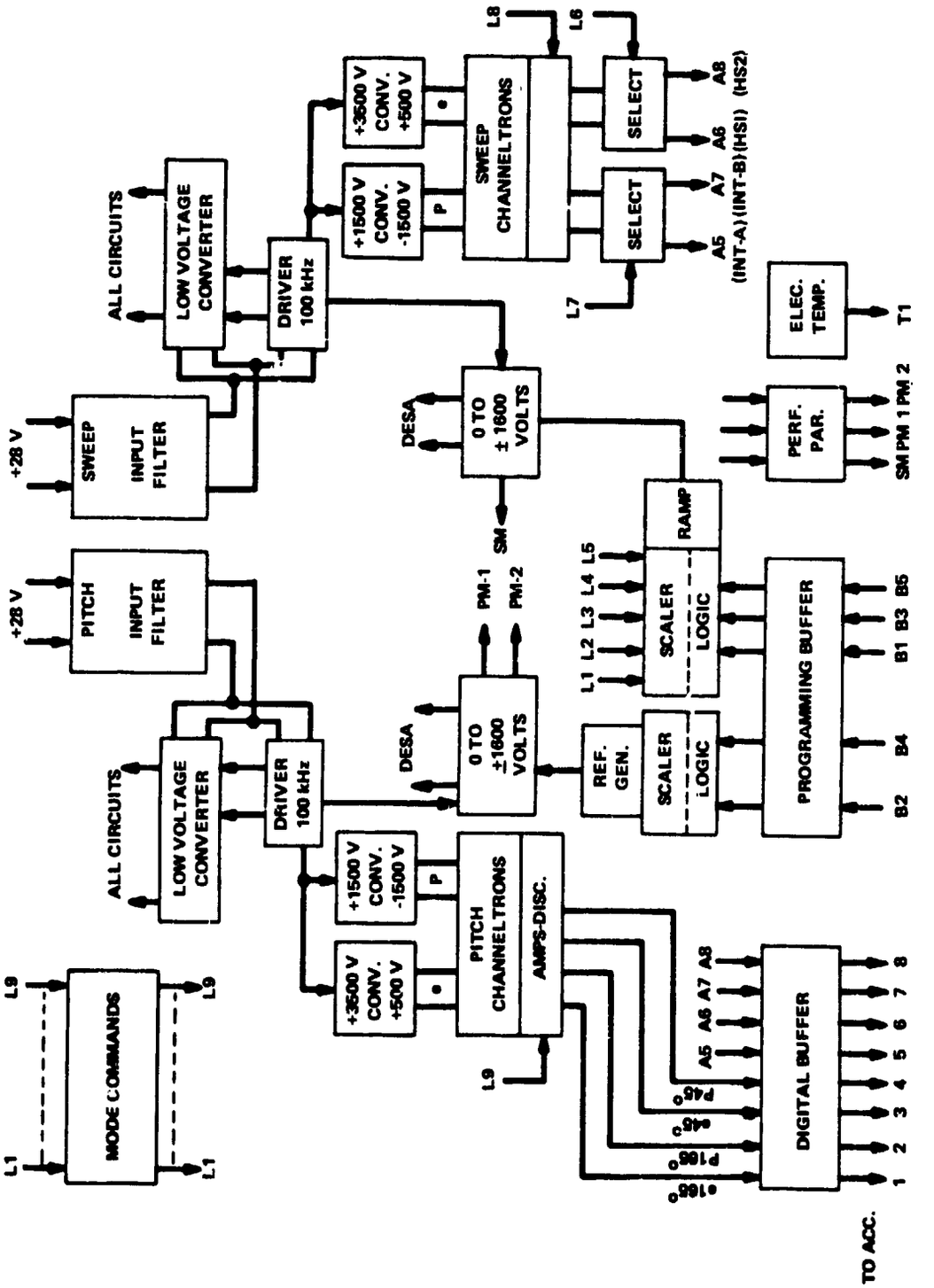

Figure 4-5. UNH Experiment Block Diagram

C-2

This experiment did not use any radioactive sources for testing purposes, either internal or external, and there was no in-flight calibration sequence. However, one of the programming signals supplied by the EME encoder, termed background data enable, caused a reverse bias of approximately 10 volts to be placed on the sweep DESA electrode for 9 seconds every 93.9 minutes. This provided an analysis of the experiment operation in a "background" mode with no particles having been counted.

U. OF MINN. EXPERIMENT, UNIVERSITY OF MINNESOTA, DR. J. R. WINCKLER

Purpose

The purpose of the University of Minnesota experiment was to investigate the origin of Van Allen trapped radiation. This was accomplished by suitable measurements of the intensity and time variations of protons and electron radiation in the vicinity of the synchronous orbit, and by a detailed analysis of these variations and their relationship to polar and magnetic storms and other perturbations of the magnetosphere. The experiment measured the directional flux of protons and electrons, so that the pitch angle distribution of both particle types could be determined. Protons were detected in three energy bands: 20 to 50 keV, 50 to 150 keV, and 150 to 500 keV. Electrons were also detected in three energy bands: 20 to 40 keV, 100 to 200 keV, and 1 to 1.5 MeV.

Physical Description

Two identical sets of detector assemblies were used. One set was fixed looking eastward, and the other set scanned 180 degrees from north to south through west. Each assembly contained four solid-state detectors; one for protons, and three for electrons. A radioactive source and a radiation barrier were mounted on the experiment to intercept the scanning detector at two positions, providing an in-flight calibration source and a background reference. The experiment body was painted black. The detector assemblies were painted white.

Description of Operation

Figure 4-6 is the block diagram of the University of Minnesota experiment. Particles incident within a cone of 5 degrees ±1 degree half angle around the viewing direction entered each of the detector assemblies. A magnetic deflection system separated the proton and electron channels and prevented low energy electrons from impinging on the proton detectors. A magnetic field deflected the electrons to one of the three detectors, depending on the energy of the particle. The high energy electrons passed through the proton detector, which was located just in front of the high energy electron detector. Pulse amplitude and coincidence pulse methods were used to classify the particles. The pulses were amplified and fed to window discriminators. The discriminator output from both detector assemblies were fed through separate drivers to 12 digital encoder inputs. The encoder accumulated the lowest level proton and electron channel from each detector for 125 msec, providing eight readouts per second. The remaining eight channels were accumulated for 1 second and were read out once per second.

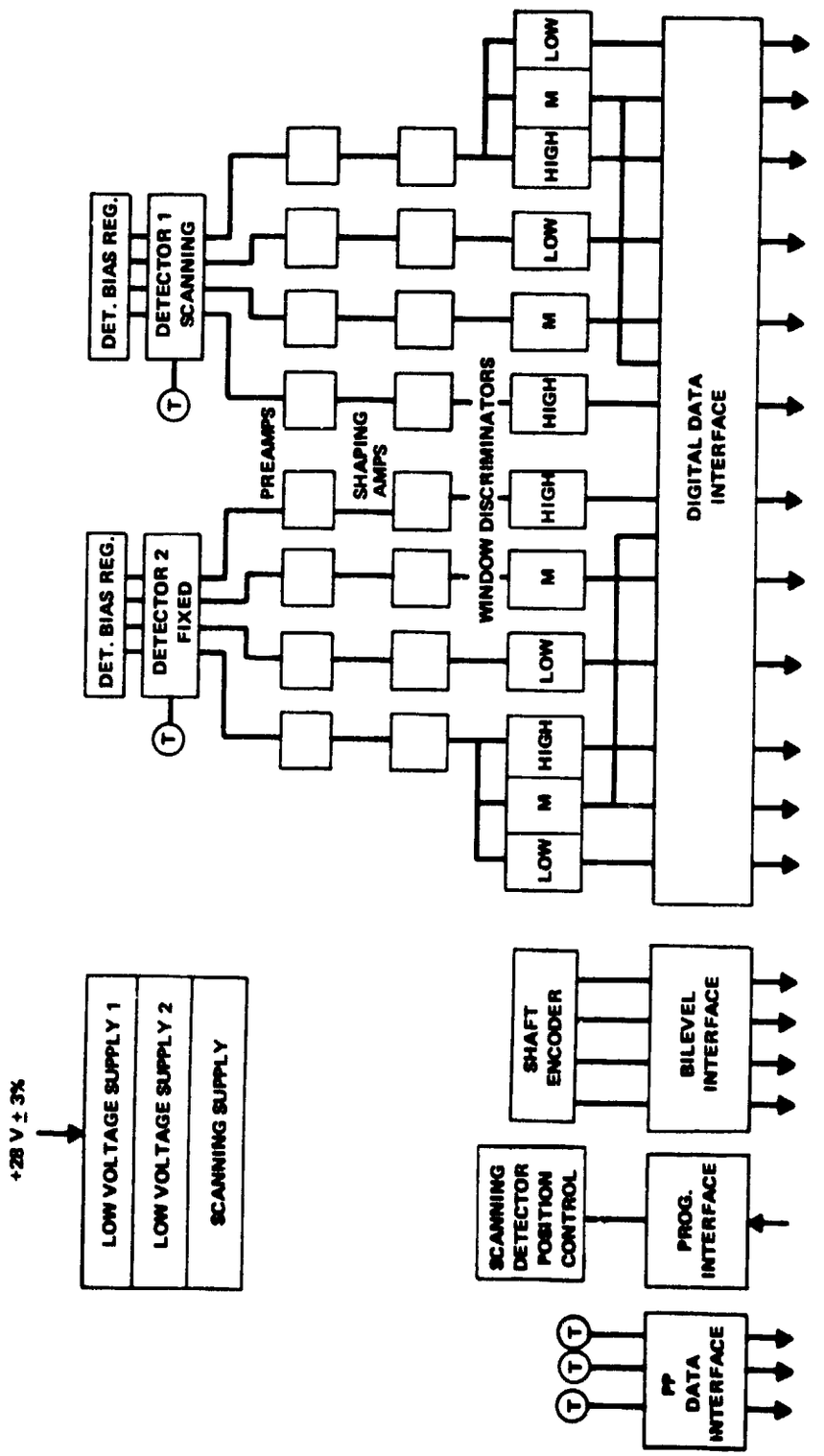

Figure 4-6. University of Minnesota Block Diagram

The scanning detector moved from north to south through west. Movement was controlled by a programming signal from the encoder (the signal was a 555-μsec pulse occurring every 8 seconds). The detector moved to 13 positions in 15 degree steps, reversing at the ends. A step occurred every 8 seconds near the start of frames 0, 8, 15, 24, 32, 40, 48, and 56. Four bits of bilevel data derived from a shaft encoder were buffered to the encoder and are read out once per frame to provide information on the sensor look angle.

Three thermistors were used to indicate temperatures of the detectors and electronics. Each thermistor voltage was transmitted to the encoder on a performance parameter line and was telemetered once every 64 seconds.

Two positions for the scanning detector did not view the space environment. For one of these, the detector faced a radioactive source composed of Promethium (Pm-147) and Strontum (Sr-90), which was used for in-flight calibration. For the other position, the detector faced a radiation shield that provided the capability of determining the background noise of the system.

SOLAR CELL RADIATION DAMAGE EXPERIMENT, HUGHES AIRCRAFT COMPANY, W. C. DUNKERLY

Purpose

The scientific objective of this experiment was to isolate and identify solar cell degradation resulting from the radiation environment in the geosynchronous orbit.

Physical Description

The experiment consisted of a small solar panel, measuring 25.4 cm X 42.2 cm in the Z-Y plane, and two identical signal processor units. The solar panel, mounted on the west face of the EME package, was divided into two substrate sections, one rigid and one flexible. The rigid substrate was 0.635-cm aluminum honeycomb covered with 0.0254-cm aluminum face sheets. The face sheet was coated with an insulating paint to electrically isolate the cells from the aluminum. The cells on the rigid substrate were individually mounted to the substrate with RTV silicone rubber adhesive, and received radiation from the front side only.

A 6.858 X 20.955-cm hole was cut out of the rigid substrate to allow the mounting of the flexible substrate. This flexible portion of the panel was a composite laminate of 0.00254-cm thick fiberglass cloth and 0.00254-cm thick Kapton banding with an epoxy adhesive. The cells were bonded to the flexible substrate, using an RTV silicon rubber.

When mounted, the flexible portion of the panel extended beyond the EME package to the south (+Y) to allow these cells to experience particulate radiation from both the front and the back.

The complete solar panel was composed of 80 experimental cells and one dummy cell. The cells were divided into 13 configurations of 5 identical cells on the rigid portion of the panel, and 3 configurations of 5 identical cells on the flexible panel (plus the dummy cell for symmetry). All cell

types used on the flexible panel were duplicated on the rigid panel to obtain comparative data on radiation from both sides, versus radiation from one side only.

Twenty cells in a group were individually wired to one of four panel connectors, each of which was connected to one of the two signal processor units. Separate lead wires were used for cell voltage and cell current. The ground return for each cell was connected to a common ground.

The solar cells used in this experiment were all 2 X 2 cm silicon types, manufactured by Heliotek. A typical cell, showing terminology used, is illustrated in Figure 4-7. Cell location configurations and characteristics are shown in Figure 4-8 and Table 4-1. The majority of the selected cells were boron doped N/P, 10-ohm-cm, 12 mil thick, and had solder coated titanium-silver contacts.

Configurations 1 through 4 had varied coverglass thickness. Configuration 5 used a plain 3-mil 7940 quartz coverslide without either the ultraviolet filter or antireflective coating. Configurations 6 and 7 were integral coated solar cells using 7940 and 7070 quartz, respectively. Configurations 8 and 9 had cells with a base resistivity of 2 ohm-cm and different cell thicknesses of 12 and 8 mils. Configuration 10 examined the characteristics of a titanium dioxide antireflective coating compared to the standard silicon monoxide coating. Configuration 12 cells were "grouted." Cell adhesive, or a similar material, was applied to the bus area and around the slide to assure protection of the solar cell and bus bar area from low energy protons. This configuration can be compared to configuration 3, which was protected using the "zero gap" dimensional coverslide-cell design, but without a special coating on the soldered bus bar areas.

The signal processor units were mounted, one on top of the other, on the underside of the EME deck near the mounting points of the panel. The signal processor units were painted black except for the contact surface between the two units and between the bottom unit (SPU-2) and the EME deck.

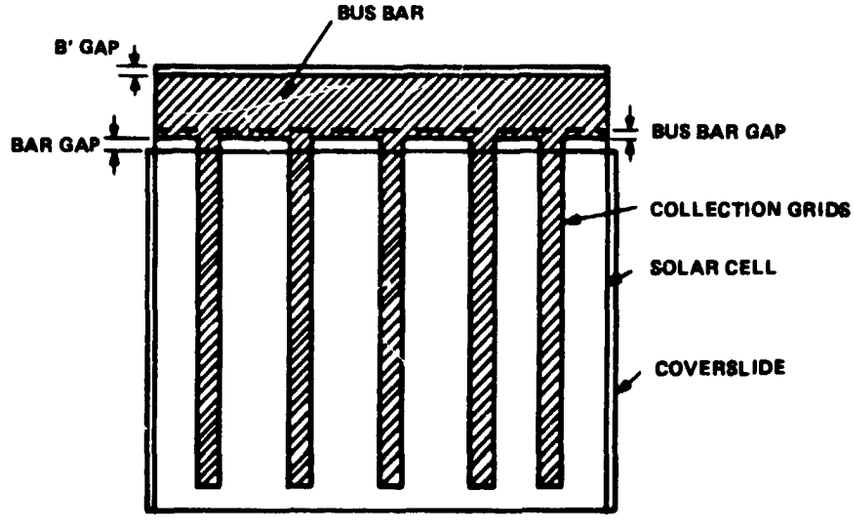

Figure 4-7. Solar Cell Terminology Chart

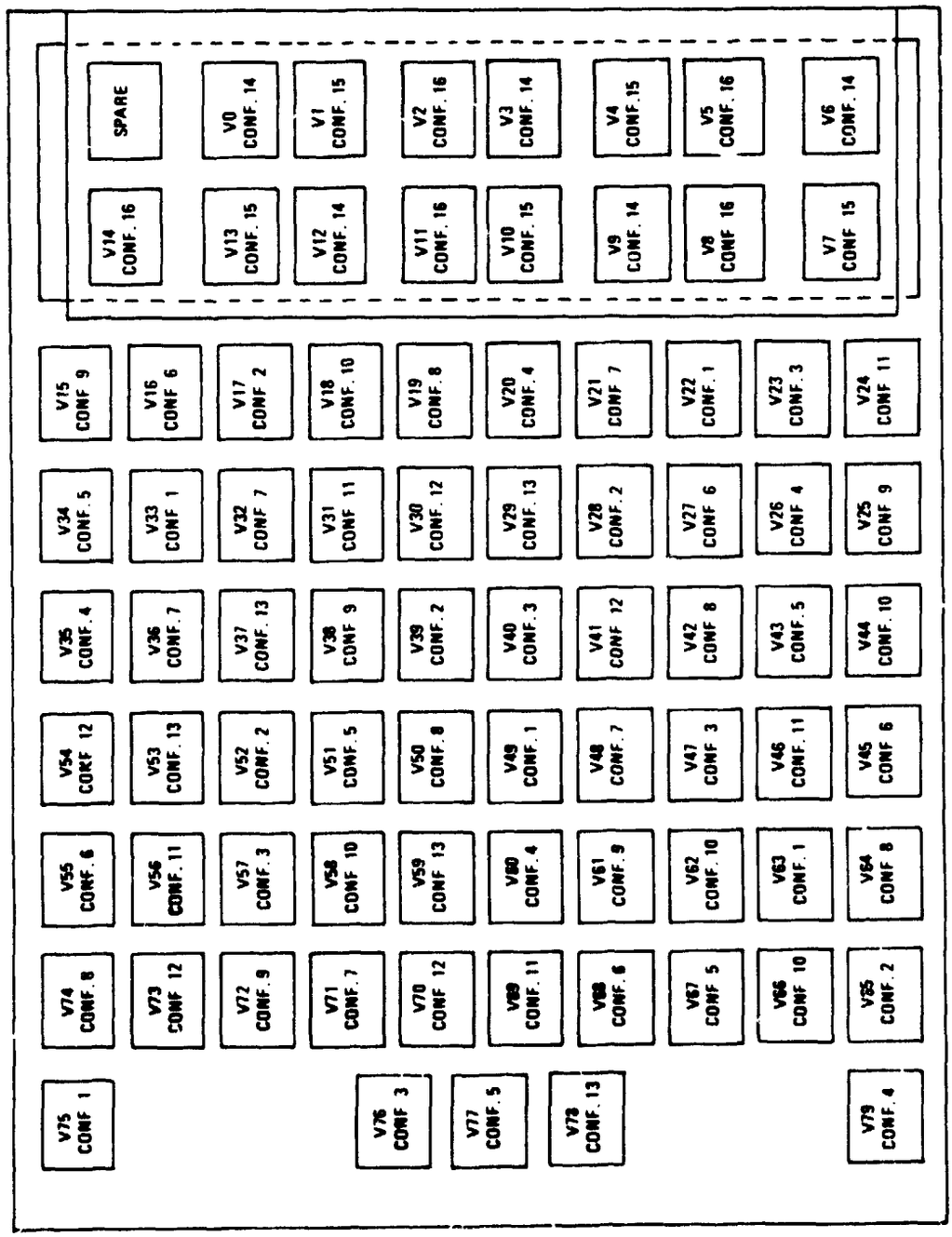

Figure 4-8. Flight Panel Cell Location and Configuration Identification

Table 4-1
Solar Cell Flight Experiment Configurations

Configuration	Resistivity (ohm-cm)	Cell Thickness (mils)	Coverslide Thickness (mils)	Remarks	Location
1	10	12	3		Rigid
2	10	12	6		Rigid
3	10	12	12		Rigid
4	10	12	30		Rigid
5	10	12	3	Plain 7940 quartz cover-glass no filter, or coatings	Rigid
6	10	12	3	7940 Integral	Rigid
7	10	12	3	7070 Integral	Rigid
8	2	12	6		Rigid
9	2	8	6		Rigid
10	2	8	6	Titanium dioxide cell antireflective coating	Rigid
11	10	8	6		Rigid
12	10	12	12	"Grouted" cell	Rigid
13	10	12	12	15 mil bar gap	Rigid
14	10	8	6		Flex-ible
15	2	8	6		Flex-ible
16	2	12	6		Flex-ible

Description of Operation

The solar cell radiation damage experiments measured the voltage-current characteristics of each of 80 solar cells. The measurements were made using two identical signal processor units, each of which analyzed 40 solar cells. A block diagram of one of the two signal processors is shown in Figure 4-9. The following description concerns operation of one unit only, since they were both identical and functioned in the same manner.

Internally, experiment operation was divided into minor frames, cells, and major frames. A minor frame was 30 msec in length and 16 minor frames (480 msec) were required to obtain complete information about one cell. Four cells were analyzed in one major frame (1.92 seconds), and 10 major frames completed the cycle for 40 cells.

To measure cell characteristics, one of the 40 cells was connected to the load resistors by the cell-select and load-select relays. The load-timing circuit controlled which load-select relay was to be energized. This circuit was incremented once each minor frame by a signal supplied by the EME encoder. The cell-timing circuit controlled which of the four cells analyzed during a major frame was currently to be analyzed. It was incremented once each 16 minor frames. The major-frame timing circuit controlled which of the 10 major frames required for the 40 cells was the current one. The initial state of this counter could be any one of the 16 possible states of four flip-flops. However, if the initial state was any one of the 6 abnormal states, the logic was such that the counter would shift to one of the 10 allowed states at the beginning of the next major frame. No provision was made for resetting the major-frame timing circuit when power was initially applied to the unit; therefore, the count could begin at any one of the 10 allowed states.

Cell current was determined from the voltage developed across an accurately known load resistor. This information was then sent through the cell-current multiplexer to the cell-current-sense amplifier and buffer, where it was conditioned for a 0 to +5.12 volt analog output to the encoder.

The output of the cell-voltage multiplexer was sent to a buffer amplifier while the voltage common or cell return was sent to a second buffer amplifier. The buffer outputs were then used to make a differential measurement of the cell voltage. As for the current readings, the cell voltage was then conditioned for the 0 to +5.12 volt analog output to the encoder.

In addition to cell analysis, the signal processor provided precision calibration voltages for both the "current" and "voltage" channels, and temperature information from thermistors on the solar panel and near the load resistors.

Calibration voltages were obtained by dividing down a -10.24 volt reference supply into four voltages that were supplied to both the cell current and cell voltage multiplexers. At the output of the divider network, these voltages were as follows:

CAL-1 500 mV
CAL-2 200 mV
CAL-3 400 mV
CAL-4 600 mV

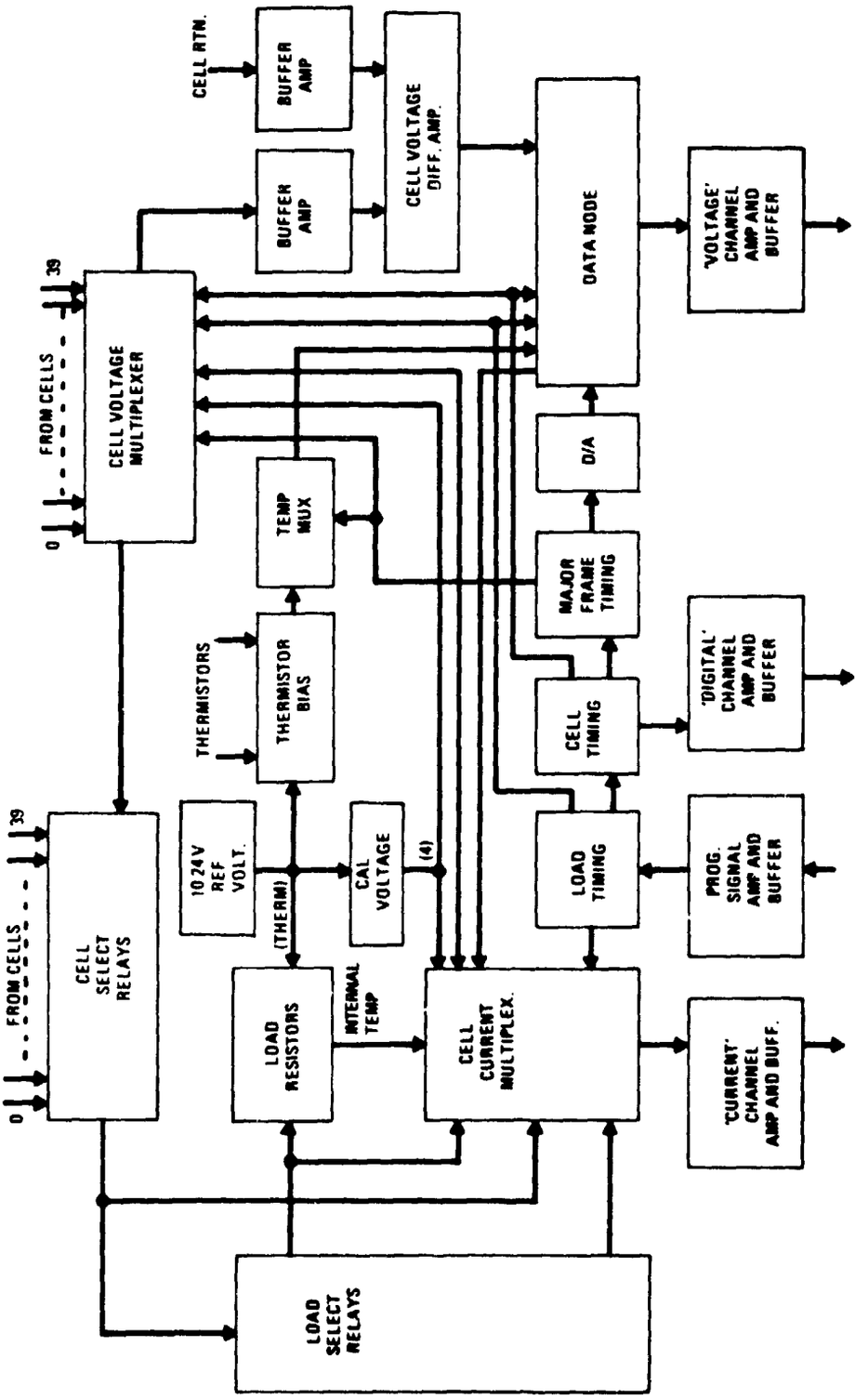

Figure 4-9. Solar Cell Experiment Block Diagram (One Signal Processor)

Seven thermistors were used in this experiment. Two of these were internal (1 per SPU) and the other five were located on the solar panel. RT1, RT3, and RT5 were on the rigid portion of the panel while RT2 and RT4 were on the flexible panel.

This experiment was normally operated once per day for a period of approximately three minutes. Experiment turn-on was initiated when the EME solar aspect sensor detected a Sun incidence of 2 degrees of normal to the solar panel. At that time, +28 volts was supplied to the signal processors and the encoder switched to a special telemetry format allotted to the solar cell experiment. After a period of 2 to 3 minutes, the encoder initiated a signal that returned telemetry to the regular format and removed power from the experiment.

During the first 12 major frames of a cell, the voltage and current information was obtained. From the four remaining minor frames of each cell, various other housekeeping and calibration information was obtained.

NASA/GSFC/NOAA EXPERIMENT, DR. A. KONRADI AND DR. T. FRITZ

Purpose

The purpose of the NASA/GSFC/NOAA experiment was to study low energy protons, side penetrating and Bremsstrahlung producing electrons, alpha particles, and various ion energy particles at synchronous altitudes. The experiment was designed to detect the following energy ranges:

Proton	20 keV to 2.1 MeV in 19 steps
Alpha	0.6 to 4 MeV in 4 steps
Light Ion	2.1 to 12.2 MeV in 6 steps
Medium Ion	9.5 to 22.7 MeV in 6 steps
Heavy Ion	$\geq$20 MeV

Detection of particle energies was accomplished by four solid-state telescopes, three of which looked outward along the Z-Z axis and the other looked south.

Physical Description

The experiment package consisted of an electronics portion, and a radiating fin extending perpendicular from the mounting base. The four telescope detectors were mounted on the fin and encased in a thermal blanket that maintained them at a suitably cold operating temperature near 0°C.

Description of Operation

Figure 4-10 is the block diagram of the NASA/GSFC/NOAA experiment. The experiment contained four solid-state detectors. Particles that entered the detectors freed a quantity of charge proportional to the energy lost by the incident particle. This charge was amplified to a voltage pulse whose amplitude was proportional to the quantity of charge, and hence, could be used to determine the incident particle type and energy. The detectors were sampled in the experiment periodically, with the timing of samples controlled by programming signals and ground commands.

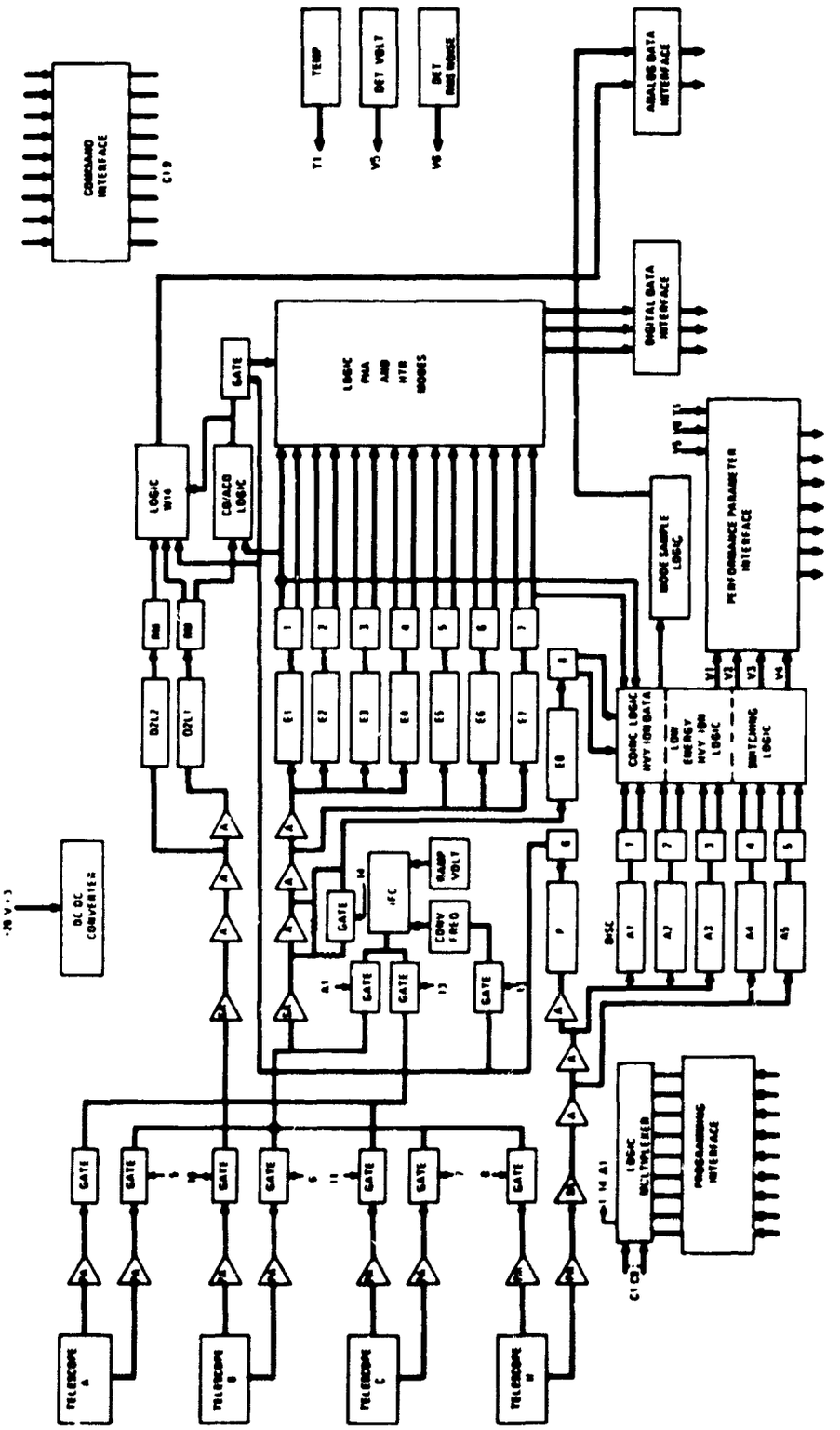

Figure 4-10. NASA/GSFC/NOAA Experiment Block Diagram

Pulses from telescopes A, B, C, and H were then gated through sampling gates and amplified. Pulse-height analysis techniques, which employed six levels of discrimination, further distinguished energy levels. Commutation of all discriminator outputs placed this data on three digital lines to the EME encoder.

The experiment, through ground commands, was capable of operating in one of two modes, normal or high-time resolution (HTR). In the normal mode, the three digital data outputs were the levels of discrimination (as previously discussed) for the four telescopes and four frames of HTR data. An experiment cycle of data was 64 frames (seconds) long. The high-time resolution mode consisted of 52 frames of HTR data and 12 frames of normal mode data. During the HTR mode, the digital outputs constantly contained some select discriminator data rather than a cycle of commutated outputs.

In addition to the above mode control, the experiment was further capable of controlling telescope gains and providing telescope anticoincidence modes through the use of ground commands. Analog data fed to the encoder provided differential telescope ratemeter outputs, alpha particle and heavy ion data, and housekeeping.

An in-flight calibration mode occurred in the experiment once every 24 hours at approximately 0600 Greenwich mean time (GMT), and lasted for 64 seconds. A programming signal from the encoder determined the exact calibration timing. A sawtooth voltage, which varied from 0 to +3.0 V with a varying period of about 12 seconds, modulated the power converter operational frequency (20 kHz). This signal was introduced into the detector amplifiers. The ramp voltage was monitored by one of the channels normally used for analog data. By comparing the counting rate of each output to the power converter frequency, a value of the transmission efficiency of a portion of the ramp voltage for a particular detector channel could be determined. By monitoring the 50 percent transmission voltage (energy of each channel), any shift in the amplifier gain or discrimination level could be measured. By calculating the voltage difference between 12-percent and 88-percent transmission voltages (energies), the detector system noise could also be measured. The operation of the coincidence logic was evaluated by enabling the coincidence override (anticoincidence) for one 12-second period. On alternate calibration periods (every other day) the calibration signal was delayed half a second. This provided a different set of data points to allow a more detailed analysis.

MDAC EXPERIMENT, MCDONNELL DOUGLAS CORPORATION, A. J. MASLEY

Purpose

The purpose of the MDAC experiment was to measure the differential energy spectrum of solar protons and alpha particles, and of trapped electrons. The data were used to study problems relating to temporal and spatial variations in these intensities. Protons were measured in 12 ranges between 0.2 MeV and 230 MeV, alphas were measured in 10 ranges between 2 MeV and 250 MeV, and electrons were measured in four ranges between 50 keV and 1 MeV. In addition, measurements of protons greater than 230 MeV and electrons greater than 1 MeV were made. The detectors looked northward and eastward.

Physical Description

The experiment consisted of two identical detector assemblies that were orthogonally oriented on the package. Each assembly consisted of a two-detector magnetic electron spectrometer, and a three-detector, proton-alpha particle telescope. The detectors were solid state, either double-diffused silicon (detectors 1, 2, 4, 6, 7, and 9) or lithium-drifted silicon (detectors 3, 5, 8, and 10). Detectors 1 through 5 were located in the north-looking detector assembly.

Description of Operation

Figure 4-11 is the block diagram of the MDAC experiment. Particles entering the detectors freed a quantity of charge that was linearly proportional to the energy that the particle lost in the detectors. Charge-sensitive amplifiers converted this charge to voltage pulses that could be related to the incident particle energy. The voltage pulses were fed to an array of amplitude threshold circuits. The outputs of the threshold circuits were fed through "veto gates" and, for the proton and alpha channels, in some cases through a seven-channel, pulse-height analyzer to complete the analysis of the particle type and energy range. Using this technique, protons, alphas, and electrons in various energy intervals were discriminated. Each orthogonal set of detectors had its own discriminators and veto gates; the pulse-height analyzer was common. The electron information was buffered to eight separate digital-data lines to the encoder. The proton-alpha information (48 channels) was multiplexed along with "data flags," and buffered to another digital-data line to the encoder.

The experiment had a data period of 25 seconds (frames) during which all proton/alpha scientific data was sampled once and electron data sampled 100 times. An experiment mode consisted of one EME frame during which two P/α channels were sampled and each electron channel was sampled four times. Experiment modes were determined by the states of the programming signals EM 1 through EM 5. The 5-bit counter in the EME encoder advanced by one on the positive going edge of EM 6 which occurred 1.97 msec after the start of word 163. Since this 5-bit counter was not in sync with the binary encoder frame counter, a data flag (EM 10) was sent to the encoder from the experiment to identify mode zero. During experiment mode zero, the P/α channels (words 64 and 164) contained no experiment scientific data, and instead read out all logic "1's." An additional data signal (EM 11) was sent to the encoder to flag the experiment in-flight calibration (IFC). EM 11 occurred immediately after the last readout (W-164) of the P/α accumulator for the first experiment mode 24, following the experiment receiving the IFC signal (EM 8) from the encoder. The encoder then changed the data flag of all "ones" in W164 to all "zeros" and read this out in the upcoming experiment mode zero. IFC lasted for 25 frames, beginning with mode zero. Readout of all "ones" in W64 of mode zero remained the same. All experiment accumulators, including P/α for modes 1-24, operated normally and recorded scientific data during IFC. IFC data was registered in a separate encoder accumulator provided for this purpose.

The experiment in-flight calibration mode provided a check on the electronics. The in-flight calibrator generated a 1,024-step staircase waveform where each step was a precisely known voltage that was modulated into 10 amplifier-compatible pulses. The segmented staircase waveform was presented to each amplifier sequentially, so that each staircase checked a particular pulse-height

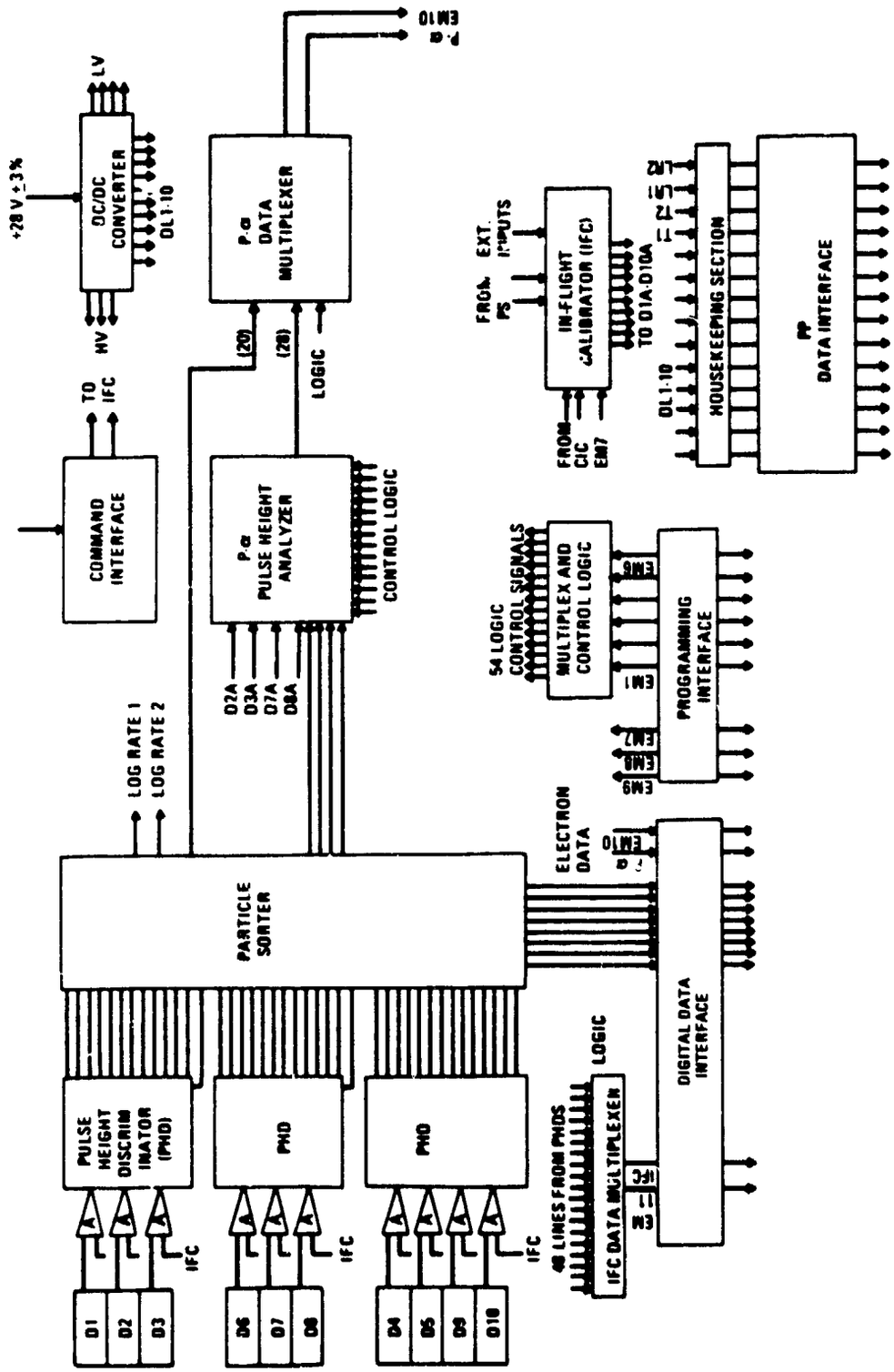

Figure 4-11. MDAC Experiment Block Diagram

discriminator. The pulse-height discriminator threshold was established by counting the number of output pulses from that discriminator. The in-flight calibrator also provided a check of operation for the amplifiers, analog commutator, driver amplifier, pulse-height analyzer, readout circuitry, and system readout timing. The 25-second IFC mode was entered once a day at approximately 0600 GMT as a result of programming from the encoder. A ground command could be used to enter or disable the IFC mode at any time.

UCSD EXPERIMENT, UNIVERSITY OF CALIFORNIA, SAN DIEGO, DR. C. McILWAIN

Purpose

The purpose of the UCSD experiment was to observe trapped particles and their interrelations in the following regions:

- Trapped radiation belts toward the equator
- N-S auroral zones
- Daytime magnetopause and interplanetary space
- Nighttime tail plasma sheets

Observed in these regions was the energy spectrum of ions above 50 eV, density versus magnetic field depression, and fluxes of auroral particles and their associations with electrons above 50 keV, and ions above 50 eV.

Physical Description

The physical configuration of the UCSD experiment was a main chassis with one fixed proton detector and two side-mounted, rotating electron-proton detectors. The rotating detectors were cylindrically shaped with a 17.1-cm diameter and a 10.2-cm height. The two rotating detectors were attached to the sides of the experiment by a 5.1-cm shaft. The experiment's detector orientation is illustrated in Figure 4-12. The main chassis was painted black and the rotating detectors were painted white. The EME thermal blanket covered both the main chassis and the rotating detectors.

Theory of Operation

Figure 4-13 is the block diagram of the UCSD experiment.

Detectors

The experiment had three detectors, two rotating and one fixed. Each rotating detector had two cylindrical, curved-plate electrostatic analyzers, one for electrons and one for protons. The fixed detector had one proton detector.

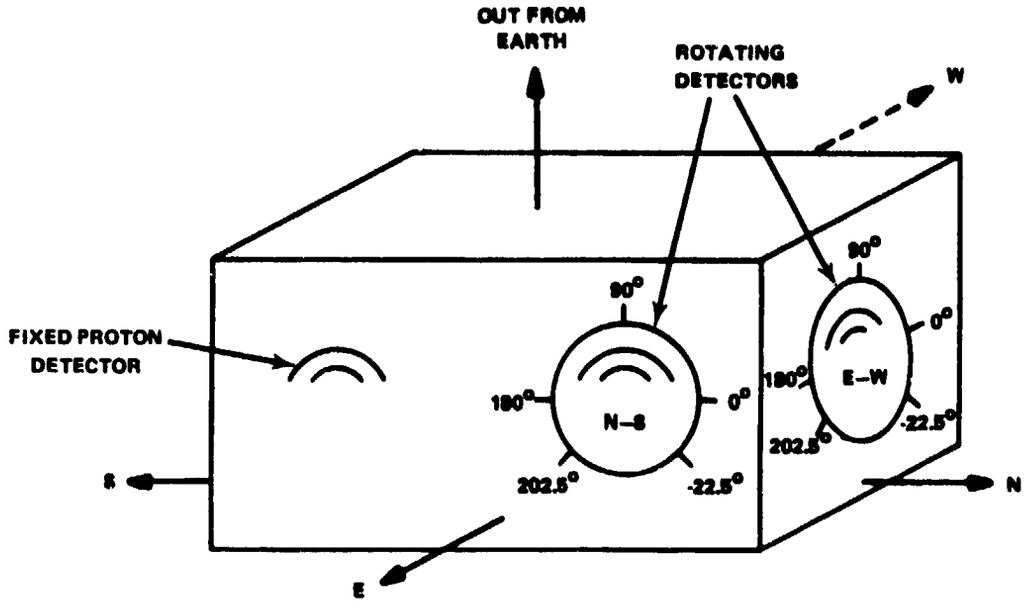

Figure 4-12. Orientation of UCSD Experiment Detectors

The geometric factor for the proton analyzer was 5×10^{-4} E cm^2 - ster-eV and for the electron analyzer was 1.5×10^{-4} E cm^2 - ster-eV. The orientation of the detectors is shown in Figure 4-12. The moveable detectors rotated about their axes in both the clockwise and counter-clockwise directions for a total of 225 degrees in approximately 0.35-degree steps. Spacecraft commands controlled the positions of these detectors by letting them move to predetermined locations or by letting them sweep continuously from one extreme to the other.

The plate voltage of the analyzers was variable and could be changed to detect discrete energy ranges. The voltage could be made to step continously from low values to high values, or to dwell on any voltage depending on ground command status.

Electronics

The operation of the electronics is divided into four parts for discussion purposes only. This was not actually the physical configuration of the electronics.

Detector Position Electronics—The rotating detectors were positioned by four phase-stepper motors. The motors, which moved in 15-degree steps and were geared down 43:1, moved the detectors in approximately 0.35-degree steps. The direction of movement was determined by the relative phase of the motor's four field windings. The amplitude and width of the motor input pulse was changed by ground command so as to adjust the input energy to overcome inertial and frictional forces. The position of the detectors was set by a binary position counter and two resolvers, one on each detector. The position counter counted motor pulses and was read out as bilevel data. The resolvers were read out as analog data performance parameters.

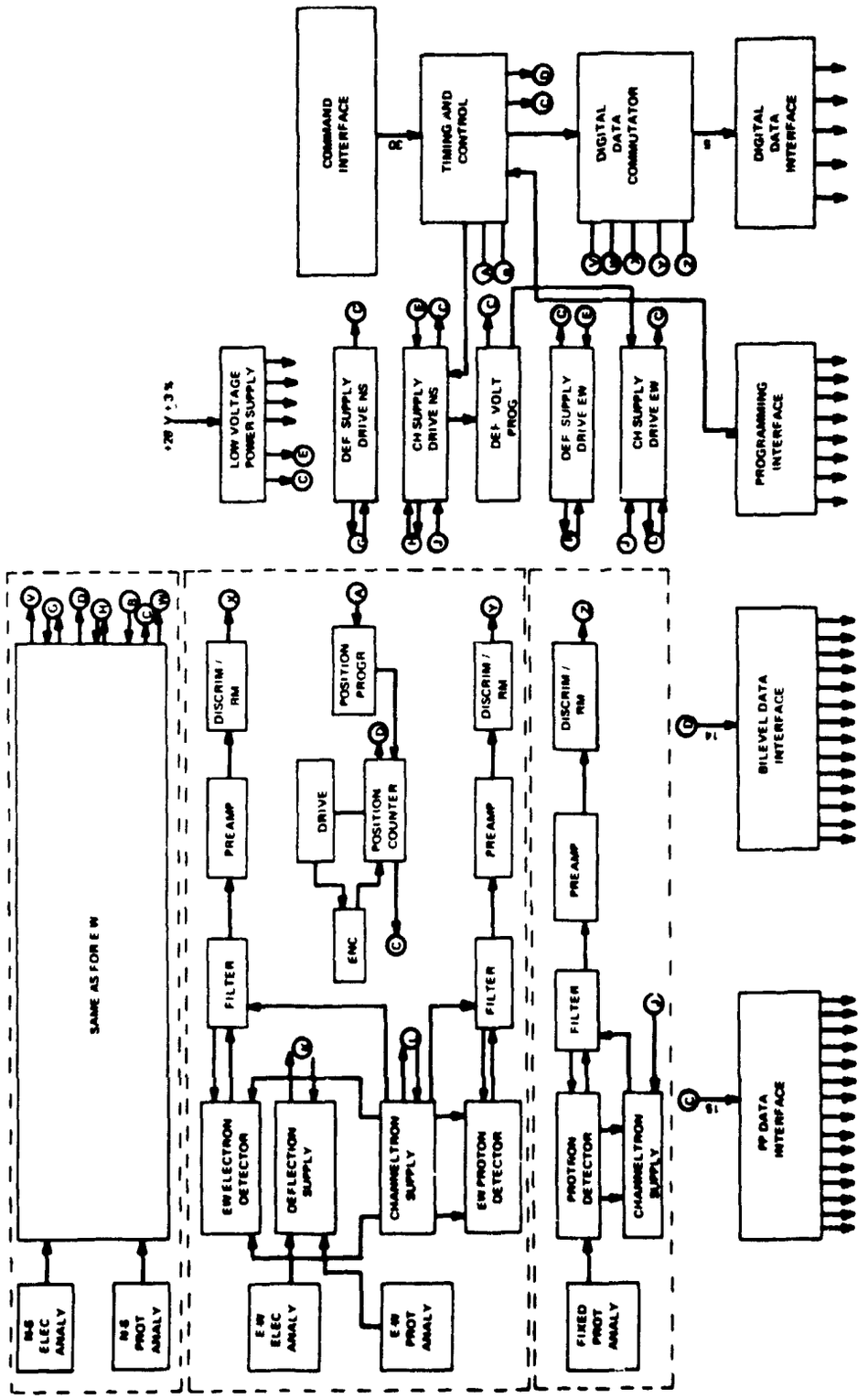

Figure 4-13. UCSD Experiment Block Diagram

The clockwise-counterclockwise rotation of the detectors was controlled by a lamp-phototransistor that changed the phase of the motor pulse when the detector had reached the end of its travel in one direction.

The initial position of the detectors after turn-on was not always known nor were they necessarily in the correct position with respect to each other. The experiment had a synchronization system by which one detector stopped and waited until the other detector caught up; then both detectors moved synchronously. The status of synchronization was read out as bilevel data.

Power Supply—There were three sections that comprised the experiment's power supply. A low-voltage section supplied the logic voltages and analog circuit voltages. There were two high-voltage sections, one for the spiraltron supply voltages and the other for the deflection plates. The spiraltron voltages were fixed voltage pairs, a positive pair for the electron spiraltron, and a negative pair for the proton spiraltrons.

The deflection-plate voltages were programmable by ground command. The plate voltages for the E-W, N-S, and fixed detectors were controlled by a single ramp generator. The output of the generator is shown in Figure 4-14. The deflection voltage was directly proportional to this signal voltage. The ramp, which looked like a continuous function, was actually composed of 64 discrete steps. When this deflection-control voltage was stepping continuously it was said to be scanning. When the signal stopped on any one step, it was said to be dwelling.

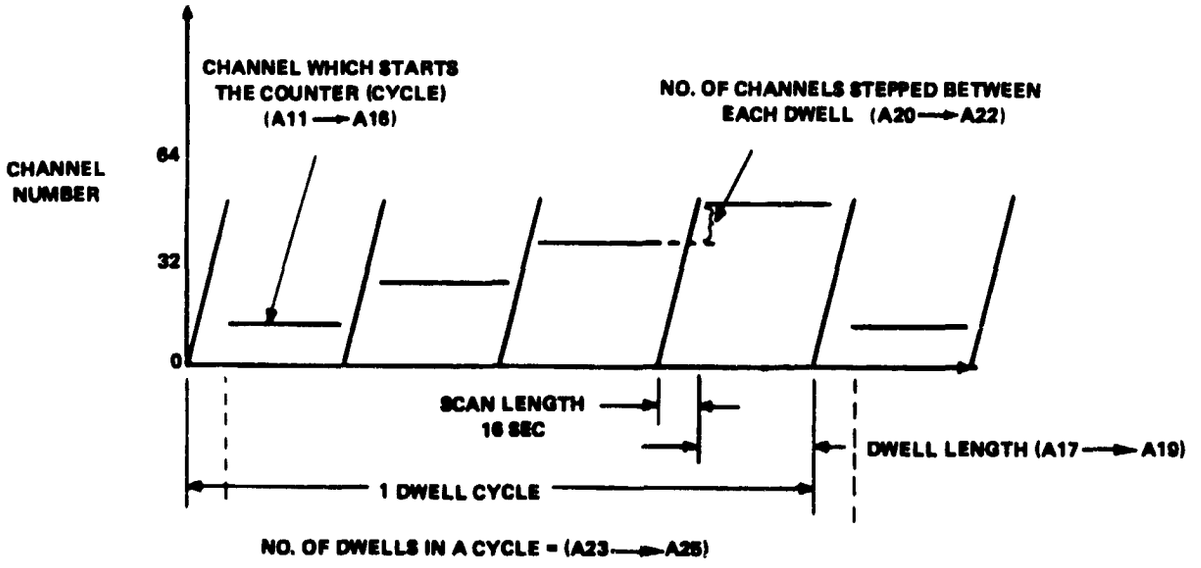

Figure 4-14. Deflection Voltage Control Commands

The length of the dwell time, number of steps between dwells, and the number of dwells in a cycle were controlled by ground command. Controlling the deflection-control voltage in this manner enabled the experiment to look for discrete energy ranges of particles, and to dwell on any energy range for given lengths of time.

Data and Data Gating–The output of each spiraltron was sent to a charge sensitive preamplifier. The output was then discriminated and shaped for the accumulator gating circuits. These circuits determined which spiraltron output would go to which encoder accumulator. The gating and timing were controlled by ground command.

Intercalibration Cycle–This cycle was used to correlate data from two detectors looking in the same direction. In this way, a relative calibration of the experiment's detectors were made. This cycle was enabled or inhibited by ground command. The cycle occurred regularly when enabled.

ASC EXPERIMENT, AEROSPACE CORPORATION, DR. G. A. PAULIKAS

Purpose

The purpose of the Aerospace experiment was to measure the omnidirectional fluxes and spectra of electrons and protons. The proton spectrum was divided into eight energy ranges: >2 MeV, >3 MeV, >8 MeV, >12 MeV, 12 to 22 MeV, 20 to 40 MeV, 30 to 60 MeV, and 40 to 100 MeV. The electron spectrum covered four energy ranges: >150 keV, >700 keV, >1.4 MeV, and >3 MeV.

Physical Description

The ASC experiment consisted of three shielded and one unshielded solid-state detectors, together with associated amplifiers, discriminators, dc/dc converter, and interface circuitry.

The unshielded detector was of the transmission type with a sensitive area 50 mm square, 230 micrometers thick, and a collimated acceptance angle of 45 degrees. A secondary detecting element, with an area 200 mm square and 100 micrometers thick, was mounted directly behind the first detecting element to inhibit ambiguous information received from particles that were energetic enough to pass completely through the first detector. A thin (0.00254 cm) nickel foil was mounted in front of the primary detector to prevent light from reaching the light sensitive detectors. In that sensor, discriminator circuitry determined the particle energy.

The remaining three detectors were cubes with dimensions of 1, 2, and 3 mm. Each detector was housed under a gold-plated, beryllium bubble. The amount of shielding over each detector, together with the discriminator circuit, determined the energy a particle must have in order to register. The detectors were mounted on Mallory discs to restrict the sensitive angle to 2π steradians. The package was painted black, except for the detectors and the gold-bottom surface.

Theory of Operation

Figure 4-15 is the block diagram of the ASC experiment. A particle entering one of the detectors produced a pulse of current where the quantity of charge released was dependent on the energy of the particle. As shown in the block diagram, pulses from the detectors were amplified and then fed to sets of discriminators. The discriminators divided the amplified pulses into four electron and eight proton channels. Each of these discriminator outputs was buffered to a digital-data input of the EME encoder. The four electron data lines were commutated by the encoder at the frame rate (1 sec) and were accumulated sequentially and repetitively, beginning with E1 in frame 0. The eight proton channels were handled similarly. The encoder commutated P1 through P8 at the frame rate. The eight lines were accumulated sequentially and repetitively, beginning with P1 in frame 0.

The experiment discriminator levels were established as follows:

Detector 1—Unshielded

E1 Electrons	>150 keV
P1 Protons	>2 keV
P2 Protons	>3 MeV
P3 Protons	>8 MeV
P8 Alphas	>12 Mev

Detector 2—1-mm Cube

E2 Electrons	>700 keV
P4 Protons	12 to 22 MeV
P5 Alphas	40 to 100 MeV

Detector 3—2-mm Cube

E3 Electrons	>1.4 MeV
P6 Protons	20 to 40 MeV

Detector 4—3-mm Cube

E4 Electrons	>3 MeV
P6 Protons	30 to 60 MeV

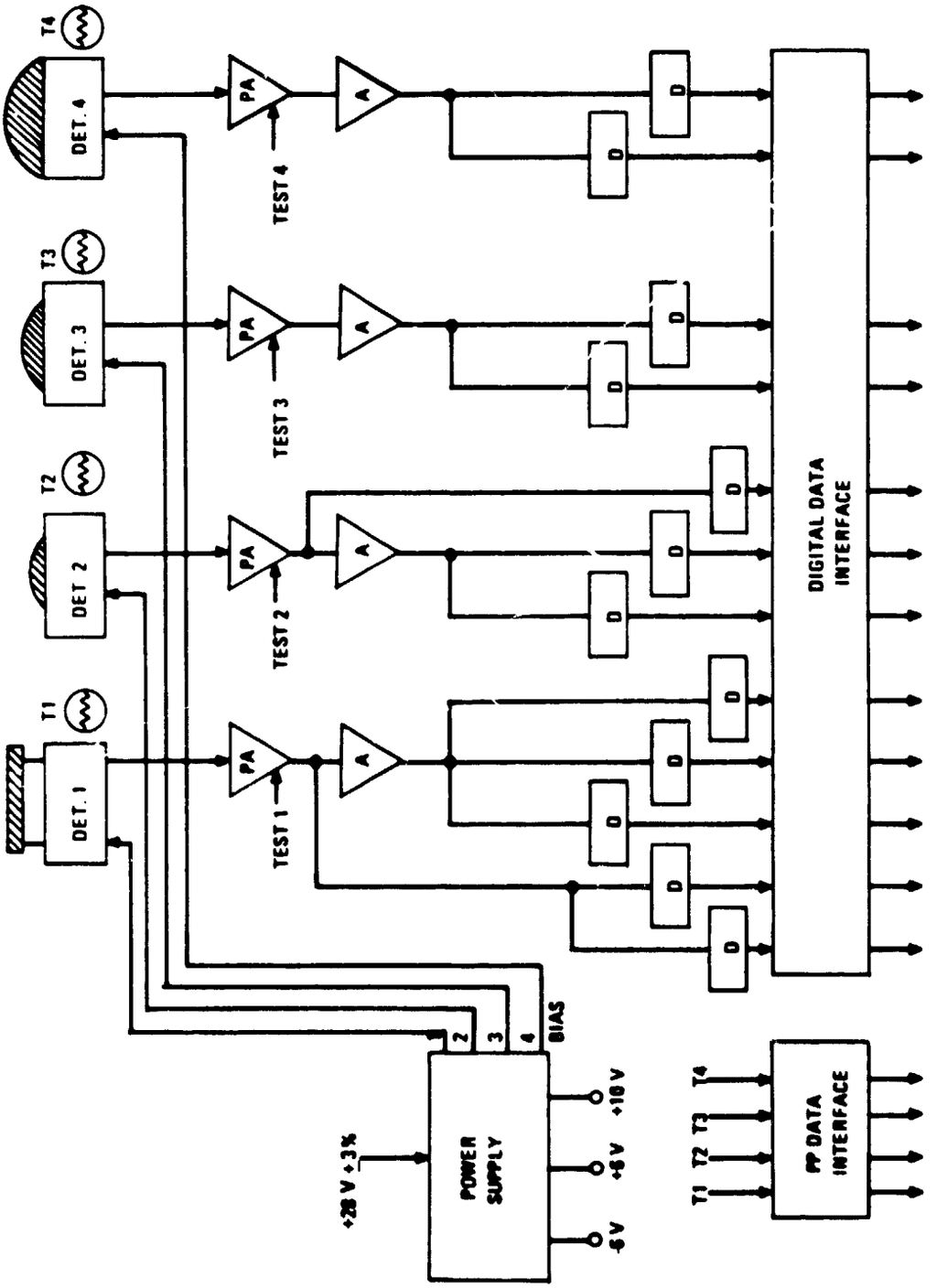

Figure 4-15. ASC Experiment Block Diagram

CHAPTER 5

EME SUPPORT HARDWARE

INTRODUCTION

The following paragraphs describe the EME encoder-programmer, command-interface control, EME power supply, system grounding, active thermal control system, and the solar aspect sensor that made up the EME flight package on ATS-6.

ENCODER

Function

The prime function of the EME pulse code modulation encoder was to receive analog and digital data from the various experiments and support equipment, and to present this information in proper sequence as serial digital-data pulse outputs in a split phase, Manchester II + 180 (Bi ϕ-L) format to two telemetry transmitter modulators. The encoder provided a real-time clock, switchable formats, and several control signals to the experiments and the command-interface control.

Encoder System

Encoder Timing

The timing for the EME encoder system was basically derived from one of two 900-kilohertz (kHz) temperature controlled crystal oscillators physically located external to the encoder. Offset control for the clocks were provided by 10-bit analog/digital (A/D) converters in the encoder that was controlled by ground command. This frequency was further divided downward in the encoder to 180 kHz, 18 kHz, 1.8 kHz, and 200 hertz (Hz) to provide various control logic signals within the encoder and to the experiments and the command-interface control (CIC). In addition, the 18-kHz and 200-Hz signals were used for generating the real-time clock input frequency and the format-word rate respectively.

Format generation was accomplished by two shift registers. A 50-bit register accepted the 200-Hz word rate from the countdown chain. A second 4-bit shift register counted every 50 words. Decoding both registers resulted in a 200-word frame rate of 1 second. Each frame was further divided into quarter sections of 50 words each. Each word consisted of nine bits.

The frame-rate output was fed into a 6-bit frame counter. The frame counter counted frames from 0 to 63, rolled over, and continued repetitively. Commutation of the system performance parameters was controlled by decoding this counter. The output of the frame counter controlled a 4-bit sequence counter that counted groups of 64 frames from 0 to 10, rolled over, and was repetitive.

The frame counter was read out in the EME formats as the six least significant bits (LSB) of word 4 and the sequence counter was read out as the four LSB's of word 5.

Format Switching

The encoder was capable of switching between two 200-word formats; one format consisted primarily of Hughes Aircraft Company (HAC) experiment data. Control signals for reliable format switching came from the CIC. When the encoder was instructed to switch to the HAC format, it did so for 2 to 3 minutes before automatically returning to the normal format. Quad-redundant-override logic in the encoder, controlled by ground commands, assured that the encoder never remained in the HAC format for longer than 2 to 3 minutes.

Programming Signals

From the encoder word decoder and control logic, programming signals to the experiments and CIC were generated. The pulse duration and repetition rate were a function of program requirements. When a programming pulse changed from the quiescent state to the logic-one state, the transition was from a nominal 0 volt to a nominal pulse 10 volts. All programming signals were buffered before leaving the encoder. All in-flight calibration (IFC) signals occurred at the beginning of the first zero- to ten-volt transition of the sequence counter following the EME hour nearest G.m.t. time given. The hour counter for the EME was the five most significant bits (MSB) of the 27-bit millisecond counter. The first zero- to ten-volt transition sequence after the hour counter decoding given below determined IFC.

0 0 1 0 0 UCLA[1] IFC

0 0 1 0 1 MDAC[2], NASA/GSFC[3] IFC

Real-Time Clock

Real-time clock information was provided by the encoder in the form of a 27-bit millisecond counter and a 9-bit day counter. The millisecond counter control was from the 1-kHz signal of the encoder timing chain.

The 27-bit millisecond counter counted from 0 to 86,399,999, rolled over to zero, and was repetitive. The 27 bits of the binary millisecond counter were read out in words 152, 153, and 154 of the pulse code modulation format. In addition, the millisecond counter had the following capabilities:

- All 27 bits could be reset by ground command
- The five MSB's (hours section) could be reset to any desired number by ground command. The remaining 22 bits were not affected.

[1]University of California at Los Angeles
[2]McDonnel-Douglas Corporation
[3]National Aeronautics and Space Administration/Goddard Space Flight Center

The 9-bit day counter counted from 0 to 511, rolled over to zero, and was repetitive. The day counter updated by one each time the millisecond counter rolled over to zero. The 9 bits of the day counter were read out in the format in word 151. The day counter was capable of being preset to any number by ground command.

Since there was no separate hour counter in the encoder, an EME hour did not have the same time span as a customary hour. One EME hour was equivalent to 69 minutes and 54,304 milliseconds and there were 21 EME hours in a day.

Digital Accumulation/Compression

Serial experiment digital data were accumulated in the encoder (with integration times ranging from 1/4 to 1 second) in one of forty 16-bit shift registers, and in all cases except one, was compressed to 9 or 10 bits by logarithmic compression. For the lone exception, no compression took place.

The maximum accumulator input rate permitted was 1 megahertz (Mhz). During a period of time lasting for 50 microseconds, each accumulator was reset to a one count and data was transferred to the 16-bit shift register. Experiment data was inhibited during this time. The number of times an experiment accumulator was inhibited per frame was a function of the experiment integration time requirements.

Four logarithmic compressors were time shared and used to compress all experiment accumulator data. A block diagram of a compressor is shown in Figure 5-1. One of 10 accumulator inputs was OR'ed into a 16-bit shift register. If the last bit in the register was not a 1, the register was shifted to the right until the last bit was a 1. A 4-bit counter counted the number of shifts required. The last bit in the register was always a 1; therefore, it was not telemetered. The next five left-most bits and the 4 bits of the shift counter were stored in a 9-bit shift register until required for telemetry readout. The next accumulator transfer pulse reset the shift register and counter and the process repeated. The error resulting from this compression was ±1/64 percent.

Digital data from all sources were OR'ed into an output stage where they were converted to split phase for telemetry.

Discrete Data

The bilevel, or discrete digital, data were handled similarly to digital data except that accumulators or logarithmic compressors were not required. Experimental data were presented to a 9-bit register in the encoder, from which they were serially shifted through the 16-bit "OR" gate to an output stage where they were converted to split phase.

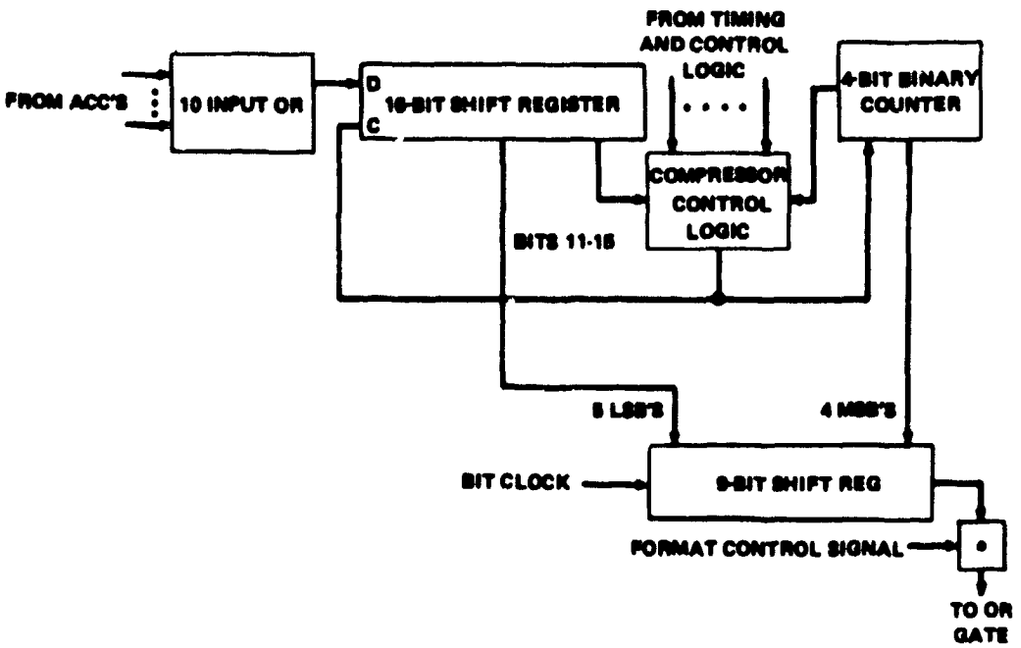

Figure 5-1. Encoder Logarithmic Compressor

Analog Data

The encoder sampled 128 housekeeping signals in a submultiplexed sequence every 64 seconds, and 40 analog signals in a multiplexed sequence every second. All analog signals were quantized to 9 bits with a maximum accuracy of 7 bits for submultiplexed signals and 9 bits for multiplexed signals.

Conversion of analog data to digital bits was performed by either of two double-ramp integrator A/D converters. The A/D process is shown in Figure 5-2. The converter output was parallel loaded into a 9-bit shift register from which it was gated serially to the split-phase output circuitry.

The multiplexer, commutator, output buffer, and A/D converter were redundant. One set handled housekeeping data exclusively read out in even frames and the other in odd frames. Each multiplexer consisted of 64 channels.

An analog ground from each experiment was commutated in the encoder and was used differentially in the A/D process to assist in establishing high accuracies.

Parity Check

A parity generator in the encoder monitored every 100 bits of the pulse code modulation data stream. Old parity was used, so that for an odd number of "1's" sampled for 100 bits, the corresponding parity bit would be a "0," for an even number the bit would be a "1." Parity bits were found in words 57 and 157 of the format.

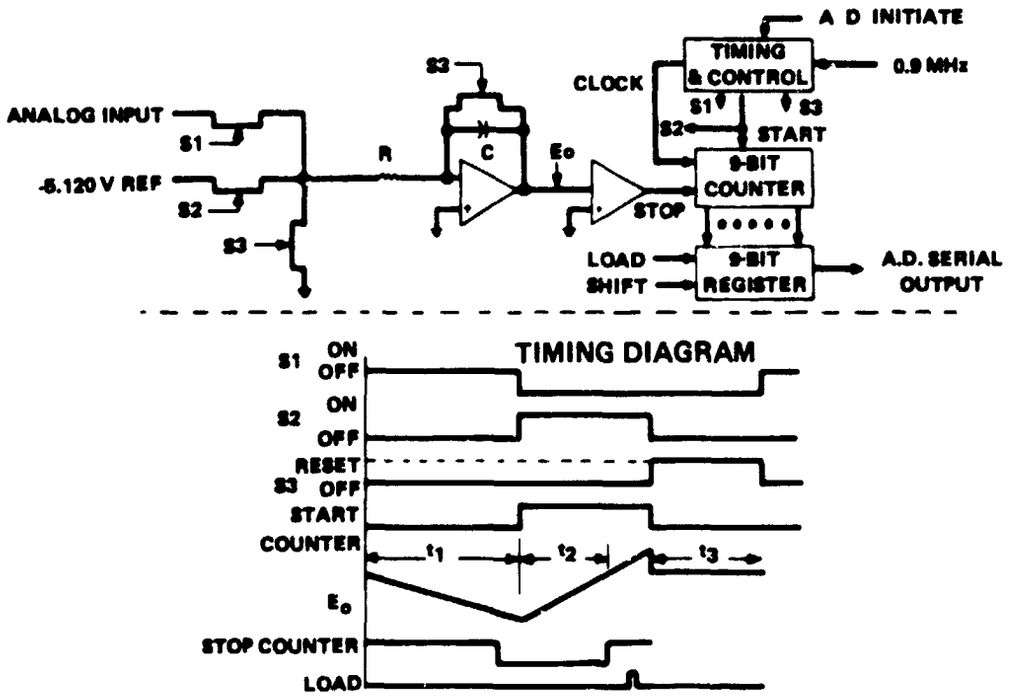

Figure 5-2. Analog/Digital Conversion Process

Telemetry Output

All data were fed through a 16-bit input "OR" gate to split phase circuitry that provided a complimentary output driver to a transformer. The "OR" gate, split phase circuitry, and transformer were all redundant.

The code used was Manchester II + 180, which was split phase level with the orientation, as shown in Figure 5-3 for "ones" and "zeros" present at the EME telemetry interface.

Interface Circuits

The encoder provided digital, programming, and analog interfaces. The digital interface circuits were exclusively Radio Corporation of America complimentary metal oxide semiconductor (CMOS). The analog circuits were composed of integrated linear amplifiers and p-channel metal oxide semiconductor (MOS) units. The CMOS devices used in this design were of the lowest power drain type available. In addition, they had the highest noise immunity and overall packing density. The analog devices were selected for low power, high packing density, low ON and high OFF resistance (analog switches), and compatibility with CMOS logic.

Typical interface circuits are shown in Figure 5-4.

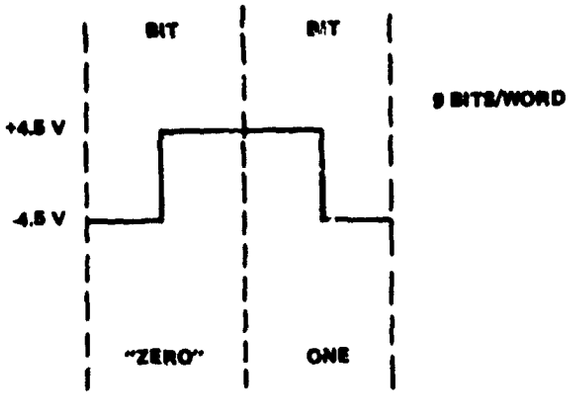

Figure 5-3. Manchester II Code

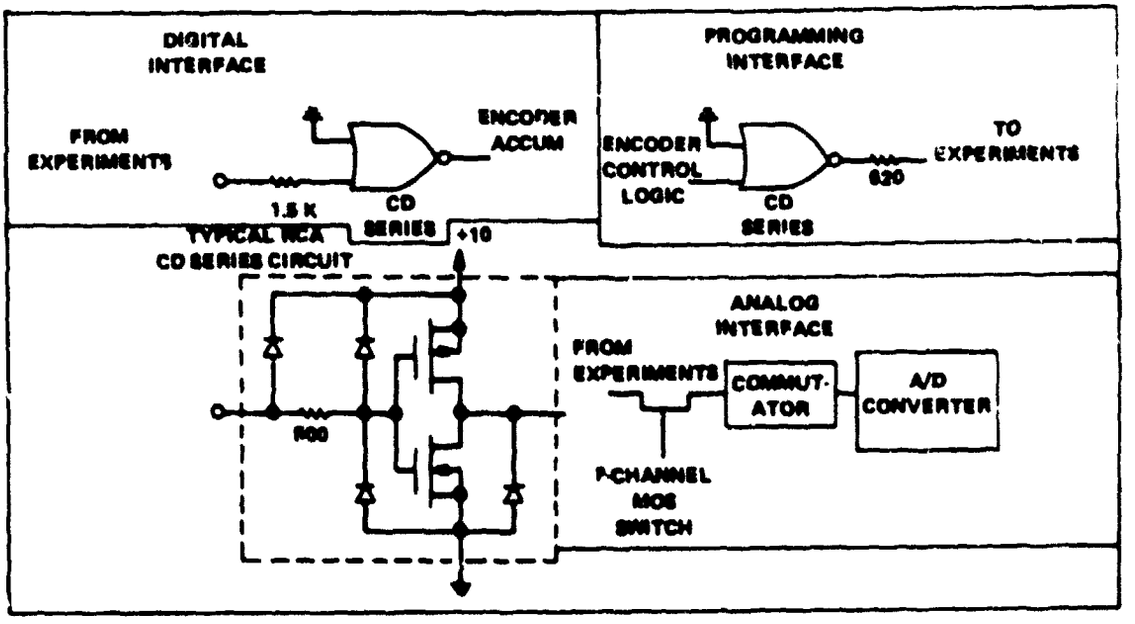

Figure 5-4. Typical Encoder Interface Circuits

COMMAND INTERFACE CONTROL

Function

The prime function of the command interface control unit was to provide a common interface between the spacecraft command receiver system and the eight scientific instruments included in the EME. In addition, the command interface control contained the logic necessary for control of the EME real-time clock system status monitor, and automatic power control for the Hughes experiment. Sun-aspect data from a remote solar-aspect sensor were also multiplexed in the command interface control for transmission through telemetry.

Command Interface Control Operation

Inputs from the Spacecraft

The EME was assigned two command words (9-bit, NRZ-L) from each spacecraft command decoder. The signals associated with each word were "ENABLE," "CLOCK," "DATA," and "EXECUTE" and had the characteristics shown in Figure 5-5. Word 1 is OCTAL 60 and Word 2 is OCTAL 70 in the data-word address field of the normal-command word.

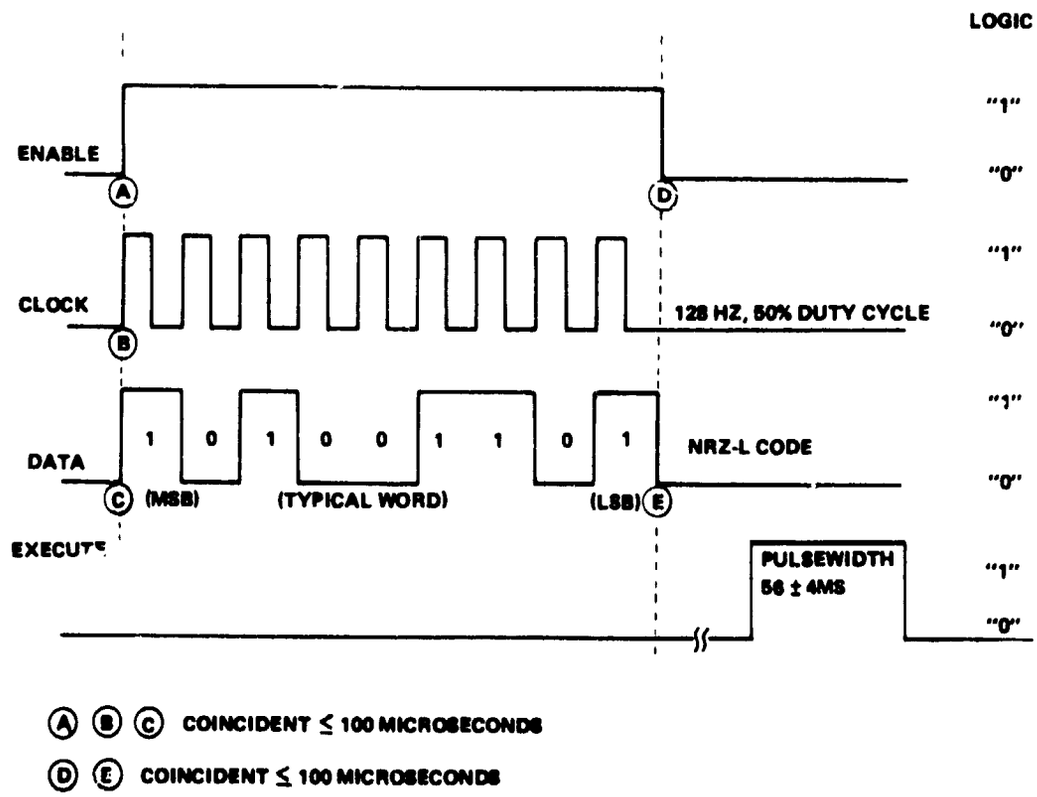

Figure 5-5. Input Timing Characteristics

Inputs from the EME Encoder

The command interface control (CIC) required 13 signals from the EME encoder-programmer. These signals were used for logic clocking, data multiplexing, and lockout of automatic power switching to the Hughes Aircraft Company (HAC) experiment.

There were 10 programming signals from the encoder that enabled the CIC to multiplex status data for the telemetry transmission. These signals were 0 volt for 5 milliseconds (ms) and +10 volts for 995 ms. The pulse occurred during the telemetry word prior to readout of data associated with a particular telemetry word in the format. That is, a pulse during word 50 enabled transmission of data that would appear in word 51.

There were two clock signals that had a period of 555 microseconds (μsec). These signals were implemented redundantly so that failure of one clock signal would not prevent selection of any command function. The duration and level of this pulse was 55 μsec at 0 volt and 500 μsec at +10 volts.

One signal line from the encoder-programmer contained the "solar cell lockout (busy)" signal. This signal was normally at 0 volt, but could go to +10 volts when the telemetry format switched from "solar cell format" to "normal format." It remained at +10 volts for 2 or 3 hours. When the signal was at +10 volts, the automatic power turn-on of the HAC experiment was disabled by overriding the solar-aspect sensor command. That is, even though the Sun was normal to the HAC experiment solar cell panel and the "HAC auto" command was on, the HAC experiment could not be turned on.

Power Distribution

A block diagram of the power control logic is shown in Figure 5-6. It should be noted that WORD 1 (W1) spacecraft command address 60, was used exclusively for logic control of power on/off commands, or commands associated with updating the EME system real-time clock. It should also be noted that circuitry and input RW1 is redundant to the OR gates and relay drivers.

Figure 5-7 is a diagram of how power was controlled and distributed by the CIC.

The experiment bus relays were redundant and normally it was only necessary to energize one relay to supply power to the rest of the EME. These bus relays were electrically latched. That is, once power had been applied to the EME and the experiment bus relay commanded on, the relay would remain energized until primary power was removed from the EME.

The relays used to control the individual experiment power were magnetically latched and the coils only drained power when the execute pulse was active. Control of the magnetic latch relays was independent of the state of the experiment bus relays, which provided a means for orbital troubleshooting.

The relay labeled SUN NORMAL/HAC LOCKOUT was controlled automatically to supply power to the HAC experiment. The signal to actuate this function was derived from a solar aspect sensor

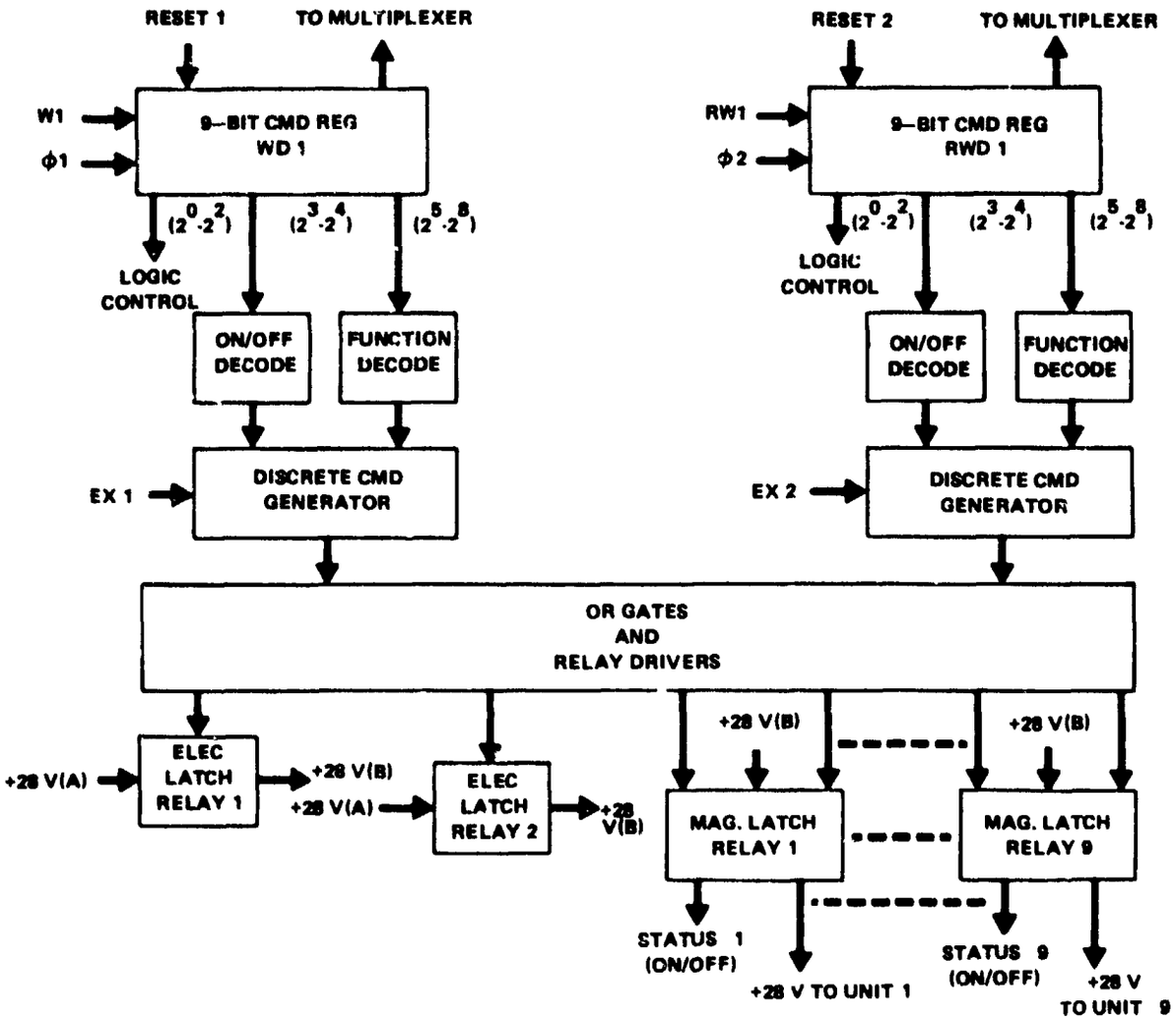

Figure 5-6. Power Control Logic

remotely from the EME. In normal orbit this relay would automatically actuate for 2 to 3 minutes once a day when the Sun was within 2 degrees of the HAC experiment solar cell panel. The lockout position was controlled by the EME encoder-programmer. This signal ensured that the telemetry format and power to the HAC experiment could not be recommenced until at least 2 to 3 hours after the panel had seen the Sun. The status of the relay state was multiplexed in the CIC for telemetry transmission.

The EME system survival heaters were powered through the off contacts of the experiment bus relays. The heaters were 15 watts each and either zero, one, or two could be selected depending on the state of the experiment bus relays. Note, that heaters could only be energized if primary power was supplied from the spacecraft to the EME.

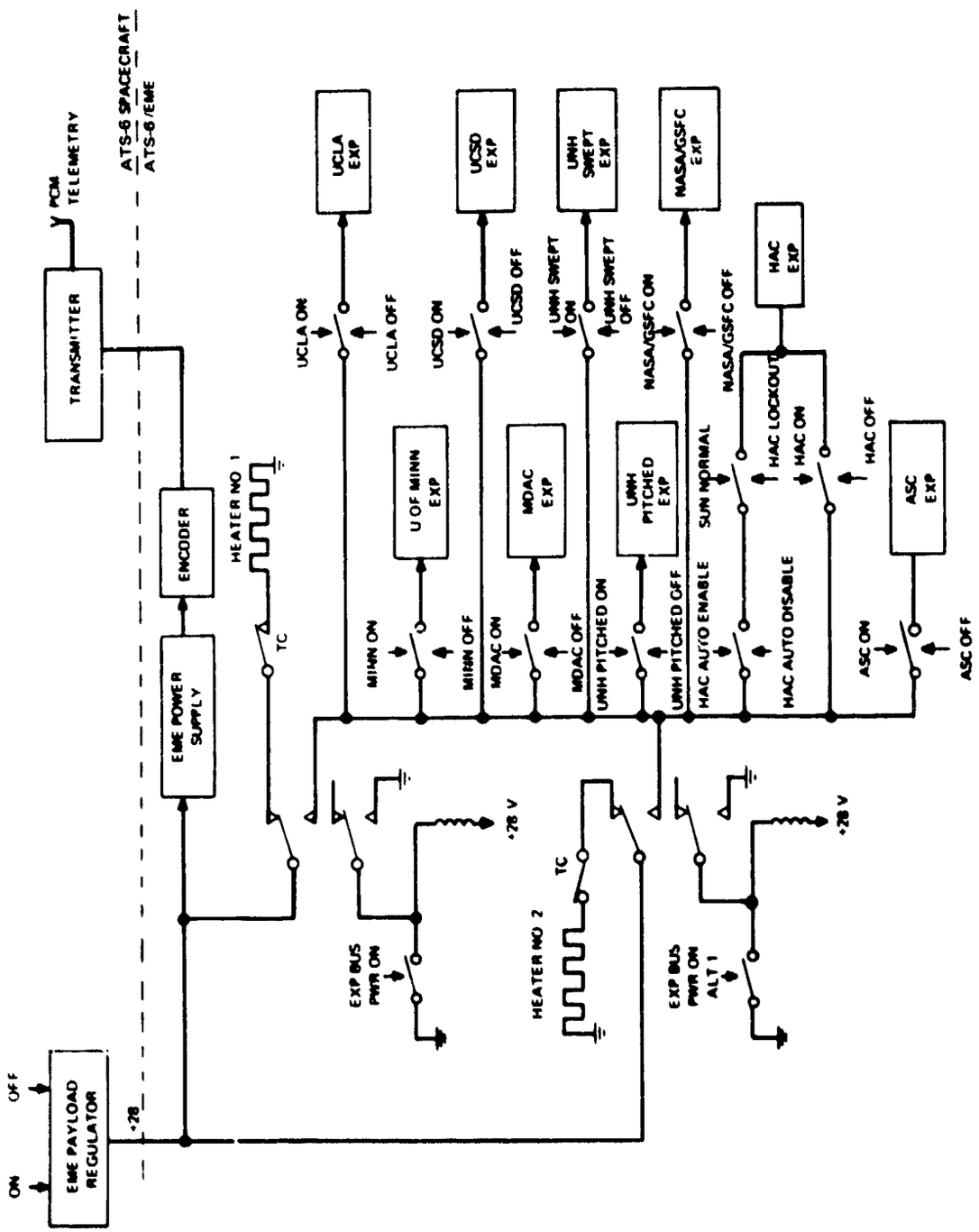

Figure 5-7. CIC Power Distribution

Mode Control Logic

The mode control logic is presented in block diagram form in Figure 5-8. One word (W2) from each spacecraft decoder, spacecraft command address 70, was used in redundant fashion to derive the individual mode commands. The redundant circuits stopped at the output of the 9-bit command registers. ATS-6/EME system requirements were for 56 mode commands, and each command had a separate address for the "1" or "0" state. To accomplish this, an 11 X 11 matrix was used to provide a maximum capability of 121 functions.

In addition to the matrix decoded functions, another command path was provided for updating the system real-time clock. This was a serial logic path that allowed updating days, hours, or the real-time clock with a single 9-bit word transmission from the ground.

The serial command path was enabled by decoding the states of particular commands in word 1 (60). The serial path was incorporated to expeditiously update the EME system real-time clock with a minimum number of ground commands.

Command Verification

The 9-bit data word had to be verified through telemetry prior to execution of that command. The verification word was found in word 102 of the EME format with the most significant bit (MSB) transmitted first in time. After command verification and execution, W102 would go to all "zeros" until the next data word was sent to the CIC. If the telemetry indicated incorrect data, the command word would be retransmitted. Both word 1 (60XXX) and word 2 (70XXX) data bits appeared in W102 and could not be distinguished.

POWER SUPPLY

The prime purpose of the power supply was to accept the single source voltage of +28 volts direct current (Vdc) ±3 percent provided by the spacecraft and condition this power to be used by the various support equipment within the EME package.

Function

The function of the power supply was to provide the necessary voltages for the pulse-code modulation encoder, the command interface control unit, the real-time clock, the automatic temperature controllers and heaters for the encoder oscillators, the solar aspect sensor, and for thermistors that were located throughout the EME package. In addition to generating these voltages, the power supply acted as an interface for all the units of the EME package. This feature was provided to implement a current sensor within the power supply that sensed the total direct current drawn by the EME package. The current sensor provided an output voltage signal to the encoder that was linear with current. This current information was telemetered as part of the pulse code modulation format.

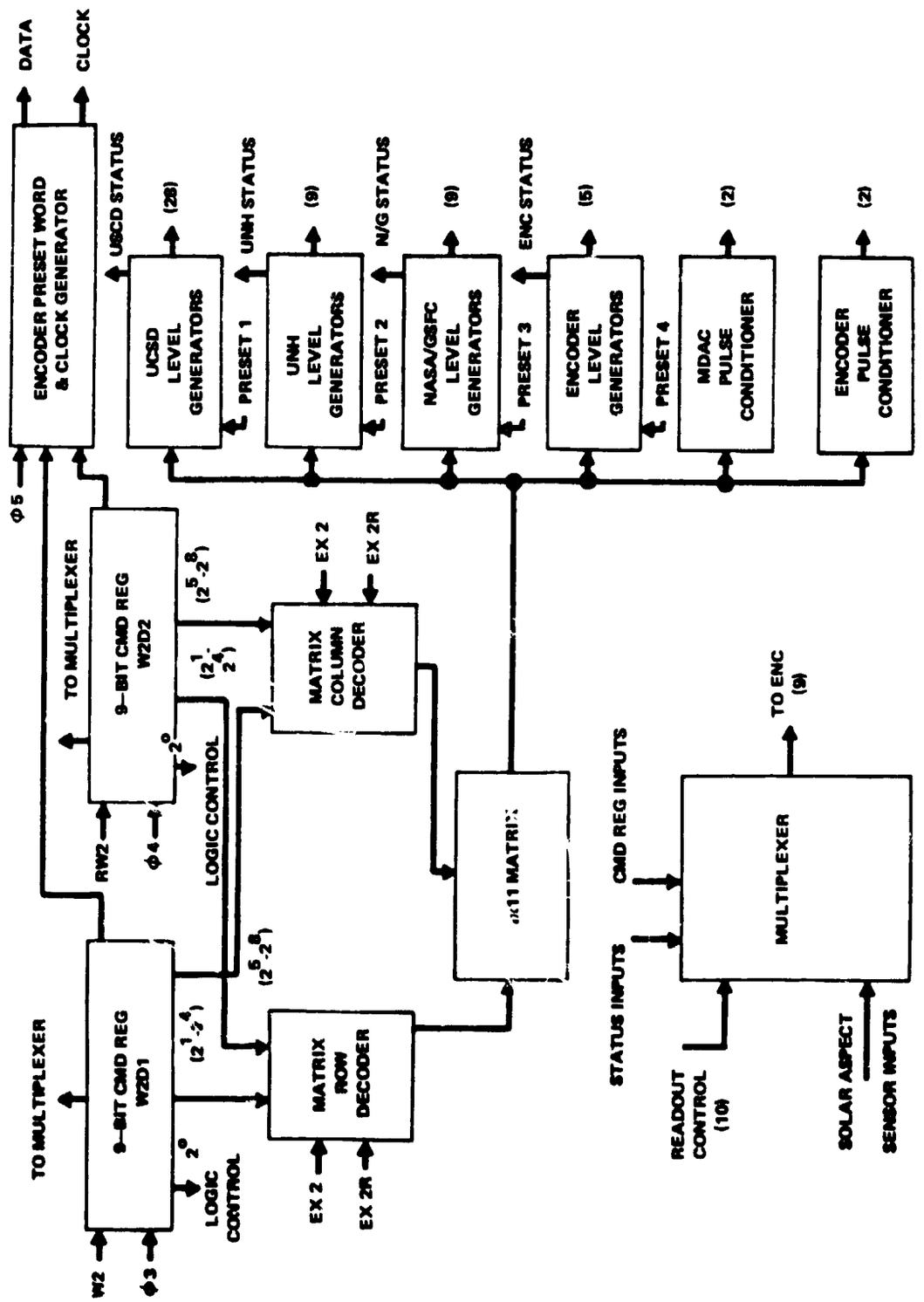

Figure 5-8. Mode Control Logic

Power Supply Operation

The power supply consisted of 10 submodules. These included seven regulators, an oscillator-driver, an inverter, and a current sensor. A block diagram of the power supply is given in Figure 5-9. The power from the spacecraft (+28 Vdc) entered the power supply and passed through an LC filter. The purpose of the LC filter was to minimize the interference between the spacecraft and the power supply. From the LC filter, the current passed through the current sensor, and then branched into two paths. One path went through an LC filter to the CIC that powered the various EME experiments and the other path went through an LC filter to the power supply, power inverter, and oscillator-driver. Again, the LC filters were used to minimize the interference between the spacecraft, the main section of the power supply, and the experiments. The path to the power inverter and oscillator-driver supplied the current to the main section of the power supply.

The oscillator-driver was a stable multivibrator that drove the power inverter to approximately 15 kHz. From the inverter, various needed ac output voltages were developed by the power transformer. These alternating current (ac) voltages were rectified and filtered to produce the required unregulated direct current (dc) voltages. Some of these unregulated dc voltages were used directly while others required more precise regulation. Where regulation was required, the unregulated dc voltage was fed into a series-type regulator. All the regulators were basically the same. They employed an integrated circuit regulator with an additional transistor output stage when additional current was required. Current limiting was done by using a resistor to sense the current. When the voltage developed across this resistor reached the desired current limiting value, the output voltage was reduced so that the output current did not increase above the limit.

The current sensing device of the current sensor consisted of two pieces of resistance wire connected in parallel between two pins of the current sensing submodule. The two pieces of wire were in series with the return path of the spacecraft 28 Vdc. Thus, the resistance wire sampled all the current coming from the spacecraft to the EME package. The voltage developed across this resistance wire was amplified by use of a linear operational amplifier to provide an output voltage that was linear with the input current. The current sensor gain was approximately 2.23 volts per ampere.

SYSTEM GROUNDING

The EME package contained a number of grounds. Special attention was given to the grounding of all circuits and units to assure direct current isolation. A diagram of the EME system grounding is given in Figure 5-10. A summary of this diagram follows.

System Ground

System ground was the one point in the EME package where signal ground and chassis ground were directly tied. From this point a ground strap was attached to the spacecraft chassis ground.

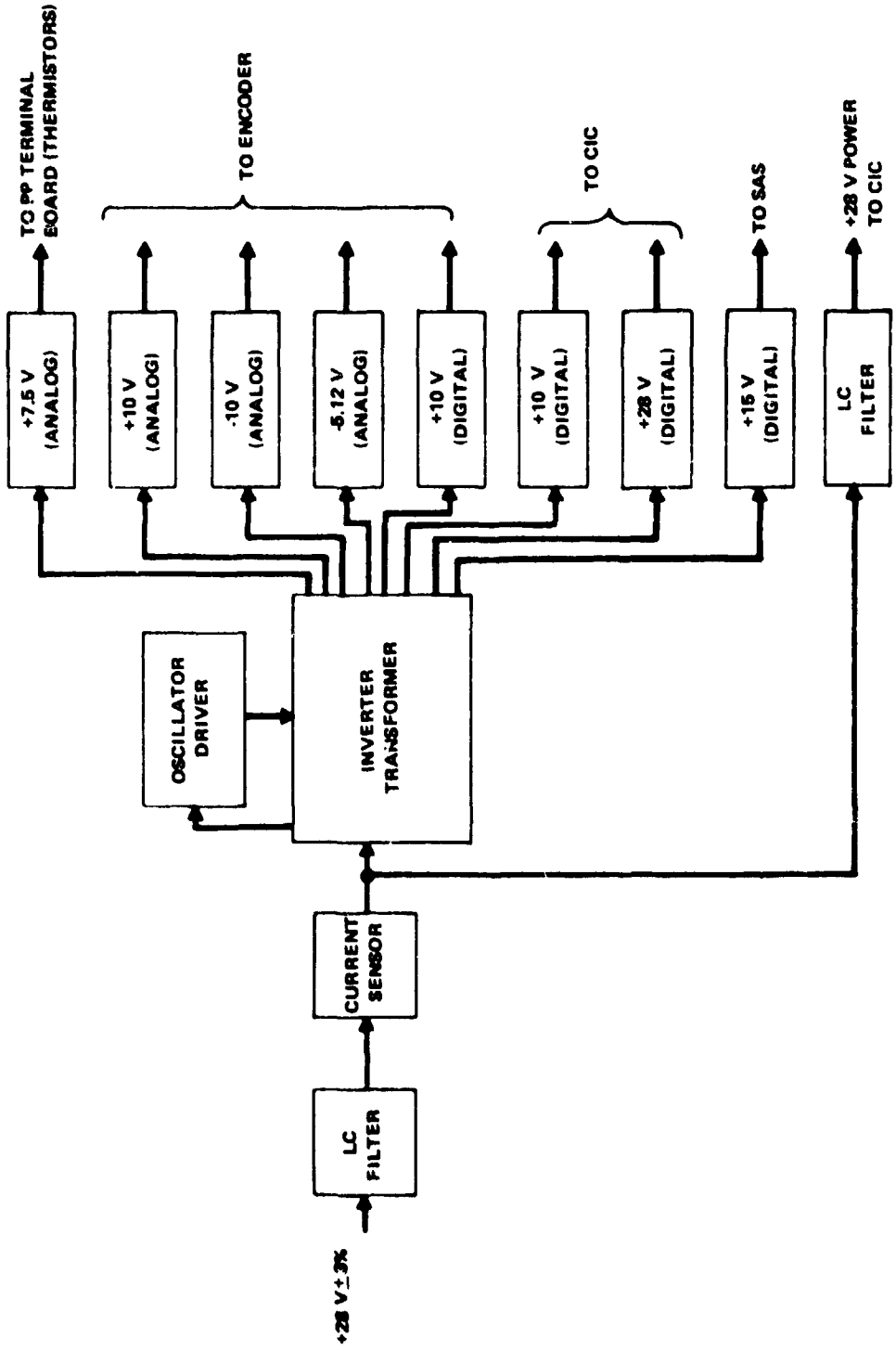

Figure 5-9. EME Power Supply Block Diagram

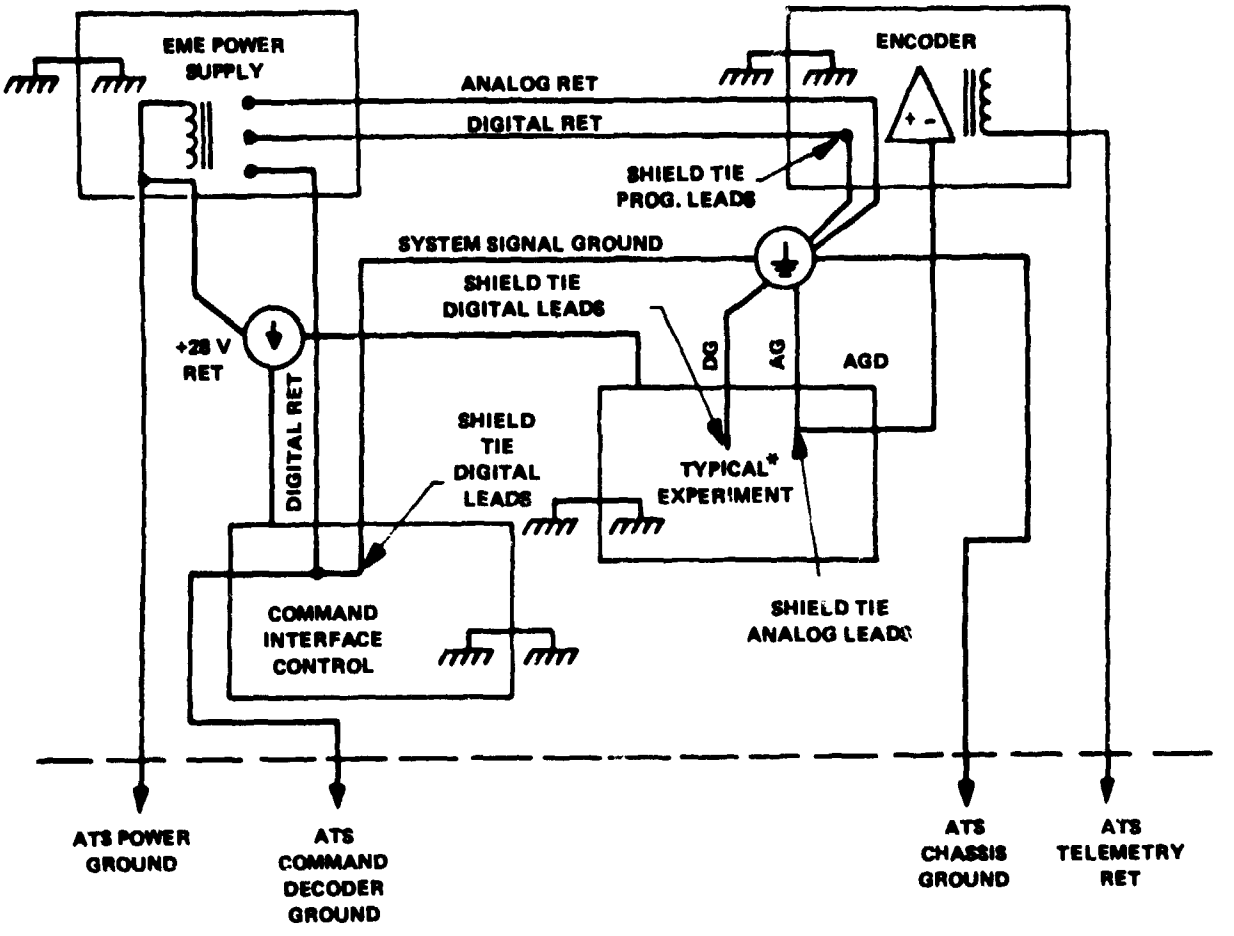

*EXPERIMENTS REQUIRING ONLY ANALOG DATA ACCURACY OF 7 BITS OR LESS NEED NOT ISOLATE DG AND AG AND ARE NOT REQUIRED TO SEND AN AGD LINE TO THE ENCODER.

Figure 5-10. ATS-6/EME Ground System

Support Equipment Grounds

Each EME support unit isolated all grounds (power, signal, and chassis) within that unit. The EME encoder further isolated digital and analog signal grounds. The EME power supply and command interface control units were referenced to spacecraft power and command returns respectively.

Experiment Grounds

With the exception of selective ac ties, all grounds were isolated within a given experiment. Experiment design and fabrication, at times, dictated the use of capacitive coupling. In those few cases, the experimenter was willing to live with the possibility of coupled system noise affecting his unit. For high accuracy data (9 bits), the experimenter further isolated analog and digital grounds (AG and DG) within his unit.

Chassis Ground

Chassis ground for all units in the EME packages was accomplished when the unit was solidly mounted to an aluminum sheet covering the honeycomb shelf. In addition, one or more AWG #20 wires were run from a connector on each unit to a ground lug near the unit. At one point in the package, chassis ground became system ground.

Telemetry Return

The remaining ground sent to tne spacecraft was one side of a transformer winding used as the telemetry modulator buffer. This ground was isolated from any other ground in the EME system.

ACTIVE THERMAL CONTROL SYSTEM

Purpose

The purpose of the active thermal control system for the ATS-6/EME package was to keep the mounting deck temperature levels and oscillations within a range of +10°C ±10°C for the EME experiments and associated support units. The thermal control of the system was obtained through the use of variable-emittance louvered radiator systems on the north and south sides of the EME package.

Physical Description

Each radiator system employed a louver assembly consisting of 12 highly polished aluminum blades enclosed by a frame of the same material. The louver blades covered a quartz-mirror radiator surface so that when the blades were closed, radiation from the quartz-mirror radiator was blocked. When the blades were open, there was a relatively free radiation interchange between the quartz radiator and outer space. The radiator surface was covered with a silica material on which silver was vapor-deposited, forming a mirror or optical solar reflector.

Each louver blade was free to rotate independently of the other blades and was also independently actuated. This independent actuation of each blade served to increase reliability and to minimize any temperature gradient from one end of the louver system to the other that might be caused by nonuniform thermal flux. Actuation was performed by bimetal springs attached to the louver blade shaft. These springs were located inside the actuator housing at the top of the louver system. Each spring was conductively and radiatively connected to the quartz radiator so that when the temperature of the radiator rose, the bimetal spring caused the louver blades to open and when the temperature dropped, the blades closed. The radiator plate was bolted to the EME mounting deck. The flatness of both mounting surfaces was maintained at 0.005 inch per inch and thermal grease was applied on each surface prior to mating.

During solar illumination, the louver blades, frame and actuator housing became very hot. For this reason, the frame was thermally isolated from the radiator plate by spacers and bushings. However, the base of the actuator system was in intimate contact with the radiator since the bimetal spring

inside sensed the radiator temperature. To minimize the heat transferred to the spring from the housing exterior, the actuator housing was heavily insulated with multilayer insulation.

With the exception of several experiment sensors that needed an opening for a clear view of space, the remaining EME structure was covered with multilayer superinsulation that was supported by a fiberglass structure. The fiberglass structure had a single layer of aluminized mylar bonded to the inside to reduce radiation coupling between the internal units and the thermal cover. The outer surface of the fiberglass was covered by a 17-layer thermal blanket whose outer layers were aluminized kapton.

Thermal sealing around the sensors that looked through holes in the thermal cover was accomplished by taping overlapping preshaped pieces of aluminized kapton to the sensor. A layer of tissueglass was then applied in the same manner. This process was continued until 17 layers of aluminized kapton were taped to the sensor.

Description of Operation

Thermal control of the EME package was accomplished by the two louvered radiator systems, and by the proper choice of sensor coatings and system insulation. Ideally, if the amount of heat absorbed and rejected by the EME system were both constant, the system temperature would be constant. Since the heat absorbed is not a constant, the louver systems provided a means of varying heat rejection as a function of temperature. As the temperature of the EME package rose, indicating an increase in absorbed heat, the louver blades opened, allowing an increased rate of heat rejection. Conversely, as the temperature dropped, the louvers closed. The louvers were mounted on the north and south sides of the EME since these sides were not directly illuminated by the Sun. Thus solar angles of incidence were limited to a minimum of 54 degrees, which minimized heat absorbed by the louvers.

The effectiveness of the louvers was reduced by leaks in the system. Because of the many experiment sensors, the EME had many leaks. Therefore, when the system deck temperature was at 0°C, the louvers were completely closed and rejected approximately 50 percent of the total system heat. The remaining heat was rejected by the sensors (38 percent), and the insulation (12 percent). As the deck temperatures rose, the louvers opened. At +20°C, the louvers radiated approximately 70 percent of the system heat, the sensors 23 percent, and the insulation 7 percent.

Under normal operation in a nominal orbit (Earth synchronous-equatorial-three axis stabilized) the thermal control system maintained the EME deck at a temperature of +10°C ±10°C. To survive all orbital conditions, the EME package also contained two 15-watt heaters operating from the main power line. Power to each of the heaters was supplied through quadredundant thermostatic switches in series with each of the two experiment bus power off contacts in the CIC. Each heater came on when the thermostatic control switch reached -15°C (5°F) and deactuated when the temperature reached -5°C (23°F).

SOLAR ASPECT SENSOR

Purpose

The solar aspect sensor detected the position of the Sun within the sensor's field of view, and provided this Sun-angle information on 14 parallel bits to the command interface control. This data was used for two purposes:

- Automatic turn-on of the HAC experiment and format when the Sun was normal, in the vertical axis, to the HAC solar panel mounted on the west face of the EME
- Provided angular information defining the orientation of the EME package

Physical Description

The solar aspect sensor had three basic components: a sensor, an electronics unit, and a sunshade. The sensor contained 16 solar cells and 2 reticles. The sensor looked through the thermal blanket to the west, and connected to the electronics unit. The electronics unit contained all the electronic components associated with the sensing system except for the solar cells. The electronics unit was located within the thermal blanket. The sunshade was made from fiberglass and was bonded to one side of the sensor. All three units were painted black except for the edges of the sensor and the mounting surface of the electronics which were bare aluminum.

Description of Operation

The sensor contained two sets of eight solar cells and two orthogonally oriented reticles to provide Sun aspect data when the Sun was within the 128 X 128-degree field of view of the sensor. The sensor looked west; its horizontal axis was defined as the Y-Y axis and the vertical axis of the sensor was its Z-Z axis (Figure 5-11).

Seven cells in each axis provided the sensors for the digital readout of Sun position by differences in current outputs for illuminated cells and nonilluminated cells. The Sun angle was encoded into a 7-bit binary number, as shown in Figure 5-12. Sunlight was passed through a reticle placed between the Sun and the solar cells. The bottom of the reticle was divided into eight sections. Each section had a solar cell behind it, and seven of the sections were subdivided into opaque and transparent segments. The top of the reticle was opaque except for a narrow transparent slit that, when illuminated, projected a bright image on the bottom of the reticle. The position of the bright image of the slit on the bottom of the reticle was a function of the angle of incidence of the light on the sensor, but the image of the slit always fell across all eight sections of the bottom of the reticle. If the bright image fell across a transparent segment of one of the sections, then the associated cell was illuminated and had a relatively large current output. If the image fell across an opaque segment, the associated cell was dark, and had relatively small current output. The transparent/opaque patterns of the reticle were laid out in such a way that as the Sun swept from -64 to +64 degrees (causing the image of the slit to move from one side of the pattern on the bottom of the reticle to the other) 128 different combinations of the seven digital readout cells were illuminated, thereby dividing the angles from -64 to +64 degrees into 128 one-degree steps.

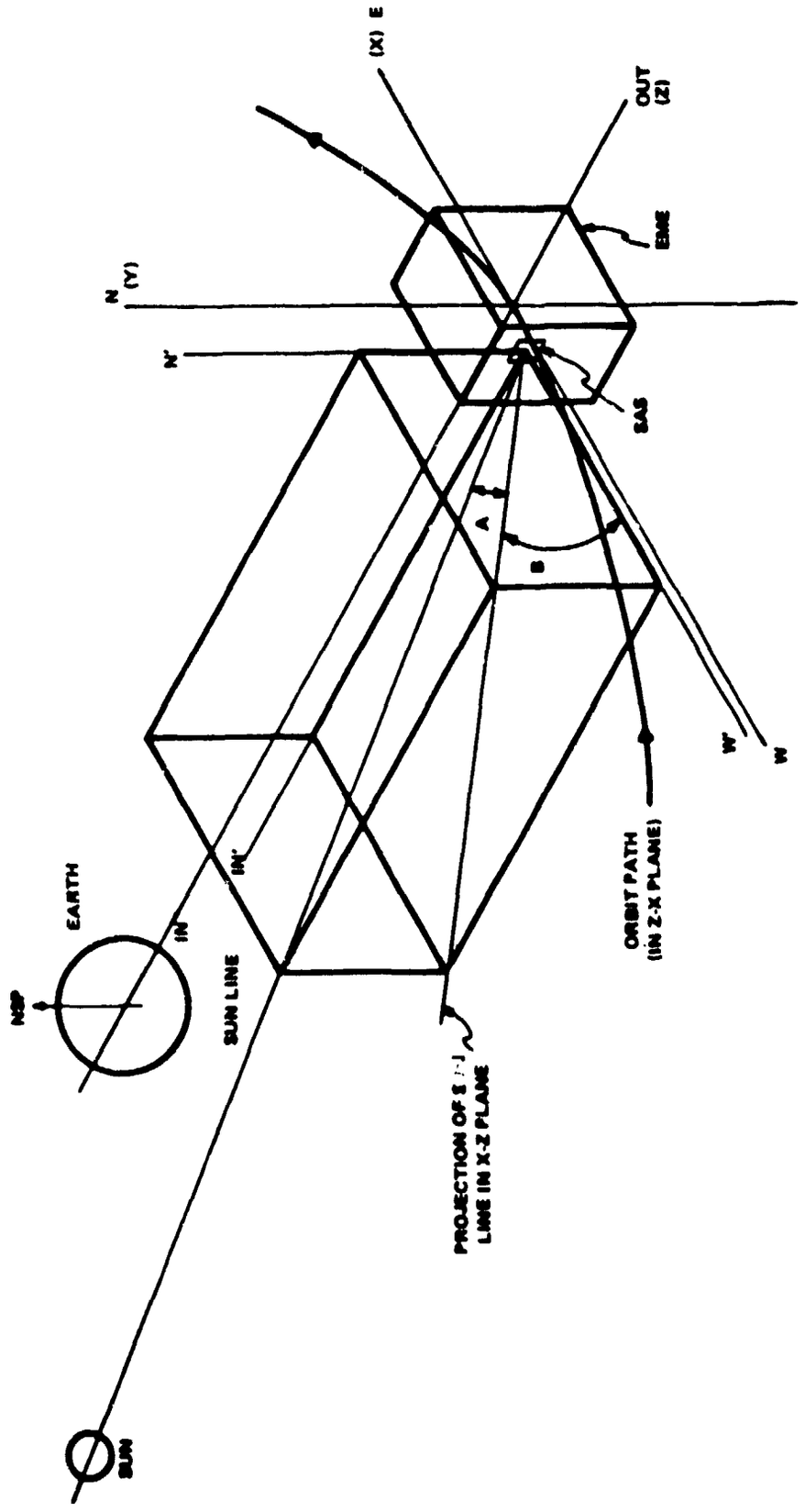

Figure 5-11. Solar Aspect Sensor Fields of View

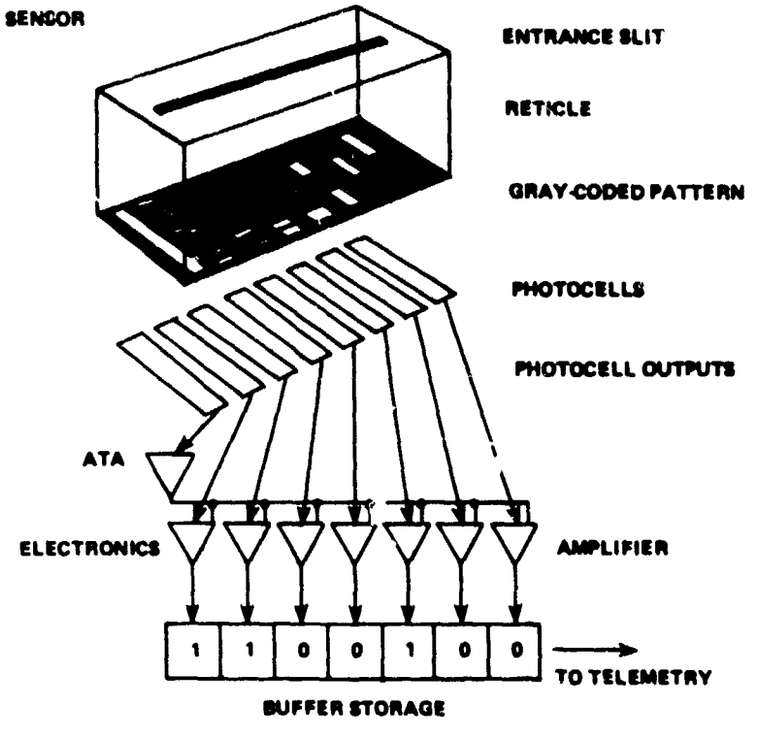

Figure 5-12. Solar Aspect Sensor Operational Diagram

The eighth section of the pattern on the bottom of the reticle was not used directly for coding the angle of the Sun. This section was transparent throughout its length so that the cell associated with it was illuminated through the entire range of angles from -64 to +64 degrees. The output of this cell was used to determine how much current was to be expected from an illuminated cell in the other seven sections, and, therefore, was an aid in determining whether the current output of the other cells was due to illuminiation or was "dark current." This was necessary because the current output of an illuminated cell depended strongly on light intensity and angle of incidence. This eighth cell, the automatic threshold adjust (ATA), was illuminated through a transparent segment that was one-half as wide as the transparent segments of the seven digital readout cells. The ATA output was, therefore, one-half the output of the other illuminated cells, and this lesser output was used as a threshold (i.e., if a cell output was greater than the ATA, the cell was considered to be a "1;" if the cell output was less than the ATA, the cell was considered to be a "0").

The output current of the 14 digital readout cells, and one of the ATA's, was fed to the electronics unit. The electronics compared each digital-readout cell current with the ATA current, and put out 14 bits of bilevel data to the CIC. This bilevel data were telemetered in W54 and W55. (Word 54 contained vertical [Z-axis] data and Word 55 contained horizontal [Y-axis] data.) The second function performed by the sensor was to provide a signal for automatic turn-on of the HAC experiment. The CIC decoded the seven bits of the vertical axis. When those bits indicated a normal incidence in this axis, the CIC provided a signal to turn the HAC on, and to switch to solar cell format, whereby this automatic feature was enabled.

The function of the shade was to prevent reflected light from reaching the sensor. The shade also had the effect of limiting the field of view in one direction to only 14 degrees from normal instead of the 64 degrees which the sensor could view. The shade was painted black to prevent significant reflections from the shade itself.

The solar aspect sensor electronics received +15 volts from the EME power supply as soon as the EME package was turned on. The solar aspect sensor system required 0.2 watt.

CHAPTER 6

SYNOPSIS OF ANOMALIES AND FAILURES OF EME

The Environmental Measurements Experiments (EME) on board the ATS-6 spacecraft consisted of eight experiments, most of which experienced problems or anomalies in the synchronous orbital environment. A summary of the failures and anomalies that occurred during the operation of the EME experiments are briefly described below.

SOLAR COSMIC RAY EXPERIMENT (McDONNELL-DOUGLAS AIRCRAFT CORPORATION)

The operation of the electron spectrometer and the particle telescope in the measurement of cosmic rays and trapped electrons and protons performed very well during all phases of the experiment. No problems were experienced during the performance of this experiment.

LOW ENERGY PROTON–ELECTRON EXPERIMENT (UNIVERSITY OF NEW HAMPSHIRE)

The purpose of this experiment was to continuously monitor the spectra and pitch angle distributions of electrons and protons from 0 to 22 kiloelectron volts (keV).

A few hours after activation of the University of New Hampshire (UNH) experiment, a serious problem was encountered where an unknown mode of interference (probably a high-voltage arc) occurred between this experiment and the EME package. Because of this, the UNH experiment was deactivated until the third year in orbit. This interference signal caused a permanent closure (short) in one or more performance parameter multiplexer (MOSFET) switches in the EME telemetry generator. Interpretation of the EME performance parameter word 58 for other experiments was not possible following this incident.

This interference also produced abnormalities on the EME clock signal that caused the clock to "jump" or become reset. The EME clock was also reset by an interference signal from some other source in the spacecraft when the UNH experiment was not operating.

LOW ENERGY PROTON EXPERIMENT (NATIONAL AERONAUTICS AND SPACE ADMINISTRATION/GODDARD SPACE FLIGHT CENTER/NATIONAL OCEANIC AND ATMOSPHERIC ADMINISTRATION

The objective of this experiment was the investigation of protons that were considered to produce storm-time extraterrestrial ring current in the geomagnetic storms. This experiment performed exceptionally well but two operational anomalies were experienced that affected the quality of the data transmitted.

One anomaly was caused by the failure of the Mosfet switches mentioned in the University of New Hampshire Low Energy Proton-Electron Experiment. This failure caused a direct-current voltage to continuously occur on one EME data channel in which the housekeeping and heavy ion data were sampled for this experiment. All of the housekeeping parameters in this case were considered useless. The heavy ion data, however, was reconstructed and completely recovered by introducing a direct-current offset voltage to the channel output signal.

The second operation anomaly resulted from the temperature of the EME platform, containing the experiment's detectors, becoming 10°C higher than the design goal. This high temperature increased the thermal noise of the solid state detectors and essentially affected only the lowest three channels of the C telescope.

ELECTRON-PROTON SPECTROMETER (UNIVERSITY OF MINNESOTA)

An electron-proton spectrometer, containing two detector assemblies (one stationary and one scanning), was used in this experiment to investigate the origin and dynamics of electrons and protons in the outer radiation zone at the synchronous orbit altitude. The higher than anticipated temperatures of the EME package caused serious problems, one of which was the increase in the thermal noise background level in the detectors. In the proton detector the noise level became unacceptable, and nine months after the launch of ATS-6, the proton detector in the fixed spectrometer failed. This failure became a serious loss and left only the scan detectors to provide data for this experiment. The proton detector in the scan system failed at 12 months. The mechanical drive for the scanning system failed January 30, 1976, after more than 19 months of continuous trouble-free operation.

The failure of the Mosfet switches mentioned in the previous experiments also affected this experiment by not providing the temperature data from all of the detectors.

AURORAL PARTICLES EXPERIMENT (UNIVERSITY OF CALIFORNIA AT SAN DIEGO)

The objective of this experiment was to determine the magnetospheric processes that contained and accelerated charged particles near the Earth, particularly those particles that are deposited into the upper atmosphere, and produce auroras. During the operation of this experiment a number of failures and anomalies were experienced and consisted of the following:

- On July 29, 1974 one of the two deflection power supplies, for the east-west rotating heads, failed. Failure was caused by the prolonged dwelling at 62 keV and to inadequate cooling. The fixed detector also failed at this time.

- The east-west detector failed to rotate on September 6, 1974.

- Starting on September 19, 1974 the north-south detector would periodically fail to rotate.

- Near the end of 1974, the east-west electron channel began to have periods of large errors caused by cross-talk from the north-south electron channel.

- The efficiencies of both the north-south ion and electron detectors degraded 10 to 20 percent from their original values beginning on May 21, 1975. Under high bias, both detectors returned to their original efficiency on September 23, 1975.

- During the month of February 1976, the north-south detectors temporarily failed to rotate at the two angles of 180 degrees and 198 degrees.

- The efficiency of the north-south detector began degrading in September 1976 in spite of operating in the high bias mode.

- Complete failure of the instrument occurred on May 15, 1977.

FLUXGATE MAGNETOMETER (UNIVERSITY OF CALIFORNIA AT LOS ANGELES)

The primary objective of this experiment was to monitor continuously the Earth's magnetic field at synchronous orbit altitude with a fluxgate magnetometer to provide data for models of the time-varying configuration of the magnetosphere.

Three serious problems occurred during the operation of the magnetometer. One of the problems was the occurrence of an interfering noise in the sensor whose magnitude was three times that inherent in the sensor.

The second problem seriously delayed the processing of the magnetometer data and was caused by anomalies in the associated attitude/orbit determination. The magnetometer data contained periodic fluctuations that produced oscillations in the transformed data and affected the study of harmonic waves so that it became almost impossible to analyze. This problem was later solved when the corrected attitude/orbit data became available.

On September 1975 the operation of the magnetometer sensor in the Y-axis failed when the offset field system would not stop hunting for the null.

SOLAR CELL RADIATION DAMAGE EXPERIMENT (HUGHES AIRCRAFT COMPANY)

The purpose of the solar cell experiment was to determine the degradation in performance of different types of solar cells when exposed to the Sun's radiation in the synchronous orbit altitude environment.

A failure of the current channel in the signal processing unit (SPU) No. 2 occurred prior to the activation of the experiment in flight and caused the loss of data from half of the solar cells and from three thermistors. One thermistor associated with the SPU No. 1 also failed, leaving only one thermistor on the flexible solar test panel to measure the panel temperature.

Because of the thermistor failure, the temperature of the signal panel was determined from the open circuit voltages of the associated solar cells.

ENERGETIC PARTICLE SPECTROMETER EXPERIMENT (AEROSPACE CORPORATION)

An energetic electron-proton spectrometer was used in this experiment to detect energetic electrons in four energy channels, energetic protons in five channels, and energetic alpha particles in three channels.

Several anomalies occured during the operation of this experiment, none of which were considered very serious.

Whenever the experimental unit reached a temperature below -10°C, an open circuit developed in one of the data channels. A large thermal gradient, occurring at the detector, was suspected of causing this open circuit. However, this malfunction resulted in only a minor loss of experimental data. Apparently the ground tests performed on this experiment at temperatures well below -10°C did not properly simulate the large thermal gradients that were encountered in space.

Under certain operational conditions, intermittent noise was observed in one detector that resulted in noisy data. This effect was largely caused by the high temperatures of the detector that reached values in excess of those expected.

Another problem that occurred was the loss of housekeeping data when the UNH experiment malfunctioned a few hours after launch of ATS-6. This malfunction produced interference with the EME data system and affected most of the experiments. The loss of this data considerably complicated the analysis of this experiment's data.

CHAPTER 7

INITIAL RESULTS FROM THE ENVIRONMENTAL MEASUREMENTS EXPERIMENTS

INTRODUCTION

This chapter presents an outline of the results obtained by the instruments during the initial operational period of the EME at 94°W longitude and a bibliography of associated published reports. The significant areas of investigation discussed are as follows:*

- Specific characteristics of the main geomagnetic field 10 degrees above the magnetic equator at a geostationary distance
- Magnetic field and particle signatures of field-aligned currents
- Plasmasphere composition and temperature
- Periodic variations in the magnetic field and particles covering variations with periods from a few seconds to a few weeks
- "Typical" particle-energy spectra role of heavy ions, and role of spacecraft charging in the geosynchronous environment.

INCLINATION OF THE MAGNETIC FIELD AT ATS-6

The University of California at Los Angeles (UCLA) magnetometer on ATS-6 consisted of an orthogonal array of three fluxgate sensors aligned with the body axes of the spacecraft. The instrument measured each component of the magnetic field to an accuracy of 1/16 gamma with a dynamic range of ±512 gamma. The root mean square (rms) noise in the bandwidth from 10^{-3} to 1 hertz (Hz) was 85 meters. The direct current (d.c.) field of the spacecraft was small; the components perpendicular to the Earth pointing axis were less than 2 gamma. Particle measurements indicated that the third component of the spacecraft field was also small.

For geophysical studies, the magnetometer data were transformed from the local body system to a geophysical coordinate system, dipole VDH. For the first year, ATS-6 was located on the geographic equator approximately 10 degrees above the magnetic equator. Field lines through the satellite passed through the magnetic equator at distances (L values) greater than 6.6 Earth radii. The H-axis of the dipole coordinate system was antiparallel to the Earth's dipole axis. The D-axis was orthogonal to a plane defined by H and a radius vector through the spacecraft; V completed the

*Refer to bibliography at the end of this chapter for details of the results that follow.

right-hand system so that V X D = H; V pointed away from the Earth parallel to the magnetic equator. At times, it was convenient to display the magnetic field data in spherical polar coordinates rather than the V, D, H system. In this case, $\hat{B}_{TOTAL}$ was the field magnitude, θ the polar angle with respect to the dipole H-axis, and ϕ the azimuthal angle measured in the VD plane positive eastward from V towards D.

Spherical polar coordinates were useful in illustrating a surprising feature of the magnetic field where ATS-6 was located. It was found that the mean field at local noon was tilted approximately 30 degrees to the dipole axis and had a magnitude of about 135 gamma.

In a dipole field, these values would be 29 degrees and 112.6 gamma. Early models of the magnetic field predicted that values should be 21 degrees and 147 gamma. These predictions were based on the physical notion that the solar wind compressed the day-side magnetosphere, increasing the field strength at synchronous orbit, and simultaneously flattening the field lines against the dipole axis. The observations, however, clearly showed that the tilt of the field was larger and the field strength, smaller, than predicted by such a model.

The differences between the ATS-6 observations and these early models can be explained if one assumes that there is significant plasma within the magnetosphere. Off the magnetic equator, such plasma would decrease the field strength and tilt the field away from the dipole axis. Since early models of the magnetopause currents neglected internal plasma, it is not surprising that these predictions were in error.

Another surprising characteristic of the mean field at ATS-6 was the obvious seasonal dependence of tilt and magnitude. The winter tilt at midnight was 10 degrees less than the summer tilt, and field magnitude was 35 gamma less. These observations suggest that the surface of magnetic symmetry at synchronous orbit does not lie in the magnetic equator at the solstices. However, because of a 1.54 degree tilt of the ATS-6 orbit relative to the geographic equator, this cannot be unambiguously demonstrated.

Magnetic Effects of Substorm-Associated Field-Aligned Currents

Transient azimuth magnetic field variations during substorms had been reported using data from ATS-1 at synchronous orbit. However, since ATS-1 is located very near the magnetic equator, it was difficult to explain why such magnetic perturbations should be observed. As is easily seen by symmetry arguments, aximuthal effects of field-aligned currents connected to both northern and southern auroral zones should cancel at the magnetic equator. Where ATS-6 was located, the azimuthal effects of field-aligned currents should not have cancelled.

Examination of daily magnetograms from ATS-6 unambiguously showed the effects of substorm-associated field-aligned currents. These effects are identical to those seen on the ground in the northern hemisphere at mid- and subauroral latitudes. These observations were entirely consistent with accepted models of substorms and field-aligned currents.

PARTICLE MEASUREMENTS ASSOCIATED WITH FIELD-ALIGNED CURRENTS

In the equatorial magnetosphere, ATS-6 was the first to observe intense beams of 1- to 10-kilo-electron volts (keV) electrons traveling parallel to the local magnetic field. The intense beams seemed to occur only within the first 10 minutes after the onset of a hot plasma injection associated with a magnetic substorm.

Observations showed that a negative spike in the eastward component was usually coincident with the occurrence of the parallel fluxes of electrons, indicating that the fluxes are contributing to currents flowing along the magnetic field. Although the origin and density of the parallel electrons are unknown, consideration of the total energy and number of particles transported guarantees that they must play an important role in key magnetospheric processes. In particular, these particles may be associated with the initial brightening of auroral arcs.

The Unexpected Existence of a Warm Plasma in the Region of the Plasmaspheric Bulge

ATS-6 observed enhancements in low-energy (warm) plasma (2 to 30 eV) occurring predominantly in the late afternoon and dusk region of the equatorial magnetosphere. These observations were particularly significant because of their possible association with the plasmasphere. This class of low-energy events often shows field-aligned anisotropies, but isotropic distributions, as well as distributions indicative of flows perpendicular to the magnetic field, were also observed.

Correlated Periodic Variations of Particles and the Magnetic Field

An unusually large number of correlated wave and particle oscillations were observed by the ATS-6 EME instruments while the satellite was located above 94°W longitude. The number of events appeared to be matched only by the variety in the wave and particle characteristics. This surprising variety of observations may have been a function of the satellite's location 10 degrees off the magnetic equator, or the result of an extremely low noise magnetometer and well designed and functioning particle instruments, or a combination of both.

Wave and Particle Observations of Pc 1 Oscillations

ATS-6, for the first time, observed Pc 1 oscillations simultaneously in magnetic and particle data in the equatorial magnetosphere.

The Pc 1 oscillations were observed predominantly within the dusk region low-energy enhancements discussed under the heading "The Unexpected Existence of a Warm Plasma in the Region of the Plasmaspheric Bulge," with periods anywhere from 1 to 10 s (the proton gyro period in this region is approximately 0.6 s). Also, the particle perturbations were observed predominantly within the low-energy detector channels (50 eV), because the flow velocity associated with waves (5 to 50 km/s) represented a small perturbation on the particle velocities at higher energies.

Particle and Field Measurements of Standing ULF Waves

Oscillating plasma flows and associated ultra-low frequency magnetic oscillations were observed with the University of California at San Diego (UCSD) particle experiment and the UCLA magnetometer experiment. On June 27, 1974, a Pc 4 event occurred that had a peak magnetic amplitude of 10 gamma and a period of 150 seconds. The transverse magnetic wave was linearly polarized in the east-west (azimuthal) direction. During a large segment of the event, the three UCSD ion detectors along the east-west axis provided two linear (polar) views in the azimuthal direction and the third viewing perpendicular to this axis was in the radial direction. From the response of these three detectors, it was possible to construct the particle-distribution function in this plane and to determine its first moment, the flow velocity (v). In this plane, the flow velocity was also linearly polarized, primarily in the east-west direction, and had a peak amplitude of 140 km/s. By constructing the vector cross product of v with the static magnetic field, it was possible to infer the electric field, E_v. Having both the E and B components of the wave, Poynting's vector, S_k, was constructed to determine the propagation characteristics of the wave. Note that the flow component parallel to B was not necessary for this calculation. The magnetic and electric components of the wave were out of phase by 90 degrees, and the value of S_k oscillated around a value of zero. The relative phase of the wave components and the behavior of S_k were consistent with an interpretation of the event as the occurrence of the fundamental mode of a standing hydromagnetic wave on the ATS-6 field line; that is, there was no net flow energy.

Ring Current Proton ULF Waves

Seventy-one cases of ultra-low frequency oscillations of protonflux intensities were detected by the National Oceanic and Atmospheric Administration (NOAA) instruments from June 11 to September 16, 1974. The oscillation periods ranged from 40 seconds to 6 minutes that corresponded to Pc 4 and Pc 5 in magnetic pulsation terminology. Most of the waves were observed in the dusk region of the magnetosphere.

The low frequency Pc 4 wave typically had a maximum amplitude of approximately 10, primarily in the v-component. Spectral analysis showed that the signal was linearly polarized, radially inward in the meridian plane. Since the ambient field was tilted inward, the wave had a substantial compressional component as evident in the oscillations of the field magnitude. Examination of the v-component data suggested that the Pc 4 wave was modulating the amplitude of the Pc wave. We note, however, that the Pc 1 amplitude maxima occurred at minima of the total field; that is, during the rarefraction phase of each cycle. It seems likely, therefore, that the Pc 4 wave was not stimulating Pc 1 wave growth by compression of the proton pitch-angle distribution and ion-cyclotron instability. Instead, it was more likely that unstable plasma was being swept back and forth across the spacecraft by the electric field associated with the Pc 4 wave.

Energetic Electron Waves at Synchronous Orbit

Approximately 25 cases of well defined low frequency oscillations of electron fluxes were observed by the McDonnell-Douglas Astronautics Company (MDAC) electron spectrometer during

the first 3 months of observation. The experiment was capable of 0.25-s time resolution. However, the routine survey plots used in this preliminary data analysis contained 30-s averages, and thus oscillations having periods shorter than approximately 3 minutes could not be observed. The oscillations observed showed no local time preference. Two types of oscillations were observed: The first was characterized by phase differences between the various energy channels indicating energy-dependent dispersion of the electron waves; the second type of oscillation observed was characterized by complete phase correlation between all of the electron channels. There was no generalization that could be made between oscillation amplitudes and energy. There existed as many cases having a maximum oscillation at low energy (50 to 100 keV), as ones having a maximum at high energy (400 to 1000 keV). The UCLA magnetometer data, plotted in the VDH dipole coordinate system, were characterized by high frequency Pc 1 waves modulated by the longer period Pc 4 waves. The electron oscillations were 180 degrees out of phase with the magnetometer oscillations.

Large-Scale Trapping Boundary Waves

Large rapid decreases in the energetic proton flux followed by even more rapid increases were characteristic of disturbed periods on ATS-6. To unambiguously interpret such observations made on a moving spacecraft, it is necessary to be able to separate spatial from temporal variations. One approach to this problem is to use proton flux gradient information, since if a flux change is accompanied by a change in the gradient, the motion of a system over the spacecraft may be inferred. The energetic proton experiments on ATS-6 were uniquely suited to determine the proton flux gradient. The University of Minnesota experiment contained two nearly identical detector assemblies, which, when directed oppositely, could examine the flux of protons orbiting about gyrocenters displaced by up to two Larmor radii from one another. Thus, the spatial flux gradient along a line between the gyrocenters could be computed. The NOAA experiment contained three detector systems directed so that the gyrocenters of protons entering these detectors laid on a line orthogonal to the line through the gyrocenters of protons entering the Minnesota experiment. As the instruments responded to overlapping energy ranges, it was possible to determine the flux gradients at a given energy using data from these two experiments.

Modulation of Energetic Electrons in Association with the Sector Boundaries of the Interplanetary Magnetic Field

The Aerospace Corporation energetic particle spectrometer aboard ATS-6 observed a periodicity in the energetic electron fluxes ($E_e > 1$ MeV) associated with the passage of sector boundaries of the interplanetary magnetic field (IMF). The changes in the electron flux associated with each boundary passage were the major variability in the electron fluxes during conditions of low solar activity.

The ATS-6 electron fluxes (hourly averages) exhibited a very pronounced periodicity that was very clearly associated with the passage of interplanetary magnetic-field sector boundaries. A limited set of data from ATS-1 and ATS-5 was available for the same time period. Such comparisons indicated that ATS-1, ATS-5, and ATS-6 all observed the modulation described; that is, the modulation was one that affected the entire magnetosphere.

A similar study was conducted using ATS-1 data from the Aerospace Corporation spectrometer taken in 1967 and 1968, the period near solar maximum. In that study, it was not possible to establish that any close correlation existed between changes in the electron fluxes observed at synchronous altitude and changes in the direction of the interplanetary field.

Sector boundary passages did give rise to major excursions in the flux levels of energetic electrons; however, equally large excursions also occurred when there were no IMF boundaries in the vicinity of the Earth.

THE EXISTENCE OF DOMINANT FLUXES OF ENERGETIC HEAVY IONS

The National Oceanic and Atmospheric Administration heavy-ion instrument provided the first definitive measurements of energetic heavy ions present in the vicinity of the geostationary orbit. The detector system was a two-element, solid-state detector telescope that incorporated an extremely thin (3.8-micrometer) front element to accomplish ion nuclear charge (Z) identification by a dE/dx and E technique. In a single reasonably isolated injection event that occurred at approximately 0030 Universal Time (UT) on June 18, 1974, the presence of ions with $Z \geq 6$ and $E \geq 4.0$ MeV in the vicinity of the geostationary orbit was established. By noting that similar detectors, carried on board the Interplanetary Monitoring Platform (IMP) H and J satellites, were responding at background levels in the interplanetary medium for 4 days surrounding this event, it was concluded that these ions were energized by the magnetosphere during these substorm-type events.

TYPICAL PARTICLE SPECTRA

It is difficult to locate particle-energy spectra measured instantaneously in the magnetosphere that cover more than a limited energy range or that display more than one particle species in the literature. The EME particle instruments were capable of performing measurements on both the electron and ion differential intensities over an energy range from less than 1 electron volt (eV) to greater than 100 million electron volts.

SPACECRAFT CHARGING EFFECTS

Spacecraft in the vicinity of the geostationary orbit have been shown to charge to various potentials that depend on conditions in the local plasma environment of the satellite. A more detailed picture of the spacecraft charging effects emerged from the ATS-6 data than was available previously. A peak in the counting rate of the low-energy (4 to 10 eV) electron detectors of the UCSD experiment was shown to be due to photoelectrons and/or secondary electrons that were emitted by the spacecraft and were returning to it. This implied the presence of a potential barrier about the spacecraft; however, the barrier, which kept out low-energy plasma electrons as well, was too large to be explained in terms of a simple space-charge effect. It now appears that the satellite was differentially charged, with parts of the spacecraft, such as the solar arrays, at a more negative potential than the main spacecraft body.

The electric-field pattern that resulted was responsible for the potential barrier effect. ATS-6 had been observed to charge to a potential of -2200 volts during sunlit conditions and to a potential of -19,000 volts during eclipse periods.

SUMMARY

These initial results from ATS-6 demonstrated the existence of two new particle populations, even though after nearly two decades of magnetospheric exploration, many researchers feel that all the significant particle populations of the magnetosphere have been identified and their morphological features well documented.

The unexpected existence of a warm plasma in the vicinity of the plasmaspheric bulge and the existence of dominant fluxes of energetic ions heavier than protons produced during substorms must now be incorporated into currently held concepts of the magnetosphere.

The initial results of the EME instruments on ATS-6 have provided significant insight into the role of currents in the magnetosphere and the probable carriers of these currents, particularly in the case of field-aligned substorm-associated currents whose particle signature has been observed for the first time near the equatorial plane.

The large variety of wave and particle interactions observed on ATS-6 will prove invaluable in delineating many of the specific acceleration and transport mechanisms active on the hot plasma distribution in the region of the geosynchronous magnetosphere. The fact that such a large variety of interactions has been observed indicates that there are probably many mechanisms at work simultaneously in any one substorm or combination of substorm events.

The bibliography presented in this document mark the beginning of what appears to have been a very successful experiment program. As further studies are undertaken involving correlations between the various EME instruments themselves, with other satellites, and with ground-based programs, even more significant results should be forthcoming.

EME BIBLIOGRAPHY

1964 Mead, G. D., "Deformation of the Geomagnetic Field by the Solar Wind," *J. Geophys. Res.* **69**, 1964, pp. 1181-1194.

1969 Coleman, P. J., Jr., and R. L. McPherron, "Fluctuations in the Distant Geomagnetic Field During Substorms: ATS-1," in *Particles and Fields in the Magnetosphere*, B. M. McCormac, ed., Advanced Study Institute, Earth's Particles and Fields, University of California, Santa Barbara, 1969, pp. 171-194.

Cummings, W. D., et. al., "Standing Alfven Waves in the Magnetosphere," *J. Geophys Res.*, **74**(3), 1969, pp. 778-793.

1972 DeForest, S. E., "Spacecraft Charging at Synchronous Orbit," *J. Geophys. Res.*, **77**(4), 1972, pp. 651-659.

1973 McPherron, R. L., et. al., "Satellite Studies of Magnetospheric Substorms on August 15, 1968. Part 9. Phenomenological Model for Substorms," *J. Geophys. Res.*, 78(16), 1973, pp. 3131-3149.

1974 Coleman, P. J., Jr., et. al., "A System for Simultaneous Measurements of Magnetic Fields at the Earth's Surface and ... Space," Institute of Geophysics, University of California, Los Angeles, California 90025, November 1974.

Olson, W. P., and K. A. Pfitzer, "A Quantitative Model of the Magnetospheric Magnetic Field," *J. Geophys. Res.*, 79, 1974, pp. 3739-3748.

Pfitzer, K. A., "The Expected Quiet Time Magnetic Field at ATS-6," McDonnell-Douglas Corp. Space Sciences Dept., August 1974.

Russell, C. T., "The Solar Wind and Magnetospheric Dynamics," in *Correlated Interplanetary and Magnetospheric Observations*, D. E. Page, ed., D. Reidel Publishing Co., Dordrecht, Holland, 1974, pp. 3-47.

1975 Anderson, H. R., and R. R. Vondrak, "Observations of Birkeland Currents at Auroral Latitudes," *Rev. Geophys. and Space Phys.*, 13(1), 1975, pp. 243-262.

McIlwain, C. E., "Auroral Electron Beams Near the Magnetic Equator," in *Nobel Symposium 30th: Physics of the Hot Plasma of the Magnetosphere*, B. Hultqvist and L. Stenflo, eds., Plenum Press, N.Y., 1975, pp. 91-112.

McPherron, R. L., et. al., "ATS-6 UCLA Fluxgate Magnetometer," *IEEE Trans: Aerospace and Electronic Systems*, AES-11(6), 1975, pp. 1110-1117.

Sugiura, M., "Identification of the Polar Cap Boundary and the Auroral Belt in the High-Altitude Magnetosphere: A Model for Field-Aligned Currents," *J. Geophys. Res.*, 80(16), 1975, pp. 2057-2068.

Svalgaard, L., *An Atlas of Interplanetary Sector Structure 1957-1974*, Stanford University Institute for Plasma Research Report 629, June 1975.

Walker, R. J., et. al., "Substorm Associated Particle Boundary Motion in Synchronous Orbit," (Abstract). *EOS: Transactions of the American Geophysical Union*, 56(1), 1975, p. 422.

1976 Fritz, T. A., and B. Wilken, "Substorm Generated Fluxes of Heavy Ions at the Geostationary Orbit," in *Magnetospheric Particles and Fields*, B. M. McCormac, ed., D. Reidel Publishing Co., Dordrecht, Holland, 1976, pp. 171-179.

Su, S.-Y., et. al., "Repeated Sharp Flux Dropouts Observed at 6.6 R_E During a Geomagnetic Storm," *J. Geophys. Res.*, **81**, 1976, pp. 245-252.

Whipple, E. C., Jr., "Observation of Photoelectrons and Secondary Electrons Reflected from a Potential Barrier in the Vicinity of ATS-6," *J. Geophys. Res.*, **81**(4), 1976, pp. 715-720.

Whipple, E. C., Jr., "Theory of the Spherically Symmetric Photoelectron Sheath: A Thick Sheath Approximation and Comparison with the ATS-6 Observation of a Potential Barrier," *J. Geophys. Res.*, **81**(4), 1976, pp. 601-607.

1977 Fritz, T. A., et. al., "Significant Initial Results from the Environmental Measurements Experiment on ATS-6," *NASA Technical Paper*, **1101**, December 1977.

Su, S.-Y., et. al., "On the Propagation Direction of Ring-Current Proton ULF Waves Observed by ATS-6 at 6.6 R_E," *J. Geophys. Res.*, **82**, 1977, pp. 1859-1868.

1978 Spjeldvik, W. N., and T. A. Fritz, "Energetic Ionized Helium in the Quiet Time Radiation Belts: Theory and Comparison with Observations," *J. Geophys. Res.*, **83**, 1978, p. 654.

Spjeldvik, W. N., and T. A. Fritz, "Composition of Hot Plasmas in the Inner Magnetosphere: Observations and Theoretical Analysis of Protons, Helium Ions, and Oxygen Ions," *Space Research VIII*, M. J. Rycroft and A. C. Strickland, eds., Oxford, England, Pergamon Press, 1978, pp. 317-320.

Wilken, B., et. al., "Substorm-associated Injections of Energetic Ions Observed by GEOS-1 and ATS-6 In and Near Synchronous Altitude," *Advances in Magnetospheric Physics with GEOS-1 and ISEE*, K. Knott, A. Durney, and K. Ogilvie, ed., D. Reidel Publishing Co., Dordrecht, Holland, 1979, pp. 327-337. (Also published in *Space Science Review*, **22**, 1978, p. 647.)

1979 "ATS-6 Handbook," June 1979, University of California, San Diego, La Jolla, California, Department of Physics, Space Physics Group.

Paulikas, G. A., and J. B. Blake, "Final Report, Reduction and Analysis of ATS-6 Data (1 November 1978-30 June 1979)," Aerospace Report No. ATR-79 (7642)-3 prepared for NASA Goddard Space Flight Center, Space Sciences Laboratory, Laboratory Operations, The Aerospace Corporation, El Segundo, California, 90245, 1 June 1979.

Singer, H. J., et. al., "The Spatial Structure of PC3, 4, and 5 Pulsations Near the Magnetospheric Equator," *Geophys. Res. Lts.*, **6**, 1979, p. 889.

Su, S.-Y., et. al., "On the Energy-Dependent Modulation of the ULF Ion Flux Oscillations Observed at Small Pitch Angles," *J. Geophys. Res.*, **84**, 1979, p. 6510.

Wilken, B., et. al., "Multiple Satellite Observations of Large Scale Trapping Boundary Motion, In: *Proceedings of Magnetospheric Boundary Layers*," Conference, Alpbach, Austria 11-15 June 1979, *ESA SP-148*, **161**, 1979.

1980 Konradi, A., et. al., "Average Properties of Energetic Heavy Ions at the Geostationary Orbit," *J. Geophys. Res.*, **85**, 1980, p. 5149.

Su, S.-Y., et al., "Observations of ULF Oscillations in the Ion Fluxes at Small Pitch Angles with ATS-6," *J. Geophys. Res.*, **85**, 1980, p. 515.

CHAPTER 8

U.S./U.S.S.R. MAGNETOMETER EXPERIMENT

PURPOSE

The U.S./U.S.S.R. Magnetometer Experiment (Mage) was conducted when ATS-6 was located above 35°E longitude and was designed to measure geomagnetic activity to a high order of temporal accuracy, e.g., micropulsations, substorms, and storms, using a three dimensional array of magnetometers consisting of the University of California at Los Angeles (UCLA) magnetometer aboard ATS-6 and a network of ground-based magnetometers called data collection platforms (DCP).

The experiment was designed to handle up to five DCP's. As actually conducted, three DCP's were deployed by the U.S.S.R. near the 35°E longitude geographic meridian at Archangel, Minsk, and Odessa.

The Principal Investigator was Dr. P. J. Coleman, Jr., Institute of Geophysics and Planetary Physics, University of California, Los Angeles, California. The Russian team was headed by Dr. A. Zaitsev, Institute of Terrestrial Magnetism, Ionosphere and Radio Wave Propagation (IZMIRAN); U.S.S.R. Academy of Sciences; Moscow, U.S.S.R.

BACKGROUND

In the field of magnetospheric physics, the importance of simultaneous measurements from observatory networks on the Earth's surface and spacecraft in near-Earth space has been well established. It is difficult to obtain useful sets of such measurements because of the timing uncertainties, the multiplicity of recording techniques, and the differences in the measuring instruments. Perhaps the most serious of these difficulties is that many of the measurements are recorded on film or charts. Thus, considerable effort is required to transform the records into forms that are suitable for computerized methods of analysis and display.

The Mage enabled simultaneous recording of magnetic data gathered by the three DCP's and relayed by ATS-6, and the ATS-6 magnetometer. Subsequent computer processing introduced adjustments for radio time of flight and ATS-6 attitude, and merged the DCP and the ATS-6 Environmental Measurements Experiments (EME) data for use by UCLA, IZMIRAN, and other interested organizations.

OVERALL SYSTEM DESCRIPTION

Figure 8-1 shows the radio frequency links for Mage.

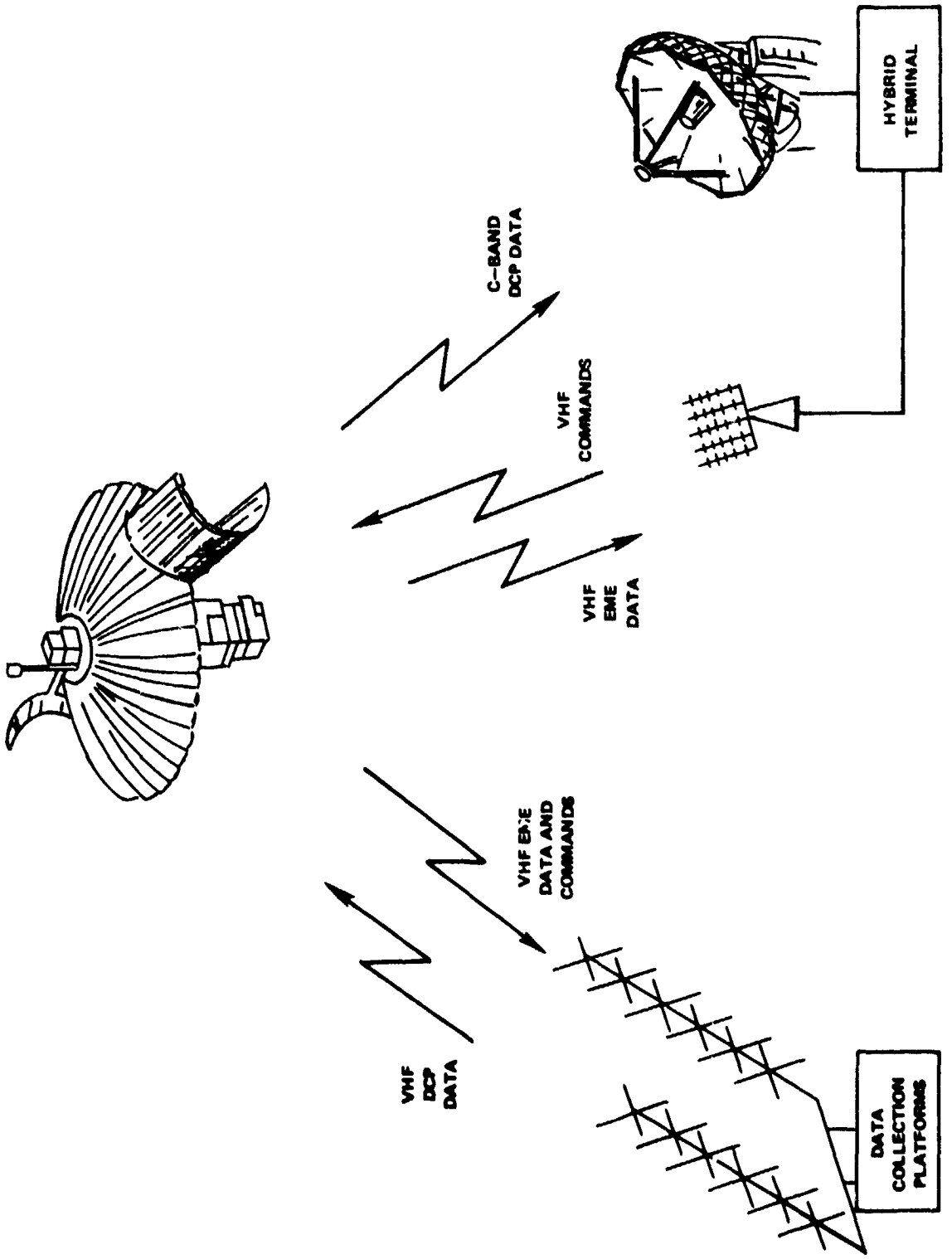

Figure 8-1. U.S./U.S.S.R. Mage Configuration

The very high frequency (vhf) downlink at 137.11 megahertz (MHz), containing the ATS-6 magnetometer data in the EME bit stream, served three purposes. It provided the ATS-6 magnetometer data for permanent recording at the Madrid Hybrid Terminal, it provided synchronizing and timing signals for the U.S.S.R. DCP's and it relayed the DCP on-off commands initiated by the hybrid station that were transmitted to the spacecraft over the normal EME command link at 154.20 MHz.

Each DCP transmitted its magnetometer and other data at 300 bits per second (bps) to the spacecraft using on-off keying (OOK) by vhf on its individual frequency assignment (Minsk, 150.687 MHz; Odessa, 150.719 MHz; and Archangel, 150.740 MHz). The spacecraft was operated in the vhf X C-band PLACE* (remodulation) mode, so the C-band downlink carrier was phase modulated by three subcarriers (687 kHz, 719 kHz and 740 kHz) each of which was keyed by the respective DCP bit stream.

At the hybrid terminal, the C-band downlink was received and demodulated to recover the data from the three DCP's which was recorded on magnetic tape. The DCP data was processed at Goddard Space Flight Center (GSFC), sent to UCLA for ATS-6 attitude processing, and then returned to GSFC where it was merged with the ATS-6 EME magnetometer data to produce the final tape that was distributed to UCLA and the U.S.S.R.

SYSTEM HARDWARE

Data Collection Platform

A data collection platform was located at each remote observatory in the system. Each DCP encoded the measurements of interest and telemetered the data to ATS-6. Figure 8-2 is a block diagram of the DCP. The DCP included separate fixed transmit and receive crossed-yagi vhf antennas of approximately 10 decibels gain pointed at the geostationary ATS-6 and a 200-watt transmitter (amplitude modulation). Circular polarization was employed to minimize the effect of Faraday rotation on signal strength.

When the hybrid station and the spacecraft were available to acquire data from DCP's, the "DCP transmitter on" command was sent from the control station to the spacecraft over the EME command link and relayed by the spacecraft to the DCP by the EME telemetry link. The EME data were telemetered from the spacecraft by pulse code modulation (pcm) at 1800 bps with the format as shown in Figure 8-3. The EME telemetry was decoded by a bit, word, and frame synchronizer in the DCP. The decoded signal was then used to synchronize the analog multiplexer and the analog-to-digital converter at one-sixth the incoming rate or 300 bps. Synchronization of the DCP digital system by the EME telemetry signal resulted in one-to-one correspondence between the digital information from each of the remote stations and that from the EME on board ATS-6. The synchronization was performed to simplify the formatting of the DCP data at the receiving and recording

*Position Location and Aircraft Communications Experiment

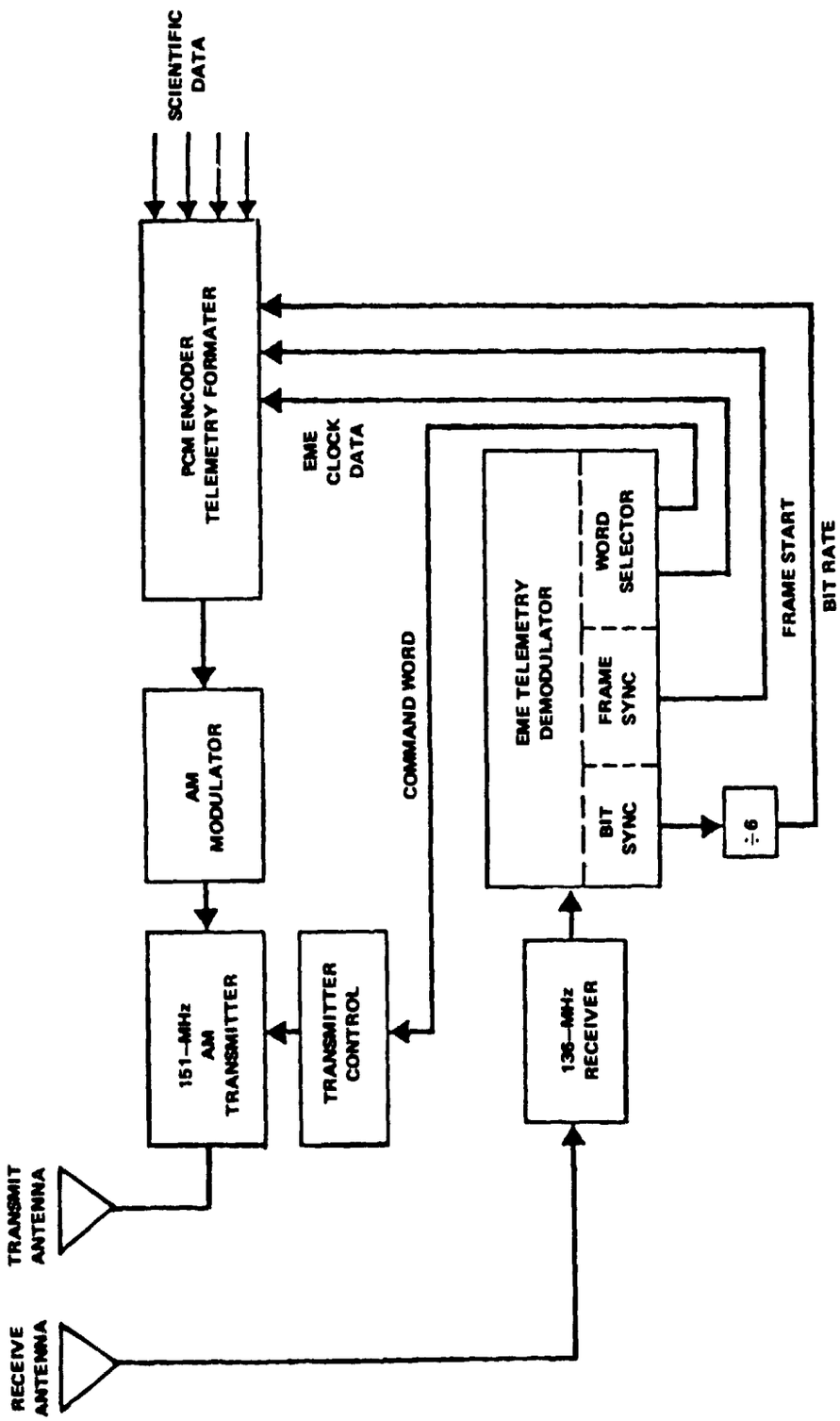

Figure 8-2. Data Collection Platform

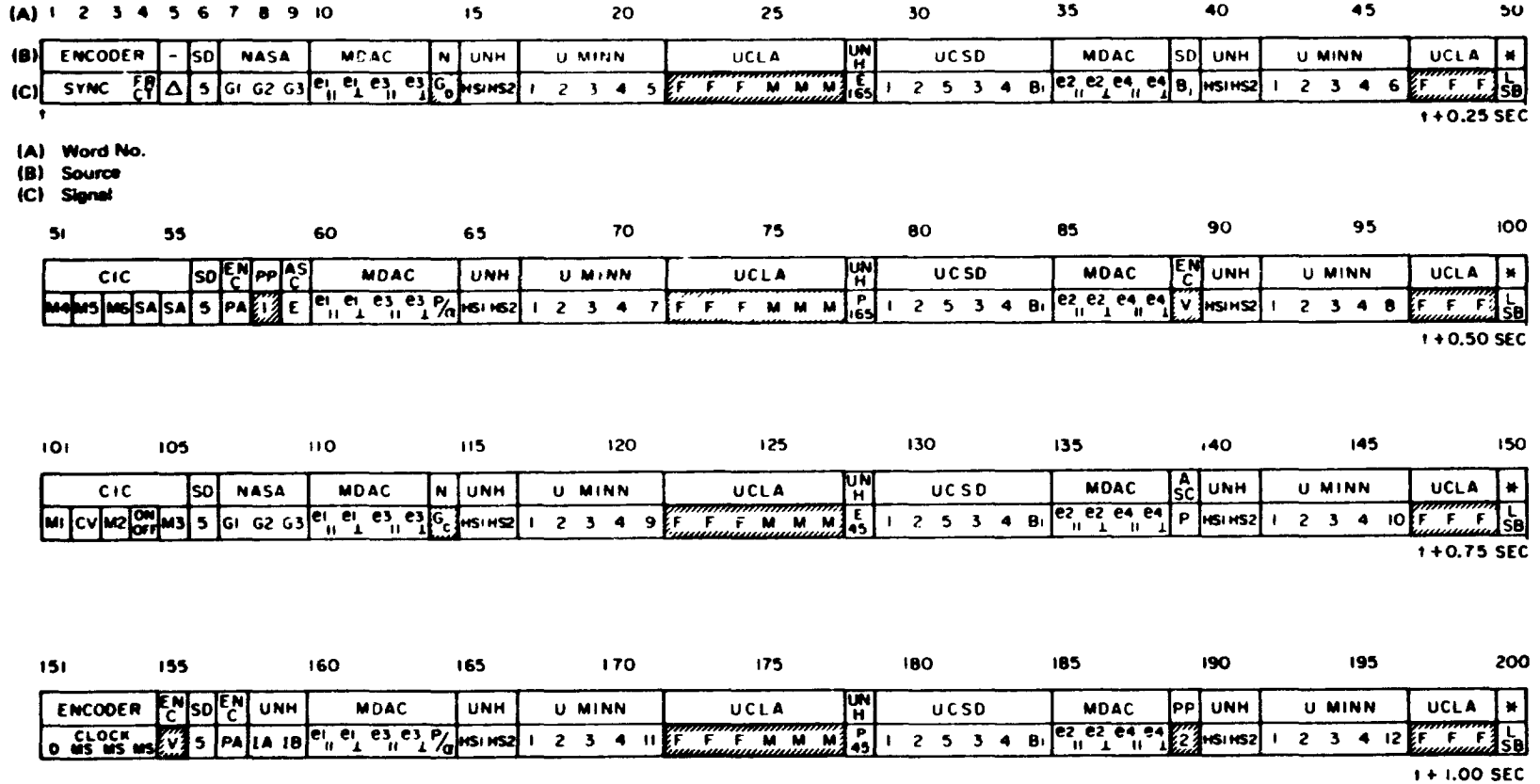

* SHARED BY MDAC & UCSD FOR READOUT OF LSB'S OF UCSD 1,2,3,4,5, AND MDAC $e_{1\parallel}$, $e_{1\perp}$, ACCUMULATORS (8 BITS AVAILABLE)

Δ 4 MSB MINN POSITION – 1B UNH BACKGROUND ID – 4 LSB SEQUENCE COUNTER

NOTE:

1 WORD LENGTH 9 BITS
2 BIT RATE 1800 BITS/SECOND
3 WORD TIME 5.0 MILLISECONDS
4 SHADED AREAS INDICATE ANALOG SIGNALS
5 PA PARITY BITS
6 CV COMMAND VERIFICATION
7 SA SUN ASPECT SENSOR
8 N NASA/GSFC
9 SD UCSD
10 V VOLTAGE MONITOR
11 M MODE IDENTS

Figure 8-3. ATS-6 Telemetry Format—EME Main Frame

stations. Later corrections for the differences in radio path links from each DCP to the spacecraft, enabled the data from all stations to be timed to an accuracy of a few milliseconds.

The analog multiplexer sampled X-, Y-, and Z-axis magnetic data and sent it to the analog-to-digital converter where it was converted to digital information. The digital data were then used to key a vhf transmitter on and off at 300 bps.

The transmitted DCP bit stream format is shown in Figure 8-4.

Presence of the "DCP transmitter on" command word (70552) enabled the transmitter; absence of the 70552 command word for a period of 5 minutes shut the transmitter off.

Spacecraft Configuration

ATS-6 was configured in the vhf X C-band PLACE (remodulation) mode using the Earth-coverage horn to transmit at C-band to the hybrid station. In the PLACE mode, the uplink vhf signals at 150.687 MHz (Minsk), 150.719 MHz (Odessa) and 150.740 MHz (Archangel) were downconverted to baseband to 687 kHz, 719 kHz, and 740 kHz, respectively. These signals phase-modulated the downlink C-band carrier. The spacecraft transponder bandwidth was selected for 12 MHz and the low-pass filter (approximately 2.5 MHz bandwidth) was employed prior to C-band modulation.

Madrid Hybrid Terminal

Figure 8-5 shows the hybrid terminal configured for the Mage.

The downlink C-band carrier bearing the three subcarriers, each corresponding to a DCP, was down-converted to 70 MHz and demodulated (phase modulation). The resulting signals at 687 kHz, 719 kHz and 740 kHz were then demodulated (amplitude modulation) recovering the Minsk, Odessa, and Archangel data respectively and recorded on a 10-track analog tape recorder.

The EME vhf telemetry data was recorded on a separate tape.

DATA REDUCTION

Figure 8-6 shows the Mage data flow.

The DCP telemetry and the EME telemetry were recorded at the hybrid station on separate tapes, DCPRAN and EMERAN, respectively, and mailed to GSFC for processing. At the Goddard Space Flight Center Information Processing Division (IPD), the data from the UCLA magnetometer aboard ATS-6 were extracted from the EMERAN tapes and transferred to other tapes, EMEMAG, that were mailed to UCLA along with separate tapes, ATSATT, containing data on the attitude and location of ATS-6. From these, UCLA produced digital tapes, REDMAG, containing accurately timed reduced magnetometer data, that were then shipped to IPD. Meanwhile, IPD, having digitized the data on the DCPRAN tapes and performed data quality editing to produce new tapes, DCPTLM,

ATS–6

MAGNETOMETER

DCP U.S.S.R. FORMAT

GID INPUT

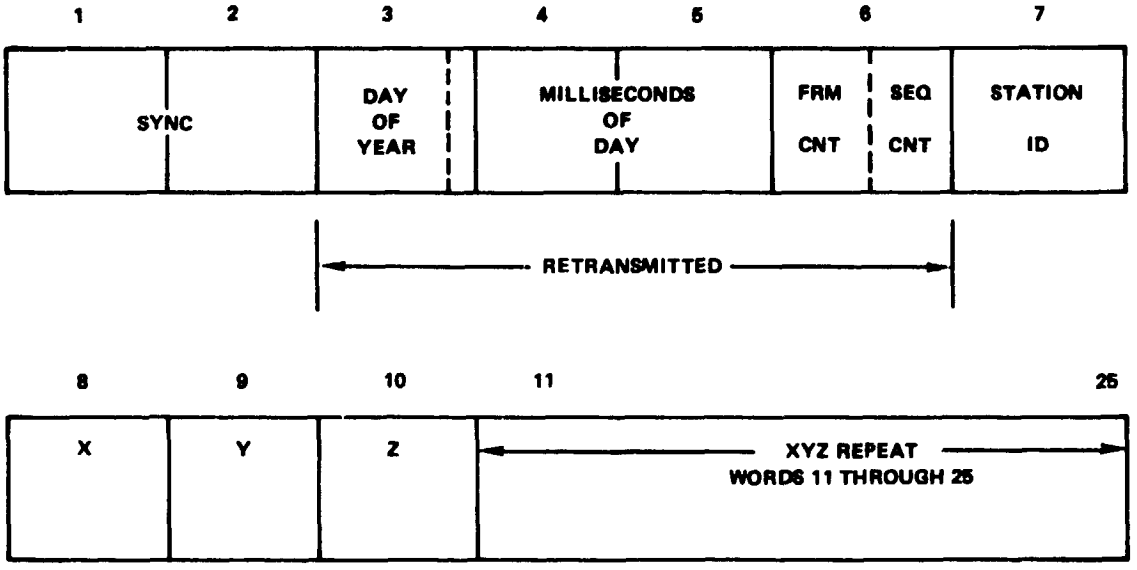

WORD 1, 2 SYNC = 76551460

3, 4, 5 CLOCK = EME WORDS 151, 152, 153, 154

6 SEQUENCE COUNT = EME WORD 5 BIT $2^3 \cdot 2^0$
BIT $2^3 \cdot 2^0$ OCTAL - 0 THROUGH 12

6 FRAME COUNT = EME WORD 4 BIT $2^5 \cdot 2^0$
BIT $2^{11} \cdot 2^6$ OCTAL - 0 THROUGH 63

7 STATION ID = USSR - DEFINED

Figure 8-4. DCP Data Format

merged the DCPTLM and REDMAG tapes to produce the DCPEME tapes which was the Mage output. Copies of the DCPEME tape were sent to UCLA and the U.S.S.R.

EXPERIMENT BACKGROUND

The initial UCLA concept paper of November 1974 detailed the requirements and envisioned the use of up to ten DCP's to be located in the Eastern Hemisphere. The basic concept as presented did not change, but some of the engineering details did.

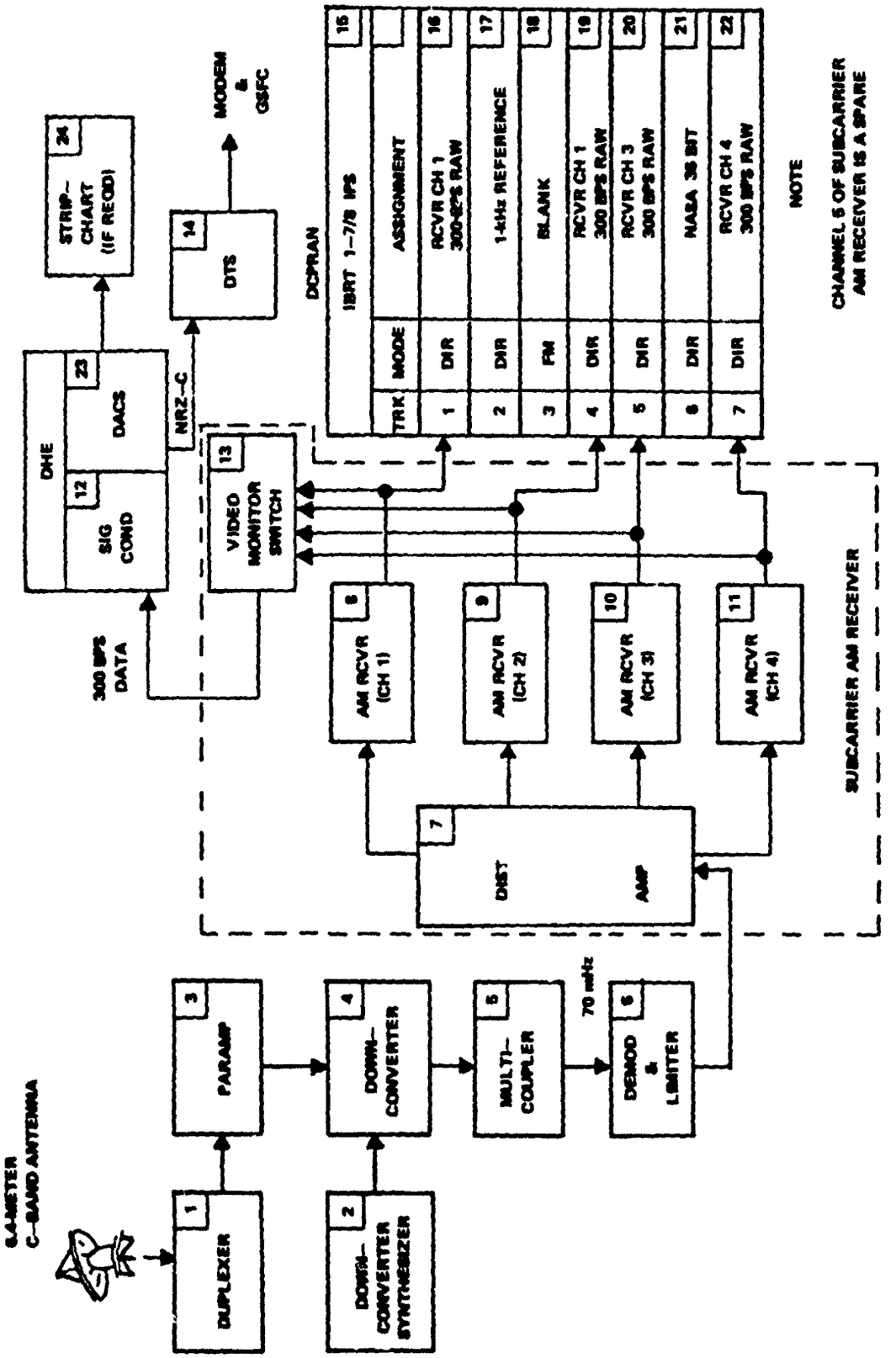

Figure 8-5. Hybrid Terminal Configured for the Mage

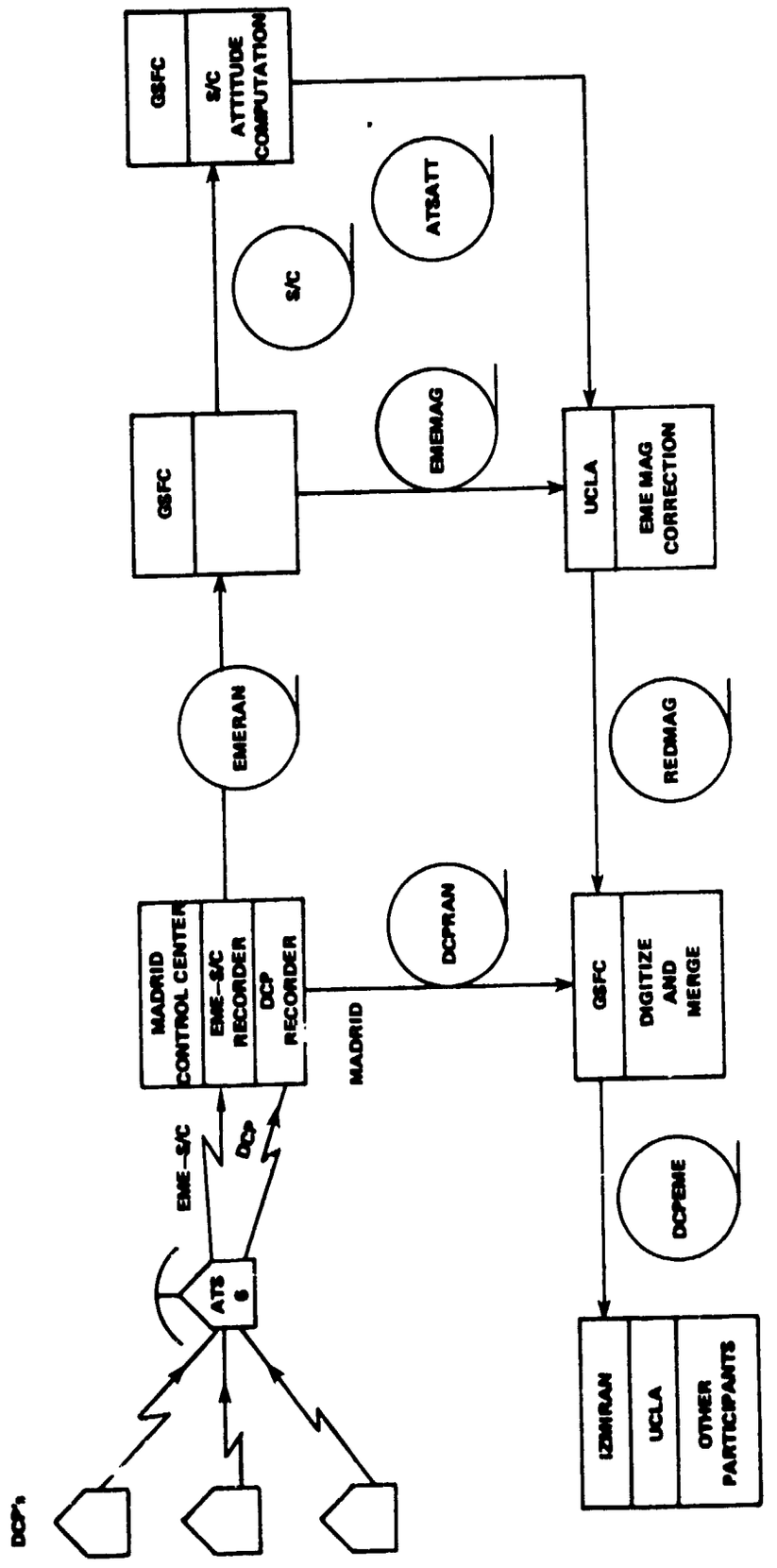

Figure 8-6. Mage Data Flow

During early and late 1975, the radio link decibel (dB) budgets were developed. These confirmed that the use of 10-dB antennas and 200-watt transmitters for the DCP's would be adequate. However, some considerable effort was expended before it was decided to use the ATS-6 remodulation (PLACE) rather than the frequency translation mode for the return data link and to arrive at an optimum configuration for the hybrid station receiver. The decisions were arrived at after considering relative costs and performance analyses, and after reviewing the results of intermodulation level measurements conducted through the spacecraft from Rosman Ground Station. By this time, budgetary considerations in implementing the hybrid station channel demodulators permitted the use of no more than five DCP's and a frequency plan was adopted that was designed to minimize intermodulation and crosstalk problems between the DCP channels.

Early in the planning stage it was thought that assigning DCP vhf transmit frequencies in a region 0.55 to 1.50 MHz higher than the spacecraft 150-MHz intermediate frequency would enable the use of inexpensive standard amplitude modulation (AM) broadcast radios in implementing the channel demodulators at the hybrid station. A number of factors conspired against this arrangement, however, and the channel demodulators were designed and fabricated at Goddard Space Flight Center.

While the above work was proceeding, the detailed effort in the data processing area was commenced at Goddard Space Flight Center (GSFC) with the initial effort being directed toward enabling data quality checks in time for the upcoming visit to GSFC by the U.S.S.R. scientists with their breadboard DCP. This visit took place during the latter part of April and the first half of May 1975.

The tests on the U.S.S.R. breadboard equipment followed an agreed upon test plan and consisted first of laboratory tests, and then tests with Rosman Ground Station through the spacecraft. A number of equipment deficiencies were encountered, mainly involving a vhf receiver incompatible with the EME bit stream modulation format and a serious transmitter-to-receiver radio frequency (rf) cross-talk problem. With the temporary substitution of GSFC items and components, the system demonstrated satisfactory data handling performance with bit-error rates on the order of 10^{-5}. The U.S.S.R. team headed back to the Soviet Union apparently with an adequate understanding of the problems involved and the methods of solution to be incorporated into their final DCP hardware.

During this period, some of the logistics were initially worked out, and shortly after the U.S.S.R. team departed, an in-orbit test plan was submitted to them to enable an orderly test and checkout procedure with the hybrid station using the final hardware deployed in the U.S.S.R.

Then followed a period from mid-May to mid-August 1975 (at which time the initial in-orbit operation commenced) during which the U.S.S.R. was fabricating their DCP's at IZMIRAN and GSFC was readying the data processing system and fabricating the channel demodulators to be shipped to the hybrid station.

The U.S.S.R. team, proceeding according to their plan, was fabricating and testing their DCP's at IZMIRAN prior to deploying them one at a time to the observatory sites. By early August, they reported that they were receiving the ATS-6 EME telemetry with their first unit (destined for

Minsk) with no errors. On request to GSFC, they conducted transmit tests (150.687 MHz) for the first time on August 14 to determine if there was sufficient isolation between their transmitter and receiver.

The first series of tests were completed on the first DCP at Minsk by the end of August 1975. On September 5, 1975, a number of tests were conducted using the Johannesburg (Joburg) command transmitter operating at 150.690 MHz. Among those were tests run at 30 watts used to simulate the effective isotropic radiated power expected from the DCP's. Measurements at the hybrid station indicated that the presence of the hybrid station command carrier at either 148.26 MHz or 154.20 MHz had no impact on performance even though the presence of 154.20 MHz reduced the measured carrier-to-noise ratio (C/N) somewhat. The signal-to-noise (S/N) ratio was 8 dB less than that observed in similar tests with Rosman Ground Station and the U.S.S.R. breadboard. At least 5 dB of the anomaly was explained on the basis of the ATS-6 "European" antenna pointing used during the Joburg tests.

On September 8, the EME Y-axis magnetometer failed. This, of course, impacted the gathering of scientific data, but tests continued with the DCP's.

The channel receiver components were installed at the hybrid station in the latter part of September 1975, in time for the tests on the second DCP (150.740 MHz) destined for Archangel. This enabled data quality checks. The 70552 EME command "DCP transmitter on" from the hybrid station was implemented during this series of tests. Noisy signals were encountered by the U.S.S.R. (found to be due to a broken cable) and they reported that they could not maintain synchronization with the EME telemetry. It was not until the last of October 1975, that tests were resumed from Archangel.

Tests from Odessa (150.719 MHz) commenced on November 17 and tests using all three DCP's began on November 19, 1975. Spurious 7.8-kHz sidebands were noted occasionally at the hybrid station; later these were found to be associated with the presence of the normal command 7.805-kHz logic 1 tone.

Data quality checks were made by IPD at Goddard Space Flight Center both in real time and from the tapes mailed from the hybrid terminal. These revealed DCP data formatting errors of various kinds that were not to be resolved until April 1976 by the U.S.S.R. team. Minsk went out because of an electrical storm just prior to December 2, 1975, and did not return to the air until mid-January 1976.

A test on December 3, 1975, with Minsk and Archangel, confirmed what had been found previously using the U.S.S.R. breadboard and Rosman Ground Station, that even though the presence of the Radio Beacon Experiment carriers reduced the S/N ratios somewhat, no apparent effect on data quality was seen.

It was a matter of some interest that during the tests of December 5, 1975, significant vhf signal enhancements were observed independently by the U.S. and U.S.S.R., the former at the hybrid terminal on the return link, and the latter on the EME telemetry link to the DCP's at Minsk and Archangel.

Tests resumed with a four-day series commencing on January 20, 1976, with all three DCP's exhibiting data formatting difficulties of various sorts and Archangel experiencing modulation depth problems. The formatting errors prompted a two-way TWX interchange between GSFC and the U.S.S.R. team on January 27, 1976, in which GSFC described the formatting errors. Tests during the first week in February exhibited much the same difficulties as the previous series.

Tests with all three DCP's were resumed on March 14, 1976, with much improved data formatting and excellent frame sync lock on Minsk and Odessa. By March 19, the Minsk and Archangel data formatters were operating properly, but Odessa was not straightened out until over a month later.

Routine data gathering commenced during the first part of April 1976. Frame sync lock was generally reported to be 95 percent or better. Measured bit-error rate ranged from slightly less than 10^{-2} to about 10^{-3}. Two factors contributed to the higher than expected error rate. First, the signal-to-noise ratios were significantly lower than anticipated (thought to be, but by no means conclusively, due to suppression of the desired signals by terrestrial vhf sources entering the spacecraft on the uplink). Secondly, fading was encountered at vhf on these mid- and high-latitude paths. As it turned out, adequate scientific data required that valid data points occur only every few seconds, so that overall the data-gathering performance of the system was more than satisfactory despite the comparatively high error rate.

During the subsequent months, data processing was completed and the tapes were delivered to the U.S.S.R. It was not until one-and-a-half to two years later, that the U.S.S.R. sent a team (not the original) to UCLA for a series of conferences concerning the tapes. It appeared that the U.S.S.R. team was having difficulty reading the tapes. Nothing has been heard from that group since, and no U.S.S.R. published results are known.

CONCLUSIONS

In most respects, the Mage was a tremendous success. It demonstrated for the first time the actuality of simultaneously recording data from spacially separated magnetometers in real time to an accuracy of a few milliseconds. The data processing employed by the Mage eliminated the tedious task of reducing data from charts, films, etc., with its inherent inaccuracies. The liaison among all parties involved in the experiment was outstanding and probably was as good as that experienced during the Apollo-Soyuz program regarding the interchange between the U.S. and U.S.S.R. teams.

The percent data coverage was high. It was somewhat disappointing that the U.S.S.R. magnetometers could measure only to a sensitivity of 1 gamma (γ) whereas the UCLA ATS-6 magnetometer was capable of 1/16 γ. Wavelike disturbances in the Earth's magnetic field typically experience perturbations of greater than 1 γ for those having a period on the order of 500 s. Disturbances having periods on the order of 10 s typically have amplitudes that are small fractions of a γ and so presumably could not be recorded by the U.S.S.R. magnetometers.

It can only be speculated that the U.S.S.R. attached some importance to the experiment as evidenced by their visit to UCLA well after the completion of the experiment to resolve their difficulties

in reading the data tapes. It is a matter of further speculation as to whether they will publish the results of the findings in the literature.

APPENDIX

ACRONYMS AND ABBREVIATIONS

A

A	ampere
Å	Angstrom
ABC	analog backup controller
AC	attitude control
a.c.	alternating current
ACE	actuator control electronics
ACP	acquisition control program
acq.	acquisition
ACS	attitude control subsystem
ACSN	Appalachian Community Service Network
A/D	analog to digital
ADC	analog-to-digital converter
ADPE	automatic data processing equipment
ADS	automatic deployment sequencer
ADSS	auxiliary digital Sun sensor
ADVM	adaptive delta voice modulation
A/E	absorbtivity t emissivity
Aerosat	aeronautical satellite
AES	Ahmedabad Earth Station
AESP	Appalachian Education Satellite Project
af	audio frequency
AFC	automatic frequency control
AFTE	Advanced Thermal Control Flight Experiment
AGC	automatic gain control
AGE	aerospace ground equipment
Ah	ampere-hour
AID	Agency for International Development
AIDSAT	Agency for International Development Television Demonstration
AIR	All India Radio
ALC	automatic level control
ALED	Alaska Education Experiment
am, AM	amplitude-modulation
AMP	amplifier
AOS	acquisition of satellite
APM	antenna pattern measurement

APT	automatic picture transmission
ARC	Appalachian Regional Commission
ASC	Aerospace Corporation
ASP	automated sequential processor
ASSY	assembly
ASTP	Apollo-Soyuz Test Program
ASTP-TV	ASTP television coverage experiment
ATA	automatic threshold adjust
AT&T	American Telephone and Telegraph (Spacecraft)
ATC	air traffic control, active thermal control
ATFE	Advanced Thermal Control Flight Experiment
atm, ATMOS	atmosphere(s)
ATS	Applications Technology Satellite
ATS-6	Applications Technology Satellite-6
ATSOCC	ATS Operations Control Center
ATS-R	ATS ranging
ATSSIM	ATS simulator
Atten	attenuator (attenuation)
Aux	auxiliary

B

B&E	Broadcast and Engineering
BAM	building attenuation measurement
BB	baseband
BER	bit error rate
bps	bits per second
BRC	Balcones Research Center
BSA	bit synchronization acquisition
BTC	binary time code
BTE	bench test equipment
Btu	British thermal unit
BW	bandwidth

C

C	Celsius
Cap Com	Capsule Communicator
CCIR	International Radio Consultative Committee
CDD	command/decoder distributor
CEE	designator for "career education course for elementary-grade teachers"
CES	designator for "career education course for secondary-grade teachers"
CESP	computer executive system program
CFSS	coarse/fine Sun sensors

CIC	command interface control
CIE	cesium ion engine
C/L	capacitance-to-inductance
cm	centimeter
CM	communications module
C/M	carrier-to-multipath
CMD	command
CMOS	complimentary metal oxide semiconductor
C/N_o	carrier power to spectral noise density ratio
CNR, C/N	carrier-to-noise ratio
cntr	center
Comsat	Communications Satellite Corporation
ConUS, CONUS	Continental United States
CONV	converter
COSMOS	complimentary symmetry metal oxide semiconductor
CPI	cross polarization isolation
CPR	cross polarization ratio
CPU	central processing unit
CRT	cathode-ray tube
CSM	command-service module
CSP	command service program
CSS	coarse Sun sensor
CTNE	Companie Telephonica Nacional de Espana
CW	carrier wave, continuous wave

D

DA	design adequacy
D/A	digital to analog
DACU	data acquisition and control unit
DAF	Data Acquisition Facility
dB	decibel
dBi	decibel isotropic (gain relative to an isotropic antenna)
dB/K	decibel per degree Kelvin
dBm	decibels referred to 1 milliwatt
dBW	decibel (reference level 1 watt)
DC	downconverter
d.c.	direct current
DCP	data collection platforms
DDDF	duplex digital data formatter
DDS	digital Sun sensor
DECPSK	differentially encoded coherent phase shift key (modulated)
DEG, deg	degree

DEM	digital evaluation mode
Depl	deployment
DES	Delhi Earth Station
DESA	double electrostatic analyzer
DIB	data input buffer
div	division
DIX	data interface transmitter
DJS	Dzhusaly (designator)
DLO	dual local oscillator
DM	docking module
DOC	digital operational controller
DOD	depth-of-discharge
DOT	Department of Transportation
DOT/FAA	The Department of Transportation/Federal Avaiation Administration
DOT/TSC	The Department of Transportation/Transportation Systems Center
DPRI	diagnostic and prescriptive reading instruction
DR	Copenhagen (designator)
DRR	data recorder/reproducer
DRS	direct reception system
DSS	digital Sun sensor
DSU	data switching unit
DTS	data transmission system
DUT	Denver Uplink Terminal

E

EBU	European Broadcast Union
ECH	Earth-coverage horn
ECI	Earth centered inertial
e.d.t., EDT	eastern daylight time
e.i.r.p.	effective isotropic radiated power
EME	Environmental Measurements Experiments
emi, EMI	electromagnetic interference
EML	equivalent monomolecular layer
enc	encoder
Eng.	engineering
EOL	end-of-life
EPIRB	Emergency Position Indicating Radio Beacon
EPS	electrical power subsystem
ERP	effective radiated power
ES	Earth sensor
ESA	Earth sensor assembly, European Space Agency
ESA/PSA	Earth sensor assembly/Polaris sensor assembly
e.s.t., EST	eastern standard time

ETR	Eastern Test Range
eV	electronvolt
EVM	Earth-viewing module
EVT	Eupatoria (designator)

F

f	frequency
F	Fahrenheit
FAA	Federal Aviation Administration
FCC	Federal Communications Commission
FCHP	feedback-controlled variable conductance heat pipe
FCP	flight computer program
FCT	fixed calibration terminal
f/d	ratio of focal distance to diameter
FDM	frequency diversity modulation; frequency division multiplexer
fm, FM	frequency modulated
FOV	field-of-view
FOWG	Flight Operations Working Group
Freq.	frequency
FRMS	Federation of Rocky Mountain States
fsk	frequency shift keying
FSS	fine Sun sensor
ft	foot, feet
FT	frequency translation
ft-lb	foot-pound
FTO	functional test objective
FTS	Federal Telecommunications System

G

g	grams, gravity
G	gain
GAC	ground attitude control
GEOS-3	Geodetic Earth-Orbiting Satellite-3
GFRP	graphite fiber reinforced plastic
GHz	gigahertz
gm	gram
G.m.t., GMT	Greenwich mean time
GRD	ground
GRP	group
GSFC	Goddard Space Flight Center
G/T	dB/K, gain over temperature
GTT	ground transmit terminal
GVHRR	Geosynchronous Very High Resolution Radiometer

H

HAC	Hughes Aircraft Company
HDRSS	high data rate storage system
HET	Health, Education, Telecommunications (experiment)
HEW	Department of Health, Education, and Welfare
hf	high frequency
HGA	high gain antenna
HI	Honeywell International
HPBW	half power bandwidth
HR	hour
HSE	high-speed execute
HTR	heater; high-time resolution
Hz	hertz

I

IBM	International Business Machines
IDT	image dissector tube
IEB	interface electronics box
i.f.	intermediate frequency
IFC	in-flight calibration
IHS	Indian Health Service (Alaska)
IHSDL	interferometer high speed data link
IM	intermodulation
IMF	interplanetary magnetic field
IMP	Interplanetary Monitoring Platform
in.	inch
in.-oz	inch-ounce
Intelsat	International Telecommunications Satellite
INTF	interferometer
I/O	input/output
IPD	Information Processing Division
IR	infrared
IRAC	Interdepartment Radio Advisory Committee
ISRO	Indian Space Research Organization
IT	intensive terminal
ITS	Institute of Telecommunications Sciences
ITU	International Telecommunications Union
I-V	current voltage
IW	inertia wheel
IZMIRAN	Institute of Terrestrial Magnetism, Ionosphere and Radio Wave Propagation

J

JAM	jet-assist mode
Joburg	Johannesburg (designator)
JSC	Johnson Space Center

K

K	Kelvin
kbps	kilobits per second
keV	kiloelectronvolt
kg	kilogram
kHz	kilohertz
km	kilometer
KSC	Kennedy Space Center
kW	kilowatt

L

lb	pound
LC	inductive-capacitance
LD	linear detector
LFT	long form test
LIC	load interface circuit
LLD	lower level discriminator
LO	local oscillator
LOS	line-of-sight
LRIR	limb radiance inversion radiometer
LSB	least significant bit
LT	local time
LV	local vertical
L.V.	latch valve

M

m	meter
m^2	square meter
mA	milliamperes
Mad	Madrid
MAD-HYB	Madrid Hybrid
Mage	U.S./U.S.S.R. Magnetometer Experiment
Marad	Maritime Administration
MASEP	main sequential program
Max.	maximum

MCC-H	Mission Control Center, Houston
MCC-M	Mission Control Center, Moscow
MDAC	McDonnell-Douglas Aircraft Corporation
MDHS	meteorological data handling system
MESC	magnetoelectrostatic plasma
MeV	megaelectronvolts
MHz	megahertz
μf	microfarad
μm	micrometer (micron)
μs, μsec	microsecond
MILA	Merritt Island Launch Annex
min, MIN	minute
mlb	millipound
MMW	Millimeter Wave Experiment
mN	millinewton
MOCC	Multisatellite Operations Control Center
MOCR	Mission Operations Control Room
MONO	monopulse
MOR	Mission Operations Room
MOS	metal oxide semiconductor
MSB	most significant bit
ms, msec	millisecond
m/s	meters per second
MT	multitone
mV	millivolts
mW	milliwatt
MWE	Millimeter Wave Experiment
MW XMTR	microwave transmitter

N

N	Newton
NAFEC	National Aviation Facilities Experiment Center
NASA	National Aeronautics and Space Administration
Nascom	NASA Communications Network
NBFM	narrowband frequency modulation
NCC	Network Coordination Center
NCE	normal command encoder
NDR	Hamburg (designator)
nm	nanometer
NMRC	National Maritime Research Center
NOAA	National Oceanic and Atmospheric Administration
N/P	negative/positive
NRL	Naval Research Laboratories

ns	nanosecond
NTSC	National Television System Committee color (U.S.)

O

O&M	operations and maintenance
OC	orbit control
OCJ	orbit control jet
OCP	operational control program
o.d.	outside diameter
OD	Operations and Distribution (Center)
omni	omnidirectional
OSR	optical solar reflectors
OSU	Ohio State University
OYA	Helsinki (designator)

P

PA	power amplifier, preamplifier
PAL	phase alternation live color (Europe)
PAM	pulse amplitude modulated
PAO	Public Affairs Office
PARAMP	parametric amplifier
PB	phonetically balanced
PBS	Public Broadcasting Service
P_c	course phase measurement
pcm, PCM	pulse code modulation
pcm/fsk/am	pulse code modulation/frequency shift keying/amplitude modulation
PCT	portable calibration terminal
PCU	power control unit
PDM	pulse duration modulation
pf	picofarad
PFD	power flux density
PFF	prime-focus feed
PGE	PLACE ground equipment
PIC	power interface circuit
PLACE	Position Location and Aircraft Communications Experiment
PLU	Project Look-Up
PM	phase-modulated
PN	pseudo-noise
POCC	Project Operations Control Center
p-p	peak-to-peak
PPK	Petropavlovsk-Kamchatski (designator)
ppm	parts per million

P_R	reference (phase) signal
P_{rgi}	power received at ground into an isotropic antenna
P_{rsi}	power received at spacecraft into an isotropic antenna
PRU	power regulation unit
PSA	Polaris sensor assembly
P_{SF}	probability function
psia	pounds per square inch absolute
PSK	phase shift keyed
Pv	vernier phase measurement
pW	picowatt
PWR	power

Q

QCM	Quartz-crystal microbalance contamination monitor
Q-M	quadrature phase modulation

R

Radsta	U.S. Coast Guard Radio Station
R&RR	range and range rate
RBE	Radio Beacon Expriment
RCA	Radio Corporation of America
RCC	Resource Coordinating Center
RCV	receive
RDA	rotating detector assembly
REC	receive
Ref., REF	reference
Rel	release
RESA	Regional Education Service Agency
rf	radio frequency
RFC	radio-frequency compatibility
rfi	radio frequency interference
RFIME	Radio Fequency Interference Measurement Experiment
RGA	rate-gyro assembly
RME	Rocky Mountain East
RMPBN	Rocky Mountain Public Broadcast Network
rms	root mean square
RMW	Rocky Mountain West
ROT	receive-only terminal
rpm	revolutions per minute
RR	rain rate

S

S/A	solar array
SAPPSAC	Spacecraft Attitude Precision Pointing and Slewing Adaptive Control (Experiment)
SAR	search and rescue
S&R	surveillance and ranging
Satcom	Satellite Communications
SC	sudden commencement
S/C	spacecraft
SCAMA	switching, conferencing, and monitoring arrangement
SCAMP	small command antenna medium power
SE	system effectiveness
sec, s	second
SECAM	Sequential Couleurs a Memoire (III) color (U.S.S.R.)
SEL	Space Environment Laboratory
SENS	sensor
S.G.	signal generator
SITE	Satellite Instructional Television Experiment
SITEC	sudden increase in total electron content
SIU	squib interface unit
S-IVB	Saturn IB second stage
SMSD	spin motor sync detector
SNR, S/N	signal-to-noise ratio
Spec	specification
SPS	spacecraft propulsion subsystem
SPU	signal processing unit
sr	steradian
SR	Stockholm (designator)
SRT	SAPPSAC remote terminal
SSC	sudden storm commencement
SSEA	Sun sensor electronics assembly
SSR	Staff Support Room
STA	station
STADAN	Space Tracking and Data Acquisition Network
STDN	Spaceflight Tracking and Data Network
STRUCT	structural
SWBT	Southwestern Bell Telephone Company
SYN	synthesizer
SYNC	synchronous
SYSSIM	system simulator

T

T&C	telemetry and command
TACH	tachometer
T&CS	telemetry and command subsystem
T&DRE	Tracking and Data Relay Experiment
TART	transmit and receive terminal
TASO	Television Allocation Study Organization
TBC	time base corrector
TCD	transponder command decoder
TCS	telemetry and command subsystem, thermal control subsystem
TDA	tunnel diode amplifier
TDRE	Tracking and Data Relay Experiment
TEMP	temperature
THIR	temperature-humidity infrared radiometer
TID	traveling ionospheric disturbances
TLM, TM	telemetry
TORQ	torquer
TRUST	Television Relay Using Small Terminals
TSM	thermal structural model
TSP	telemetry service program
TSU	temperature (control) and signal (conditioning) unit
TT/N	test-tone signal-to-noise ratio
TTY	teletype
TV	television
TVOC	Television Operational Control Centers
TWT	traveling wave tube
TWTA	traveling wave tube amplifier

U

UC	upconverter
UCLA	University of California at Los Angeles
UCSD	University of California at San Diego
uhf	ultrahigh frequency
UK	United Kingdom
UKTV	University of Kentucky Television
ulf	ultralow frequency
UNH	University of New Hampshire
U.S.	United States
USA	ubiquitous spectrum analyzer
USAF	United States Air Force
USCG	United States Coast Guard
USK	Ussuriisk (designator)

U.S.S.R.	Union of Soviet Socialist Republics
UT	universal time
UV	ultraviolet

V

v	velocity
V	volt
VA	Veterans Administration
VCA	voltage controlled amplifier
VCHP	passive "cold-reservoir" variable conductance heat pipe
VCXO	voltage controlled crystal oscillator
Vdc	volts direct current
V/deg	volts per degree
Vert.	vertical
vhf, VHF	very high frequency
VHRR	very high resolution radiometer
VIP	versatile information processor
VIRS	vertical interval reference signal
VITS	vertical interval test signals
VPI	Virginia Polytechnic Institute
vs.	versus
VSWR	voltage standing-wave ratio
V/T	voltage/temperature
VTR	video-tape recorder
VU MTR	VU meter

W

W	watt
WAMI	Washington, Alaska, Montana, Idaho (medical education)
WBDU	Wideband Data Unit
WBVCO	wideband voltage-controlled oscillator
WHL, WH	wheel

X

XMIT	transmit
XMTR	transmitter
XTAL	crystal
XTAL DET.	crystal detector

Y

YIRU	yaw inertial reference unit

Z

ZAZ	Z-axis azimuth
Zcoel	Z-coelevation

BIBLIOGRAPHY

Environmental Measurements in Space

"ATS-6 Solar Cosmic Ray and Trapped Particle Experiment," Final Report, Contract No. NAS 5-22913, TRW, Defense and Space Systems Group, One Space Park, Redondo Beach, California 90278.

Erickson, K. N., et al., "A Study of Magnetosphere Dynamics During Auroral Electrojet Events by Observations of Energetic Electron Intensity Changes at Synchronous Orbit," *J. Geophys. Res.*, **84**, p. 931, 1979.

Kaye, S. M., et al., "Adiabatic Modulation of Equatorial Pitch Angle Anisotropy," *J. Geophys. Res.*, **83**, p. 2675, 1978.

Sauvaud, J. -A., and J. R. Winckler, "Dynamics of Plasma, Energetic Particles, and Fields near Synchronous Orbit in the Night Time Sector During Magnetospheric Substorms," *J. Geophys. Res.*, In Press, 1980.

Walker, R. J., et al., "Studies of the Trapped Radiation at Synchronous Orbit with the University of Minnesota ATS-6 Electron-Proton Spectrometer," *IEEE Trans. Aerosp. Electron. Syst.*, AES-11(6), p. 1131, 1975.

Walker, R. J., et al, "Substorm-Associated Particle Boundary Motion at Synchronous Orbit," *J. Geophys. Res.*, **81**, p. 5541, 1976.

Walker, R. J., et al., "Pitch Angle Dispersion of Drifting Energetic Protons at Synchronous Orbit," *J. Geophys. Res.*, **83**, p. 1595. 1978.

Magnetometer

ATS-6 Magnetometer Data Reduction System Design Document, CSC/SC-75/6055 Computer Sciences Corporation, June 1975.

Barry, J. D., and R. C. Snare, "A Fluxgate Magnetometer for the Applications Technology Satellite," *IEEE Trans. Nuclear Science*, Vol. NS-13, 1966.

Gore, W., "Analysis and Design of a Fluxgate Magnetometer," M.S. Thesis, Institute of Geophysics and Planetary Physics, U.C.L.A., Pub. 78-1445, 1974.

BIBLIOGRAPHY (continued)

Power, J. J., "A Digital Offset Fluxgate Magnetometer for Use in Remote Geomagnetic Observatories," M.S. Thesis, Institute of Geophysics and Planetary Physics, U.C.L.A., Pub. 1247-37, 1973.

Snare, R. C., and C. R. Benjamin, "A Magnetic Field Instrument for the OGO-E Spacecraft," *IEEE Trans. Nuclear Science*, Vol. NS-13, No. 6, p. 333, 1966.

Snare, R. C., and G. N. Spellman, "Digital Offset Field Generator for Spacecraft Magnetometers," Proc. Symp. on Space Mag. Explor. and Tech., Reno, Nevada, August 30, 1967.

Radio Beacon

Bouwer, S. D., et al., "ATS-6 Radio Beacon Electron Content Measurements at Ootacamund, India, October 1975-July 1976," NOAA Report UAG-74.

Davies, K., et al., "Electron Content Measurements Over the U.S.," Joint Radio Beacon Program, NOAA/MPAE/Graz, Station Report, ATS-6 94°W, Max-Planck-Institut fur Aeronomie, Postfach 20, D-3411 Katlenburg-Lindau 3, Germany, 1977.

Davies, K., G. K. Hartmann, and R. Leitinger, "A Comparison of Several Methods of Estimating the Columnar Electron Content of the Plasmasphere," *J. Atmos. Terr. Phys.*, **39**, pp. 571-580, 1977.

Davies, K., and J. D. Whitehead, "A Radio Lens in the Ionosphere," *J. Atmos. Terr. Phys.*, **39**, pp. 383-387, 1977.

Davies, K., et al., "ATS-6 Satellite Radio Beacon Measurements at Ootacamund, India," *Radio Sci.*, **14**, (1), pp. 85-95, 1979.

Davies, K., et al., "Nighttime Increases in Total Electron Content Observed With the ATS-6 Radio Beacon," *J. Geophys. Res.*, **84**, (A4), pp. 1536-1542, 1979.

Davies, K., "Overview of Published Research Using the ATS-6 Radio Beacon," *Beacon Satellite Measurements of Plasmaspheric and Ionospheric Properties*, Editor P. F. Cheacci, Research Institute for Electromagnetic Waves, Florence, Italy, pp. 1-1 through 1-49, 1979

Davies, K., et al., "ATS-6 Satellite Radio Beacon Measurements at Ootacamund, India," *Beacon Satellite Measurements of Plasmaspheric and Ionospheric Properties*, Italy, pp. 2-1 through 2-33, 1979.

Davies, K., et al., "Nighttime Increases in Total Electron Content Observed With the ATS-6 Radio Beacon," *Beacon Satellite Measurements of Plasmaspheric and Ionospheric Properties*, Italy, pp. 4-1 through 4-16, 1979.

BIBLIOGRAPHY (continued)

Davies, K., et al., "Some Measurements of Total Electron Content Made With the ATS-6 Radio Beacon," *Beacon Satellite Measurements of Plasmaspheric and Ionospheric Properties*, Italy, pp. 14-1 through 14-7, 1979.

Davies, K., et al., "Comparison of Total Electron Content Measurements Made With the ATS-6 Radio Beacon Over U.S. and Europe," *J. Atmos. Terr. Phys.*, **42**, pp. 411-416, 1980.

Davies, K., and M. P. Paul, "ATS-6 Boulder Measurements of Plasmaspheric and Total Electron Content During Phase III," *Proceedings of COSPAR Satellite Beacon Group*, Warsaw, 1980.

Davies, K., "Recent Progress in Satellite Radio Beacon Studies With Particular Emphasis on the ATS-6 Radio Beacon Experiment," *Space Sci. Rev.*, **5**, pp. 357-430, 1981.

Degenhardt, W., et al., "Determination of Travelling Ionospheric Disturbances," *J. Atmos. Terr. Phys.*, **40**, pp. 1229-1234, 1978.

Degenhardt, W., et al., "Determination of Travelling Ionospheric Disturbances," *Beacon Satellite Measurements of Plasmaspheric and Ionospheric Properties*, Italy, pp. 27-1 through 27-7, 1979.

Deshpande, M. R., et al., "Frequency Dependence of Equatorial Ionospheric Scintillations, *Proc Indian Acad. Sci.*, **87A**, (7), pp. 173-178, 1978.

Deshpande, M. R., et al., "Achievements of ATS-6 Beacon Experiment Over Indian Subcontinent," *Beacon Satellite Measurements of Plasmaspheric and Ionospheric Properties*, Italy, pp. 3-1 through 3-6, 1979.

Donnelly, R. F., et al., "Interpretation of the Shape Factor at Ootacamund, India," *Beacon Satellite Measurements of Plasmaspheric and Ionospheric Properties*, Italy, pp. 17-1 through 17-15, 1979.

Donnelly, R. F., et al., "The Equatorial Total Electron Content and Shape Factor," *J. Geophys. Res.*, **84**, pp. 7359-7364, 1979.

Heron, M. L., and K. Davies, "The Use of Low Frequency HF Beacons to Derive Layer Shape," *Beacon Satellite Measurements of Plasmaspheric and Ionospheric Properties*, Italy, pp. 43-1 through 43-8, 1979.

Okuzawa, T., and K. Davies, "Pulsations in Total Columnar Electron Content," *J. Geophys. Res.*, **86**, 1981.

Rastogi, R. G., et al., "Amplitude Scintillations of ATS-6 Radio Beacon Signals Within The Equatorial Electrojet Region (Ootacamund, dip 4°N)," *Pramana*, **8**, pp. 1-13, 1977.

BIBLIOGRAPHY (continued)

Rastogi, R. G., et al., "Daytime Satellite Radio Scintillation and Sporadic E Near the Magnetic Equator," *Geophys. Res. Letters*, **4**, (3), pp. 113-115, 1977.

Rastogi, R. G., et al., "Simultaneous Observations of Equatorial Ionospheric Scintillation on Four Frequencies," *Nature*, **273**, No. 5660, pp. 285-287, 1978.

Rastogi, R. G., et al., "Total Electron Content and F-Region Electron Density Distribution Near the Magnetic Equator in India," *J. Atmos. Terr. Phys.*, **41**, pp. 561-564, 1979.

Sethia, G., et al., "Total Electron Content from ATS-6 Group Delay Measurements at Ootacamund, India," *Beacon Satellite Measurements of Plasmaspheric and Ionospheric Properties*, Italy, pp. 14-1 through 14-7, 1979.